Towards Functional Biomorph Microcomposites

Dissertation zur Erlangung des akademischen Grades eines Doktors der Naturwissenschaften (Dr. rer. nat.)

vorgelegt von

Julian Opel

an der

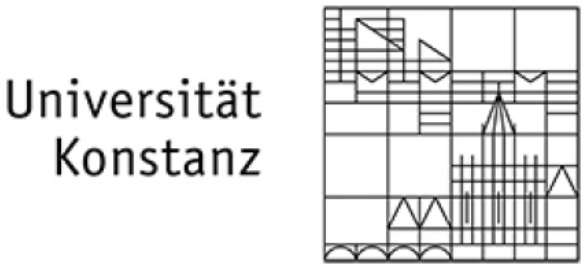

Mathematisch-naturwissenschaftliche Sektion

Fachbereich Chemie

Konstanz, 2021

Tag der mündlichen Prüfung: 22.10.2021
1. Referent: Prof. Dr. Helmut Cölfen
2. Referent: Prof. Dr. Alexander Wittemann
3. Referent: Prof. Dr. Juan-Manuel Garcia-Ruiz

When you investigate biomorphs, life is contamination. -

Juan-Manuel Garcia-Ruiz, 2015

Danksagung

Mein besonderer Dank gilt...

...Helmut Cölfen für die herausragende Betreuung, die schöne und lehrreiche Zeit in der Arbeitsgruppe sowie die Übernahme des Erstgutachtens.
...Juan-Manuel Garcia-Ruiz für die gute Betreuung und die schöne lehrreiche Zeit am IACT in Granada.
...Alexander Wittemann für die Übernahme des 2. Gutachtens.
...Matthias Kellermeier für den hilfreichen Input für Experimente und beim schreiben von Publikationen
...Elena Sturm für Support bei vielen Kristallogaphischen Fragestellungen.
...der gesamten AG Cölfen und insbesondere allen aus meinem Büro für die schöne Zeit.
...dem Team des Laboratorio Estudio Cristalografico für die tolle Zeit in Granada und insbesondere meinem Bürokollegen, Elektra, Joaquin und Leonardo.
...meinen weiteren Kooperationspartnern: Roland Kröger (York) für die Möglichkeit der ASEM Messungen; Tilman Grünewald (Grenoble) und Helga Lichtenegger (Wien) für EDLD Messungen; Marco Montalti (Bologna) für die Zusammenarbeit auf dem Gebiet der photoinduzierten Kristallisation; Knut Rurack und Mandy Hecht (Bundesamt für Materialforschung und -prüfung) für die Zusammenarbeit bei der Synthese pH sensitiver BODIPY Farbstoffe; Lisa Rosenbaum (AG Gaich) für die Synthese silanfunktionalisierten Spiropyranen; Johannes Boneberg, Peter Keim, Francois Lavergne und Lukas Siedentrop für die Unterstützung bei physikalischen Fragestellungen; Igor Zlotnikov (Dresden) und Antonia Pajares (Badajoz) für Nanoindentierungen, Karina Gense für die Bereitstellung von Inderwimperwerkzeug.
...Marina Krumova, Michael Laumann und Matthias Hagner für die Hilfestellungen im Nanolabor.
...dem Bioimaging Team unter Elisa May für die Möglichkeit die LSMs und das AxioZoom zu verwenden. Besonderen Dank an Martin Stöckl und Michael Schmalz für technischen Support.
...meinen Bachelorstudenten Cora und Ramon für die sehr gute Mitarbeit.
...meinen SPK Studenten und HiWis: Flo, Annika, Britta, Melli, Larissa, Thomas, Cathrin, Niklas, Anne, Anna-Lena, Ramon und Jessi für die hervorragende Zuarbeit.

...Domme, Britta, Pain und Andra für die Korrekturen.

...der Metrohm AG für das Drucken der Arbeit.

...meinen Freunden und meiner Familie für die moralische Unterstützung.

Publication list

Chapter 4.2-4.7 of this thesis are published in:

4.2: Opel et al., *Nanoscale*, **2015**, *7*, 17434-17440.

4.3: Opel et al., *Nanoscale Horiz.*, **2016**, *1*, 144-149.

4.4: Opel et al., *Minerals.*, **2018**, *8(2)*, 75.

4.5: Opel et al., *Adv. Funct. Mater.*, **2019**, *0*, 1902047.

4.6: Opel et al., *J. Mater. Chem. B*, **2020**, *8*, 4831-4835.

4.7: Opel et al., *Crystals*, **2019**, *9*, 157.

Contents

1 General Introduction

- *"A complex system that works is invariably found to have evolved from a simple system that worked. A complex system designed from scratch never works and cannot be patched up to make it work. You have to start over with a working simple system."* - [1] This famous statement made by John Gall, an American author, describes one philosophical approach of creating complex systems. Nowadays, this statement is known as Gall's law and can be applied to many different disciplines such as material science. Combining elementary systems exhibiting intriguing properties with additional functionalities and fusing them with further functional materials is a powerful pathway to constructing novel composites or hybrids extending the field of application for the utilized compounds. This work focuses on different self-assembled systems, especially silica-biomorphs, and their combinations. The different parts of this thesis intertwine like gear wheels as illustrated in Figure 1.1.

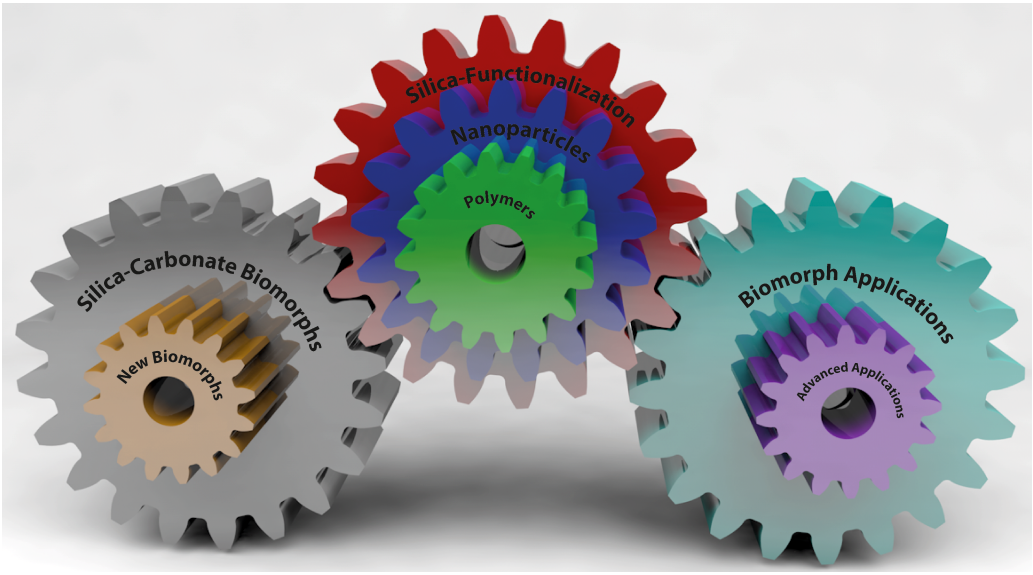

Figure 1.1: Illustration of the thesis structure combining multiple fields constituting new innovative functional materials based on silica-biomorphs.

The fundamental simple system in this thesis is a composite consisting of amorphous silicon dioxide (silica; SiO_2) and crystalline barium carbonate (witherite; $BaCO_3$). This one-of-a-kind system is able to form extraordinary morphologies in the micron range similar to living organisms. For this reason, these structures are called silica-biomorphs.[2] The outstanding self-assembled purely inorganic sculptures give rise to the desire to adapt and implement them into functional complex systems. Understanding and modifying this system constitutes the key step for the first gear wheel (grey) which

provides the bedrock for this work.

Based on the knowledge of additional functional materials, e.g. magnetite mesocrystals, and functionalization pathways, advanced systems can be created raising the complexity to the next level (central gear wheels).

In the third part (right gear wheels), the gained knowledge of the formation and functionalization mechanism is utilized for the synthesis of the complex systems targeting special applications such as biomorph-based micro-carriers. All the different parts of the simple systems must work together to fulfil their complex purpose. The overall assignment of this work is the amalgamation of the previously illustrated meshing gearwheels to design complex systems with multiple functionalities and, finally, establish a new class of biomorph-based materials.

2 State of the Art

The following sections illustrate the current state of the art for the relevant investigated topics published at the beginning of this thesis in 2015. Investigations and recent breakthroughs by other groups published during the project schedule will be set in context in the Concluding Remarks and Outlook (Chapter 7).

2.1 Biominerals

Nature is a rich source of outstanding materials stimulating the imagination of scientists for decades to understand and mimic materials' formation, morphology, and properties. Minerals, both geologic and biominerals, consist of mainly inorganic matter but the morphology of the living world differs tremendously from the non-living realm. Geologic minerals are shown in Figure 2.1 where the strict symmetry and angled facets are displayed. In this selection, the most important materials which will be discussed in this thesis are presented in their macroscopic, geological, and non-living form, i.e. earth alkaline carbonates, silica (and silicates), and iron oxides. Most of the shown minerals also appear later in this work but vary in their morphology. Figure 2.1 displays only macroscopic morphologies. Macroscopic carbonates are shown in 1 (calcite) and 7 (witherite). Calcite (trigonal crystal class, $R\bar{3}c$) shows bitrigonal-scalenohedral crystals while witherite as an orthorhombic crystal class (*Pmcn*) exhibits elongated bipyramidal morphologies with a pseudo-hexagonal outline.[3, 4] Both are supposed to be colourless but due to impurities, they show a pale brownish colour. Besides the carbonate crystals, Figure 2.1 also shows Si containing minerals (2, 3, 4, 6; SiO_2 and silicates). (2) is a Topaz (orthorhombic, *Pbmn*) which is a part of the class of the ortho-silicate minerals.[5] (3) is an α-quartz and called Morion (left-quartz, trigonal, $P3_121$). The colour originates from gamma rays and aluminium substitution induces a brownish to grey hue.[5] Minerals consisting of iron are also shown in the figure. The rose of iron (5) is formed from hematite (Fe(III) oxide, Fe_2O_3). Another iron oxide mineral is shown at number (9) as cubic magnetite crystals ($FeO \cdot Fe_2O_3$, Fe_3O_4). Another cubic iron-containing mineral is shown in (8) (pyrite, FeS_2). The ruby which is shown in (10) was selected to show the clear symmetry of minerals and because of its beauty.

In contrast to the strict symmetry of pure inorganic minerals, biominerals formed by living organisms consisting of similar inorganic components exhibit elaborate ar-

Figure 2.1: Photographs of selected crystals taken from the crystal collection of the University of Konstanz. (1) Calcite crystals ($CaCO_3$, Unterschächen/Uri/Switzerland); (2) Topaz orthorombic silicate ($Al_2[(F,OH)_2SiO_4]$); (3) Morion (SiO_2 - example for left quartz, Göschener Alp/Uri/Switzerland); (4) Mountain crystal (smoked quartz, Galenstock/ Switzerland); (5) Hematite (Fe_2O_3 - "Rose of Iron", Fedenstock/Uri/ Switzerland); (6) bi-pyramidal quartz ("Herkimer diamond", New York/USA); (7) Witherite ($BaCO_3$, Settlingsstones Mine/Northumberland/England); (8) Pyrite (FeS_2, Navajún/Spain); (9) Magnetite ($FeO \cdot Fe_2O_3$, Transversells/Piemonte/Italy), (10) Ruby (Al_2O_3, Beferona/Madagascar)

chitectures going beyond crystallographic restrictions and devouring the underlying crystal phases (Figure 2.2). A wide morphological variety from sinuous surfaces and smooth curvatures to hierarchical architectures can be attained.[6] Therefore, rounded shapes are, simply put, associated with living organisms while strict symmetric crystals with clear angled facets are attributed to the non-living world.[1] A collection of different biominerals can be seen in Figure 2.2.

These biominerals consist of nano-sized building blocks, formed in a bottom-up approach, and are integrated into the structure to provide the composite with its functionality.[6] The functional adaptation drives the appearance of morphological features resulting in remarkable structural diversity. Besides the multitude in shapes and sizes, the composition of biominerals is also versatile.[11] One of the pervasive mineral phases in nature is calcium carbonate.[12] Corals (Figure 2.2 B), Coccolith and other algeas (Figure 2.2 C,E) or sea urchins (Figure 2.2 D) are just some organisms using $CaCO_3$ as inorganic phase in their (exo)skeleton.[6–10] Nacre, a prominent example

[1] This generalizing statement is challenged in the upcoming chapters

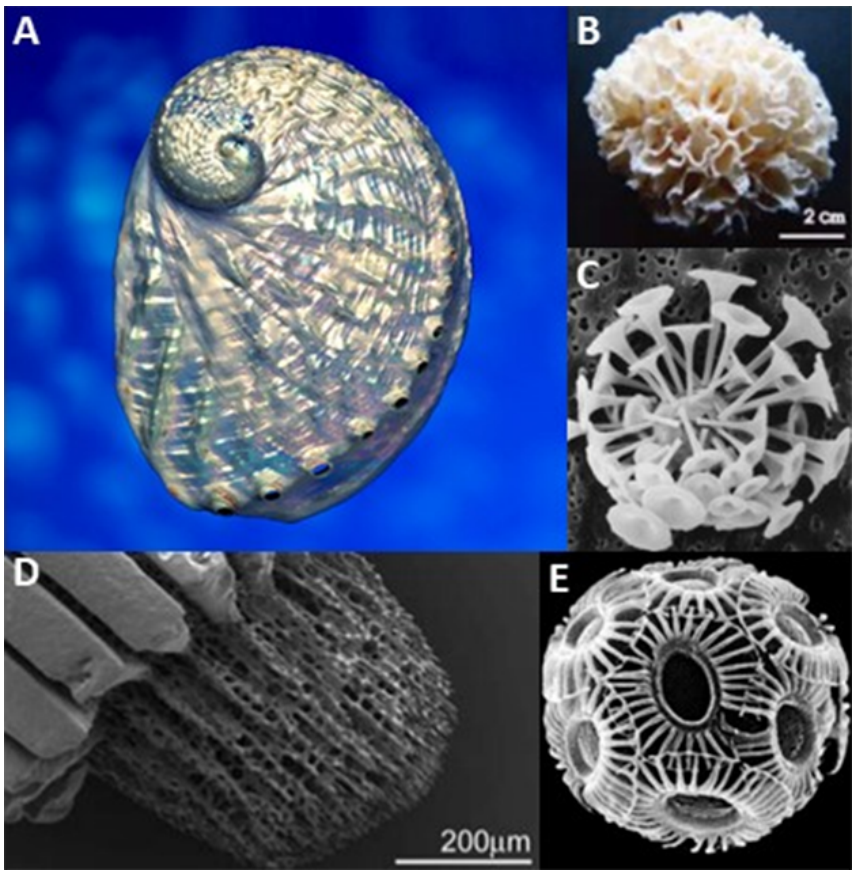

Figure 2.2: Collection of biominerals based on $CaCO_3$. A) Nacre shell (reprinted with permission from ref. [7]), B) Natural coral from southern Australia (reprinted with permission from ref. [8]). C) Marine coccolith (reprinted with permission from ref. [6]). D) Tip of a sea urchin spine (reprinted with permission from ref. [9]). E) Heterococcolith (reprinted with permission from ref. [10])

for $CaCO_3$ biominerals, can be found in specific mussel shells (e.g., *Haliotis pulcherina*)[7] and is composed of 95 wt.% $CaCO_3$ (aragonite) mineralized in a structural organic framework.[7, 13, 14] The organic matrix facilitates the partial orientation of the mineral phase.[15]

It is still under investigation how these structures are formed and how the growth is controlled by living organisms.[12, 16–24] Biominerals consist predominantly of inorganic phases and only minor amounts of organic components. Organic constituents influence the structural formation process and define the properties of the biomineral pivotally on all length scales. During the structural formation process a high degree of orientation of the building blocks is gained, leading to hierarchical architectures.

One example of the inner hierarchical structure of a biomineral is shown in Figure 2.3 A.[23] Here, a sea urchin spine was investigated with microtomography (μCT) measurements to show the complex porous setup on the cm to mm range. Within the porous structure, void spaces are interspersed with a composite of amorphous

and crystalline materials. The mineral phase includes crystalline calcium carbonate (calcite) and amorphous calcium carbonate (ACC) as well as biomolecules. It is assumed that the spines form from an ACC precursor phase[9, 25] bearing a sufficient amount of macromolecules and Mg^{2+} ions. This stabilizes the amorphous phase and so prevents fast crystallization.[26–29] The ACC precursor phase most likely acts as an ion reservoir for the crystallization of calcite, which partly expels or includes biomacromolecules.[30] The calcite crystals are hierarchically ordered and form mesocrystalline parts, which will be explained in Chapter 2.3.

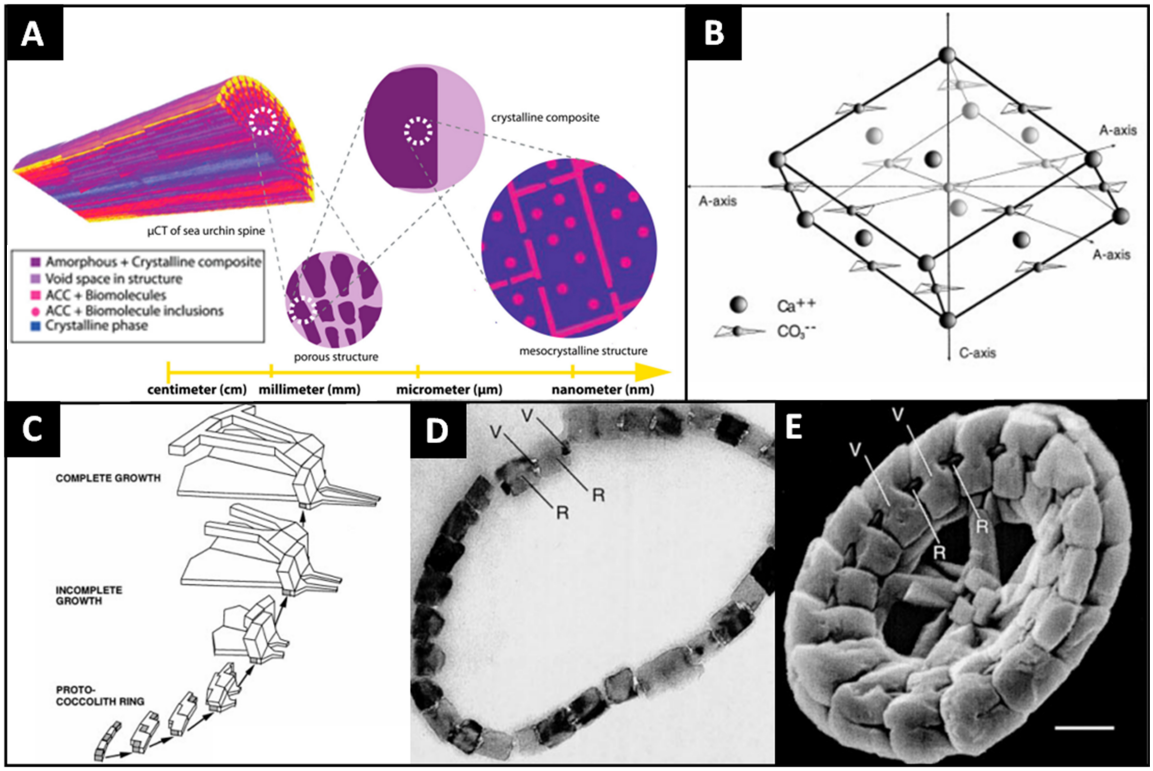

Figure 2.3: Structure of biominerals. A) Inner structure (microtomographic image) of a sea urchin spine (reprinted with permission from ref. [23]). B) Crystal structure of calcite. C) A coccolith growth sequence with the three typical stages. D) Transmission electron micrograph of the proto-coccolith stage. E) Scanning electron micrograph of the intermediate stage of a coccolith growth (reprinted from ref. [10], scale bars not defined by the author).

The crystal structure of calcite is shown in Figure 2.3 B. Depending on the additives, e.g. the macromolecules in the sea urchin spine, the crystal growth is highly influenced and the crystal morphology varies. Besides the quite large sea urchin spine, even smaller species have mechanisms to influence the crystal growth of calcite to their special needs; a group of these species are the coccoliths. An example of how these species form exoskeletons with $CaCO_3$ is also shown in Figure 2.3 C-E. Their formation starts with nucleation of a proto-coccolith ring of simple crystals with a vertically oriented c-axis. These parts are named V-units. They are linked to the radially oriented units

(R-units) and are found in the early stages in the proto-coccolith ring (*cf.* Figure 2.3 D).[10, 31] In the micrograph two types of nuclei are shown which are linked to the postulated V- and R-units. According to Young *et al.*, these two units grow from their distinct crystal units towards an intermediate incomplete growth stage until the final superstructure is formed.[10] The nucleation as well as the growth of the crystal are considered as distinct stages in the biomineral formation.
These two systems are summarized examples of how complex the biomineralization process can become.
Nature follows different approaches to control biomineralization. According to Mann *et al.*, the following key points are involved:[11]

- chemical control
- spatial control
- structural control
- morphological control
- constructional control

Chemical control includes physicochemical factors and processes, such as solubility, supersaturation, nucleation, and particle growth. Furthermore, it includes the media as well as additives which influence the mentioned parameters.[17, 32, 33]
Spatial control describes the mineral formation in confined spaces where the building blocks (atoms, ions, and molecules) are selectively transported gaining control over the chemistry and kinetics.[11]
The structural control describes the templating during mineral formation through an organic matrix, containing functional groups acting as nucleation sites or capping agents.[34]
The morphological control confines the available space and conducts the crystal growth towards specific directions. Here, an amorphous precursor phase can influence the morphology of a growing crystal.[29, 35]
Constructional control reflects the material's hierarchical architecture built via the assembly of individual building blocks over several length scales.
Additives play a ubiquitous role in biomineral formation: tuning functionality, controlling size as well as shape, and influencing their growth. The mineral forms in the

living and non-living world can, therefore, be explained by the presence or absence of these organic (and inorganic) additives. As the only difference are the additives, material scientists questioned themselves how to adapt their synthetic approaches to nature and mimic the biominerals with the goal to create artificial and synthetic materials surpassing their natural archetypes.

The idea of synthetic biominerals and bio-inspired materials can be realized by various approaches. In Figure 2.4 a selection of such materials is shown and the synthesis according to the following approaches:

- molecular templates
- supramolecular templates
- surface templates

which differ mainly in the chosen additives.[17]

By equipping molecules with functional groups, a certain degree of selectivity to control nucleation, crystal growth, and stabilization of the nanoparticle is given. The scheme presented in Figure 2.4 A, displays the process of a core-shell synthesis of CdSe-ZnS particles with a bifunctional peptide as a molecular template.[36] The peptide has a special amino acid sequence which provides selectivity to both cations needed in the final material. The cadmium binding domain of the peptide interacts with the provided Cd^{2+} ions in a first step followed by the addition of NaHSe resulting in well-defined and peptide-stabilized CdSe crystals. Afterwards, the material is incubated in a $ZnCl_2$ solution and the second zinc-binding domain of the peptide binds the available zinc ions to control the formation of the ZnS shell around the CdSe cores. As a final product, core-shell particles were obtained through a molecular-templated process, inspired by biomineralization controlled by small molecules.

In the next examples (Figure 2.4 B and C) synthetic biominerals were prepared *via* the supramolecular template route. In B the synthesis of CdS was controlled using coordination of the ions at a polymer nanoribbon resulting in nanoscopic CdS helices.[37] Within these helices, the CdS forms 4 to 8 nm large polycrystalline domains. The whole structure of the assembly comes from the organic supramolecular template which contains a triblock architecture called dendron rod coils. The cartoon illustrates how the blue helix serves as a template for the polycrystalline CdS (yellow) growth along the supramolecular surface. In Figure 2.4 C another supramolecular-templated

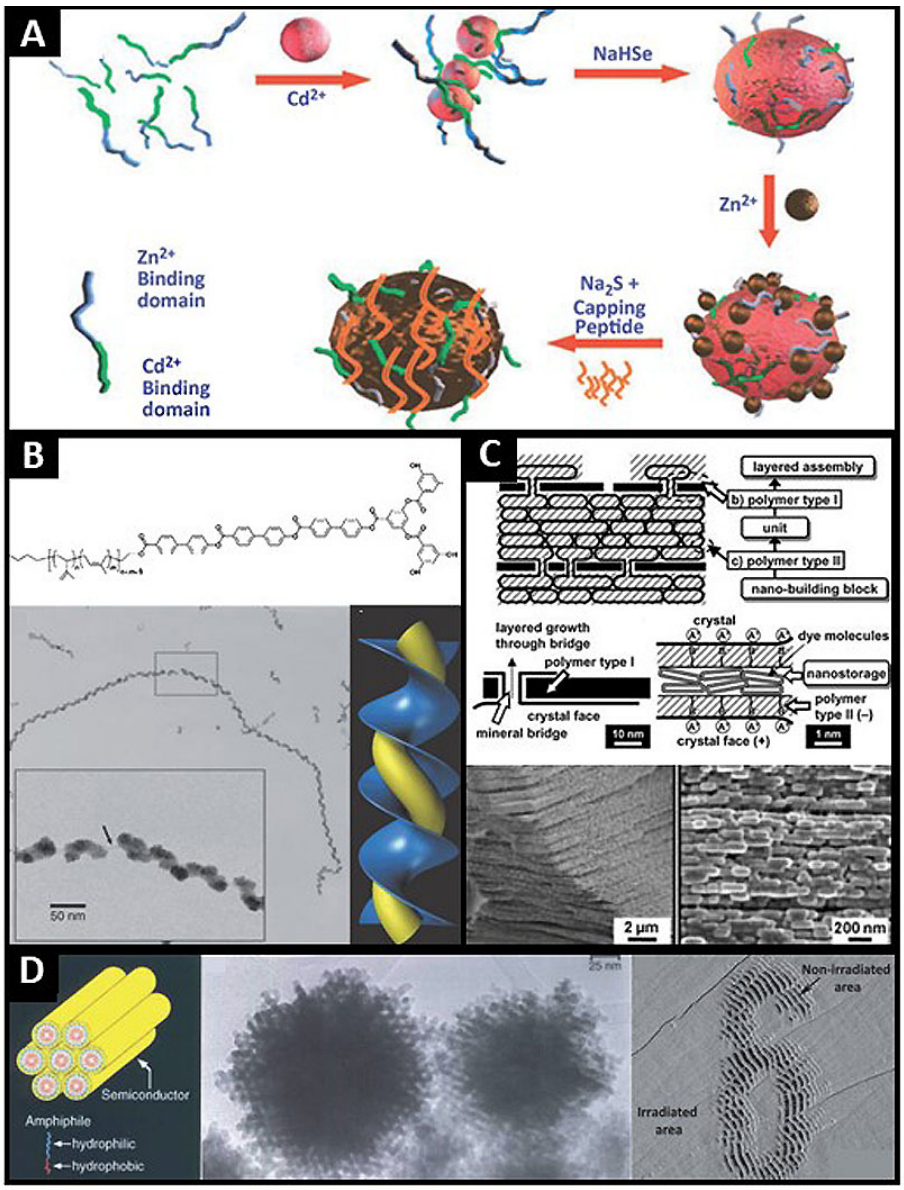

Figure 2.4: A) Illustration of a biomineral inspired synthesis of core-shell nanoparticles of CdSe with ZnS through bifunctional peptides (reprinted with permission from ref. [36]). B) Chemical structure of dendron rod coil, a TEM image of CdS helicoidal structures precipitated in the presence of the rod coil, and a 3D animated figure how CdS (yellow) is templated (reprinted with permission from ref. [37]). C) Schematic illustration of nacreous layer formation of K_2SO_4-PAA composites and the corresponding SEM images (reprinted with permission from ref. [20]). D) Cartoon of CdS formation around self-assembled amphiphiles and its corresponding TEM image (reprinted with permission from ref. [38]). On the right side of D) calcite crystals formed on a PVA-SbQ photomask (reprinted with permission from ref. [39]).

approach is shown. Here, the authors mimic nacre by preparing a hierarchically organized structure of K_2SO_4 and polyacrylic acid (PAA).[20] The structure consists of crystal plates which are up to 1 μm thick and form an oriented assembly. The structural appearance resembles nacre and is fabricated as illustrated in the figure. To achieve the hierarchical structure, two polymer types are involved - soluble and insoluble ones. The layered assembly is controlled through the insoluble polymer (type I)

and can be compared to chitin and hydrophobic proteins in biominerals.[40, 41] The next layer can be formed *via* a mineral bridge. The soluble additives (type II) containing polar groups (e.g. amines, carboxylates or hydroxides) interact with the polar surfaces of the crystals to produce building blocks with controlled morphology and orientation. In case of the mimetic nacre from Oaki *et al.*, the PAA functions as the soluble type II additive, and its excess which is not interacting with the crystal surfaces acts as a type I additive. This example demonstrates the action mechanism of supramolecular templates for creating biomimetic materials.[20]

The example of a surface-templated approach shown in Figure 2.4 D is the formation of biomimetic materials on organized surfaces. A modification of the surface can directly influence the nucleation, a crystals' orientation, polymorphism, and morphology of the forming crystals.[42–44] This allows a controlled formation of films and arrays. These surfaces can be 2D or 3D. A 2D example is presented on the right side in the scanning electron micrograph: a substrate was coated with a poly(vinyl alcohol) (PVA) with a photosensitive PVA derivate with styrylpyridinium groups (SbQ). Applying a mask (e.g. the number 6 as shown in the figure) allows a selective light-induced formation of $CaCO_3$ crystals.[39, 45] On the left side a 3D assembly of amphiphiles was used to create an organic-inorganic composite with CdS as the inorganic phase.[38] This structure can be obtained using an oleyl block which forms the core of the segments while a hydrophilic domain is exposed to the solution and can work as a nucleation site for the CdS crystals.

In this chapter, exemplary biominerals and presented biomimetic approaches demonstrate the huge variety of structures and functionalities that have been discovered in this field so far. The uniting component was that organic matter fused with inorganic crystals outclass the pure inorganic substance in its properties. If only organic matter is suited for these purposes will be answered in the upcoming chapters.

2.2 Silica-Biomorphs

The above-described principles of biomineralization state that only organic additives are suitable as crystal growth modifiers and allow the formation of hierarchically ordered structures. So far, only slight impacts of inorganic additives are mentioned and they draw far less attention in the mineralization processes. One example of inorganic additives and their effect on mineralization is the influence of Mg^{2+} ions on the poly-

morphism of $CaCO_3$.[46] The potential to modify the materials and even to enable the formation of superstructures was considered rather limited for simple inorganic additives. Due to this assumed limited impact of inorganics, silica (SiO_2) - another simple inorganic species which forms in gels - was considered an ideal media for the growth of large single crystals and gained popularity in the renaissance of crystal growth in gels in the early 1980s.[47, 48] In abiotic environments the formation of life-like morphologies with non-crystallographic orientation was unthinkable until Garcia-Ruiz *et al.* discovered crystal aggregates in silica-gels with very unusual shapes.[49, 50] These forms mimic natural appearances and are therefore named silica-biomorphs. These findings challenge the determination of biogenicity only by morphology as an indicator of life.[2]

2.2.1 A Unique Appearance - General Introduction to Silica-Biomorphs

Silica-biomorphs are an outstanding finding in the field of self-organized, pure inorganic matter. They are formed in moderately alkaline silica sols if earth-alkaline metal ions like Ba^{2+}, Sr^{2+} or Ca^{2+} are present.[51–53] They appear in multiple forms which are shown in the morphodrome in Figure 2.5.[51]

As shown in Figure 2.5, biomorphs can be quite compact and resemble worm-like beings (first picture) or show more leaf-like and fragile appearances. Between these structures, there are different transition states and structural mixtures.[54] The main research aspect in this field is to understand the system, the formation process, and parameters which allow to manipulate the final shape. The first discovered morphologies were twisted ribbons, helicoidal and leaf-like structures.[50] They were grown in silica gels and named *induced morphology crystal aggregates* (IMCAs). The experimental setup filled with silica gel is shown in Figure 2.6 A (adapted from [50] and redesigned). Inside of a gel cassette, silica gel was prepared by acidifying a sodium silicate solution.[49] After gelification, the gel was overlayed with an earth-alkaline metal ion solution or a cation and anion precursor solution were injected. The material formation occurred close to the centre of the gel cassette. In the first experiments ever performed, biomorphs appeared at the gel-earth-alkaline solution interface. It was quite surprising because the chosen counter ion in these experiments was sulfate and barite ($BaSO_4$) crystals were expected in the centre. After investing the formed structures which looked like biological contamination, the formed crystalline material

Figure 2.5: SEM morphodrome of different silica biomorph motifs. (reprinted with permission from ref.[51])

turned out to be witherite ($BaCO_3$). Through counter diffusion of dissolved carbonate from the gel to the gel-liquid interface and the cation into the gel, the formation of biomorphs occured at various positions within the gel. In later studies, an additional carbonate source was placed on the other side of the gel or directly inside the gel.[50, 55] Besides the gel capillary experiments, identical architectures were obtained from diluted silica sols with SiO_2 contents of 250 to 1000 ppm and an earth-alkaline metal ion concentration of 5 mM up to 0.5 M.[52–54, 56–59] Compared to gels with an initial pH of 9.3-9.8 [60], the structures in solution are formed at initial pH values of 10.2 to 11.1.[61] Furthermore, Figure 2.6 B-D shows the main morphologies that were obtained in these conditions. A substitution of barium ions with strontium ions resulted in the same structures. An explanation for this finding is that strontianite ($SrCO_3$) forms nearly identical crystal architectures as witherite ($BaCO_3$) as they are isomorphic minerals and part of the orthorhombic group *Pmcn*.[58, 62] Also, the interactions of the lattice surfaces with the surrounding medium are nearly identical which results in a comparable growth mechanism. Lighter earth-alkaline carbonates,

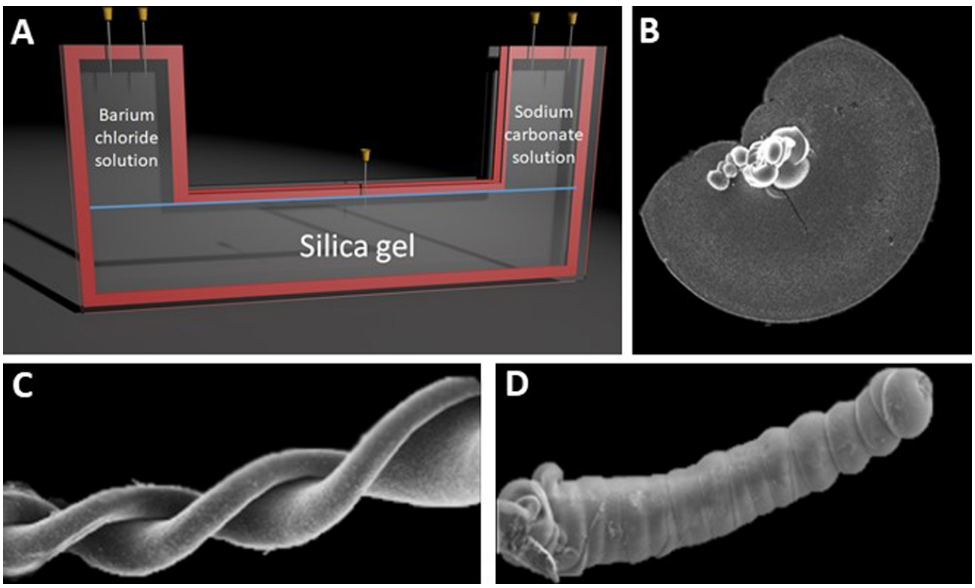

Figure 2.6: A) Adapted scheme of the gel capillary of the first growth of biomorphs. B)-D): scanning electron micrographs of a biomorph sheet (B), helix (C) and a biomorph worm (D) (adapted with permission from ref. [51]).

especially the rhombohedral magnesite ($MgCO_3$) and calcite ($CaCO_3$)[2] with the space group $R\bar{3}c$ did not produce structures fitting the definition of biomorphs. Biomorphs are defined as purely inorganic crystal aggregates with elaborate life-like architectures and complex curved morphologies. Nonetheless, calcite also forms/formed interesting structures in silica gels. e.g. finger-like structures which are cleaved rhombohedral crystals, linked through their c-axis.[63, 64] Further calcite structures which appear in the presence of silica show a three-fold symmetry with a mutual angulation of 120° that originates from selective adsorption of silica species on the {110} calcite face, transforming the crystals from rhombohedral to star-like shapes.[64–66] When modifying the reaction conditions towards aragonite formation (a polymorph of calcium carbonate with orthorhombic crystal class and isomorph to witherite and strontianite) structures were achieved that can be considered real biomorphs.[67] Unfortunately, twisted ribbons and helicoidal structures were not obtained from calcium carbonate. A possible explanation for this finding might be the higher polarity of small cations and their hydration as well as their different interaction with the silicate species. This agrees well with their tendency to promote silica condensation (v_{cond}) with decreasing cation size:[51]

$$v_{cond} \propto c(Ba^{2+}) < c(Sr^{2+}) << c(Ca^{2+}) < c(Mg^{2+}) \quad (1)$$

As the velocity of the silica condensation also influences the crystal precipitation these

[2] Biomorphic structures were later found for aragonite and monohydro calcite.

two processes influence each other and lead to a further variety of life-like shapes.

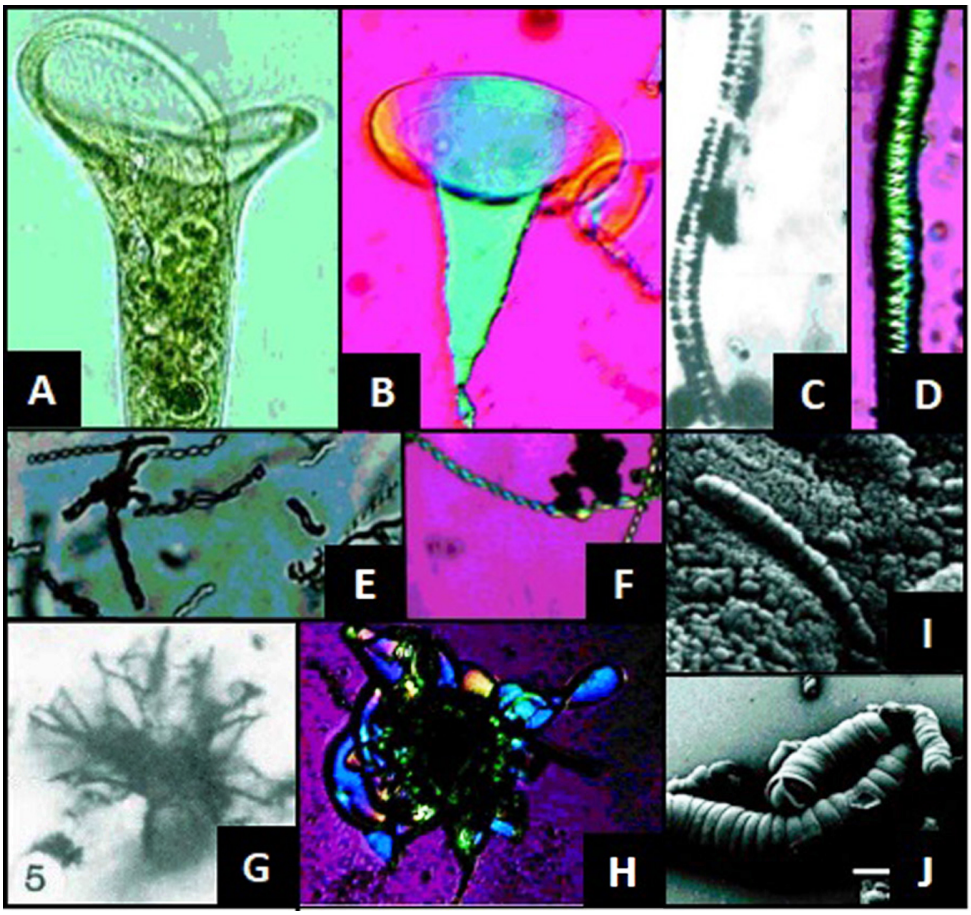

Figure 2.7: Comparison of naturally occurring morphologies and pure inorganic biomorphs. A) Optical microscopy image of a protist *Stentor roeseli* compared to a trumpet-like silica biomorph (B). C) Optical microscopy image of a late Precambrian microfossil (*Calyptothrix annulata*) found in bitter springs (central Australia) compared to a biomorph worm (D). E) Optical micrograph of bacteria *G. ferrudinea* and helicoidal biomorphs (F). G) Optical microscopy image of a middle Precambrian Duck Creek microfossil *Eoastrion* (found in western Australia) compared to silica biomorph leaves (H). I) SEM image of a carbonate aggregate found on the Martian meteorite ALH84001 and an SEM image of a biomorph worm (J). (Images are reprinted from [2, 68])

Due to the fascinating shapes formed in this abiotic system that resemble structures occurring in the living world, the term biomorphs was established and is nowadays a common expression used to describe these composites. The occurrence of such shapes in purely inorganic systems mandates an additional task for the research concerning biomorphs because many ancient microfossils show similar structures.[2] The determination techniques to specify the biogenicity of microstructured fossils is thus challenged because there cannot be a strict distinction between an organic and inorganic form based only on its morphology.[2, 52, 69, 70] Figure 2.7 shows multiple examples of how silica-biomorphs mimic living organisms or fossils. Therefore, the morphology alone seems to be an ambiguous indicator of biogenicity at best, which was also the

title of a manuscript published in 2002 by García-Ruiz *et al.* in Astrobiology.[2] The examples shown in Figure 2.7 were reprinted from this publication and demonstrate the huge morphological variety of silica-biomorphs. In this figure, biomorphs are distinguished from their natural equivalents by the purple background in the polarized light microscopy images (PLM). In A, a protist (*Stentor roeseli*, microscopic living being) in a trumpet-like shape is mimicked by a trumpet-shaped silica biomorph which is shown in Figure 2.7 B. Another micrograph of a living being is shown in E. Here, the presented bacteria exhibit a helicoidal shape. This shape can also be formed by silica-biomorphs as shown in the PLM image F. Microfossils found in ancient rocks are shown in C and G. Again, these morphologies can also be exhibited by silica biomorphs, e.g. in D as a worm-like braid or in Figure 2.7 H as an aggregate of multiple biomorph leaves. Besides finding primitive life on earth and ancient rocks, space provides further interesting morphological formations (*cf.* Figure 2.7 I) which also resembles living beings or a silica-biomorph which is shown in J.

2.2.2 Composition of Biomorphs

Different analytical technics can be employed to investigate the composition of silica-biomorphs. X-ray diffraction analysis provides information about the crystalline phases of the biomorphs, namely the carbonates.[2, 57, 59] The amorphous silica layer can be investigated with spectroscopic methods like infrared (IR) or energy-dispersive X-ray spectroscopy (EDX).[8, 54, 58, 62, 67, 71] While investigating the morphology with scanning electron microscopy, an EDX analysis can be performed at the same time resulting in space-resolved spectra. A layer of silica nanoparticles with typical diameters between 50 and 150 nm can be observed around the silica-biomorphs. Depending on the growth time and chosen conditions, the relative amount of silica compared to the earth-alkaline metal content seems rather low (approximately 5-50 at.%). These huge deviations originate mainly from the silica shell that covers the whole structure. Also, the region where the measurement was performed influences the result tremendously. One reason is that EDX measurements are surface sensitive and, as mentioned before, biomorphs are mainly covered in a silica shell resulting in a higher silicon content compared to the core material. Ground biomorphs yielded a far more realistic amount of the Si/Ba ratio of 0.2-0.3.[71] If the structures did not contain an outer silica membrane the Si/Ba ratio was even lower (0.02 to 0.1).[54] Therefore, the silica content

within the core material linking the nanocrystals can be considered quite low.
Another interesting way to investigate the composition of biomorphs is by dissolving the components selectively. Inserting the structures in sodium hydroxide solution dissolves the silica while acids, e.g. diluted acetic acid, result in the dissolution of the inner carbonate core. In this way, a hollow biomorph structure which consists only of the outer silica skin is obtained. These structures maintain their original morphology and are called biomorph ghosts (*cf.* Figure 2.8 A).[2, 52, 56, 59, 62, 71]

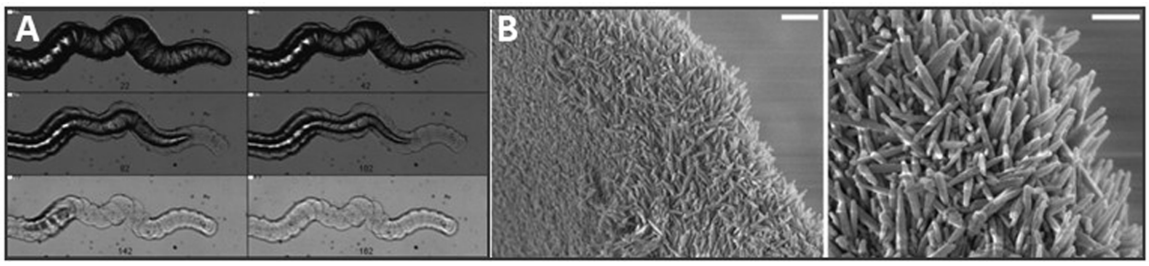

Figure 2.8: Composition of biomorphs. A) time-resolved image of a biomorph worm in diluted acetic acid (reprinted from ref. [2]). B) Close up view of exposed witherite crystals in a biomorph sheet (scale left 1 μm and right 500 nm; reprinted from ref. [51])

While dissolving the carbonate core with diluted acids, space-filling silica networks were found in a few cases allowing for the assumption that the crystal phase bears co-precipitated silica. Due to its rare appearance, it can further be assumed that the amount of co-precipitated silica varies between each experiment and structures.[62]
Immersing the biomorphs in quite concentrated NaOH solution (1 M) exposes the polycrystalline architecture. Figure 2.8 B shows a close-up scanning electron micrograph of a biomorph sheet without an outer colloidal silica membrane. The crystals look quite uniform and are partly radially aligned. Each crystal can be seen as an individual nanorod which exhibits a pseudohexagonal habit.[54] This shape is common for aragonite-type carbonates and the result of a twinning along the {110} plane.[72] The obtained rods are 200 to 400 nm long and 5 to 100 nm in width.[52, 56, 57, 71, 73] The amount of silica (in fact silicon) inside of the nanorods can be up to 5%. It is unknown how the Si amount interacts with the nanocrystals, but it can be assumed that silicate ions are incorporated into the carbonate lattice. This incorporation promotes the pseudo-hexagonal growth and modifies the cell parameters which was observed in X-ray diffraction studies.[59] Besides incorporation of silicate species in the crystal structure itself, a coating of the single nanorods with a thin silica layer is discussed. This could not be verified yet but the growth conditions would allow such an assumption.[54, 62] This might also explain the stability of the nanorods and the

certain amount of silica that can be found in the bulk material of silica-biomorphs. Additionally to coating, it might bridge the single units together. After understanding the composition of biomorphs, it is mandatory to investigate the formation process to be able to influence the biomorph form, composition, and functionality.

2.2.3 Formation Mechanism

The formation process of silica biomorphs can be separated into three fundamental stages which were revealed by Kellermeier *et al.* and each stage can be separated by the bulk pH value of the growth solution.[54]

Stage 1: globular particle formation through fractal branching

Despite the multiple morphologies which can manifest at the end of the growth process, all structures originate from a single micron-sized carbonate crystal. This crystal nucleates once the carbonate concentration in the alkaline solution, which gradually increases through the diffusion of atmospheric CO_2 into the mixture, reaches the critical supersaturation. During the growth of the crystal, silicate species induce a poisoning resulting in the branching of the crystal tip.[53, 74] This branching process can be seen in Figure 2.9 A) in the time-resolved light microscopy images where the first and second generation of branching can be monitored. Figures 2.9 B-D provide the corresponding scanning electron micrographs of these stages.[51] Despite the orthorhombic crystal class of witherite (*Pmcn*), a hexagonal appearance can be observed in Figure 2.9 E as the initial crystal of the dumbbells.[74] This phenomenon results from the twinning of the crystal that is quite common for the isomorphic $CaCO_3$ polymorph aragonite as well. The continuous branching initiates the so-called "rod to dumbbell to sphere" mechanism which can be found in many systems, e.g. in fluorapatite.[75] This mechanism is illustrated in Figure 2.9 F and supported by the SEM images in G and H.[75] In the beginning, the silica poisoning affects the splitting along the basal {001} plane or the bipyramidal faces at the {102} and {021} plane. At this stage, the silica does not adsorb onto the surfaces and, as a consequence, it is pushed ahead of the growing crystal. This has already been reported for other systems[76, 77] and results in first-generation branches which encounter poisoning as well. This results in the next generation of fractal branching. Through the ongoing branching, the structures evolve into the cauliflower forms which are shown in Figure 2.9 F, G and H. Silica itself

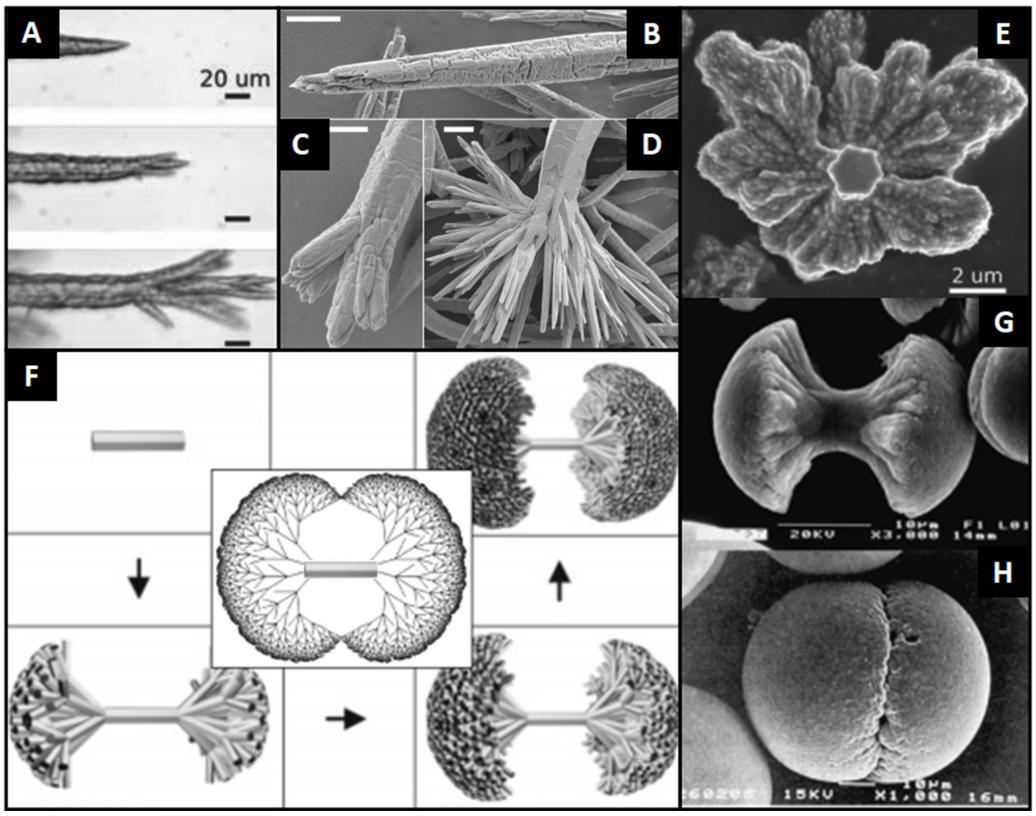

Figure 2.9: The formation mechanism of the globular apex or dumbbells. A) Light microscopic time-lapse images of a growing witherite crystal including the first and second generation of branching. B-D) Scanning electron micrographs of a single witherite crystal before branching (B), after the first branching (C) and multiple branchings steps (D). E) SEM image of an open dumbbell exposing the pseudo-hexagonal starting crystal. F) Computerized visualization of the dumbbell formation. G, H) SEM images of dumbbells (here fluorapatite) at an early stage (G) and after the full dumbbell formation (H). (Scale bars are: A: 20 μm; B, C, D: 5 μm; E: 2 μm; G,H: 10 μm. Images are reproduced with permission from [51, 74, 75].)

is nearly not absorbed during all these branching processes resulting in Si/Ba atomic ratios < 0.01.[54] This very low Si/Ba ratio can be explained with the high pH of the growth solution and the majority amount of silica remaining dissolved. It can further be assumed that the fractal branched mother crystal's evolution to the dumbbells is supported by nanoscale building blocks of carbonate. These subunits may be co-aligned along with their *c*-axis and may exhibit single crystal-like diffraction patterns. If this is true, these particles match the definition of mesocrystals (will be explained in Chapter 2.3).[75, 78] Even if it is not fully discovered for this particular system, the model of the impurity-induced branching in crystallographic and in later generations also non-crystallographic angles is broadly accepted. The obtained globular sphere serves as the starting point for even more complex morphologies. The first stage is terminated once all active growth sites on a globular apex are blocked by silica. This goes hand in hand with a significantly lower pH value. The next stage is initialized

once the supersaturation of carbonate and the corresponding earth-alkaline metal ion is high enough to induce further carbonate nucleation. The morphologies formed in the second stage determine the final shape of the silica-biomorph.

Stage 2: polycrystalline growth

This stage is initialized through nucleation of carbonate crystals that orient themselves to the underlying lattice of the globular particle. The crystals begin to generate a growth front leading to polycrystalline mineralization. They are generated frequently under the present conditions, but their growth is directly aborted by interfering silica. Due to the direct abortion of the crystal growth, the continuously increasing saturation pressure on the carbonate system can only be relieved through new carbonate nucleation. This phenomenon results in a continuous formation of nanocrystalline building blocks within this stage.[74] The building blocks attach and assemble to form laminar segments.

It is crucial to understand why the crystal growth is blocked on the nanoscale and how the attachment of the building blocks works to create superstructural motifs on the micron scale. For this reason, the pH dependence of silica and carbonate formation must be understood. In the pH range where the biomorph formation occurs, typically between 9 and 11, carbonate and bicarbonate exist in an equilibrium (*cf.* Figure 2.10 B). Formation of earth-alkaline metal carbonates and their precipitation continuously shifts the equilibrium while acidifying the solution. This continued release of protons reduces the solubility of silica by forming free silanol groups (Si-OH) which can further undergo polycondensation. Therefore, two pH-coupled reactions operate within this system:

- earth-alkaline metal carbonate precipitation lowers the pH through proton release
- silica condensation consumes released protons and increases the pH.

The silica biomorph formation includes a stage where an autocatalytic co-precipitation is continuously forming the two building units. This process is illustrated in Figure 2.10 A.[51] This autocatalytic process resembles other oscillating reactions which are deflected from their equilibrium state like the popular Belousov-Zhabontinsky reaction.[82] In the illustration, the carbonate nanorods are formed (red) and covered

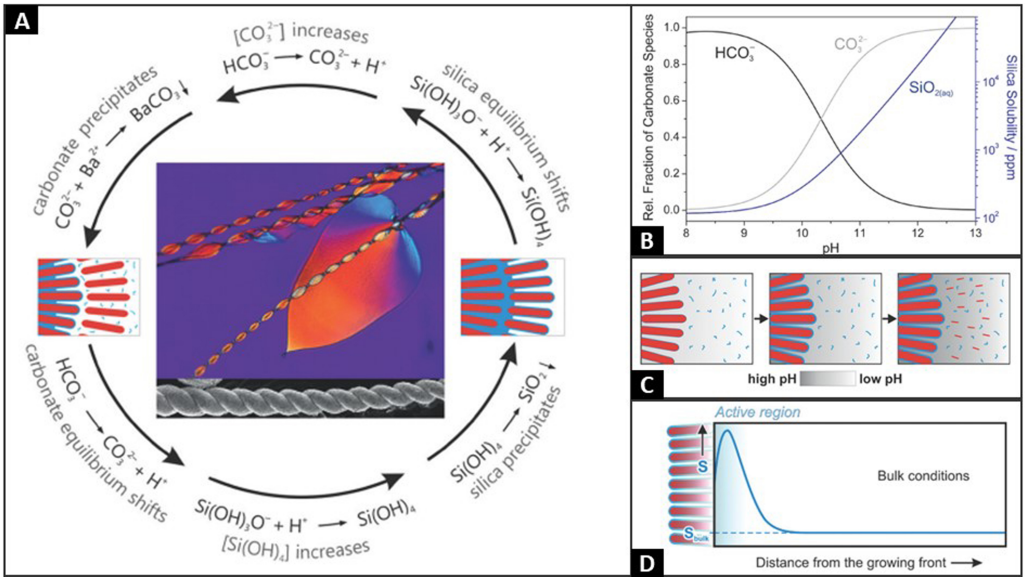

Figure 2.10: A) Autocatalytic co-precipitation depending on released protons in a witherite-silica system. B) Distribution of the carbonate (black) and bicarbonate (grey) species as a function of the pH and the solubility of silica as a function of the pH (blue curve and second y-axis; reprinted from ref. [51, 79]). C) Schematic illustration of the ongoing silica condensation and its influence on the pH (reprinted from ref. [80]). D) Profile of the supersaturation as a function of the distance from the growth front of silica and witherite (reprinted from ref. [81]).

by a thin silica layer(blue). Therefore, this cyclic process should result in local pH gradients as shown in Figure 2.10 C. Once the carbonate is precipitated directly at the growth front, the local pH close to the front decreases resulting in a promoted silica condensation close to the edge of the structure. While silica is formed, the pH close to the growth front is increased again leading to further carbonate nucleation events. Therefore, it can be assumed that the material formation is not equally distributed in the whole bulk solution. It seems to be a local effect which is observed in an active region close to the growth front of the biomorph. This is also illustrated in Figure 2.10 D.[81] Nevertheless, until the beginning of this thesis, the local pH changes were not yet proven by experiments. Also, the assumed pH oscillation is not represented in the bulk solution. In fact, the bulk pH decreases over time through the ongoing diffusion of atmospheric CO2 into the solution.[3] Another interesting finding is that the bulk solution does not reach a sufficient supersaturation level to allow homogeneous nucleation (Figure 2.10 D).[54, 61, 81]

The presented growth mechanism explains the material formation including the sizes of the building blocks but not how the complex shapes in this stage are formed. A quasi-two-dimensional radial growth of biomorph sheets around a globular apex would

[3]Investigations from 2016 by Nakouzi *et al.* showed biomorph formation under CO_2 exclusion and constant bulk pH values.[83]

be expected (*cf.* Figure 2.11 A).[74] Illustration A shows how a typical growth front consists of merging co-aligned nanorods (red) connected through silica (blue). The question remains how more complex structures evolve out of these structures. Surprisingly, the growth of biomorphs does not follow an unhindered radial expansion of the 2D sheets with a nearly constant radial growth velocity of V_ρ. In fact, it is limited in most cases through curling at the rims. This curl is shown in Figure 2.11 B. In the SEM image, it can be seen that also the nanocrystals align within the curl. This curling is the true origin of the smooth curvatures and life-like appearances of silica biomorphs. The curling has two consequences for the resulting superstructure:

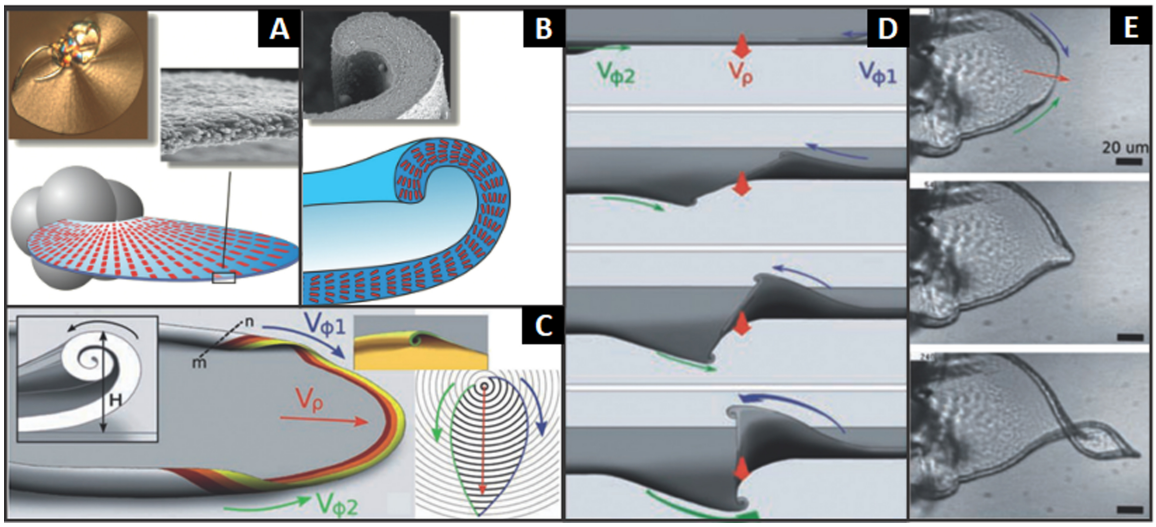

Figure 2.11: A) Biomorph sheet and illustration of the quasi 2D-growth. B) Illustration of the curl of a biomorph sheet with its corresponding SEM image. C) Schematic illustration of the tangential propagation of curls on a biomorph sheet. D) Schematic view on the edge to show how the azimuthal growth velocities and the height form a regular helix. E) Light microscopic time-lapse images of a forming helicoidal structure. (reprinted with permission from ref. [51, 74, 80])

- It hinders radial enlargement of the structure
- The curls itself propagate along the rim of the sheet

This means that most of the biomorph sheets emerge in a leaf-like form and not as a disc. The propagating curls result in a limitation or a transformation of the growth. This depends on the orientation of the curls as well. First, we will take a look at the simplest example that is illustrated in Figure 2.11 C: a biomorph sheet growth with the radial growth velocity V_ρ, which is typical $1\frac{\mu m}{min}$.[51] The rims of the sheet exhibit curls which arrest the radial growth and are propagating with the azimuthal growth velocities $V_{\phi 1}$ and $V_{\phi 2}$. Assuming that the azimuthal growth velocities are slightly

higher than the radial one, both curls encounter each other at the tip of the biomorph sheet. Here, the growth will be stopped once the curls have a similar height (H) and do not have the same orientation. The symmetry of the sheets varies due to the differences in the azimuthal growth velocities. If they are nearly identical they result in a nearly perfect cardioid.[74]

Accordingly, the morphology of each structure depends strongly on the described empiric parameters. The next shown example demonstrates the formation of a helicoidal structure. Here, the orientation of the two propagating curls is identical (both clockwise or both anticlockwise). The helix formation is displayed in Figure 2.11 D and E. Once the curls approach with an approximately identical velocity and the same height, the sheet begins to wind around itself resulting in a helicoidal shape. This can be seen in the light microscopy images in Figure 2.11 E. The helicoids are also not identical. Depending on the different growth velocities and the height of the curls, the structures vary. To obtain a nearly perfect helicoidal structure the growth velocities should be nearly the same:

$$V_{\phi 1} \approx V_{\phi 2} \approx V_{\rho} \tag{2}$$

If structures exhibit a more tightly wound shape, the growth follows this condition:

$$V_{\phi 1} \approx V_{\phi 2} >> V_{\rho} \tag{3}$$

The last main structure of silica biomorphs is the worm-like braid. As they are the predominant motif, their growth should also be explainable through the defined parameters. Observations allow the suggestion that a biomorph worm is developed once one curl is significantly larger and propagates much faster than its counterpart:

$$H_1 >> H_2 \qquad \text{and} \qquad V_{\phi 1} >> V_{\phi 2} \tag{4}$$

All these parameters do slightly vary at each growth front of each structure. Therefore, all biomorphs are unique and inimitable. at this stage, the final shape of the biomorphs is defined and will be finished and preserved within the last stage

Stage 3: Aging effects and secondary precipitations

In this stage, the polycrystalline growth of nanoparticle building blocks is finished. The pH of the bulk solution has dropped significantly. The biomorphs are finished with an outer layer of silica passivating the structure. If the structures stay in the

growth solution longer, the silica layer becomes thicker. With increased growth times, more carbon dioxide is dissolved in the solution and at a certain point, further carbonate crystals precipitate and grow. At this stage, no coupled co-precipitation occurs anymore. These newly formed crystals attach to the structures as well. These secondary processes will get more important later.

2.3 Mesocrystals

As mentioned before, biominerals and biomorphs can exhibit mesocrystalline regions. To understand what this means, the concept of mesocrystals needs to be introduced. The definition of a mesocrystal was given by Cölfen and Sturm stating that a mesocrystal is a *"nanostructured material with a defined long-range order at the atomic scale, which can be inferred from the existence of an essentially sharp wide-angle diffraction pattern together with clear evidence that the material consists of individual nanoparticle building blocks."*[84]

This means mesocrystals result from an oriented alignment of nanocrystalline building blocks.[85, 86] First, it is essential to understand how nanocrystals can be formed and why they are interesting as a material. In general, nanoscopic particles have a size between 1 and 1000 nm in at least one dimension.[87] They exhibit outstanding properties which can differ from their macroscopic equivalents caused by the much higher surface to volume ratio. Changed properties can be optical[88], catalytic[89], chemical[90], physical[91], electronical[92], and magnetic[93]. The synthesis of nanoparticles can be achieved by two methods - the top-down and bottom-up approach. In the top-down-approach, a bulk material is broken down into nanoparticles. This can be done mechanically, chemically or through lithographic methods.[94] The more widely applied bottom-up approach results in much more monodisperse particles by building the particles from a (molecular) precursor which forms activation clusters that can grow into nanoparticles. To control size and shape, stabilizers are commonly used to prevent the particles from aggregation and secondary growth effects, e.g. Ostwald ripening.[95]

Like all other nanoscopic structures, mesocrystals are thermodynamically unstable and, therefore, an intermediate state of a macroscopic crystal. In the schematic illustration in Figure 2.12 mesocrystal formation processes are described. The synthesis starts via a bottom-up approach from ions or molecules from a single-source sys-

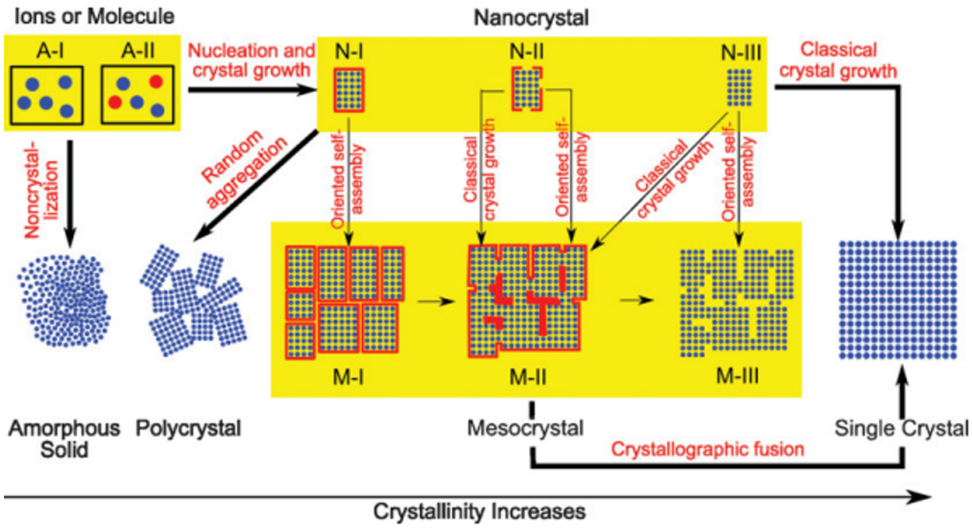

Figure 2.12: Schematic illustration of different formation pathways of mesocrystals. Initial states A-I and A-II generate nanoscopic intermediates N-I (stabilized), N-II(partly stabilized) and N-III (not stabilized). These particles can generate mesocrystals (M-I - M-III) via different pathways and may form a final single crystal (reprinted with permission from ref. [96]).

tem (A-I), e.g. gold nanoparticles, or multi-source system (A-II), e.g. calcium carbonate. From this stage, they can remain as non-nucleated precursors in solution or start to nucleate in a non-classical crystallization process to form an amorphous solid or nanoscopic crystals that continue to grow (also non-crystalline particles can be formed, but for the sake of introducing mesocrystals these materials are omitted here). The nanoscopic crystals can be stabilized with surfactants which lower the surface tension and ensure that the nanoparticles stay dispersed. In the scheme, stabilized (N-I), partly stabilized (N-II) and non-stabilized particles (N-III) are presented. Depending on the stabilization, the mesocrystal formation might differ. If the nanocrystals precipitate very rapidly without any order, a random aggregation is formed resulting in a polycrystal. If the nanoparticles undergo an oriented assembly, mesocrystals I to III can be formed. In mesocrystal M-I the nanocrystals are isolated and strictly separated through the stabilizer layer. In M-II the layer is not fully surrounding the particles anymore and a fusion or bridging can occur to fuse the crystals. A direct mesocrystal formation via classical crystal growth is also possible. The same goes for non-stabilized nanocrystals forming M-III mesocrystals without stabilizing agent within the structure. A transformation from mesocrystal M-I to M-III is possible. This process is not reversible. The obtained materials can also be separated by their type and properties:

- A → N-I → M-I is the classical mesocrystal formation
- A → N-II → M-II is the formation of bridged nanocrystals

- A → N-III → M-II → M-III describes the formation of porous single crystals
- A → N-III → M-III illustrates the formation of sponged crystals.

Also, the final transformation from thermodynamically unstable mesocrystals to single crystals is not reversible. This step can be achieved through classical crystal growth and fusion of the building blocks. The crystallinity of the materials increases from the left to the right side of the scheme.[96]
To visualize the definition for mesocrystals Figure 2.13 shows schematic illustrations and diffraction patterns of single crystals, colloidal crystals and crystalline powders as well as a mesocrystal.

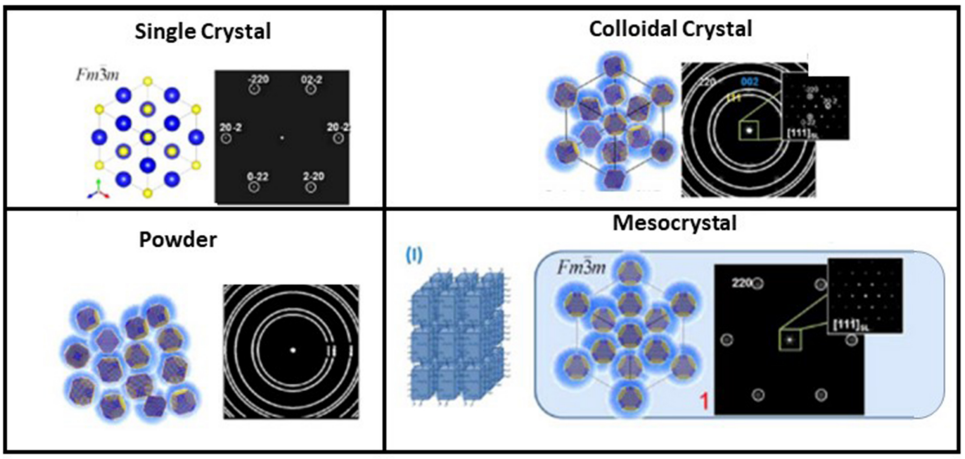

Figure 2.13: Illustration of the differences of single crystals, colloidal crystals, crystalline powders and mesocrystals (adapted with permission from ref.[78]).[78, 97]

A single crystal exhibits a well defined wide angel diffraction pattern and has a long-range order of atoms. It is not made of nanoparticular building blocks. Colloidal crystals show superstructural defined reflections in the small-angle region but do not show a long-range orientation. Therefore, the diffraction patterns resemble that of a crystalline powder. The mesocrystal shows a defined diffraction pattern in the wide-angle region due to the nearly perfectly aligned nanocrystals while in the small-angle region, superstructure reflections appear. If the alignment of the nanoparticular building blocks is not perfect, the reflexes can smear out, but a defined face and pattern identification remains possible. In general, two types of mesocrystals exist: Type I mesocrystals consist of monodisperse particles and show a single crystalline pattern in small and wide-angle regions while Type II mesocrystals show a mutual orientation of polydisperse crystals meaning that single-crystalline patterns are only found in the wide-angle region and rings appear in the small-angle region. This work focuses on

Type I mesocrystals and, accordingly, skips a deeper explanation of Type II.

As mentioned before, mesocrystalline parts can be found in biominerals and most probably also in silica-biomorphs. In the following, the focus will be on synthetic mesocrystals which are produced by lab-made nanocrystals with very well defined geometry and functionalities. The exemplary system introduced in the following consists of magnetite nanocrystals formed using a heating-up method. The principle is shown in Figure 2.14. The scheme presented in A shows the pathway to create and analyze the building blocks which can be used for mesocrystal formation. The composition of the nanocrystals can be determined using, for example, X-ray absorption near-edge spectroscopy (XANES) to distinguish between the possible products, magnetite (Fe_3O_4) and maghemite (γ-Fe_2O_3). The magnetic properties can be investigated with SQUID measurements, and the shape of the formed nanocrystals can be analyzed by transmission electron microscopy (TEM) and high-resolution TEM (HRTEM). The formation of

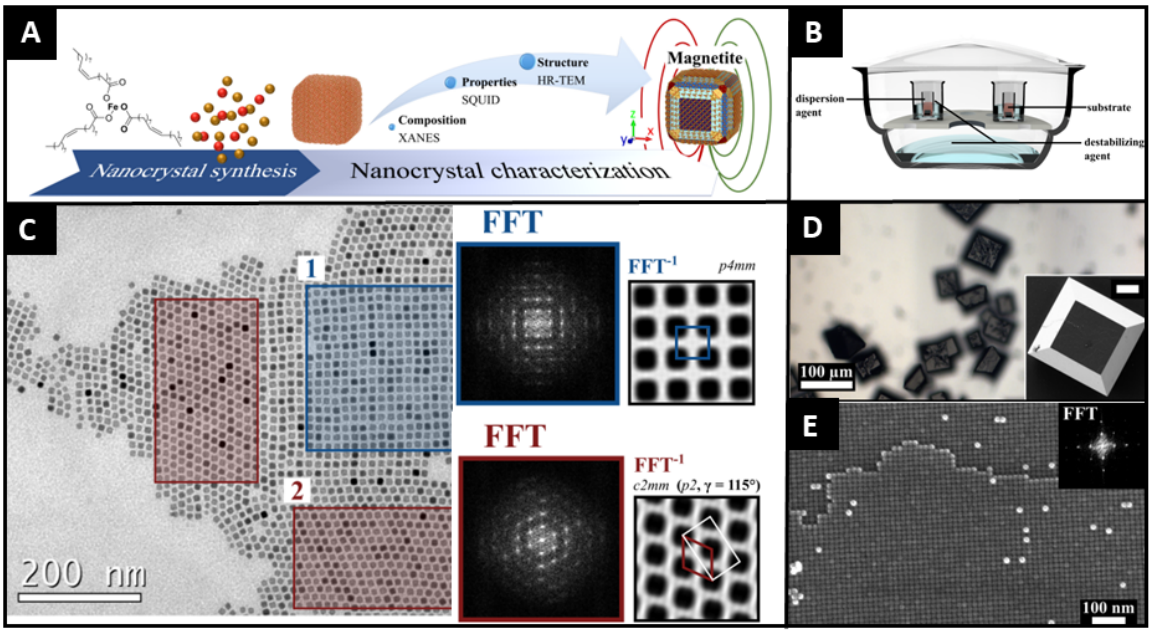

Figure 2.14: Synthetic route to magnetite mesocrystals. A) Scheme of the nanoparticle formation using iron(III) oleate as a precursor creating magnetite mesocrystals. B) Counter-diffusion experiment setup to create magnetite mesocrystals from magnetite nanocrystals. C) TEM image of a 2D monolayer of magnetite mesocrystals showing the assembly into two different lattices which are shown in the corresponding fast Fourier transformed (FFT) images. D) Reflective light micrograph of 3D magnetite mesocrystals. E) SEM images of 3D mesocrystals.[98, 99]

the shown iron oxide mesocrystals was done using a counter-diffusion method shown in Figure 2.14 B. The nanoparticle dispersion was placed into a vial containing a silicon wafer. The small vial was placed into a beaker containing an anti-solvent (in this case ethanol) which continuously diffused into the nanoparticle dispersion lowering the solubility of the particles. The particles begin to accumulate (comparable to nucle-

ation of molecular building blocks) and attach on the substrate (silicon wafer) and the glass of the vial. The formed agglomerates continuously grow into mesocrystals. The nanoparticle dispersion changes its color from black to colorless, and the volume in the vial increases through the infiltration of anti-solvent.[100] A close-up of the alignment can be seen in the transmission electron micrograph shown in Figure 2.14 C.[4] Here, a monolayer of cubic particles can be seen.[98, 99] The nanoparticles assemble in two different patterns highlighted by blue and red rectangles. The fast Fourier transformation (FFT) of the selected areas give a more detailed insight into the packing. In the blue rectangle, a primitive packing is shown which corresponds to the *p*4*mm* symmetry group while the particles in the red areas can be compared to a *c*2*mm* group. In the 3D space, the mesocrystals are investigated by light microscopy. In reflective light, bright field, the mesocrystals can be seen as up to 50 μm large squares (*cf.* Figure 2.14 D). The inset shows an SEM image of a similar crystal. At higher magnifications, the SEM shows more details of the packing of the nanocrystals into a 3D mesocrystal shown in Figure 2.14 E. An FFT of this picture can be generated as well to highlight the high degree of nanoparticle order. The obtained mesocrystals were grown on Si substrates and TEM grids. If it would be possible to let them grow on selected parts of a microsized architecture, this concept could be used as an additional functionalization approach.

To sum up the introduction chapter, I would like to compare the presented self-assembled systems and provide a short overview of the variety of morphologies of mineralized inorganic matter in the fields of biominerals formed by nature, biomorphs and synthetic mesocrystals based on lab-made nanocrystals.[6, 11, 16] The following table summarizes the differences and similarities between these systems.

Table 1: Comparison of self-assembled materials discussed in this thesis.

	Biominerals	**Biomorphs**	**Synthetic Mesocrystals**
Hybrid material	Yes	No	Yes
Typical composition	organic template and nanostructured minerals	Silica and earth-alkaline metal carbonate	stabilized nanoparticles and nanocrystals
Size range	multiple cm	1-500 μm	up to mm
Dominant nanostructure	nanocrystals	nanocrystals	anisotropic nanoparticles or nanocrystals
Present in nature	Yes	Maybe (pseudo fossils)	No

[4] For the monolayer formation and investigation with the TEM, Brunner *et al.* used the solvent-evaporation method and not the gas-phase-diffusion.

In summary, there are clear differences between the presented self-assembled systems but they also have a lot of things in common. Biomorphs and biominerals can exhibit mesocrystalline parts, biomorphs can create formations which resembles biominerals. As there are some linkages between the systems, advantages can be harnessed by combining the different systems to improve their properties and reveal synergistic effects. Their combination can lead to multifunctional and complex systems going far beyond the functions a single system can achieve.

3 Scope of the Thesis

This work should follow a pathway to transform a geochemical system, namely silica-biomorphs, into a multi-functional material. Therefore, it is essential to learn more about the formation process and morphogenesis.

To understand the formation mechanism, the postulation of oscillating pH variations and local pH-drops must be proven. As normal pH indicators do not provide satisfactory detection of local pH changes in the micrometre range, pH-sensitive fluorescence dyes should be used. With confocal fluorescence microscopy, a very high z-resolution is accessible and therefore the local pH changes directly at the growth front can be visualized.

Once the mechanism is proven, strategies to modify and influence the biomorph growth will be tested. As the growth is strongly influenced by parameters like the pH, modified growth conditions will influence the pH and result in tuned morphologies. A broader variety of shapes helps to design shape-related applications for this system.

Tuning the micro composites for a special application needs pathways to apply functionalities in the structures. Therefore, functionalization routes will be developed to equip the structures with different features. These features can be fluorescence for improved in-situ investigations, magnetized for a response in a magnetic field, catalytic, conductive and much more. As a toolbox for providing functionalities onto the biomorphs, the silica shell will be modified with silane chemistry. The usage of this tool will allow the incorporation of further functional materials like several types of nanoparticles.

Once a functionalization towards a responding property was successful, the composite character might allow multi-functionality. As a selective dissolution of either silica or carbonate is possible, also at least a double functionalization might be possible. With multi-functional architectures, a new class of materials can be realized.

Appling functionality *via* organic materials, e.g. polymers, the biomorphs can be hybridized. Furthermore, a structuration of an organic component through an inorganic structure was never accomplished before and can be seen as an inverted biomineral where the structure conducting component is the inorganic one.

4 Results

4.1 Preamble

This chapter displays the results produced during the last years. For increased readability, the subsections are not presented in their chronological order of publication. Instead, they are ordered by their subject beginning from fundamental investigations of silica-carbonate composites, routes to their functionalization, and their usage as a functional material. Parts of the publications like experimental and supplementary information are omitted in the Results sections and presented later in the corresponding chapters. All cited references are summarized in a shared library. The sections were taken from my publications as first author and marked as such right before their corresponding abstracts. Each chapter which was published includes its own introduction which was literally reprinted from the publications. Thus, dealing with the same main topic, repetitions in regard to content cannot be avoided. All publications included in this thesis were finalized during my PhD even if some results were obtained during my Master studies. The work done during the PhD is described prior to each chapter. Depending on the journals which published my work, the language may switch between British and American English.

4.2 Probing Local pH-Based Precipitation in Self-Assembled Silica-Carbonate Hybrid Materials

This chapter is published in *Nanoscale*, **2015**, *7*, 17434-17440. SEM imaging, data analysis, and writing the article was performed in the first three months of my PhD (May 2015 - August 2015). This chapter was accepted as a paper on the 8th of September 2015. As the manuscript is published in an RSC journal, the authors keep the copyright, which allows a reprint for this thesis.

4.2.1 Abstract

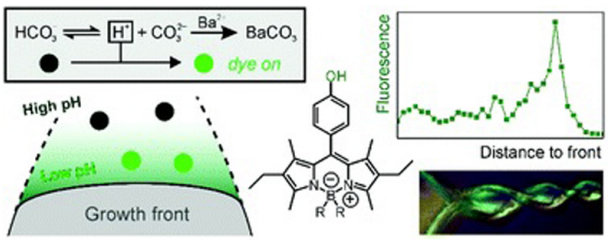

Figure 4.1: Graphical abstract of Opel *et al.* 2015.[101]

Crystallisation of barium carbonate in the presence of silica can lead to the spontaneous assembly of highly complex superstructures, consisting of uniform and largely co-oriented $BaCO_3$ nanocrystals that are interspersed by a matrix of amorphous silica. The formation of these biomimetic architectures (so-called silica biomorphs) is thought to be driven by a dynamic interplay between the components, in which subtle changes of conditions trigger ordered mineralisation at the nanoscale. In particular, it has been proposed that local pH gradients at growing fronts play a crucial role in the process of morphogenesis. In the present work, we have used a special pH-sensitive fluorescent dye to directly trace these presumed local fluctuations by means of confocal laser scanning microscopy. Our data demonstrate the existence of an active region near the growth front, where the pH is locally decreased with respect to the alkaline bulk solution on a length scale of few microns. This observation provides fundamental and, for the first time, direct experimental support for the current picture of the mechanism underlying the formation of these peculiar materials. On the other hand, the absence of any temporal oscillations in the local pH – another key feature of the envisaged mechanism – challenges the notion of autocatalytic phenomena in such systems and raises new questions about the actual role of silica as an additive in the crystallisation process.

4.2.2 Introducion

Silica biomorphs are a unique class of inorganic-inorganic hybrid materials, which form via bottom-up self-assembly of simple molecular species but nonetheless display remarkably complex shapes and structures,[49–52, 80, 102, 103] comparable to solid composite frameworks generated by organisms during biomineralisation[11, 104] as well as artificial counterparts produced in vitro through state-of-the-art biomimetic crystal engineering and morphosynthesis.[17, 105, 106] Just by precipitating alkaline-earth carbonates in the presence of dissolved silica (usually by slow diffusion of carbon dioxide into silica-containing solutions of corresponding metal salts),[52, 54, 57, 58] a broad variety of smoothly curved, non-crystallographic architectures can be obtained (Fig. 4.2). Characteristic morphologies range from flat sheets (Fig. 4.2 a,b) over worm-like braids (Fig. 4.2 c) to, most prominently, regular helicoids (Fig. 4.2 d,e), but also include more elaborate 3D entities reminiscent of corals or flowers.[8, 51, 56, 62, 67, 71, 102] The formation of these unusual structures essentially occurs in a spontaneous manner as long as certain boundary conditions are met, in first place that the pH of the growth medium is sufficiently, but not too alkaline (typically between 9 and 11).[53, 60, 61] Under these circumstances, the components self-assemble into intricate superstructures that can otherwise only be achieved with the aid of relatively complex organic (macro)molecules or matrices, thus rendering silica biomorphs easy-to-handle model systems for investigating fundamental principles of self-organisation, in addition to their relevance in the context of primitive life detection.[2, 52] On the micrometre level, growth of $BaCO_3$ biomorphs was reported to proceed along a sequence of phenomenological stages.[51, 54, 61, 74, 80, 107] First, an initially nucleated carbonate seed crystal experiences fractal branching[76] induced by the poisoning influence of oligomeric silicate species, and thus evolves from a pseudohexagonal rod into increasingly bifurcated forms that eventually show raspberry- or cauliflower-like morphologies (Fig. 4.2 f). With time, these globular clusters develop laminar excrescences, which usually grow flat and in contact with the walls of the vessel or the solution-air interface in the following. At some point, the sheets may curl and adopt scrolled margins, thus giving rise to the more complex curved ultrastructures (i.e. helicoids and worms),[74, 80] likely governed by the role of extrinsic and intrinsic surfaces in the process of morphogenesis.[107]

At the nanoscale, silica biomorphs were found to consist of a multitude of fairly uni-

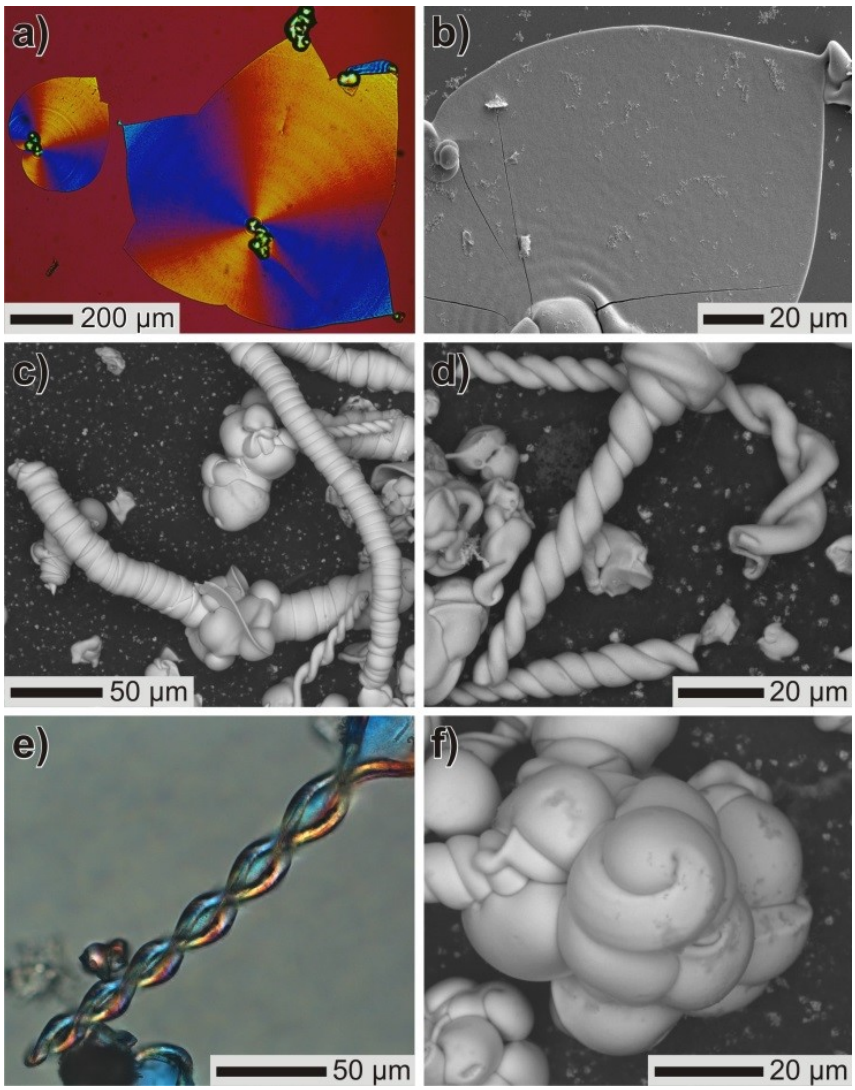

Figure 4.2: Typical morphologies of silica biomorphs: (a,e) polarised optical and (b-d,f) SEM micrographs of (a,b) even sheets, (c) worm-like aggregates, (d,e) twisted filaments, and (f) globular precursor particles.

form rod-like carbonate crystallites, typically about 200-300 nm and 50 nm wide,[51, 52, 54] each carrying a greater or lesser amount of associated silica[8, 54, 67] and being mutually arranged to establish some specific long-range orientational order.[51, 56] The driving force underlying the formation and continuous supply of these nanosized building units was suggested to rely on a dynamic interplay of carbonate and silicate species at molecular scales, based on the inverse pH-dependent solubilities of the components.[51, 60, 61, 74, 79, 80, 108] The key point in the proposed model is that during crystallisation of any carbonate material in moderately alkaline solutions, the pH should be decreased at the surface of growing particles relative to the bulk due to

dissociation of nearby bicarbonate ions[5], e.g. according to:

$$Ba^{2+} + HCO_3^- \longrightarrow BaCO_3 + H^+ \quad (5)$$

This is thought to impact the speciation of silica by protonating charged silicate oligomers, hence promoting condensation reactions and ultimately leading to precipitation of silica around the carbonate particles. Continued silica polycondensation is in turn expected to re-increase the local pH (owing to the consumption of acidic Si-OH groups) and, with it, raise the supersaturation of carbonate, eventually triggering a novel event of nucleation and thus maintaining an autocatalytic cycle of alternating co-mineralisation[81] While the described mechanism is able to explain many experimental observations[51] and may be used to tailor or even program the morphological evolution in these systems,[102] it has remained an essentially theoretical framework up to date. Indeed, the notion that growth processes occur only at local scales in the vicinity of active fronts has been confirmed indirectly by analyses of the growth behaviour in stirred solutions,[81] but still, concrete evidence supporting the proposed scenario is missing. Here we provide, for the first time, experimental data that directly prove the envisaged local decrease in pH during the formation of silica biomorphs. To that end, we have used a special H^+-sensitive fluorescent dye, capable of indicating subtle changes of pH in a spatially confined environment.

4.2.3 Analytical Approach

In order to study local pH gradients during the formation of biomorphs, it is necessary to collect signal selectively from the growth front of single evolving crystal aggregates. Confocal laser scanning microscopy (CLSM) is a very promising technique for this purpose, due to its ability to deliver information from well-defined and highly limited depths of focus in the sample, thus avoiding superimposition of signal across the entire penetrated volume as in conventional optical microscopy. Sheets (Fig. 4.2 a-b) are obviously the most suitable morphology for such analyses, because they grow in a quasi-two dimensional fashion along interfaces and hence, focusing the bottom of the measurement cell should allow for easy monitoring of their development in situ. If, furthermore, a fluorescent dye is added to the mother solution that responds to protons

[5]Note that the fraction of HCO_3^- ions existing in equilibrium with CO_3^{2-} is significant at conditions typical for the formation of biomorphs, ranging from ca. 20% at pH 11 to 90% at pH 9.[79, 108]

released (or consumed) during mineralisation, then local changes of pH at the growth front should become directly visible.

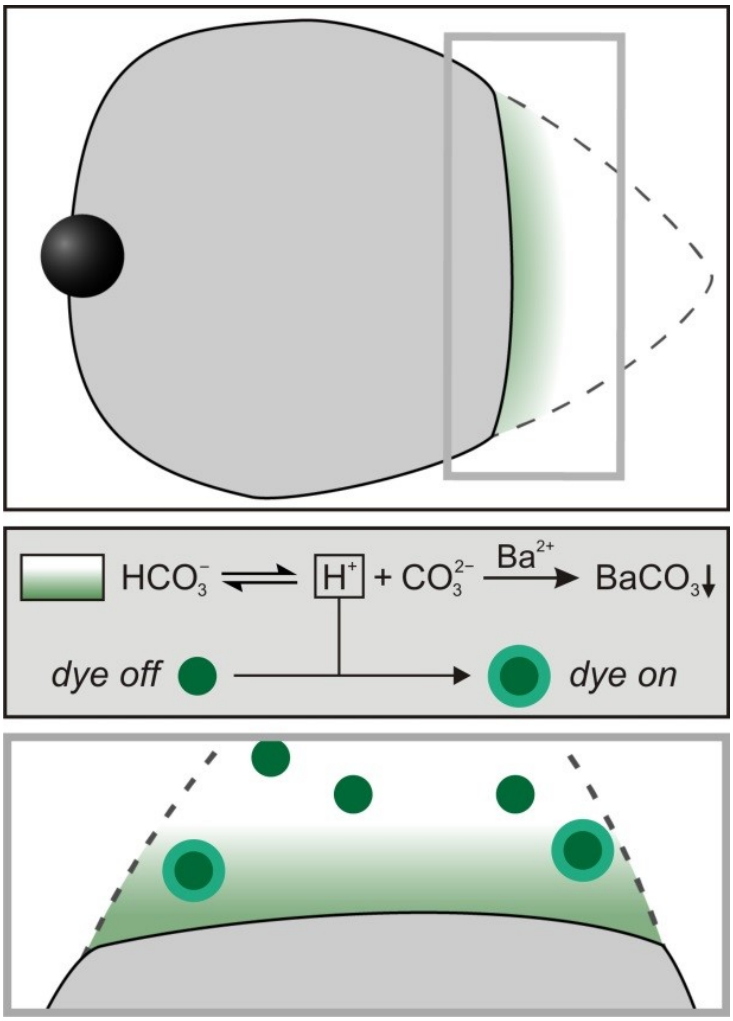

Figure 4.3: Schematic drawing of the experiment: a growing biomorph sheet (top panel) decreases the pH in the vicinity of its active front (corresponding gradient indicated in green), as bicarbonate ions will dissociate to restore the local HCO_3^-/CO_3^{2-} equilibrium during $BaCO_3$ precipitation (middle panel). A suitable fluorescent dye (green circles) will respond to the locally increased proton concentrations by changing its emission behaviour, ideally switching on its fluorescence at a given excitation wavelength in regions where the pH falls below a certain threshold (bottom panel).

Fig. 4.3 shows a scheme illustrating the basic idea behind the experiment.The dye chosen in this work was a boron dipyrromethene (BODIPY) derivative bearing an acidic phenol functional group (1, BDP-OH, *cf.* inset in Fig. 3, R = F), which recently was reported to show a decrease in fluorescence intensity with increasing pH over a dynamic range of ca. 9-11.5 in 1:1 mixtures of ethanol and water, with an emission maximum at 532 nm and a pKa of 9.98.[109] This behaviour was ascribed to fluorescence quenching via efficient electron transfer induced by the electron-rich phenolate moiety, leading to a complete switch-off of fluorescence at sufficiently high pH values. Since growth of

biomorphs does hardly tolerate the presence of any organic (co)solvents,[58] the first step in our study was to investigate the pH-dependence of the fluorescence of BDP-OH in pure water, or rather in aqueous solutions containing barium ions and silica at concentrations typical for biomorph syntheses (to check for potential interferences of these ions). A corresponding plot of the fluorescent intensity as a function of pH is given in Fig. 4.4 (black squares). It is evident that the dye still responds to changes in pH under these conditions, exhibiting a continuous decrease in relative intensity between pH 9 and 11.5. The pKa determined in the aqueous solution is 10.34 and thus slightly higher than what was found in H_2O/EtOH in the absence of Ba^{2+} and silica.[109] Nonetheless, the working range of the dye should in principle still be suitable for probing the formation process of biomorphs, which usually occurs at bulk pH values of 10-11.[61]

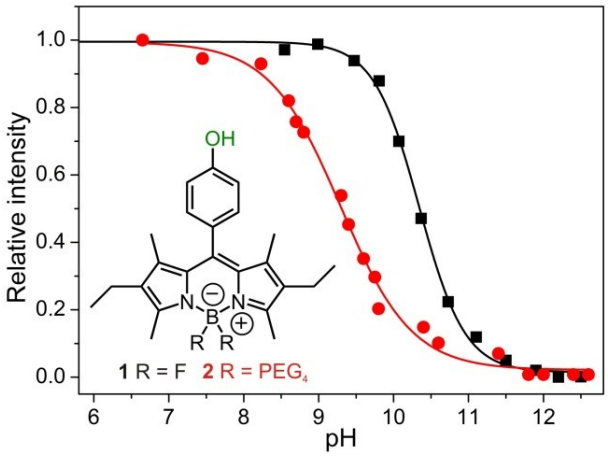

Figure 4.4: Normalised intensity of fluorescence displayed by the dyes BDP-OH (black) and BDP-PEG (red) at different pH levels. Values were derived from the maximum of the emission peak at 532 nm (see Fig. 9.1 on page 113). Data were recorded at a constant dye concentration of 1 μM. Inset: molecular structure of the BODIPY dyes, where the acidic and thus pH-sensitive phenol-OH group is highlighted in green.

However, even though the solubility of BDP-OH in pure water was high enough to allow for pKa determination, it turned out that the dye was prone to aggregation in solution and adsorption/deposition onto solid surfaces (e.g. vessel walls or biomorphs), which obviously complicates analyses as described above. Therefore, we have modified the molecular structure of the dye, replacing each of the two fluorine substituents by tetramers of ethylene glycol (EG_4) in order to obtain derivatives with enhanced water solubility (**2**, BDP-PEG, *cf.* inset in Fig. 4.4, R = EG_4) (see Section 8 for details on experimental procedures and synthesis protocols). Pegylation significantly reduced dye agglomeration, and moreover had a beneficial effect on its spectral properties, shifting

the pKa towards lower values (9.29). From the pH-dependent fluorescence intensities shown in Fig. 4.4 (red circles), it can be deduced that BDP-PEG will essentially be colourless in the bulk growth solution (pH > 10), while it should switch on its fluorescence in local regions where the pH becomes ¡ 10 due to proton release (which seems realistic in view of the proposed mechanism). Thus, BDP-PEG appears to be a promising candidate to meet the dye requirements in an experiment as depicted by Fig. 4.3, and therefore was used for most of the analyses conducted in this study. Before turning to the results of these measurements, it is worth noting that previous efforts with conventional optical pH indicators failed, primarily because dyes covering the relevant pH regime normally contain anionic groups (like carboxylates) that strongly interact with the Ba^{2+} ions in solution and form precipitates when added at concentrations typically required to give significant colouration and measurable effects (mM range). In this context, the main advantage of fluorescent dyes is their superior sensitivity, i.e. that they deliver good signal even when applied at concentrations that are orders of magnitude lower (μm range).

4.2.4 Results and Discussion

Fig. 4.5 shows laser scanning microscopy images depicting the early stages of the formation of a biomorph in the presence of the fluorescent dye BDP-PEG Just before the appearance of a distinct structure, a faint turbidity can be discerned in the transmission image (Fig. 4.5a), indicating the onset of mineralisation, while the fluorescence channel does not display any noticeable features (Fig. 4.5 c). After some delay, a raspberry-like particle is observed (Fig. 4.5 b), which results from fractal branching of $BaCO_3$ crystals in silica-containing solutions (*cf.* Fig. 4.2 f) and is known to be a typical precursor of the more complex biomorphic morphologies. Interestingly, fluorescence is selectively enhanced in the vicinity of this carbonate aggregate, as evidenced by Fig. 4.5 d. These findings can be quantified by plotting the intensities of transmitted light and fluorescence as a function of time (Fig. 4.5 e). As expected, the transmission signal is initially high and then decreases as the fractal structure nucleates and grows, which essentially occurs within a period of about 30 s. The fluorescence intensity, on the other hand, is generally rather low and drifts prior to crystallisation. However, even though the measured changes are relatively small, there is a distinct peak in fluorescence shortly after the response in transmission, which is well above background

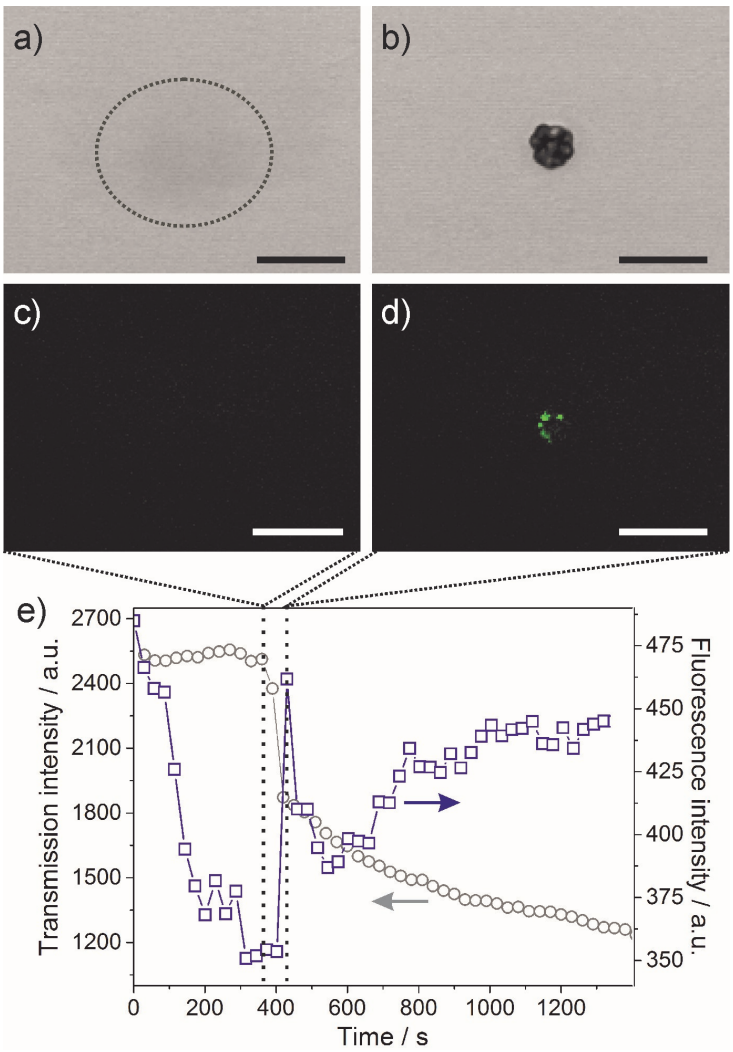

Figure 4.5: Growth of a fractal barium carbonate aggregate in the presence of silica, as viewed by CLSM in (a-b) transmission and (c-d) fluorescence mode. The dashed ellipsoid in (a) highlights a slightly blurred region, in which the structure appears about 30 s later (b). (e) Plot of the transmission (grey circles) and fluorescence (blue squares) intensities measured in the area shown in (a-d) over time before, during and after the formation of the carbonate structure. The vertical dashed lines mark the times corresponding to the images above. Scale bars in (a-d) are 20 μm.

fluctuations and also becomes clearly evident in the corresponding image (Fig. 4.5 d). According to the data shown in Fig. 4.4, this suggests that the pH around the globular particle is lower than in the surrounding bulk solution for a certain time, i.e. during the formation of the aggregate. These results are already a first indication that precipitation of barium carbonate in alkaline media indeed leads to a local pH decrease at active surfaces, as envisaged in the current model for the formation mechanism of these materials.[51, 60, 61, 74, 79–81] In order to substantiate these observations and in particular to also show that this effect is a local phenomenon,[81] we performed further CLSM analyses at higher magnification, mainly following the growth of flat sheets (for reasons outlined above). One such structure is shown in Fig. 4.6 at two distinct stages

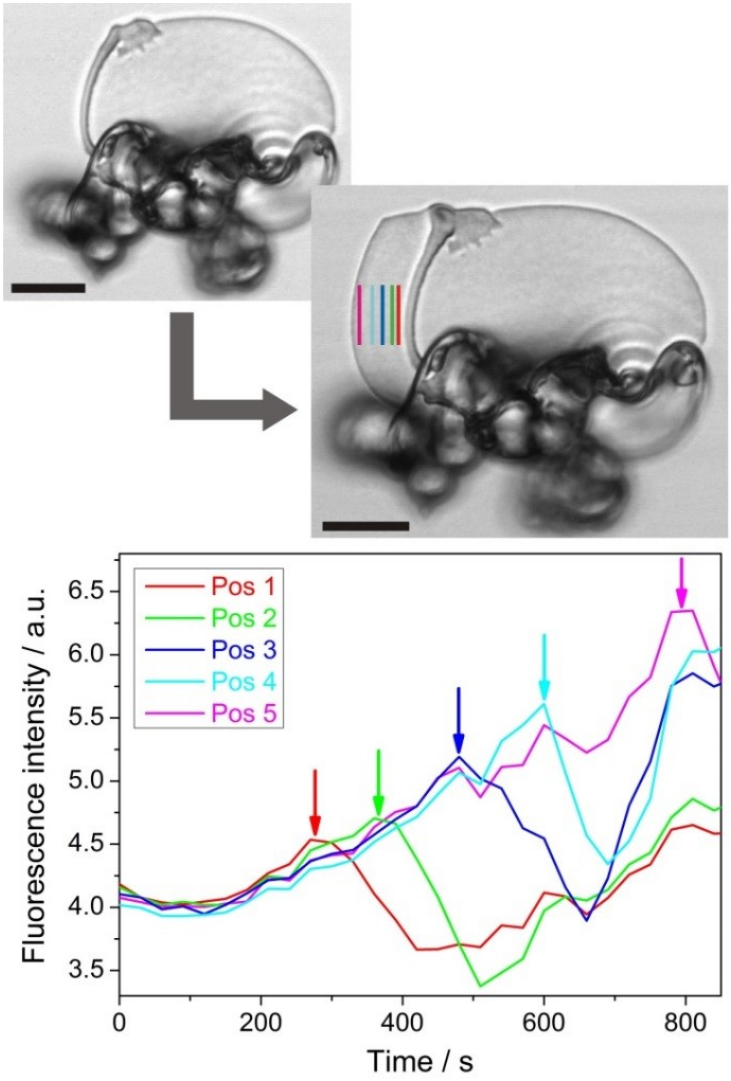

Figure 4.6: In-situ monitoring of pH changes during the formation of silica biomorphs in solution. Top: confocal micrographs of a flat sheet at the beginning and at the end of the observed period (time lapse: 15 min). Bottom: Plots of the fluorescence intensity as a function of time, measured at different positions relative to the edge of the sheet in the first image (indicated by vertical lines with the same colour code). Scale bars are 10 μm.

of evolution in the presence of BDP-PEG. The coloured vertical lines mark different positions relative the growth front (which in this example moves from right to left), at which the fluorescence intensity was continuously monitored. Time-dependent traces resulting from these measurements (graph in Fig. 4.6) again display a maximum in fluorescence; however, now the signal does not come from the entire structure, but only from a confined area (here about 3 μm wide) at the respective indicated spot. With growing distance to the initial position of the sheet edge, the maximum in intensity is continuously shifted to later times. Obviously, fluorescence starts to increase when the growth front approaches the monitored position (at around 150-200 s in Fig. 4.7) and reaches the highest value just before the sheet edge passes. Subsequently, a

relatively sharp decrease in intensity is observed. This suggests strongly that there is a zone nearby the growth front, in which the pH is locally reduced and gradually increases from the rim of the evolving aggregate towards the more alkaline bulk solution – well in line with the hypothetical situation drawn schematically in Fig. 4.3. Fig. 4.7 shows another example for a sheet growing in alkaline silica solutions con-

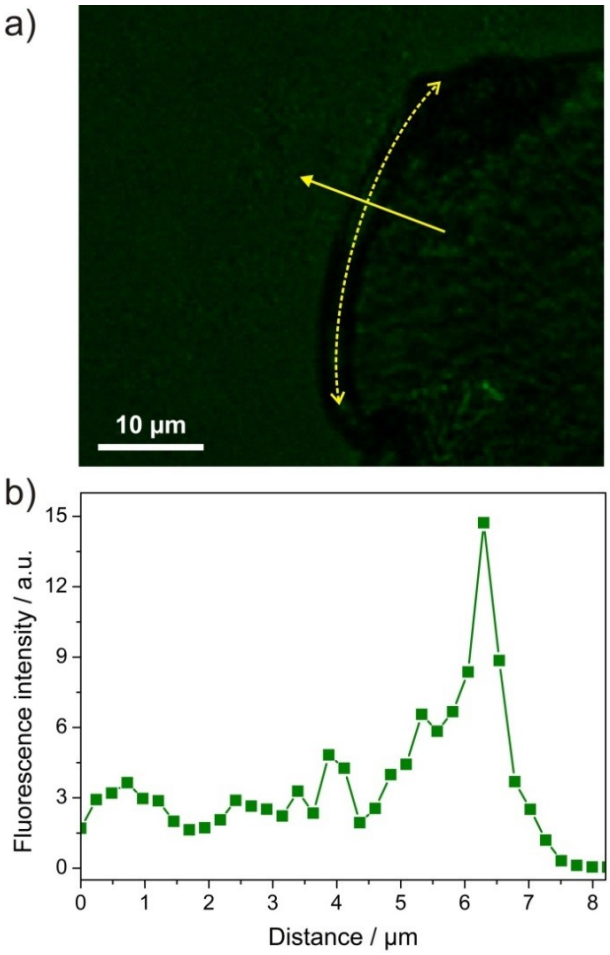

Figure 4.7: Local pH gradients in silica biomorphs. a) Fluorescence image of the edge of a sheet growing from right to left. The arrows visualise how line scans of fluorescence intensity were performed along the normal to the surface at different azimuthal angles. b) Resulting intensity-distance profile , clearly evidencing the local decrease in pH near the growing front.

taining BDP-PEG. In this case, the local pH decrease can already be discerned in the fluorescence image (Fig. 4.7 a) as a layer of slightly higher brightness around the rim of the aggregate. To confirm this effect, we have performed fluorescence line scans along the normal to the surface from the edge of the sheet outwards (*cf.* full arrow in Fig. 4.7 a). Integration over different azimuthal angles, as illustrated by the dashed arrow in Fig. 4.7 a, led to the intensity-distance profile displayed in Fig. 4.7 b. This data unambiguously demonstrates the existence of a pH gradient at the active front of growing biomorphs, most likely originating from the dissociation of bicarbonate ions

during the formation of $BaCO_3$ (as described above). From the results shown in Fig. 4.7, the thickness of this region can be estimated to ca. 2 μm (at the given level of sensitivity), which is in good agreement with indirect predictions made on the basis of simple fluid dynamics considerations in experiments at different stirring rates.[81] It is worth noting that in none of our assays, there was any sign for a cycling of the local pH, which one would expect if carbonate and silica were mineralised in an alternating fashion according to the idea of coupled co-precipitation.[74, 81, 81] Although we cannot yet translate the measured fluorescence values quantitatively into actual pH changes , it seems as if the pH at the front is continually lower than in the bulk. Indeed, the lack of any oscillating behaviour may be due to limited temporal and/or spatial resolution in the current setup, or insufficient sensitivity of the used dye. Nevertheless, our data strongly suggest that carbonate crystallisation dominates the local pH and that there is little influence of silica in this context – at least under the conditions investigated in the present work. This conclusion is supported by the fact that the amount of silica co-precipitated with the carbonate phase during the growth process is relatively low, with Si/Ba atomic ratios in the core of biomorphs typically ranging from 0.05 to 0.10.[54] Constant reduction of the pH at the growth front would imply that the supersaturation of silica is locally enhanced at all times (thus facilitating its incorporation into the forming aggregate), whereas the driving force for carbonate precipitation would in this case always be somewhat depressed at the active surface as compared to the bulk. In our opinion, this is a feasible scenario as it was shown that the bulk mother solution of biomorphs is sufficiently supersaturated throughout the entire growth process[61] and hence $BaCO_3$ crystallisation does actually not need a local increase in supersaturation, while this is not necessarily true for silica. On the other hand, the high nucleation density observed in these materials (as manifested in the myriads of nanocrystals constituting the structures) could then no longer be explained on the basis of a locally increased driving force for precipitation.[51, 81] Most probably, this behaviour is caused by the presence of silica, which may act as an efficient inhibitor for carbonate growth (thus restricting the size of the crystallites to the nanoscale)[110] and/or accelerate nucleation by lowering interfacial energies through epitaxial matching.[111]

4.2.5 Conclusion and Outlook

In this work, we have developed a water-soluble fluorescent dye with pH sensitivity in the alkaline regime, in order to probe local changes in conditions during the formation of biomimetic silica-carbonate hybrid structures. Our results reveal the existence of a spatially confined region close to the front of growing aggregates, in which the pH is significantly reduced as compared to the bulk medium, thus lending direct experimental support to the postulated formation mechanism. This local pH gradient was found to extend over lengths of few microns into the solution and persisted over time periods of several minutes, while no oscillative behaviour could bedetected. This finding challenges the notion of autocatalytic processes in these systems and stresses the role of silica as a growth-inhibiting additive. Although the present approach does not allow the quantification of local pH at every point in time, it nevertheless highlights the potential of fluorescent dyes to directly trace local precipitation phenomena in self-assembled silica-carbonate materials. Future work will befocused on the design of yet more suitable probes possessing two distinctly fluorescent species in their protonated and deprotonated form, the study of different experimental conditions in terms of pH and species concentrations, as well as on translating measured fluorescence intensities into actual local pH values.

4.3 Structural Transition of Inorganic Silica-Carbonate Composites Towards Curved Life-Like Morphologies

This chapter is published in *Minerals*, **2018**, *8(2)*, 75. This chapter was accepted as a paper on the 14th of February 2018. As the manuscript was published in an MDPI journal, the authors keep the copyright, which allows a reprint for this thesis.

4.3.1 Abstract

The self-assembly of alkaline-earth carbonates in the presence of silica at high pH leads to a unique class of composite materials displaying a broad variety of self-assembled superstructures with complex morphologies. A detailed understanding of the formation process of these purely inorganic architectures is crucial for their implications in the context of primitive life detection as well as for their use in the synthesis of advanced biomimetic materials. Recently, great efforts have been made to gain insight into the molecular mechanisms driving self-assembly in these systems, resulting in a consistent model for morphogenesis at ambient conditions. In the present work, we build on this knowledge and investigate the influence of temperature, supersaturation and an added multivalent cation as parameters by which the shape of the forming superstructures can be controlled. In particular, we focus on trumpet- and coral-like structures which quantitatively replace the well-characterised sheets and worm-like braids at elevated temperature and in the presence of additional ions, respectively. The observed morphological changes are discussed in light of the recently proposed formation mechanism with the aim to ultimately understand and control the major physicochemical factors governing the self-assembly process.

4.3.2 Introduction

Silica biomorphs are an interesting type of self-assembling inorganic-inorganic composite materials with remarkably complex architectures. They form in silica-rich solutions at high pH in the presence of alkaline-earth metal cations like barium, strontium and calcium under ambient conditions [50, 52, 54, 57, 74, 107]. Upon diffusion of atmospheric carbon dioxide into the system, slow crystallisation of carbonate under the influence of dissolved silicate species results in the spontaneous formation of unusual ultrastructures that consist of uniform elongated carbonate nanocrystals (approximately 200-300 nm long), which maintain long-range co-orientation and are in-

terspersed by certain amounts of amorphous silica, the whole structure is surrounded by a silica skin (typical Si/Ba ratios are 0.1-0.3) [54, 71]. On the multi-micron scale, these assemblies display intricate morphologies such as flat sheets, helicoids or tightly wound worms, as shown in Figure 4.8. While most of the work on silica biomorphs has been carried out with witherite ($BaCO_3$) as the carbonate phase [54], there is increasing evidence that similar structures can also be obtained with other carbonates, including orthorhombic analogues like strontianite ($SrCO_3$) [58, 62] or aragonite ($CaCO_3$) [8, 59, 67].

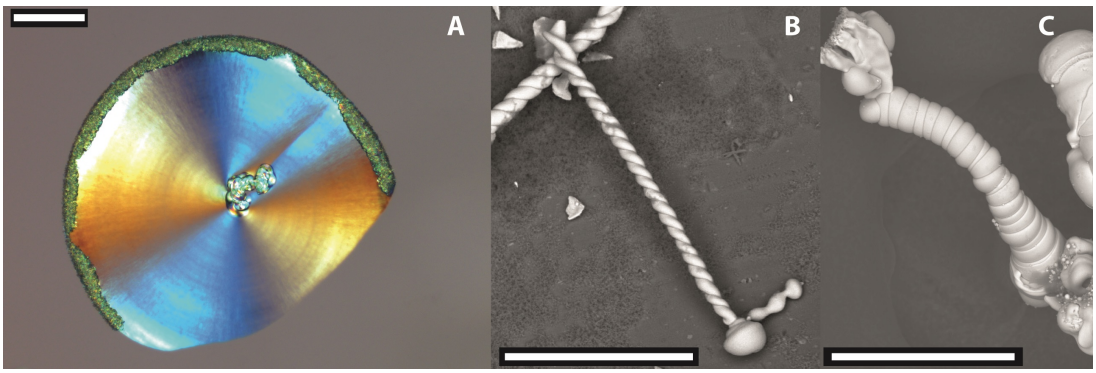

Figure 4.8: Polarised light microscopy (PLM) and SEM images of the most common architectures displayed by silica biomorph structures grown at room temperature from solutions containing 8.9 mM silica and 5 mM barium chloride: A) flat sheet, B) regular helicoid, C) tightly wound worm. Scale bars: 100 μm.

The mechanisms enabling the structural and morphological complexity observed in this simple inorganic system have been investigated in detail over the past decade, focusing on both the molecular interactions driving self-assembly at the nanoscale and phenomenological aspects determining the final appearance at the micro- and nanoscales [57, 101, 112–114]. With respect to the latter, it was found that growth of biomorphs occurs in two general stages. At the beginning of the crystallisation process, small witherite crystals nucleate and grow in a more or less classical way. With time, oligomeric silica species induce fractal branching at the tips of the carbonate crystal, causing progressive bifurcation and ultimately resulting in closed cauliflowerlike spherulites [2, 74, 80, 81]. At this point, the system passes into the second stage, which is characterised by polycrystalline growth, i.e. numerous nanocrystals are nucleated continuously and/or episodically and co-assemble into aggregates with shapes beyond any constraints of crystallographic symmetry. Typically, the first type of morphologies observed in this stage are flat sheets (Figure 4.8A), which grow along vessel walls or the solution–air interface. Randomly, these laminar structures start to curl at their

rim and assume a new (orthogonal) growth direction along the perimeter of the sheet, which arrests radial advancement and gives birth to more complex three-dimensional shapes. The final morphology is then determined by the interplay of various local parameters, including the relative velocities of growth for different segments as well as their heights. The most common twisted forms obtained at ambient conditions are double helices (Figure 4.8B) and more tightly scrolled so-called worms (Figure 4.8C) [74]. In many cases, the carbonate-rich core of the aggregates becomes covered by a layer of amorphous silica, as a result of secondary silica precipitation in the later stages of growth when the bulk pH has been lowered (due to CO_2 uptake) to values where the solubility of silica is noticeably decreased [115].

At the molecular level, the unique behaviour of these inorganic precipitation systems has been ascribed to the pH-mediated coupling of the speciations of carbonate and silicate in solution [74].As the two components have opposite trends in terms of solubility as a function of pH, it was proposed that they continuously stimulate each other's mineralisation by periodic changes in the local conditions at actively growing fronts: carbonate crystallisation reduces the pH in the microenvironment and thus increases the local supersaturation of silica, which in turn will precipitate and thereby re-increase the pH-shifting the local carbonate speciation to the side of CO_3^{2-} and hence triggering a new event of carbonate nucleation. This coupled chemistry allows numerous silica-coated carbonate nanocrystals to be produced and integrated into the forming superstructures as building units. Indeed, the postulated local pH-cycling at the growing front could be verified experimentally in recent studies by using pH-sensitive fluorescent dyes [101, 113]. Interestingly, most of the observations supporting the mechanisms described above were made for the formation of biomorphs in solution or gels under ambient conditions and within a narrow range of concentrations suitable for the growth of the most striking morphologies. However, it is well known already from early works [69] that the structural variety of silica biomorphs is not at all limited to the forms displayed in Figure 4.8, but can be significantly expanded by adjusting conditions such as pH, salinity and temperature, or by introducing certain additives that are able to interfere with the growth process [51, 57, 60, 61, 71, 116, 117]. In the present work, we have re-evaluated the role of temperature in biomorph formation, in order to discuss corresponding changes of structure and morphology in light of the current model of morphogenesis. We show that temperature variation is a straightforward means to obtain further interesting ultrastructures, if the conditions are carefully

chosen. The resulting narrow distribution of morphologies highlights the possibility of shape control in these systems, which seems crucial for the targeted design of related materials with potential for actual applications [118, 119]. Further experiments performed in the presence of added multivalent ions at room temperature expand the range of accessible morphologies and provide support for a morphogenetic scenario in which the relative rates of silica and carbonate mineralisation determine the evolution of the system on the micron scale.

4.3.3 Results and Discussion

In order to investigate the effect of temperature on the formation of silica biomorphs, barium carbonate was crystallised using silica-containing solutions at a fixed composition ([SiO_2] = 17.8 mM and pH = 11.3 (at 25 °C) before mixing with $BaCl_2$ solution) and varying the temperature between 5 and 50 °C. Figure 4.9 provides an overview on characteristic structures formed at different temperatures and barium concentrations (i.e., a so-called morphodrome).

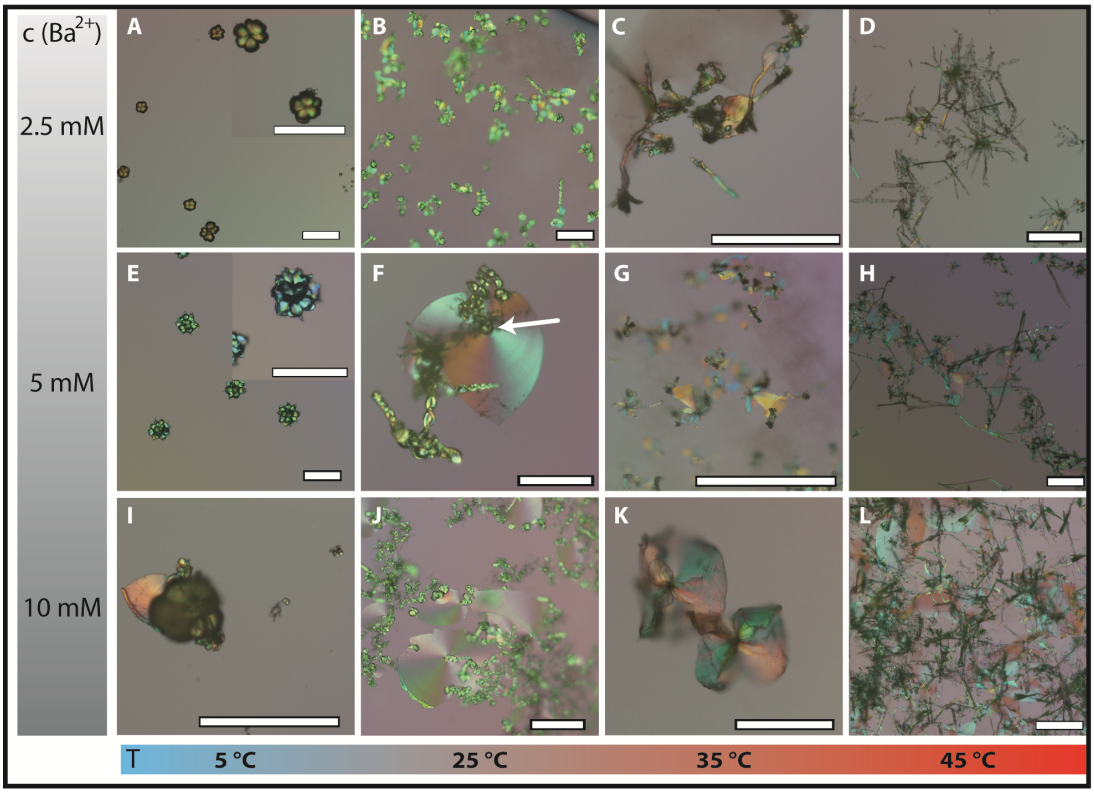

Figure 4.9: (A–L) PLM images of typical biomorphic morphologies obtained at varying barium concentrations and temperatures (as indicated) after a growth period of 12 h using a silica solution with [SiO_2] = 8.9 mM and an initial pH of 11.3 (determined at 25 °C before mixing with barium chloride solution). Note the presence of peculiar 3D trumpet-like shapes in (G), as visualised by the optical depth of field. The arrow in (F) indicates a closed globular particle, from which a polycrystalline sheet- like aggregate has emerged. Scale bars are 200 μm.

Under "standard" conditions (25 °C and 5 mM $BaCl_2$, Figure 4.9F), extended flat sheets and helicoids (often intergrown) are observed, as expected and similar to the structures shown in Figure 4.8. These morphologies can thus be considered as a reference. We note that most of these complex structures emerge from small closed globular particles (or aggregates thereof, as indicated by the arrow in Figure 4.9F). They form in the fractal regime which has to be very short/fast for such small and discrete morphologies to be observed at the end of the chosen period of growth (12 h).
When the barium concentration is increased to 10 mM (Figure 4.9J), the total number of aggregates is higher and in particular the sheets grew slightly larger on average. In turn, a Ba^{2+} concentration of 2.5 mM results in fewer, smaller, and less defined structures (Figure 4.9B), but generally the morphologies are not strongly altered at both higher and lower amounts of cations in the given concentration range. By contrast, lowering the temperature to 5 °C changes the picture fundamentally, as most of the morphologies observed at 2.5 and 5 mM $BaCl_2$ were isolated globular or cauliflower-like structures (Figures 4.9A and 4.9E), and only few poorly developed polycrystalline aggregates were formed at 10 mM even after 24 h (such as the small sheet in Figure 4.9I). This indicates that growth is terminated at the end of the fractal stage in most cases, i.e., the system fails to enter the second stage of dynamic nanocrystal formation and aggregation. In other words, the conditions prevailing in these experiments do not allow for chemically coupled co-precipitation to be initiated and/or maintained. Probably, this behaviour is related to temperature-dependent changes in the kinetics of carbonate and/or silica mineralisation, caused by differences in either diffusive transport of reactants or the relative rates of precipitation. Generally, the following trends and related consequences are expected with increasing temperature:

- Decrease in the solubility of $BaCO_3$ [120]: higher carbonate supersaturation, higher driving force for carbonate precipitation (thermodynamic factor);
- Decrease in the solubility of CO_2 in water [121]: reduced rate of CO_2 uptake from the atmosphere, slower carbonate precipitation due to diffusion limitation (kinetic factor);
- Acceleration of silica condensation kinetics [122]: reduced rate of silica polymerisation, faster SiO_2 precipitation (kinetic factor);
- Increased solubility of silica [123]: decrease in silica supersaturation, lower driv-

ing force for precipitation (thermodynamic factor);

- Increase in the ionic product of water [124]: higher effective pH at the same composition, leading to lower carbonate solubility and higher silica solubility (thermodynamic factor).

Based on these qualitative considerations, it seems reasonable to assume that the growth rates of both silica and carbonate are not sufficiently high to allow for complex ultrastructures to form at lower temperatures. This can be resolved to some extent by increasing the barium concentration (Figure 4.9I), but the influence of temperature appears to be dominant.

At higher temperatures (35 and 45 °C), there are also regions in the morphodrome where well-developed biomorphs are barely observed. This is particularly true for lower and higher barium concentration (Figures 4.9C, D, K and L). In the former case (2.5 mM $BaCl_2$), the slower rate of carbonate formation (lower supersaturation and reduced CO_2 uptake) can probably not supply enough building units to keep the pace of the accelerated silica condensation processes. In turn, at 10 mM $BaCl_2$ another effect comes into play, namely the electrostatic screening of negative charges on silicate species by dissolved divalent cations like Ba^{2+} [116]. This bridging interaction catalyses silica condensation and—along with the higher temperature—is expected to accelerate silica precipitation kinetics in a way that is less or not suitable for coupling with carbonate formation. As opposed to that, proper conditions for 3D self-assembly are still maintained at the "standard" barium concentration of 5 mM and temperatures up to 45 °C. Here, however, the resulting biomorphs show substantially different morphologies than at room temperature and 5 mM Ba^{2+} ion concentration, with large ($> 100\ \mu m$) trumpetlike forms representing the major population of ultrastructures. When the temperature is increased to 45 °C the biomorphic landscape changes again and highly branched crystal networks are observed, as shown in Figures 4.9D,H,L. These structures likely derive from a fractal route that shows substantially different branching behaviour than at room temperature. Here, the initial pseudo-hexagonal twinned crystal core transforms into an open star-like architecture that is poorly filled with silica–carbonate composite matter. In some cases, sheet-like domains are formed in between branches, but these structures are often heavily bended and limited in their growth by the mother crystal branches (cf. Figure 4.9H). This suggests that an increase in temperature changes the branching kinetics, presumably via modulated interactions

between growing carbonate surfaces and dissolved silicate species that adsorb specifically on certain witherite faces. One potential scenario is that the accelerated carbonate precipitation gives the silica less time to interfere. Alternatively, the speciation of silica in solution may shift to larger oligomers that show different affinities to interact with specific carbonate faces, thus resulting in a different branching behaviour. In any case, high temperature in combination with high barium concentrations leads to a significant increase in the amount of precipitated matter (probably due to faster carbonate and silica formation). This is shown in Figure 4.9L, where large networks of tubular filaments and/or twisted ribbons are seen along with various other types of biomorphic morphologies. Interestingly, these forms are much thinner than biomorphs grown at ambient temperature, again indicating important changes in relative growth rates of the components. In summary, the most outstanding feature of the morphodrome established in our study was the formation of biomorphic ultrastructures with trumpetlike appearance. They can sporadically be obtained at temperatures above 30 °C and replace all sheet-like and most twisted morphologies at temperatures above 40 °C. The formation process of the trumpetlike structures was analysed in more detail, in particular with respect to both differences and similarities compared to biomorph growth at room temperature, which leads to twisted (worms and helicoids) and flat sheet-like (as described in previous works [51, 54, 74] and shown in Figure 4.8). Figure 4.10 provides schematic representations of the occurring processes (panels A and B–E) along with selected SEM images showing the relevant stages of growth (panels F–H). Despite the absence of any of the three "standard" morphologies, the nature of the polycrystalline growth mechanism in the second stage of morphogenesis seems comparable to the corresponding processes at room temperature, based on the characteristic thickness oscillations observed for example in Figure 3H and detailed analysis of the texture of the aggregates at the nanoscale [54, 101, 114]. Consequently, the main difference leading to distinct final shapes must occur at the beginning of the structure formation. As at ambient conditions, morphogenesis starts with fractal branching of a twinned pseudo-hexagonal witherite crystal due to the poisoning influence of oligomeric silica species (Figure 4.10A). Closer analysis of the carbonate surfaces suggests that adsorption of silicate species (Bittarello et al. [125]) will mainly occur on the positively charged (110) faces but also on the polar (010) faces (cf. Figure 4.10A). At higher temperatures, the branching behaviour is different, though, and the first step is a splitting into up to six crystal arms, as silicate-covered (110) and (010)

faces are blocked while the remaining (021) and (111) faces can serve for heterogeneous nucleation of the up to six crystal arms in a more or less unhindered fashion, as indicated in Figure 4.10A. This process repeats itself and produces second-generation branches. Increasing the temperature leads to more ordered and larger branched enti-

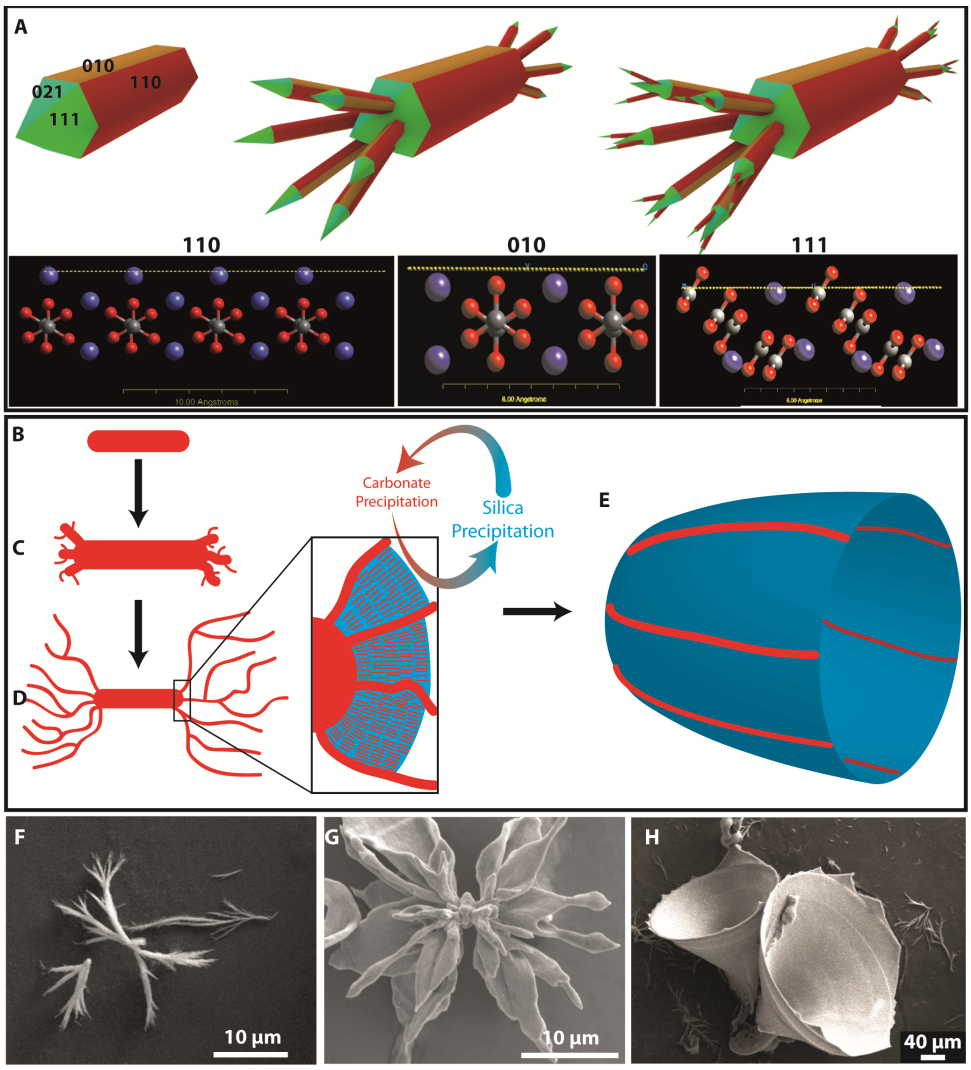

Figure 4.10: Formation of trumpet-like morphologies at 45 °C and 5 mM $BaCl_2$. (A) Scheme of a primary witherite crystal (top), which successively becomes branched due to specific interactions of silica with different faces of the carbonate crystal. Vacuum surface cuts of these faces (bottom) indicate that the (110) faces are positively charged and thus prone to be blocked by negatively charged silicate species. Also, (010) is polar and therefore also likely to interact with negative silica species. Further growth thus occurs through the neutral (021) and (111) faces, so that up to six branches can emerge from the pseudo-hexagonal base. Repetition of this process leads to multiple branching generations. (B–E) Schematic overview of the growth process of a trumpet-like structure: an initial elongated $BaCO_3$ twin crystal seed grows and undergoes fractal branching as described in (A). At high temperature, this leads to open architectures with large branches, between which polycrystalline growth (i.e., autocatalytic co-precipitation of silica/witherite nanoparticles) occurs and slowly fills up the empty space (inset). Depending on the orientation of the branching, trumpet-like aggregates are formed. (F– H) SEM micrographs of the initial stage of open fractal branching (F), followed by filling of the branches with biomorphic composite material (G), ultimately leading to trumpet-like forms (H).

ties as drawn in Figures 4.10B-D, compared to the much smaller and heavily bifurcated dumbbell-shaped, spherical or raspberry-like forms observed at room temperature (cf. Figure 4.8). This suggests that branching at high temperature is more symmetric and of lower dimensionality than at ambient conditions, where a much higher branching density and thus much less symmetric architectures are observed. In other words, branching is more chaotic at low temperature and becomes well-defined at high temperature. This could be related to changes in silica condensation kinetics at higher temperatures, leading to different silica speciation and thus to different affinities of silicate species to adsorb on the different relevant carbonate faces, as already proposed above. That, together with changes in the growth rates of carbonate faces, could explain the different branching behaviour at elevated temperatures [120, 122]. Once these open branched structures are formed (Figure 4.10F), the system enters into the second stage of morphogenesis, where the accelerated kinetics of the precipitation of both components leads to a fortification of the autocatalytic mechanism, which then seems to stay in the tolerant zone for coupled co-precipitation to work. However, the resulting nanocrystals do not assemble into the well-known shapes observed at room temperature, but seem to fill the space in between the large branches formed in the first stage of fractal branching (Figure 4.10G), leading to selective biomorphic growth from open branched fractals into trumpet-like structures (Figure 3H) according to a mechanism as indicated schematically in Figures 4.10D–E. Thereby, each structure is unique and shows its own interesting shape, which seems to depend on the orientation of the branches. The pathway to the trumpet structure skips the formation of globular particles and leads directly to 3D architectures of silica–barium carbonate composites with curved surfaces. The dominant effect causing this behaviour could be the increased silica solubility, which allows the system more time to develop in a defined manner throughout the fractal stage. Then, the second stage of morphogenesis is entered before a high degree of branching would lead to closed globular structures. Interestingly, the multiple limbs lead to only one final trumpet structure in most cases, suggesting that the different smaller leaf-like domains fuse to one surface or only the most pronounced leaf develops to the final shape.

During the secondary growth process, the orientation of the growing crystals is crucial. When the experiments are conducted under the same conditions but in petri dishes, where the surface/volume ratio is much higher than in the linbro plates, the reaction leads to trumpet-like structures with wider spreading exhausts. Some examples of

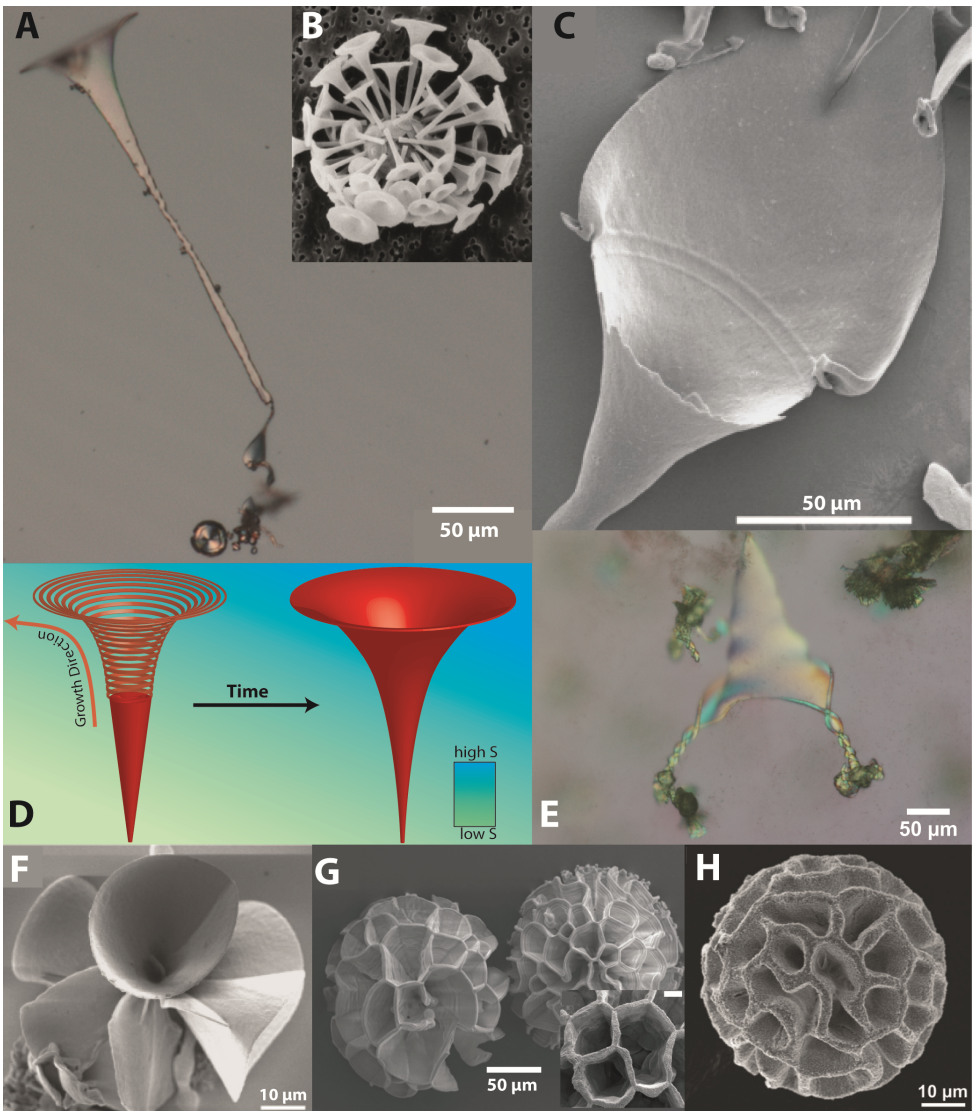

Figure 4.11: Biomorphs with lifelike morphologies. (A,C) PLM and SEM images of biomorphs in the shape of a marine coccolith. Formed from solution, containing 5 mM Ba 2+ and 9 mM silica at 40 °C. (B) SEM image of a natural marine coccolith (Reproduced with permission from ref. [6], Copyright 2012 Wiley-VCH Verlag GmbH & Co KGaA). (D) Schematic illustration of the formation process of coccolith morphologies illustrating the supersaturation gradient into the solution. (E) PLM micrograph of a biomorph structure grown at higher temperature (40 °C) showing a trumpet structure exfolding into two helicoidal structures. (F) SEM micrograph of a flower-like biomorph grown from a 5 mM Ba 2+ solution containing alkaline silica sol at 50 °C. (G) SEM micrograph of a coral-like biomorph structure grown at higher Ba^{2+} concentration (250 mM; scale bar of the inlet: 10 μm) (H) SEM micrograph grown from a 5 mM Ba^{2+} solution containing alkaline silica sol with 1 mM La^{3+} ions.

these forms are shown in Figures 4.11A and C. As it can be noticed, these structures look similar to a marine coccolith element (cf. Figure 4B) [6]. A model of the possible mechanism is presented in Figure 4.11D. When linbro plates are used, supersaturation is lower and biomorphic aggregates have a narrower shape. Since the petri dish setup favours the availability of CO_2 and therefore the carbonate in the growing front, a higher supersaturation with respect to barium carbonate and a consequently sharper

drop of pH (and higher supersaturation with respect to silica) would be explained. This phenomenon is even more evident once the precipitation occurs nearer to the solution/atmosphere interface. It would also explain the spreading of the branches due to a faster (secondary) growth stage. A similar behaviour was already observed in higher concentrated solution and the spreading could be triggered with a CO_2 burst [102]. Therefore, it can be assumed that this sharp saturation gradient explains this behaviour when completely upright structures are forming. When tilted structures form under the influence of the CO_2 , biomorphic aggregates develop irregular exhaust orientation as the one shown in Figure 4.11C. Additionally, a continuum of different morphologies can be detected in Figures 4.11A, C, and F. In Figure 4.11A a transformation from a sheet over a small ribbon to the final trumpet can be found while C shows a reverse exfoliation from a rolled-up trumpet to a 2D sheet-like structure while Figure 4.11E demonstrates a continuum of shapes and a transition of a trumpet at elevated temperatures into two helicoidal structures.

Further lifelike morphologies can be produced by increasing the barium concentration (Figure 4.11G; $[Ba^{2+}]$ = 250–500 mM), which shift the formation mechanism as well [56]. The obtained brain coral-like structures skip the formation of a globular centre, have a nearly perfect spherical shape, and consist of a network of interpenetrating sheet-like units which merge out of the leaf-like parts liked at the seed crystal (similar pathway presented in Figure 4.10). Their formation is already described by Hyde et al. [56] and reviewed here with consideration of newly obtained knowledge. The formation of these structures follows a similar pathway compared to the trumpets because their formation skips the production of a globular centre. Coral-like architectures can be obtained in a modified way with 5 mM Ba^{2+} ions in solution by using modifiers such as cationic surfactants like CTAB [71] or multivalent ions like La^{3+}. Using such modifiers, similar but more homogenous morphologies were obtained and are shown in the SEM micrograph in Figure 4.11H. The formation is again influenced in the first stage of the formation which is in good accordance with time-resolved experiments with CTAB additions. An addition of CTAB after a few minutes does not lead to coral structures and "standard" biomorphs will be obtained. At first sight, it is comprehensible that an increase of the pure number of multivalent ions like Ba^{2+} (tested before) or La^{3+} has a similar effect on the system despite the effect on silica precipitation, which is in good accordance with the Schulze–Hardy law [126]. A faster silica formation and a reduced colloidal stability by multivalent cations show similarity to the ultrastruc-

tures obtained at elevated temperature. Multivalent ions are known as efficient agents to bridge charged colloids or oligomers like silica [127]. Furthermore, these ions will not be free charged ions within this system due to their tendencies to form complexes with hydroxide, carbonate, and silicate ions to reduce their effective charge. In the end it should be noted that La^{3+} as an additive has less effect on the carbonate precipitation rate and that no significant lanthanum adsorption within the $BaCO_3$ lattice was detected. Additionally, a higher ionic strength depresses the CO_2 uptake rate and its solubility in water, which again leads to a deterioration of the carbonate formation [128]. Therefore, we can assume an extreme of a reduced fractal regime time in the case of coral-like structures. As shown in literature, upon the addition of sodium chloride (note the single charge of Na^+) to the standard procedure, the process will not enter the second stage at all and the crystal formation stops after the formation of the globular particles formed in the first stage (described by Eiblmeier et al. [116]). A reason for this might be the shifting of the equilibrium of free and sodium-coordinated silicate species to the sodium terminated side [129]. Therefore, less silica is available for the autocatalytic process, which is in line with observations made with decreased silica concentrations, and the resident time in the fractal regime is much longer and globules are formed.

4.3.4 Conclusion

The presented work describes the influence of several parameters on biomorph growth and highlights the formation process of reported and unreported lifelike morphologies. The individual impact of the temperature, supersaturation, and ions as additives on carbonate and silica formation is discussed in detail and meaningful, plausible explanations were given for the formation mechanism of the strongly bended morphologies. We showed a linkage between coral- and trumpet-like structures and that a continuum of shapes is possible. Influences of the various and further tuning parameters like the effects of the growth direction and surface/volume ratio were tested. The most exciting growth conditions to lifelike morphologies were highlighted and allow a superior reproducibility.

4.4 Functionalization of Silica-Carbonate Biomorphs

This chapter is published in *Nanoscale Horiz.*, **2016**, *1*, 144-149. Part of the results for this publication was produced during my master thesis in 2015. The finalization, the writing of the article as well as supplementary results, e.g. related to the pPCDA were produced during the PhD (May 2015 - December 2015). This chapter was accepted as a paper on the 11th of January 2016. As the manuscript was published in an RSC journal, the authors keep the copyright, which allows a reprint for this thesis.

4.4.1 Abstract

Biomorphs are a unique class of self-organised silica-carbonate mineral structures with elaborate shapes. Here we report first approaches to modify these complex inorganic architectures through silane chemistry, binding of nanoparticles, and organic polymerisation. This leads to functional nanostructures in which the complexity of the originally inorganic template is preserved, and offers new diagnostic tools to study the mechanisms underlying their formation.

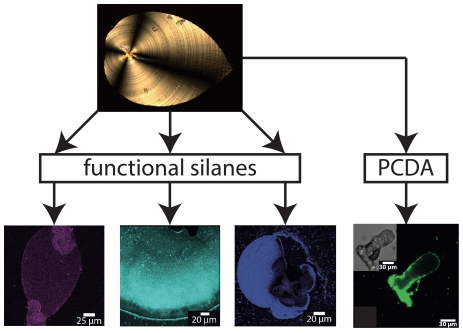

Figure 4.12: Graphical abstract of Opel *et al.* 2016.[119]

4.4.2 Conceptual Insight

Biomorphs are a unique class of self-organised nanostructured silica–carbonate mineral structures with elaborate shapes. This complexity of shapes is otherwise only formed in the living world in form of biominerals. We want to utilize the unique inorganic biomorph structures to add function to create nanostructured materials with complex shape and new and emergent properties. Here we report first approaches to modify these inorganic architectures through silane chemistry, binding of nanoparticles, and organic polymerisation. This leads to functional nano-structures in which the complexity of the originally inorganic template is preserved. The reported three examples already show the large variability of our approach and especially the post-functionalization with silanes provides the possibility to attach a variety of functional nanoparticles.Therefore, our study introduces a new and variable platform towards novel functional nanostructured materials with complex shapes.

4.4.3 Introduction

Crystallisation of alkaline-earth metal carbonates in the presence of silica at high pH can result in fascinating hybrid structures with curved morphologies and ordered textures across several length scales.[51] These so-called "biomorphs" consist of innumerous carbonate nanocrystals that are stabilised by co-precipitating silicate species and self-assemble into delicate forms like regular helicoids or sinuous sheets, which may eventually become sheathed by an outer skin of silica on the micron level.[54] Despite the absence of any organic matter, the obtained structures closely mimic biomineral frameworks produced by living organisms[104] and moreover resemble some of the oldest putative microfossils.[52] Therefore, biomorphs have been used as a model system to study biomimetic self-organisation[102] and serve as a vital proof that complex curved forms are not exclusive to the living world.[2] Over the past ten years, the mechanism for the formation of these unusual inorganic-inorganic hybrid structures has been investigated in depth, leading to a meanwhile convergent picture of autocatalytic reaction coupling being the driving force for self-assembly at the nanoscale.[74, 81] In particular, it was shown that local changes in pH at the growth front trigger the dynamic co-mineralisation of silica and carbonate due to their inverse trends of solubility with pH, as depicted schematically in Figure 4.13 a-c and described in more detail elsewhere.[101] The result is an array of crystalline carbonate nanoparticles (dark-grey rods in Figure 4.13) embedded in a more or less continuous matrix of amorphous silica (light-grey domains in Figure 4.13 c), which subsequently evolves free from crystallographic constraints towards curved superstructures.[107] Even though biomorphs exhibit many interesting features in terms of structure and morphology, they still consist of plain inorganic compounds (usually $BaCO_3$ and SiO_2) and thus bear little to no distinct functionality. To address this issue and widen the scope of biomorphs towards materials science, we have started to chemically modify the inorganic nanostructures, either in situ during their formation or by post-treatment. Here we present three different approaches to achieve "functional" biomorphs: (1) silane co-condensation, (2) immobilisation of metal nanoparticles and quantum dots, and (3) organic polymerisation. All three concepts yield hybrid materials with enhanced functionality and equal structural complexity as inherited from the self-assembly process of biomorphs.

4.4.4 Results and Discussion

The idea behind Approach (1) was to selectively modify the silica component in biomorphs and introduce functional groups via alkoxysilane chemistry.[130] In fact, Voinescu *et al.* have shown that biomorphs can be formed with tetraethoxysilane (TEOS) as an alternative organic silica source instead of commonly used inorganic water glass (sodium silicate solution).[58] To obtain typical biomorphic structures, the TEOS (ca. 9 mM) was pre-hydrolysed in water with sodium hydroxide before adding Ba^{2+} ions (5 mM) to the alkaline solution (pH 10-11) and inducing crystallisation by exposure to atmospheric CO_2. Based on this recipe, we grew biomorphs from mixtures of TEOS and functional triethoxysilanes like 3-mercaptopropyltriethoxysilane (3-MPTES, for introducing thiol groups), 3-aminopropyltriethoxysilane (3-APTES, for amine groups) and 3-(2,4-dinitrophenylamino)propyltriethoxysilane (DNPTES, carrying a fluorescent label) (see Sections S1 and S2 in the ESI† for experimental details). Figure 4.13 summarises the results of an experiment in which 5 vol% of TEOS were replaced by DNPTES. Confocal laser scanning microscopy (CLSM) images (Figure 4.13 h and i) clearly evidence that the obtained biomorphs display strong fluorescence, demonstrating successful incorporation of the functional silane into the structure in a one-pot synthesis. Bright and homogeneous fluorescence signal from all parts of the aggregates moreover suggests that co-condensation of TEOS and DNPTES leads to a statistical distribution of the fluorescent dye in the silica component of the biomorph, showing that this simple method enables a complete functionalisation of the entire structure. Apart from that, the incorporation of fluorescent groups allows the siliceous component to be easily detected and located. As already mentioned above, silica can be present both as an external skin and – to a greater or lesser extent – also in the bulk material around and in-between the carbonate nanocrystals. This can be analysed in detail by selective dissolution experiments.[2] For example, by immersing the as-grown aggregates into dilute acid (0.03 M HOAc), the carbonate component can be removed quantitatively within minutes. This leaves a hollow structure of fluorescent silica (Figure 4.13 f and h), corresponding to the thick outer skin covering the whole crystal assembly. On the other hand, treatment with base (1 M NaOH) dissolves this outer skin and exposes the inner carbonate-rich core (Figure 4.13 g and i). Owing to the fluorescent label, we are now able to confirm that silica is also an integral part of the inner structure (which is still under debate[54]), where it presumably serves as a “glue” holding the carbonate

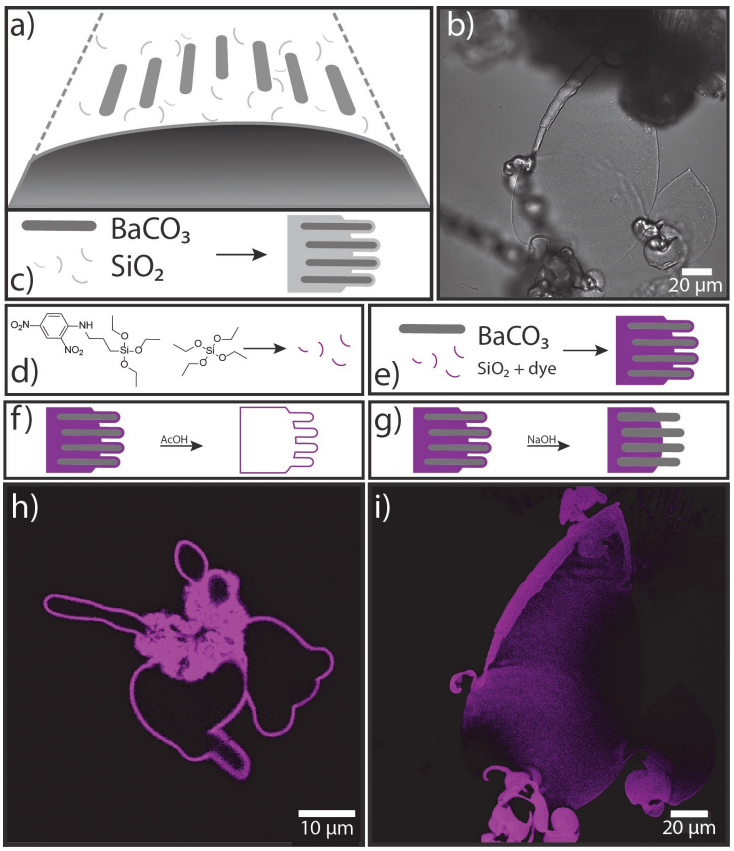

Figure 4.13: In-situ functionalisation of biomorphs by silane co-condensation. a) Schematic drawing of the growth of a biomorph by the continuous formation of carbonate nanocrystals (dark-grey rods) in the presence of silicate species (thin light-grey threads). b) CLSM image (transmission channel) of a biomorph sheet. c) Co-precipitation of BaCO3 nanocrystals and unfunctionalised amorphous silica. d) Co-condensation of TEOS and DNPTES into fluorescent "functional" silica. e) Incorporation of fluorescently labeled silanes into the siliceous component of biomorphs (magenta-coloured domains). f) Selective dissolution of the carbonate component by acid post-treatment, leading to a hollow silica structure. g) Partial dissolution of the (outer) silica component by NaOH post-treatment. h and i) CLSM images (fluorescence channel) of functional biomorphs after acid and base treatment, respectively.

crystals together. The fact that this part of the silica was not dissolved in NaOH indicates that it is intimately associated to the carbonate phase – which is well in line with the proposed model of autocatalytic co-mineralisation of the two components at the nanoscale.[74, 81] We note that pre-hydrolysis of the silanes proved to be crucial to obtain characteristic biomorphic structures directly in solution. This emphasises the key role of silica speciation in the process of morphogenesis. Besides the above-described in-situ functionalisation of biomorphs by co-condensation of alkoxysilanes with TEOS, we also conducted post-functionalisation experiments with already grown structures. Freshly harvested biomorphs are expected to carry free silanol groups at the surface of their outer silica skin (Figure 4.14 a and b), to which functional silanes can be coupled via well-known surface modification methods.[131] In this way, a broad

range of functional groups can be imparted on the biomorphs, as illustrated by Figure 4.14. Using the fluorescent silane DNPTES (Figure 4.14 c), structures similar to those

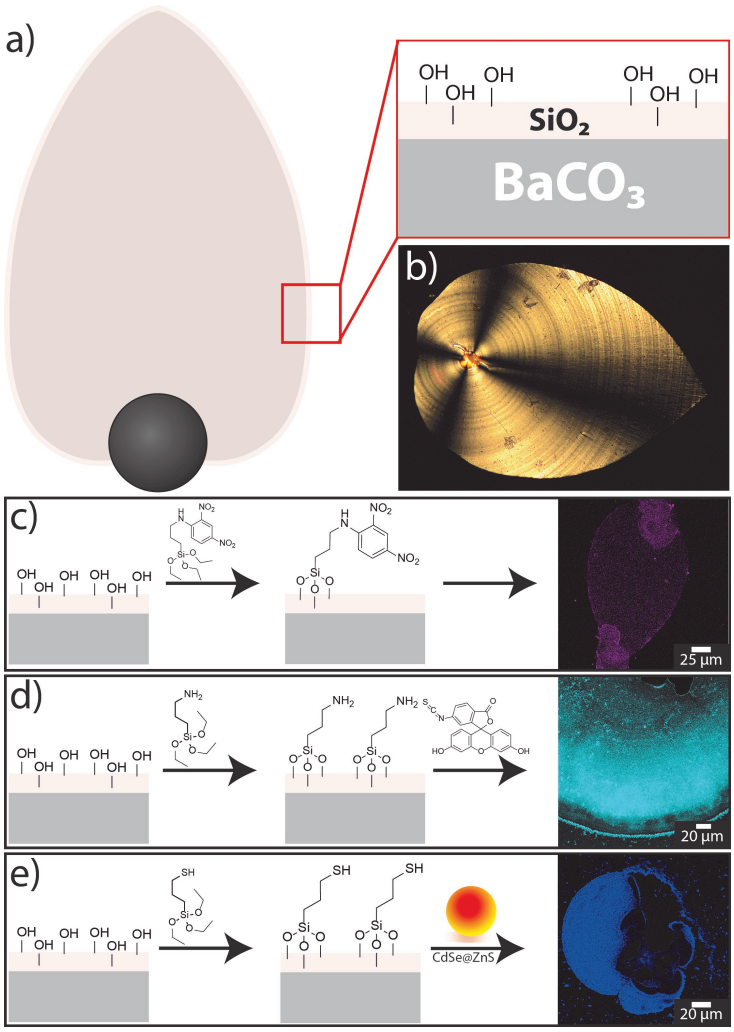

Figure 4.14: Post-functionalisation of biomorphs with different trialkoxysilanes. a) Schematic drawing of a biomorph sheet with a thick outer silica skin carrying free silanol groups accessible for coupling reactions. b) Polarised optical micrograph of a typical biomorph sheet. c-e) Schemes for the post-silanisation of as-grown biomorphs with c) DNPTES, d) 3-APTES and further functionalisation with FITC, e) 3-MPTES and subsequent binding of CdSe@ZnS quantum dots. In all cases, successful functionalisation is proven by corresponding CLSM images (right).

in Figure 4.13 were obtained, but in this case, no fluorescence could be detected in the inner part (after treatment with 1 M NaOH), indicating that only the silica in the outer skin is accessible for silane coupling. Nevertheless, bright fluorescence from the outer parts confirms that surface functionalisation by post-treatment is possible. Based on these results, further functional groups were tested. For instance, amine groups were introduced by the silane 3-APTES (Figure 4.14 d); their presence at the surface was confirmed by direct coupling of isothiocyanate dyes like FITC (fluorescein isothiocyanate),[132] which were subsequently again detected via their fluorescence

(*cf.* CLSM image in Figure 4.14 d). Other organic compounds can be coupled to the amine groups on the biomorph surface in the same way. Post-functionalisation of the structures with thiol groups was performed using the silane 3-MPTES (Figure 4.14 e). The presence of surface-bound thiol groups was verified with Ellman's reagent,[133] which forms nitrothiobenzoate (NTB) adducts in slightly alkaline solutions that can be detected and quantified by their absorption at 408 nm. With the recipe used in this study, about 1 µmol/g thiol groups could be anchored on the biomorphs (see Section S3 and Figure S1 in the ESI† for details). Having shown that biomorphs can readily be functionalised by either in-situ or post-silanisation, we now turn to Approach (2) of our work, i.e. the immobilisation of functional nanoparticles on the surface of the aggregates. To achieve this, we made use of the thiol-bearing biomorphs obtained as described above (Figure 4.14 e), since SH groups have a strong affinity to bind to certain metals and minerals. As a proof of concept, two distinct types of nanoparticles were chosen here: CdSe@ZnS core-shell quantum dots (QDs), about 9 nm in diameter (with dcore = 4 nm), and spherical gold nanoparticles (AuNPs) with an average size of 14 nm. In both cases, the thiol-modified biomorphs were incubated in dispersions of the nanoparticles for several hours and rinsed afterwards to remove any loosely adhering material. Figure 4.14 e shows the result for a biomorph that was exposed to the quantum dots. The strong fluorescence from the flat part of the sheet-like structure demonstrates successful immobilisation of the QDs at the surface (note that the black regions in the CLSM image are out of focus and hence do not show fluorescence here). In addition, the presence of cadmium and zinc was verified by EDX measurements (atomic ratio: Ba:Si:Zn:Cd = 1:0.6:0.05:0.01). In the case of the AuNPs, surface modification cannot be directly confirmed by fluorescence microscopy. While EDX analyses traced certain amounts of gold at the surface (atomic ratio: Ba:Si:Au = 0.94:1:0.01), two further methods were used to study the prepared hybrid materials. First, the biomorphs were crushed after functionalisation and investigated by means of transmission electron microscopy (TEM). The resulting images show small AuNPs covering the larger silica spheres (see Figure S2a in the ESI†), supporting the assumption that the metal nanoparticles bind to the thiol groups at the silica surface. Second, we used catalytic reactions to prove the presence of AuNPs on the structures without destroying them (Figure 4.15). The chosen test reactions were the reduction of 4-nitrophenol (pNP) with sodium borohydride16 and the reduction of resazurin with hydroxylamine (*cf.* Figure 4.15 c).[134, 135] In the latter case, the formed resorufin

could easily be observed by CLSM as a strongly fluorescent area around the biomorphic structures (Figure 4.15 b), suggesting that the reaction occurred directly on the surface where the AuNPs were immobilised (note that unfunctionalised structures did not show this behaviour). The resazurin-to-resorufin reaction also occurred without AuNP-bearing biomorphs, but at a much slower rate. This shows that the surface-bound gold particles act as a catalyst in this reaction, hence imparting distinct functionality to the biomorph structure. The reduction of pNP by $NaBH_4$ in the presence

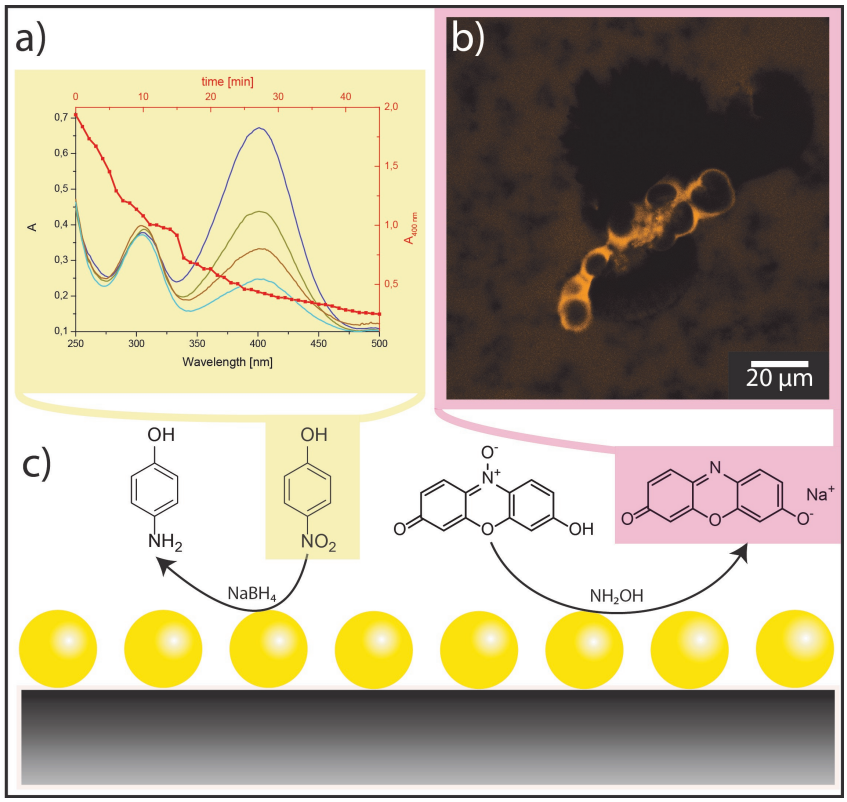

Figure 4.15: Catalytic reactions with AuNPs immobilised on biomorphs. a) UV-Vis spectra showing the reduction of p-nitrophenol by NaBH4. b) CLSM image of a AuNP-bearing biomorph in a solution of resazurin and hydroxylamine. The formation of the reduced state (resarufin) can be detected by enhanced fluorescence at the surface of the biomorph. c) Schematic drawing of the two test reactions using the immobilised particles as catalyst. The coloured molecules were analytically observed.

of gold-functionalised biomorphs was traced by UV/Vis spectroscopy (Figure 4.15 a). In particular, the strong absorption band of pNP at 400 nm was used to monitor the progress of the reaction. The thick red line in Figure 4.15a shows the change in the peak area as a function of time. It is evident that functional biomorph structures can efficiently catalyse this reaction as well (note that pNP is not reduced by $NaBH_4$ in the absence of Au). Based on reaction rates derived from similar tests under various conditions, and by using the EDX results for intact AuNP@Biomorph structures as well as UV-Vis data from gold colloid dispersions, the loading of Au nanoparticles on the inor-

ganic template was determined to be in a range of 0.03-0.7 nmol/g (see Section S4 and Figure S2 in ESI†). Taken together, the experiments described above clearly illustrate that functional nanoparticles can be immobilised on biomorphs, and that this yields complex ternary hybrid nanostructures with interesting catalytic properties.

Finally, in Approach (3), we made attempts to coat and/or fill as-grown biomorphs by a polymer, so as to imprint the structure of the hard inorganic template into soft organic material (Figure 4.16). In order to avoid uncontrolled bulk polymerisation, it is necessary to have a monomer that first binds onto the silica-carbonate aggregates and then polymerises in and/or around the inorganic architecture. A suitable candidate in this context is 10,12-pentacosadiynoic acid (PCDA), a monomer showing strong affinity to bind on carbonate surfaces via its carboxyl groups.[136] Moreover, PCDA polymerisation can be conveniently triggered by exposure to UV light (*cf.* Figure 4.16 e).

Thus, we removed the outer silica skin from native biomorphs by leaching in 1 M NaOH and subsequently incubated the exposed carbonate core in a solution of PCDA. After replacing the supernatant, the PCDA adsorbed on the biomorphs was polymerised by illumination at 365 nm. SEM images of the resulting structures (Figure 4.16 c) show that the treated biomorphs (a worm-like morphology in the present example) had a rougher appearance than their native analogues (Figure 4.16 a) and were more or less completely covered by a material with flake-like morphologies typical for poly(PCDA). This notion is corroborated by optical micrographs of the samples (Figure 4.16 d), in which the biomorphs display a blue-coloured rim, again characteristic of polymerised PCDA (note that poly(PCDA) can exist in two distinct forms, one blue and one red, between which the polymer can switch upon heating or cooling).[137, 138] The presence of poly(PCDA) on the crystal aggregates could furthermore be clearly demonstrated by IR and Raman analyses of biomorphs before and after functionalisation (see Section S5 and Figure S3 in the ESI†). Another beneficial property of PCDA is that its polymerised form shows significant fluorescence. This allowed us to localise the polymer in the as-obtained hybrids by confocal microscopy. Corresponding images (Figure 4.16 b) reveal that the polymerisation process led to the formation of a continuous organic shell around the biomorphs (as confirmed by Z-stacking image series) – or in other words, that the morphology of the inorganic architecture was transferred to the emerging organic phase. Actually, this situation is inverse to common biological and biomimetic mineralisation, where usually an organic template controls the

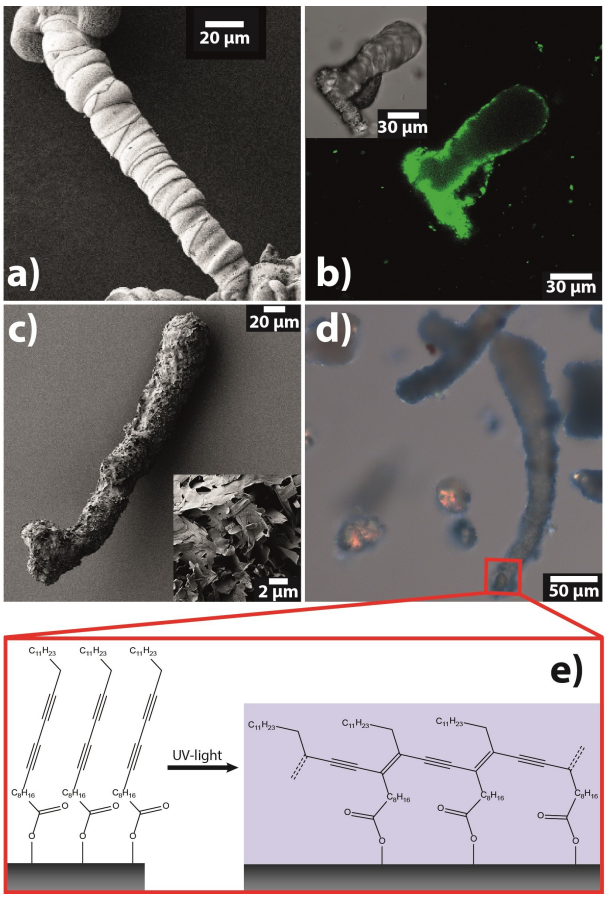

Figure 4.16: Organic polymerisation on biomorphs. a) SEM image of a structure with worm-like morphology before functionalisation. b) CLSM images (main window: fluorescence channel ($\lambda_{ext.}$ = 561 nm), inset: transmission channel) of another worm-like structure after functionalisation. c) SEM image of a poly(PCDA)-coated worm. The inset shows a zoom on the surface of the aggregate, revealing the flake-like character of the polymer coating. d) Optical micrograph of biomorphs after functionalisation, showing the characteristic blue colour of poly(PCDA). e) Schematic drawing of the polymerisation of PCDA molecules adsorbed on the biomorph surface.

shape (and structure) of a forming inorganic phase.[105] On the other hand, our analyses suggest that polymerisation did not occur in the bulk volume of the biomorphs (*cf.* Figure 4.16b), presumably due to insufficient infiltration of the PCDA monomer into the dense nanostructure. This becomes further evident when the carbonate core is dissolved in acid, leaving hollow polymer shells behind.

4.4.5 Conclusion

In summary, our results highlight different approaches to add functionality to self-organised silica-carbonate structures by rather straightforward means. We have shown that silane chemistry serves as a versatile toolbox for molecular functionalisation of the silica component in biomorphs, either by direct co-condensation during self-assembly or afterwards through surface modification, while in both cases the complex ultra-

structures of the inorganic-inorganic hybrids are preserved. This represents a notable and non-trivial achievement when considering that even slightest variations in the growth conditions can change the shape and texture of biomorphs dramatically.[58] These experiments have provided new insights into the role and distribution of silica in the aggregates by direct visualisation via fluorescent labeling. Apart from such structural information, biomorphs carrying dinitrophenyl groups could be interesting materials for the field of non-linear optics (NLO).[139, 140] DNPTES-labeled silica is known to exhibit second order non-linearity due to the non-centrosymmetric environment, and hence it should show second harmonic generation (SHG) phenomena if the dyes are aligned.[140, 141] In addition to fluorescent labeling, post-silanisation of biomorphs also allows for anchoring various functional groups such as amines or thiols at the surface, which can then be used for further functionalisation. In the present work, this strategy was employed to generate biomorph-based superstructures of semiconductor and metal nanoparticles as first examples to demonstrate the variability of our approach. The resulting materials may show special optical properties, for instance through the coupling of the surface plasmons of nanoparticles immobilised on helicoidal structures,[2, 51, 52, 54, 74, 81, 101, 102, 107] leading to chiral plasmonics on single biomorphs.[142, 143] We are furthermore confident that also other functional materials can be bound to the biomorph surfaces in a similar way. In particular, it would be desirable to orient magnetic or electric dipoles along the sinuous landscape provided by the inorganic template, as this is expected to produce complex couplings and thus give rise to new physical properties. For example, oriented attachment of suitable magnetic nanoparticles (such as iron oxides) on existing biomorph architectures could lead to long-range ordered superstructures through self-assembly,[144, 145] which in the case of twisted morphologies may yield micropropellers capable of navigating in an applied external magnetic field.[118, 146] In turn, electric dipole coupling could be realised by using anisotropic semiconductor nanoparticles like zinc oxide.[147] Finally, selective dissolution of the inner carbonate core gives easy access to hollow frameworks of functional materials with complex shapes and additional possible advantages in terms of properties and applications.[148] Post-functionalisation thus appears to be a simple and universal method with great potential to benefit from the unique structures of biomorphs in the design of nanoparticle assemblies with new collective and emergent properties, which remain to be explored. Along the same lines, it is possible to shape organic matter by in-situ polymerisation

of suitable pre-adsorbed monomers on the inorganic architectures. This bears fascinating – though inverted – analogies to biomineralisation and may have profound implications for primitive life detection[2, 52] as well as the early evolution of increasingly complex organic matter.

4.5 Symbiosis of Silica-Biomorphs and Magnetite Mesocrystals

This chapter is published in *Adv. Funct. Mater.*, **2019**, *0*, 1902047. This chapter was accepted as a communication on the 18th of July 2019. As the manuscript was published in Wiley journal, the authors keep the copyright, which allows a reprint for this thesis.

4.5.1 Abstract

Silica biomorphs are extraordinary inorganic superstructures formed via autocatalytic co-precipitation and bottom-up self-assembly of alkaline-earth carbonates and silica. However, they show no inherent functionality except for their striking textural motifs and curved morphologies. This work presents strategies to magnetize silica biomorphs, thus creating thermally-stable ceramic microswimmers with unique elaborate shapes. This is achieved by growing superparamagnetic magnetite mesocrystals on and around the complex curved surfaces of biomorphs, while keeping their morphology and maintaining mesocrystal integrity. Selective mesocrystal formation on certain parts of the substrates is induced by chemical modification of the biomorph surface, increasing the loading of magnetite on the silica-carbonate structures and, in suitable cases, rendering them able to respond to external magnetic fields and move as microswimmer entities. In this way, the complex ultrastructure of silica biomorphs has been successfully used as template for functional ceramics. Furthermore, selective dissolution of the carbonate core from the biomorphs leads to hollow magnetic structures that could be filled with actives, thus serving as microcarriers with considerable loading capacity.

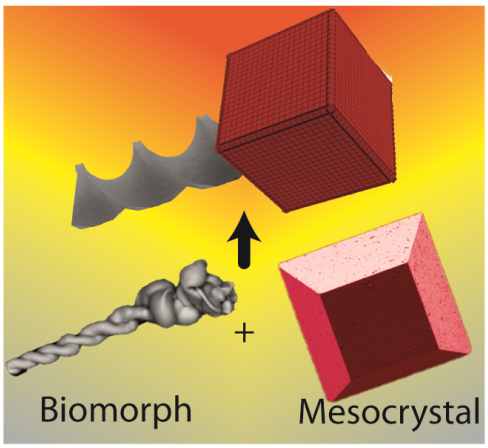

Figure 4.17: Graphical abstract of Opel *et al.* 2019.

4.5.2 Introduction

Controlled movement on the microscale is a worthwhile goal in materials science. In principle, it necessitates a swimming unit and a responding unit or engine, which interacts with outer fields or converts fuel.[118] However, so far, it has been challenging

to fabricate microswimmers with varying complex shapes within a single batch, which may enable interesting features such as self-propelling. Silica-carbonate "biomorphs" could be promising archetypes for the design of such swimming units, since they form spontaneously by self-assembly and grow into elaborate curved architectures on the multi-micron to millimeter scale.[51, 102, 149] Among the morphologies commonly displayed by these inorganic-inorganic hybrids, the most interesting shapes for swimming or carrying applications are the chiral filamentous forms, i.e. worm-like braids, helicoids and twisted ribbons. All these peculiar structures can be obtained in a simple one-pot synthesis from aqueous media at ambient conditions. Indeed biomorphs form upon addition of alkaline-earth metal cations like barium, strontium or calcium to alkaline, silica-rich solutions or gels, with subsequent diffusion of atmospheric CO_2 triggering the slow crystallization of carbonates under the influence of silicate species.[74, 81] The formation of complex ultrastructures relies on an autocatalytic co-precipitation mechanism that produces uniform carbonate nanocrystals, which self-assemble on the mesoscale and become embedded in a matrix of amorphous silica.[51] The rich structural variety of biomorphs is shown in Figure 4.18 a-e (also compare with Figure 9.7 in the Supporting Information (SI) for an overview on typical structures obtained from a single batch) can be explained based on differences in local growth velocities during the formation process, which can induce local curling and thus give rise to curved and twisted architectures.[74, 81] Once these structures are formed and self-assembly has ceased, secondary precipitation of silica (due to the lowered bulk pH) often leads to the deposition of a continuous skin of amorphous silica all over the structures.[115] Moreover, long reaction times can also cause secondary precipitation of (regular) carbonate crystals, which typically grow more or less selectively at the apex of the structures and their outer edges. In this stage, no coupled precipitation occurs and carbonate formation is preferred (note that both of these secondary processes will be used for functionalization below).

While many previous studies on silica biomorphs were focused on their morphogenesis and structural control[59, 71, 102, 150, 151] as well as relevance for primitive life detection,[52] possible functional properties of biomorphs have hardly been explored until recently. The first successful surface functionalization of the as-obtained silica-carbonate hybrids was achieved using silane chemistry in combination with nanoparticles or by controlled polymerization of organic matter around the inorganic template.[119] Later, the entire bulk composition of biomorphs was changed after growth

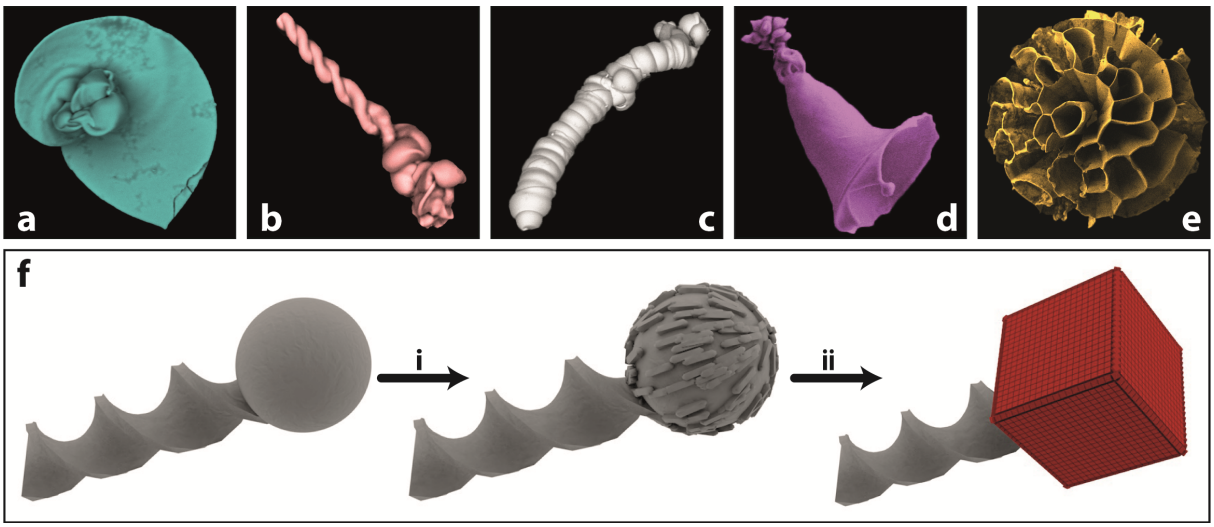

Figure 4.18: Morphological variety of silica-biomorphs and the approach to magnetize them. a-e) Scanning electron micrographs in false colors of a biomorphs sheet (a), helix (b), worm-like braid (c), trumpet (d) and coral (e). f) Magnetization approach with magnetite mesocrystals. Methodological approach of the magnetization of silica biomorphs by heterogenous nucleation of magnetite mesocrystals. In the first step (i) decoration of the globular end with witherite crystals followed by the selective mesocrystal formation (ii).

by ion exchange and subsequent conversion to semi-conducting perovskites.[152] In the present work, we have investigated the potential of biomorphs to serve as swimming units in microscale motors able to operate even at high temperature. Biomorph shaped which have a potential as a swimming unit are the helicoidally and the worm-like braids (*cf.* Figure 4.18b,c) and therefore this work focuses on this two types of morphologies.

To control the movement of silica biomorphs on the micronscale, they need to be equipped with a suitable engine or responding unit. One such engine could in principle be iron oxide catalysts, which would have to be immobilized on the biomorph surface, where they could then decompose hydrogen peroxide and generate gas bubbles that drive the motion of the microswimmers, as reported previously for other systems.[118, 153] However, since the size of biomorphs is typically in the range of at least tens of micrometers, they are likely too heavy to be propelled by this type of motor (unpublished preliminary work). Instead, they require a stronger driving force – such as that provided by an external physical field. Here we have chosen to equip silica biomorphs with a magnetic responding unit that should allow them to navigate in an applied magnetic field. A suitable responding unit for magnetic biomorph microswimmers was obtained by particle-based crystallization, namely the assembly of superparamagnetic magnetite nanoparticles into "mesocrystals".[84, 85] Mesocrystals are superstructures consisting of nanocrystals that share the preferred crystallographic

orientation over long-range distances. Compared to bulk materials, nanocrystals often show outstanding size-dependent properties, but in turn they are difficult to handle as a material.[154, 155] The assembly of nanocrystals into mesocrystals provides an important route to processability while maintaining the unique properties of nanocrystals during "scale-up" to micron-sized or even macroscopic structures. In the case of magnetite (Fe_3O_4), nanocrystals with sizes less than 30 nm show superparamagnetic behavior at room temperature.[156, 157] This behavior allows to affect mesocrystal formation using a magnetic field to create rather uncommon mesocrystals (in terms of morphology and structure) as compared to those formed without the influence of a magnetic field.[158] However, the superparamagnetic properties of the nanocrystals are preserved as reported for millimeter-sized mesocrystals e.g. by Yin et al.[159] Such magnetic mesocrystals seem to be a perfectly suited responding unit for microswimmers upon interaction with external magnetic fields. Uniting the concepts of silica biomorphs and magnetite mesocrystals, a variety of new self-assembled ultrastructures with interesting functional properties can be prepared via explicitly simple approaches, as summarized in Figure 1f. In this approach a selective anchor point should be generated at its end with witherite crystals followed by the mesocrystal formation. The most promising symbiosis between barium carbonate (witherite) biomorphs and superparamagnetic mesocrystals – leading to high temperature stable (up to 420°C), ceramic, responsive microarchitectures – is highlighted in this work.

4.5.3 Results and Discussion

Magnetite mesocrystals as responding unit for microswimmers were formed via gas diffusion of an anti-solvent into an organic solvent based dispersion of magnetite nanoparticles stabilized by oleic acid (see the SI for details on the synthesis and a sketch of the setup used for the formation of mesocrystals (Figure 9.8 a)). The mesocrystals form on silicon wafers by a continuous and slow decrease of the colloidal stability of the nanoparticle dispersion, leading to well-defined superstructures as shown in Figure 2b and c. Their morphology can be described as a tetragonal truncated pyramid exposing a p4mm projected symmetry on the basal (001) face, which shows p4mm plane group symmetry of nanoparticles packing.[15] To act as responding unit, these mesocrystals must crystallize on carbonate-rich surfaces as commonly displayed by biomorphs. This precondition was tested by replacing the usual silicon wafer as

growth substrate with single crystals of aragonite (see Figure 9.8 b in the SI) and calcite (see Figure 9.8 c in the SI). Indeed, magnetite mesocrystals were found to grow on carbonate surfaces, with preferred occurrence on notches and roughness, indicating heterogeneous nucleation. Based on these observations, as-grown biomorphs were used directly and without any further chemical modification as microscopic substrates to create magnetic microswimmers in a straightforward procedure (Route III in Figure 4.19 a). The result is shown in Figure 4.19 g, demonstrating a successful combination of a biomorph worm and quite large magnetite mesocrystals, which have grown around the globular apex from which the worm has emerged. Here, selective attachment of the mesocrystals to the apex is ascribed to the presence of regular witherite crystals (i.e. bare carbonate surfaces without significant amounts of silica) on this part of the biomorph (as shown by Figure 4.19 i and Figure S3 in the SI), which have been generated by increasing the growth time from 8-10 h (bulk pH: 10.5) to 16-48 h (bulk pH: 8.5). At the lower bulk pH, the chemical coupling between carbonate and silicate speciation is no longer active, and hence the two components mineralize independently from one another (yielding regular carbonate crystals at the apex and a continuous silica skin over the rest of the aggregate). When the size of the magnetite mesocrystals is decreased (by adding less oleic acid stabilizer in the nanoparticle dispersion), the regular carbonate crystals covering the apex become visible and the selective growth of many small mesocrystals on these surfaces is clearly observed (see Figure 4.19 h and i). To further increase the mesocrystal loading, the surface of the biomorphs was modified in different ways, as summarized by the scheme in Figure 4.19 a. This provides a toolbox allowing for the controlled deposition of mesocrystals at various positions of the biomorph. For instance, treating the as-grown biomorphs with NaOH solution removes the outer silica layer (as proven by IR spectroscopy, *cf.* Figure 4.19 d) and exposes their bare core, which consists mainly of co-aligned barium carbonate nanorods (Route I in Figure 4.19 a). Such rough carbonate-rich surfaces should be an excellent substrate for the immobilization of magnetite nanocrystals enabling magnetite mesocrystal formation. Moreover, the obtained biomorphs without silica shell can be used to hydrophobize the surface via adsorption of a layer of oleic acid (Route II in Figure 4.19 a; binding of oleic acid to the bare biomorph surface is confirmed by the two IR bands at 2852 and 2922 cm^{-1} in the black spectrum in Figure 4.19d). A hydrophobic surface should lead to enhanced interaction with the oleic acid stabilizer shell around the magnetite nanoparticles and thus to a denser cover-

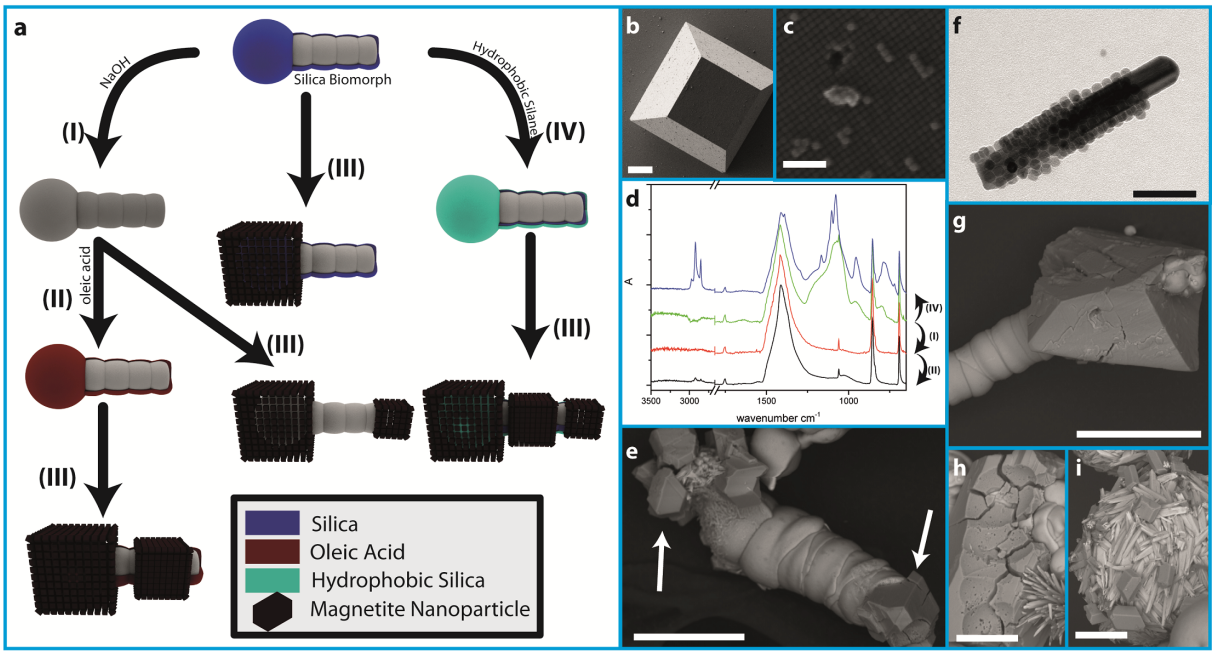

Figure 4.19: Functionalization of silica biomorphs with magnetite mesocrystals. a) Scheme illustrating the various pathways leading to different composites of magnetite mesocrystals and worm-like silica biomorphs. (I) Dissolution of the outer silica shell of biomorphs with NaOH solution to obtain "naked" carbonate surfaces. (II) Subsequent hydrophobization of the naked biomorph with oleic acid. (III) Magnetite mesocrystal formation via "gas diffusion method" on top of the biomorph structure at different, potentially multiple positions. (IV) Hydrophobization of the outer silica shell via post-treatment with alkyl triethoxysilanes. The indicated positions and amounts of the mesocrystals covering the biomorph worm are meant to illustrate the quality and selectivity of the functionalization. b,c) Scanning electron microscopy (SEM) images of magnetite mesocrystals grown from THF solution upon destabilization via gas diffusion. d) IR spectra of biomorphs after modification according to pathways I, II and IV in (a). e) SEM image showing the successful formation of magnetite mesocrystals (white arrows) around the apex and the tip of a worm-like biomorph that has been post-functionalized with dodecyl triethoxysilane. f) TEM image of a carbonate nanocrystal obtained from the core of a biomorph, which was functionalized with oleic acid and subsequently became covered with magnetite nanocubes. g) SEM image of an unfunctionalized silica biomorph after mesocrystal formation. h) SEM image of a magnetite mesocrystal showing a negative imprint of a biomorph worm around which it originally grew. i) SEM image of the apex of a biomorph worm, which shows pronounced overgrowth with regular barium carbonate crystals (long rods), which themselves have been decorated by small magnetite mesocrystals (grown at reduced oleic acid concentration). Scale bars are (b) 10 μm, (c and f) 100 nm, (e and g) 50 μm, and (h and i) 25 μm. (Scale bars B: 10 μm; C, F: 100 nm; E, G: 50 μm; H, I: 25 μm)

age of the entire structure with the nanoparticles. Alternatively, biomorphs that still carry an outer silica skin can be hydrophobized by using alkyl triethoxysilanes (e.g. octadecyltriethoxysilane) (Route IV in Figure 4.19 a).[119] Again, successful functionalization is shown by IR spectroscopy (Figure 4.19 d). Having obtained a collection of biomorphs exposing different surface chemistries (neat silica (hydrophilic), silane-modified silica (hydrophobic), neat carbonate (hydrophilic) and oleic acid-modified carbonate (hydrophobic)), we tested their ability to act as substrates for enhanced

magnetite mesocrystal formation. Bare carbonate as well as hydrophobized surfaces (regardless of whether silanes or oleic acid are used) showed an increased, though less site-specific adsorption of magnetite nanoparticles at various positions all over the biomorph architecture. The strong affinity of magnetite nanoparticles towards bare or hydrophobized surfaces is also supported by TEM studies on crushed specimens: Figure 4.19 f shows a single carbonate nanorod, which is decorated by numerous smaller magnetite particles. Analysis of several such carbonate rods suggests that they are covered with mono- or multilayers of magnetite nanocubes on most faces. Due to the strong affinity for magnetite to bind, bare carbonate and hydrophobic surfaces thus favor mesocrystal formation on several different positions on one given biomorph architecture (*cf.* white arrows in Figure 4.19 e), while on untreated biomorphs, rough areas like those carrying secondary witherite crystals (usually the globular apex, *cf.* Figure 4.19 i) become preferentially overgrown by magnetite mesocrystals. The formation and growth of mesocrystals can also occur in-between two or several neighbouring biomorph structures, where the available (reduced) space is filled by the mesocrystals with no noticeable interference due to the confinement. One such example can be seen in Figure 4.19 h, where a negative imprint of a biomorph worm is present on the mesocrystal (presumably the two domains were torn apart during isolation). This underlines the adaptability of the mesocrystals to existing template structures without abandoning the co-orientation of their nanoparticulate building units. In the light of the different presented functionalization methods as well as the broad intrinsic structural variability of silica biomorphs (including numerous other interesting morphologies beyond those addressed here, such as coral- or flower-like forms), it seems obvious that a large spectrum of magnetic microarchitectures can be designed using the concept introduced above. With respect to microswimmer applications, each of these forms may show different hydrodynamic behavior and thus can be selected from the morphological pool for a given purpose.

To test the response of the mesocrystal-biomorph composites to an external magnetic field, they were placed in a Petri dish that was mounted on a fixed platform under a light microscope (*cf.* Figure 4.20 a-c). A permanent magnet (100 mT at the sample/ 290 mT at the magnet surface) was then fixed to the stage of the microscope underneath the sample, enabling an exact tracking of the position of the magnet. First, the swimming behavior in liquid media was studied by placing a magnetic microstructure (biomorph worm carrying two magnetite mesocrystals) on the surface of a highly vis-

cous aqueous solution of poly(ethylene glycol) (MW = 8000 g/mol; 50 wt%; η = 325.5 mPa·s), on which it floated randomly when no external field was applied. In the presence of the magnet, the superstructure can travel along predefined pathways through the solution (*cf.* Figure 4.20 b and Movie S1 in the SI). Figure 4.20 b' shows a time-lapse sequence of images illustrating the linear movement of the responsive microarchitecture (see Movie S2 in the SI for the corresponding video) induced by locating the magnet at a fixed position on the right side of the field of view (indicated by the black dashed line). The biomorph microswimmer moves directly towards the magnet through the viscous medium and can also be forced to travel forth and back following a continuous displacement of the magnet (as shown by Figure 4.20 b and Movie S3 in the SI). It is furthermore evident that response of the structure is somewhat delayed with respect to the displacement of the magnet, likely due to inertial effects caused by the high viscosity of the medium. In a second experiment, a biomorph worm carrying one magnetite mesocrystal at its apex (*cf.* Figure 4.19 g) was put on a dry Petri dish, with its contact point (red dot in Figure 4.20 c) slightly displaced relative to the center of the path travelled by the moving magnet. This induces a rotating movement when the magnet passes the structure, as illustrated schematically in Figure 4.20 c and Movie S4, and observed experimentally in Figure 4.20 c' and Movie S5. Here, the self-assembled composite responds directly and with little delay (due to the lower viscosity) to the displacement of the magnet (relative magnet positions are indicated as pointing angles by the red lines in Figure 4.20 c', with 0° corresponding to the starting position). It should be noted that the biomorph-mesocrystal aggregate was not immobilized on the surface of the Petri dish, but nevertheless remained at a fixed position and only rotated. Furthermore as can be seen in Movie S5, also single mesocrystals follow the movement of the magnet. They are a byproduct from the preparation procedure. This shows that the motion of the microarchitecture can be precisely controlled in the dry state if the applied forces are not too pronounced. All these observations clearly demonstrate that magnetite mesocrystals attached to silica biomorphs indeed work as responding units in an external magnetic field, enabling controlled movement on the micronscale.

Another very promising aspect about these materials is the possibility to transform the magnetized architectures into hollow microcarriers, which can be easily achieved by removing the carbonate core with dilute acid, leaving behind a hollow silica "ghost" that still carries the mesocrystal responding unit. Such structures could serve as carriers for molecular cargo, which after filling with actives travel to predefined locations

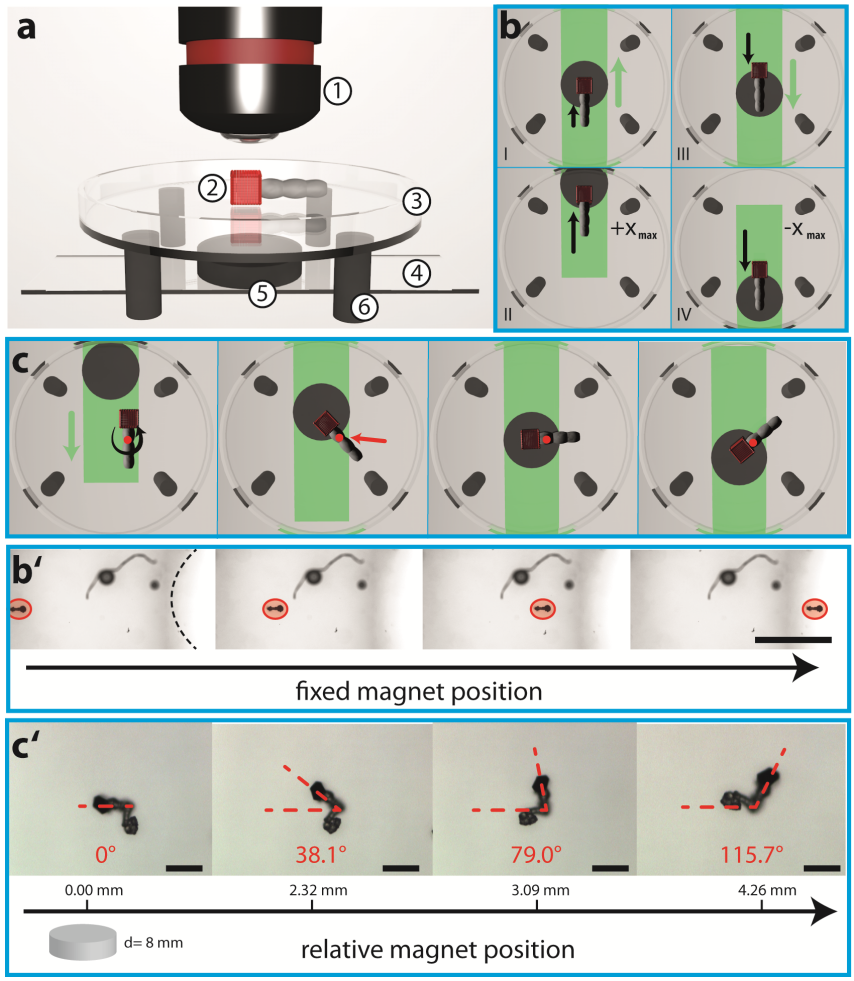

Figure 4.20: Biomorphs as responsive microarchitectures. a) Schematic illustration of the experimental setup used to move magnetized biomorphs in an external magnetic field. 1: objective, 2: sample, 3: fixed Petri dish, 4: moving glass slide, 5: permanent magnet, 6: holders for Petri dish. Moving the object holder will only displace the magnet (and not the sample), whose relative position is tracked at all times. b) Sketch of a linear displacement of a magnetized biomorph across a highly viscous aqueous PEG solution guided by a permanent magnet. Green and black arrows indicate the movement of the glass slide carrying the magnet below the Petri dish and the delayed response of the biomorph above, respectively. b') Snapshots of an experiment according to the setup in (b), where the magnet is located at the right end of the field of view as indicated by the dashed black line, while the magnetized microstructure (highlighted in red) is moving towards it. Scale bars are 1 mm. c) Sketch of a rotating movement (indicated by the black arrow) of a dry magnetized biomorph in response to a linear displacement of the permanent magnet (green arrow). The red dot marks the position where the biomorph is fixed to the substrate (rotation axis), which in this case is not centered on the path travelled by the magnet. c') Snapshots of an experiment according to the setup in (c). The biomorph-mesocrystal composite responds to the movement of the magnet (relative positions are given below the micrographs) by rotation as indicated by the drawn angles. Scale bars are 100 μm.

and release their cargo there (targeted micro-release and/or spatial reaction control in microenvironments). Movie S6 in the SI shows such a hollow ghost and its ability for controlled movement in an external magnetic field (note that this structure moves through a less viscous acetic acid solution and therefore the response to the moving

magnet has no visible delay compared to the experiments in PEG solution). It could further be envisaged that the hollow silica framework is functionalized by silane chemistry to enable selective uptake and release. At least, one should keep in mind that for a pure inorganic system with these responsive architectures, a high thermal stability is expected. To further investigate the thermal stability of mesocrystal-biomorph composites, the magnetite mesocrystals were annealed at different temperatures in the range between 350°C and 500°C, which is below the decomposition temperautre of barium carbonate (SI Materials and Methods). Within the tested temperature range, the specimens preserve the initial shape of the mesocrystals, however at 350°C - 420°C the magnetite nanoparticles partially fuse together forming "mosaic" structures on the aggregate surfaces. At 500°C, the phase transformation of magnetite to hematite is observed and the faces of the specimens are overgrown by plate-like nanocrystals (Figure 9.10 a). Morphologically and compositionally the mesocrystal-biomorph composites should therefore be stable at least up to 420°C. At even higher temperatures (1000°C) the outer shape of the composite is still preserved (Figure 9.10 b) but new phases (incl. barium silicate, barium oxide, crystalline SiO_2 (tridymite) and hematite) have replaced the original materials which also goes along with a change of the magnetic responsivity.

4.5.4 Conclusion

In summary, our work highlights the successful symbiosis of two prominent examples for complex self-assembly in the field of crystallization: silica biomorphs and mesocrystals. Their combination leads to functional microscopic ultrastructures in straightforward processes at ambient conditions. Given the large variety of morphologies and structures accessible within one batch of biomorph synthesis (going far beyond the proof of concept established in this work), numerous types of responsive microtools can be generated in just a few processing steps. By targeted modification of the surfaces of silica biomorphs, the adsorption of superparamagnetite nanoparticles and their assembly into mesocrystals on the biomorph substrate can be controlled. This approach gives access to magnetic microarchitectures that can be applied as responsive tools ranging from microswimmers over microcarriers to micromanipulators. In the present work, it was demonstrated that external magnetic fields can be used to precisely control the movements of the architectures in a simplified setup. Since

these structures are composed of purely inorganic material, they show high temperature stability. Finally, the possibility to remove certain components selectively – e.g. carbonate by acid or silica by base post-treatment, leaving a hollow silica ghost or an open porous carbonate network, respectively – offers further handles for enhanced functionality, such as the incorporation and/or transport of active compounds, which could eventually enable targeted release from the moving structure.

4.6 Light-Switchable Anchors on Magnetized Biomorphic Micro Carriers

This chapter is published in *J. Mater. Chem. B*, **2020**, *8*, 4831. This chapter was accepted as a communication on the 10th of June 2020. As the manuscript was published in an RSC journal, the authors keep the copyright, which allows a reprint for this thesis.

4.6.1 Abstract

Microcarriers with the ability to release and catch substances are highly desired metamaterials and difficult to obtain. Herein, we report a straightforward strategy to these materials by combining silica-biomorphs with mesocrystals. An easy access to microcarrier hulls with covalently bound spiropyrans as light switchable anchorpoints is presented.

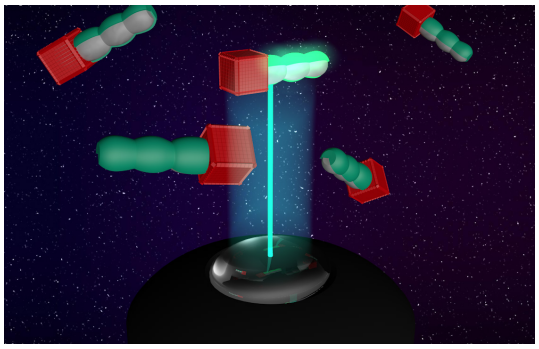

Figure 4.21: Graphical abstract of Opel *et al.* 2020.

4.6.2 Introduction

The so-called silica-biomorphs are purely inorganic composite materials that exhibit outstanding shapes.[51, 52, 74] Their preparation is performed in alkaline, silica-rich solutions containing earth-alkaline metal ions, like Ba^{2+}, Sr^{2+} or Ca^{2+}.[149, 160] The formation mechanism is assumed to be based on autocatalytic co precipitation of earth-alkaline carbonates and silica linked to a local pH cycling induced by alternating silica and carbonate precipitation.[81, 101, 113] The huge variety of self-assembled carbonate nanorods is interesting for several applications. The elongated shape of worm-like and helicoidal shaped biomorphs bear the potential to be used as microcarrier hulls.[161] Magnetic nanoparticles like magnetite nanocubes are used as responding unit, which is needed for controlled movement through various media.[162, 163] The benefit of this system is the ability to attach mesocrystals at specific sides of the biomorph (cf. Fig. 4.22).[98, 161] Mesocrystals form in a non-classical pathway via the oriented assembly of non-spherical nanocrystals into superlattices.[85, 106] In order to create further functionality, the structures must be equipped with an additional responding unit that allows addressing of a

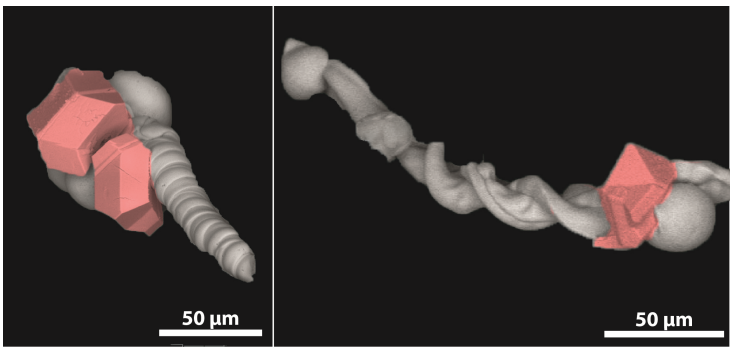

Figure 4.22: Scanning electron micrographs of a biomorph worm (left) and a biomorph helix (right) decorated with magnetite mesocrystals (highlighted in red) at the globular apex of the structures.

switchable anchor point for controlled compound load/release. Previous works employ post functionalization by use of silane coupling chemistry.[119, 161]

The incorporation of light-switchable molecules to various systems and the development of so called dynamic materials came into the focus of attention during the last decades. Not only the synthesis of materials for data storage[164], electronic devices[165] or sensors[166] but also the biological applications of photo-responsive compounds, e.g. in photopharmacology,[167–169] have been investigated. Photo-switchable molecules show reversible transformation between at least two different thermodynamically stable isomers induced by irradiation with light of a particular wavelength. Among the wide range of photo-switches, spiropyrans achieved a privileged status since they enable production of materials that are responsive to multiple external stimuli in an orthogonal fashion. The two isomeric structures of a spiropyran show vastly different properties, which results in an isomerization process that is not only induced by irradiation with light but also by several other external stimuli including temperature, solvent or pH-value.[170] In addition, covalent attachment of spiropyran units to a solid support results in numerous advantages compared to the non-immobilized counterparts, including an improved fatigue resistance[171, 172], or the possibility to obtain biocompatible photoresponsive materials.[173, 174]

The incorporation of silane-containing switchable molecules like spiropyrans is a desired method to new metamaterials.[170, 175] The typical structural formula of a spiroindolinopyran (SP) is shown in Fig. 4.23, consisting of an indoline and a chromene moiety, which are connected via a spiro center. The isomeric merocyanine (MC) is accessible by heterolytic cleavage of the Cspiro-O bond induced by irradiation with UV-light. Population of the excited state is followed by an intersystem crossing process

to the corresponding triplet state in which the ring opening takes place.[176] Internal rotation in the ground state to the cis- and trans-isomers is in most cases followed by a thermal isomerization to the trans-isomer. The open-ring isomer exists as either zwitterionic (**2**) or quinoidal species (**3**). The merocyanine often shows strong fluores-

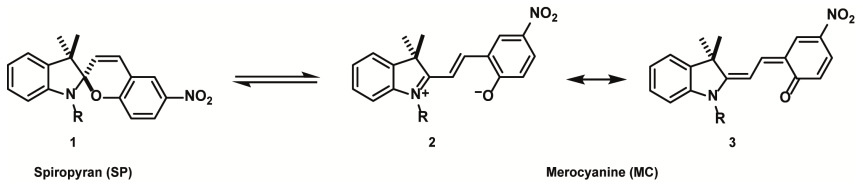

Figure 4.23: Typical structural formula of a spiroindolinopyran

cence and exhibits a remarkably higher affinity to different chemical structures[177], a property that is caused by the additional free oxygen acting as a donor function. The zwitterionic merocyanine has already been described as a ligand for (divalent) metal ions[178–180] whereas the neutral spiropyran is a rather unfavorable donor. Utilizing the huge differences in the properties of the isomers, multi-fluorescent hybrid particles[181], traps for ions[182] or small molecules[175] are prepared, the hydrophobicity of solid surfaces[183] can be tuned reversibly, or the electrochemical properties of a surface[184] are controlled. Reverse isomerization to the initial spiro compound is possible to occur by either thermal relaxation or irradiation with visible light. These properties moved the spiropyran-merocyanine system to the focus of our interest with regard to the design of a magnetized biomorphic microcarrier system.

4.6.3 Results and Discussion

The synthesis of a silane-functionalized spiropyran is desired for a carrier system based on mesocrystal-biomorph composites (MCBCs). Spiropyrans for the desired silica-modification were already published in literature[175], but accessibility and feasibility were improved in this approach. Based on a literature-known synthesis of a spiropyran bearing a carboxylic acid group[185], the desired compound was accessible by peptide coupling with 3 aminopropyl triethoxysilane. The reaction scheme is shown in Fig. 4.24 A. Compound **7** was subsequently immobilized on silica biomorphs. The attachment of functional silanes to various biomorphs was already proven and allowed the desired functionalization of the particle surface with spiropyrans.15 The scheme of this procedure is shown in Fig. 4.24 B.

Silica-biomorphs were precipitated from barium-containing alkaline silica sol through

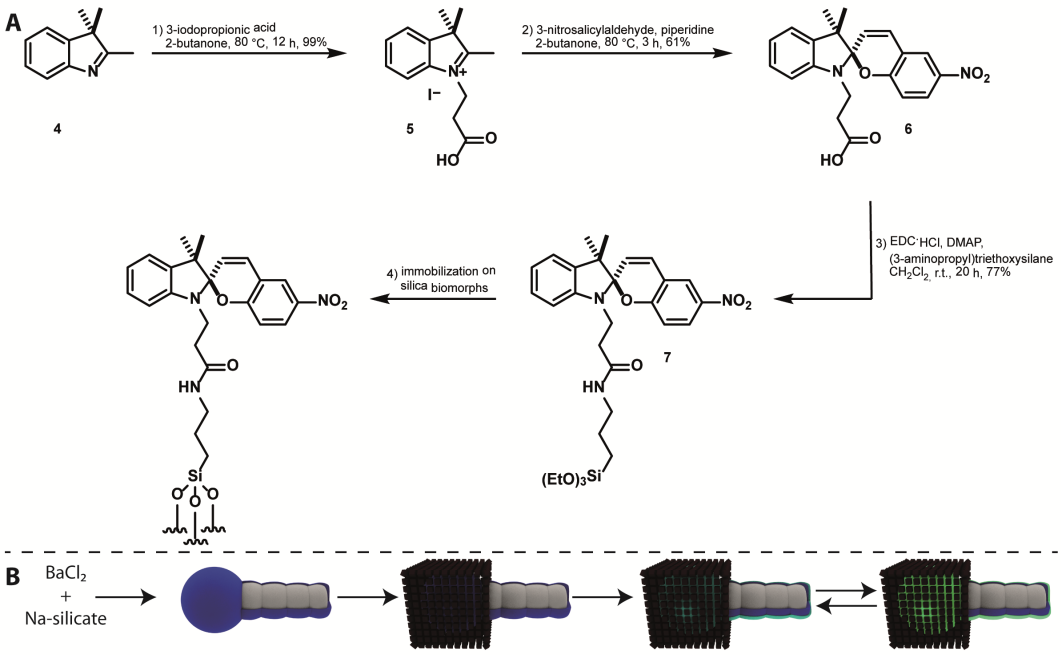

Figure 4.24: A) Synthesis route of the silanefunctionalized spiropyran (target compound 7). B) Formation scheme of the light switchable MCBCs via the selective formation of magnetite mesocrystals around silica-biomorphs tips and the post functionalization of their silica shell with compound 7 and its ability of light induced switching on the MCBC surface which induces the glowing (bright green).

continued CO_2 diffusion into the sol. The structures remained in the mother sol for 16 h to reach the secondary precipitation stage, where an outer silica shell and additional witherite attach to the structures.[161] A thicker silica layer around the structures is desirable to improve stability once the inner core dissolves for an improved carrier capacity of the MCBCs. Selective secondary precipitation of witherite crystals around the tips of the structures is desired to induce heterogeneous magnetite mesocrystal formation. The obtained solid from the biomorph synthesis was rinsed several times with deionized water and dried. The biomorph powder mainly consisted of worm-like braids and helicoidal structures, decorated with witherite crystals on the former globular tips of the biomorphs. The structures were transferred into a magnetite nanocube solution in THF containing a certain amount of oleic acid. The biomorphs act as substrates for the mesocrystal formation. Mesocrystals were formed through gas phase diffusion of the anti-solvent (ethanol) into the magnetite nanocube solution. The particle, as well as the oleic acid concentration were accurately chosen in order to generate mesocrystals in the range of the tip size (cf. Fig. 4.22). Decreased nanocube concentration leads to smaller mesocrystals and a lower total magnetite loading of the structures. The result is a different responding behaviour in the magnetic field. Decreased oleic

acid concentration results in an increased number of smaller mesocrystals. The total magnetite loading stayed constant.9 Obtained MCBCs allow a further post functionalization treatment with synthesized compound **7** by incubation of the structures in a 1 wt.% solution in ethanol/water (95:5) for several hours. The generated functionalized silica layer can be seen in the Fig. 4.24 B as blue layer in the SP form. UV-irradiation of the material induces the spiro-compound to switch to the MC form, which is indicated by the glowing green colored layer (Fig. 4.24 B). As previously mentioned in literature, the vastly different properties of the two isomers can be further used for selective catch and release of compounds.[175]

To prove the postulated scheme of the formation of light switchable MCBCs, laser scanning microscopy (LSM) was used. A selective switching of the SP by using the bleach mode was induced with a different wavelength. Therefore, the excitation and emission spectra of compound **7** were recorded and are shown in Fig. 4.25 A. The black spectrum shows the excitation spectrum of the SP form detecting the intensity of fluorescence at 625 nm while the excitation wavelength changes. The spectrum has a maximum at 555 nm and a shoulder at 520 nm. In addition, several emission spectra were measured to elaborate the obtained fluorescence as subject of the excitation wavelength. Using an excitation wavelength of 555 nm, the highest fluorescence intensity was obtained (green spectrum), while an excitation wavelength of 490 nm exhibited lower fluorescence yields (blue spectrum). Nevertheless, 490 nm excitation is the most important result due to the equipped analysing lasers on the LSM. For the fluorescence experiments on the LSM, the imaging was performed with a 488 nm laser (1% laser power, pin hole: 1 au).

Imaging the structures with visible light continuously decreased the obtained fluorescence. The degradation of fluorescence is worse with the 555 nm laser, which was additionally chosen in other experiments to turn off the fluorescence while switching the MC back to the SP form. To generate a high amount of fluorescent MCs on the surface, the structures were “bleached” in a region of interest (ROI) with a 405 nm laser (20% laser power, 4 scans). One result is shown in Fig. 4.25 B. The bleaching of the ROI occurred after the first and every third following cycle, indicated by the bluish bars. The measured data originated from a programmed times series. Continuous decrease of the fluorescence intensity in the 3 steps after excitation to a level lower than before the bleaching explains the ongoing decrease of the overall fluorescence intensity. The effect becomes even clearer by considering several cycles. An example is shown in Fig.

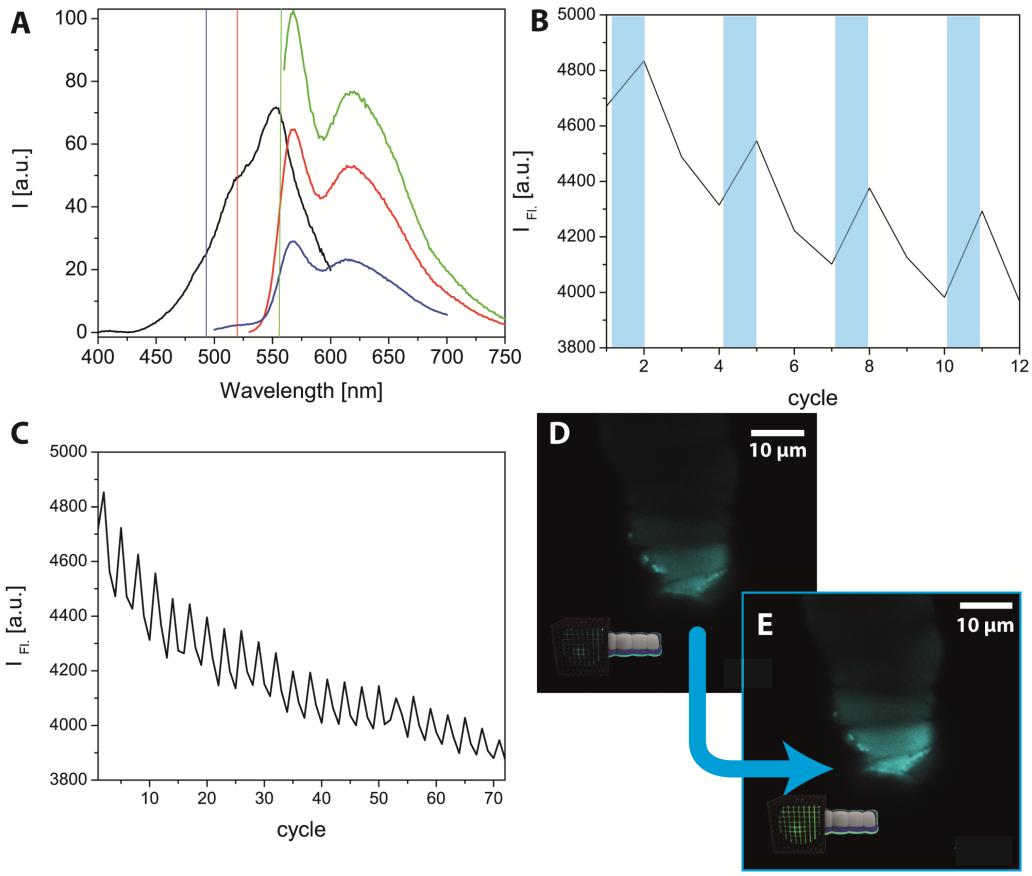

Figure 4.25: A) Excitation (black) and emission spectra of the synthesized compound 7 in ethanol. The vertical coloured lines correspond to the excitation wavelength (blue: 490 nm; red: 520 nm; green: 555 nm). B) ROI (region of interest) intensity measurement over twelve scanning cycles on the LSM. Bleaching of the region (405 nm; 20% laser power; 4 scans; after the 1st and every following 3rd image) is indicated as bluish areas. C) Long-term cycling at the ROI over 72 cycles with the same settings chosen for B. D) LSM image (excitation wavelength: 488 nm, 1 % laser power) in false colours of a SP functionalized structure in the OFF (SP) state. E) LSM image of a SP functionalized structure in the ON (MC) state.

4.25 C, where 72 cycles are recorded in the same area. To visualize this effect, Fig. 4.25 D shows a functionalized MCBC in its OFF state, before the frame was illuminated with 405 nm light. Fig. 4.25 E shows the activated structure after excitation. It has to be mentioned that the pictures show a lower end of a functionalized biomorph worm, and the lowest part is in focus. The pin hole cuts off the fluorescent light emitted from the upper part, allowing an improved image quality and spatial resolution. Therefore, the LSM constitutes an appropriate method to prove the incorporation of the functional silane on the structures. This has also been shown in previous works[119] and demonstrates the suitability of spiropyrans as switchable anchor points on biomorph-based microcarriers.

4.6.4 Conclusion

This work highlights a rational designed pathway to generate easily accessible microcarriers by utilising the silane chemistry toolbox linked to light switchable spiropyrans and the exceptional shaped ultrastructures called silica-biomorphs. On top a magnetite mesocrystal is used as a responding unit, which results in a full functional metamaterial extending the frontiers in all three used fields (biomorphs, mesocrystals and spiropyrans). The here described materials have potential in a number of applications. Since it is already literature known that the merocyanine form can bind metal cations[178–180], the microcarriers could be used for the transport of metal ions by a magnetic field. Ion release by switching to the spiropyran form would allow reactions of the released cations like catalysis, mineralization, complexation etc. One could also think of binding polar nanoparticles to the merocyanine form, which can be released by light at the location of interest. Also, polar drugs could be bound, transported and released. If the spiropyran form could be used for binding of unipolar species (drugs, molecules etc.), release by light switching to the merocyanine form would enhance the application spectrum of the microcarriers a lot. Future studies will show the exciting applications, which will become possible with the mesocrystal functionalized biomorph microcarriers.

4.7 Hybrid Biomimetic Materials from Silica/Carbonate Biomorphs

This chapter is published in *Crystals*, **2019**, *9*, 157. It was accepted as a communication on the 14th of March 2019. As the manuscript was published in an MDPI journal, the authors keep the copyright, which allows a reprint for this thesis.

4.7.1 Abstract

The formation of a polymer protection layer around fragile mineral architectures ensures that structures stay intact even after treatments that would normally destroy them going along with a total loss of textural information. Here we present a strategy to preserve the shape of silica-carbonate biomorphs with polymers. This method converts non-hybrid inorganic-inorganic composite materials such a silica/carbonate biomorphs into hybrid organic/carbonate composite materials similar to biominerals.

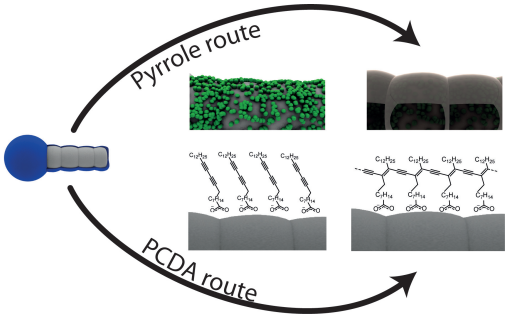

Figure 4.26: Graphical abstract of Opel *et al.* 2018.

4.7.2 Introduction

Silica-earth-alkaline carbonate composites show exceptional shapes which is so far a one-of-a-kind appearance within the field of pure inorganic composites [51, 149]. They were named silica-biomorphs due to their morphology, which resembles primitive living organisms and their inner textures mimic biominerals [52]. Compared to biominerals, which are normally hierarchically ordered hybrid composites consisting of inorganic minerals and structure conducting organic matter [6, 19, 186], biomorphs are purely inorganic composite materials, the structuring role of organic compounds being taken over by amorphous silica. They are self-organized structures that forms upon the coupled co-precipitation of silica (SiO_2) and alkaline -earth metal carbonates, namely witherite ($BaCO_3$), strontianite ($SrCO_3$) or either aragonite or monohydrocalcite ($CaCO_3$) [81, 187–189]. The formation of biomorphs can be described in three stages which are related to pH [54]. In the first stage, the initial single crystal of alkaline -earth metal carbonate experiences splitting provoked by selective adsorption of silica. Iterative splitting triggers fractal growth and eventually leads to primary glob-

ular particles [59, 74, 150]. The precipitation of the carbonate induces a local and bulk decrease of the pH that can be monitored even at this very early stage [54, 101, 113]. At this stage nearly no silica is adsorbed within the structure [54]. The second stage starts after some time (depending on the initial pH) and more complex structures form by determining the final shape of the biomorph. During this stage a polycrystalline growth of a myriad of elongated witherite nanorods with a typical size of 200-400 nm in length and 30-50 nm in thickness can be observed [54]. Once the pH drops far enough, the biomorph formation enters the last stage where only secondary precipitation processes occur. Due to the inverse solubility of silica with respect to pH [115, 129], the structures become embedded in a thick silica shell, which grows bigger if the structures mature in the mother solution.

Once extracted from the mother solution, the biomorphs can be further treated as shown in Figure 4.27. The composite is hollowed by acidic treatment. A diluted hydrochloric or acetic acid can be used to dissolve the inner part within minutes [2]. The result is a hollow structure, which is called a biomorph "ghost". Alternatively, an alkaline treatment with sodium hydroxide solution allows the removal of the silica shell and excavates the so-called "naked" biomorph (*cf.* Figure 4.27)[119]. A naked biomorph is useful for attachment of molecules or particles with carboxylate groups. One example for an attachment of a monomeric carboxylate species is 10,12-pentacosadiynoic acid (PCDA), a light-polymerizable diacetylen [119]. Poly-PCDA (pPCDA), as a member of the polydiacetylene family, comes with thermochromic properties and can be reversibly or irreversibly switched from a blue into a red state [138, 190]. Besides PCDA, conductive polymers like polypyrrole (pPy) or poly thiophenes generated a growing interest in the field of biomineral preservation and replication [191–193]. Furthermore they provide some additional functionality and are used as chemical sensors [194, 195], in drug delivery [195], as electronic devices like fuel cells [196] or electro-catalysts [197] and in combination with silica for chromatographic applications [198]. Choi et al. presented hierarchically structured pPy in helicoidal shapes and consequently, a pPy replica of a biomorph helix should also be usable as stretchable supercapacitors [199].

So far, two known strategies exist to transfer hierarchical structures of a given material into a new one of different composition. The first method is to demineralize a biomineral to obtain an organic template and re-infiltrate the matrix with the new compound [200]. TThe second strategy consists of replacing the organic matrix with a new ma-

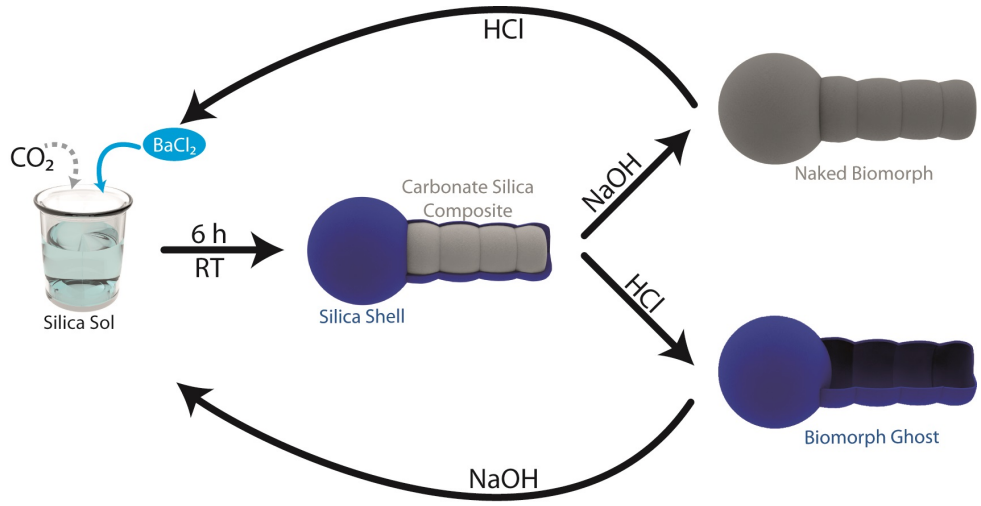

Figure 4.27: Schematic illustration of biomorph formation and pathways to dissolve each part of composite selectively and return to its precursor state. As intermediate a naked biomorph with an excavated carbonate surface or a hollow biomorph ghost can be obtained.

terial, as shown by Imai and coworkers with dyes or polymers between nanocrystals [20, 201]. We show here that a polymer layer around a biomorphic structure sustains the morphology after additional treatment with alkaline and/or acidic solutions while an unpreserved structure vanishes into its precursor state. In total, the following work demonstrates a successful preservation of micro-sculptures with two chosen straightforward pathways and elaborate a third strategy to transfer hierarchical structures into functional organic materials.

4.7.3 Results and Discussion

Preservation with pPCDA The first preservation route focuses on a light-polymerizable surfactant named PCDA. This molecule is immobilized on the witherite surface by incubating naked biomorphs (without an outer silica shell) in a mixture of sodium hydroxide, THF and water with different PCDA concentrations (120-12000 ppm). The attachment process is schematically shown in Figure 4.28 A. To make sure that only the monomer is attached on the surface the solution was pushed through a syringe filter to remove polymer particles from the solution. The naked biomorphs were immersed in the colorless solution for several hours. To ensure that the PCDA does not polymerize during the attachment process, the samples were stored in darkness. After the chosen incubation time (4-16 h) the solution was removed and the modified biomorphs were dried under reduced pressure. The obtained modified structures were investigated with scanning electron microscopy (SEM). Observation of the structures with the electron beam induces polymerization of the attached monomers to the bluish

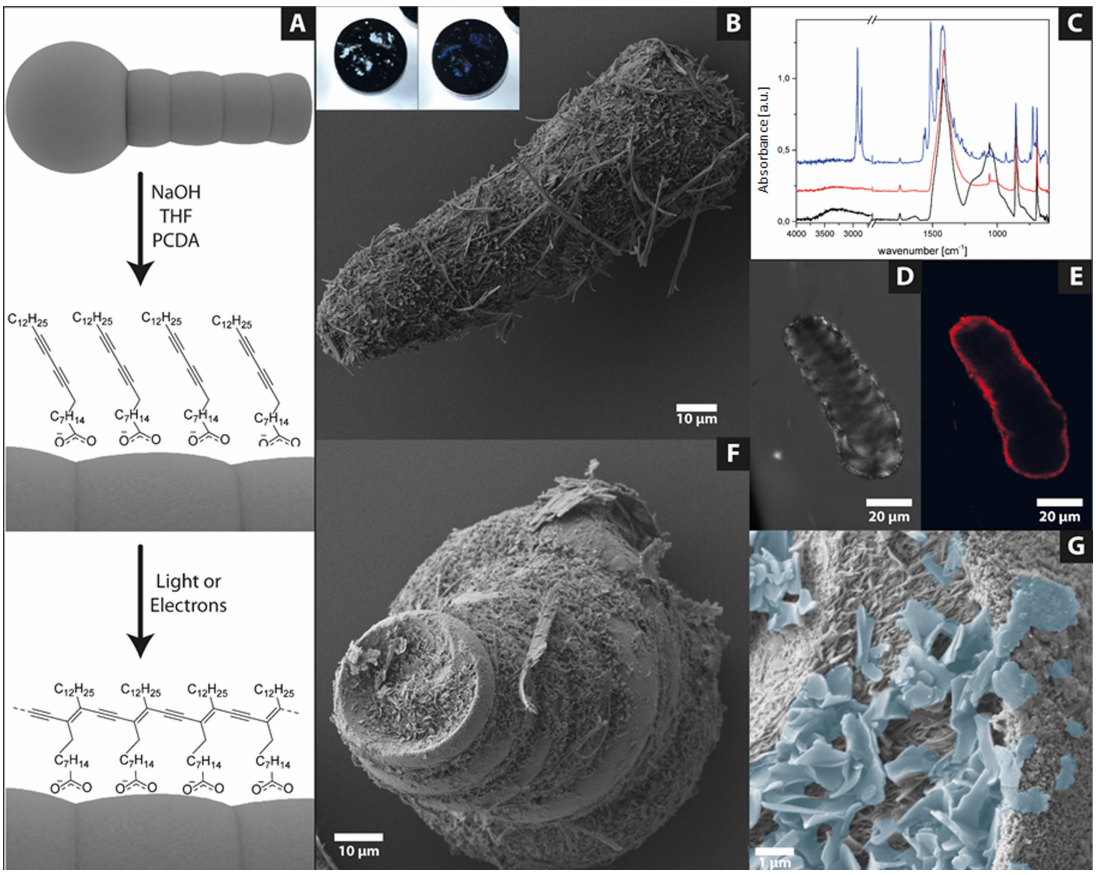

Figure 4.28: A) Scheme of biomorph coverage with PCDA and the polymerization to pPCDA. B) SEM image of a fully covered biomorph worm (inlet: colour transformation of the powder after SEM investigation; c(PCDA)=12000 ppm). C) Attenuated total reflection Fourier transformed infrared(ATR-FTIR) spectra of an untreated biomorph (black) a naked biomorph (red) and a pPCDA covered biomorph (blue). D/E) Confocal Laser scanning microscopy (cLSM) images of a fully covered biomorph worm in the transmission (D) and fluorescence (E) channel. F) SEM image of a partially covered biomorph worm (c(PCDA)=2000 ppm) with the corresponding image at higher magnification (G, the blue coloured flakes indicate the pPCDA).

pPCDA (*cf.* inlet photos of the SEM stub before and after the SEM investigation in Figure 4.28B). To demonstrate the attachment of the PCDA on the structure, the process was observed by FTIR-spectroscopy. The transformation of the silica-biomorphs to the pPCDA-biomorphs is shown in Figure 4.28C. The black spectrum shows the characteristic carbonate (witherite) vibrations as well as the most abundant signal for amorphous silica (peak at 1000 cm^{-1}). After treatment with NaOH and the transformation to the naked biomorphs, the broad peak vanishes and only the witherite signals remain (red spectrum). The modification with PCDA is observable as lines at 2870 and 2965 cm^{-1}, which are the symmetric and asymmetric C-H vibrations. The carboxyl signal of the PCDA appears at 1540 cm^{-1} which is in good accordance to the literature [190]. Choosing a higher concentration of PCDA in the functionalization solution leads to the full coverage of the biomorph worm with pPCDA flakes, which preserve

and display the outline of the structure beneath quite well. A detailed replica of the topography is not achievable with these high monomer concentrations. In previous work, we have demonstrated that the shape of the biomorph structure was preserved in acidic solutions even after removing the outer silica layer [119]. To ensure that a full coverage was achieved confocal laser scanning microscopy (cLSM) was used due to the strong fluorescence of pPCDA [119, 137] (*cf.* Figure 4.28D/E). Smoothening the reprint might be possible by reducing the amount of monomer but a full coverage is not sustainable because an enrichment of PCDA was found inside of the notches of the biomorph worm (*cf.* Figure 4.28F/G). In Figure 4.28G at higher magnification the witherite nanorods and pPCDA flakes (false coloured in blue) can be visualized alongside each other. Excavated carbonate rods are not able to resist acidic solutions and therefore, the structures vanish completely after acid treatment. Also, the pPCDA flakes do not stick together and a polymer replica of the structures does not remain. The pPCDA coverage is useful to passivate bigger carbonate structures but a smooth and detailed replica cannot be obtained. Nevertheless, it still remains a readily applicable strategy to produce inverse biominerals.

Preservation with pPy Polypyrrole has gained attention due to its ability to produce polymer replicas of biominerals like sea urchin spines [192]. Recent breakthroughs in the preparation of polymer replicas on the micro scale are a huge improvement to preserve fragile structures and it now seems transferable to silica-biomorphs [191]. To obtain a full pPy coating around a biomorph we followed the route presented in Figure 4.29A. At first $CuCl_2$ is brought onto the structure as a catalyst. Due to the rough surface of the naked biomorph, many small crystals of $CuCl_2$ attach on the surface. These small crystals do not affect the shape as can be seen in Figure 4.29B. After drying, the structures were transferred into a desiccator. On the bottom of the desiccator, pyrrole was deposited creating a pyrrole saturated atmosphere. The pyrrole molecules diffuse to the catalyst and begin to polymerize. During this process, a color change of the biomorphs can be observed by the naked eye. After 3 h the white powder turns grey and after 6 h a black powder was obtained. To ensure that the polymer layer is neither growing too big nor crosslinks the structures, the incubation time was kept at 6 h. After extracting the structures from the desiccator, the shapes of the naked biomorphs used as starting material remained nearly unchanged. Elemental analysis via energy dispersive X-ray spectroscopy (EDX) showed Ba, Cu, Cl, C, O, N and traces

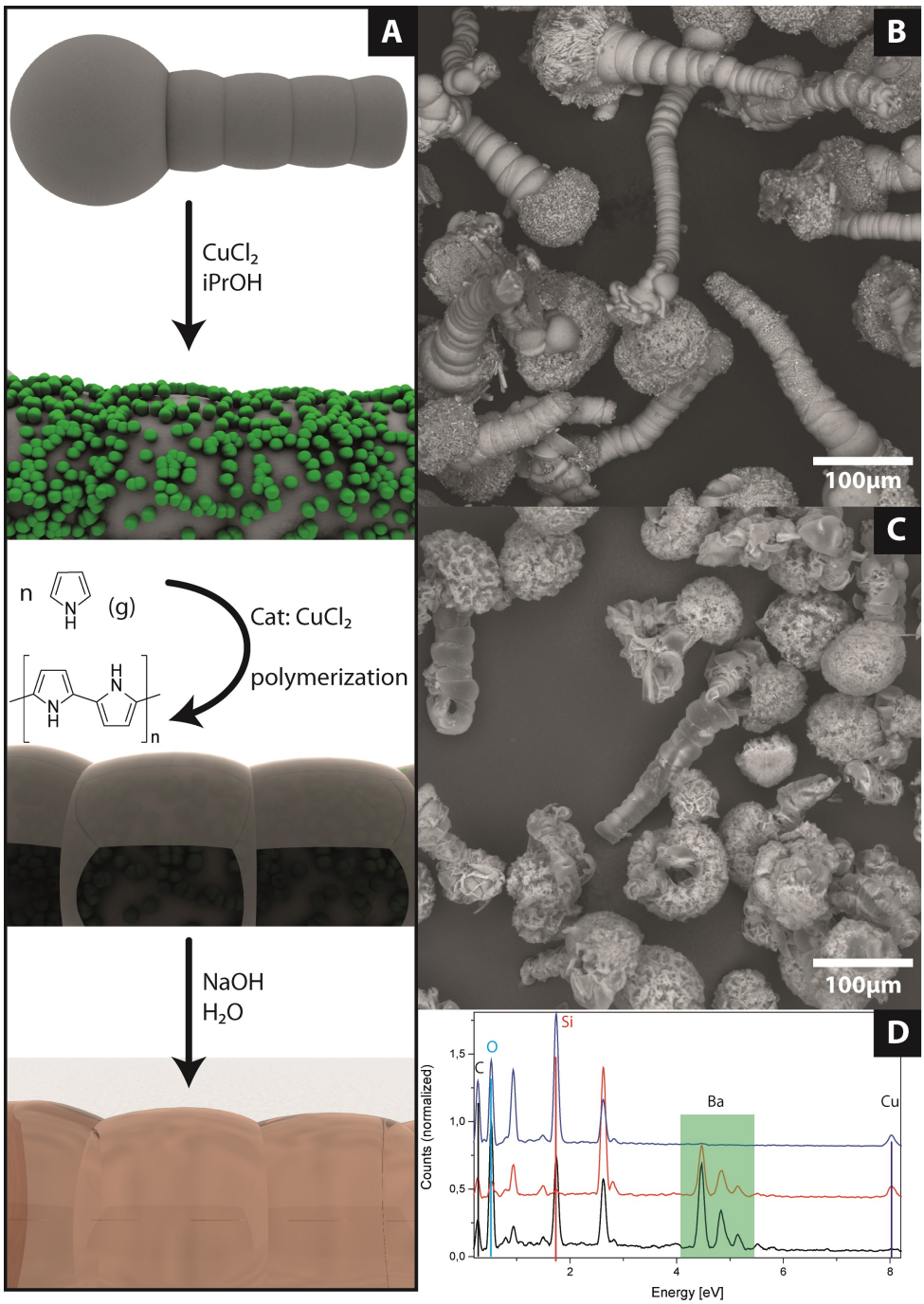

Figure 4.29: A) Schematic illustration of the pPy route to preserve biomorphic structures. $CuCl_2$ crystals are attached from iPrOH solution on the surface of a naked biomorph. In the next step pyrrole diffuse via gas phase on the surface and is polymerized by $CuCl_2$. After the polymerization the inner parts can be removed by sodium hydroxide solution. B) SEM image of catalyst crystals attached on biomorph worms. C) "Plastic" biomorphs after Polymerization of Py and removal of the inner part. D) EDX of the different steps to plastic biomorphs. The untreated biomorphs are shown in black. Naked biomorphs with $CuCl_2$ in red and the final plastic biomorpsh without inorganics are shown in blue.

of Si. Except the higher amount of N and the signals from the catalyst, the spectrum looks identical to an EDX of the naked biomorphs. The most meaningful proof of the full coverage and subsequent preservation of the biomorph form is the dissolution of the inner core which was achieved with 0.05 M acetic acid. The core dissolves much

slower compared to normal silica-biomorphs and as a result hollow structures were obtained and shown in the SEM image in Figure 4.29C. Note that the SEM images were recorded with a backscatter detector, which gives a good material contrast. The structures in Figure 4.29B show a higher contrast compared to the hollow structures without $BaCO_3$ in C. The EDX spectrum of these polymer replicas as well as their preliminary stages are shown in Figure 4.29D. The black spectrum shows the silica-biomorphs, the red spectrum the naked biomorphs with $CuCl_2$, which can be found at 8.02 eV. Here we can see that the outer silica layer has vanished and no Si signal was measured at 1.75 eV. In the upper blue spectrum, the Ba signals (green rectangular outline) have vanished and only traces of the raw material (Ba: 0.24; Si: 0.25 at.%) and the catalyst (0.4 at.%) are detected. The main component consists of carbon and nitrogen. Therefore, the pPy route is most suitable to preserve micro-sculptures on the microscale and to obtain conductive inverse biominerals.

4.7.4 Conclusion

We have achieved a full coverage of silica-carbonate composites by using PCDA and pyrrole to form an organic layer around the inorganic motifs. Thus, we have converted purely inorganic-inorganic composites into hybrids than can be named inverse biomorphs. The pathways to obtain these organic or hybrid structural motifes are described in detail and the methodology can be adapted to other microscopic biominerals or synthetic biomimetic architectures. Furthermore, the inorganic and structuring part of the biomorphs can be removed at ambient conditions resulting in a structured organic replica of the biomorph. With this straight-forward method, micro-structured functional materials can be formed and used as stretchable supercapacitors.

5 Summary

As all chapters contain an individual summary of the corresponding publication, this chapter provides a total summary of all publications and sets them in context to each other. This work presents the combination of different well-controllable systems into complex multi-functional hybrid structures. The silica-biomorphs' formation chemistry was further investigated, shedding light on the emergence of novel morphologies. The biomorphs were used as basic building units for the combination with a multitude of functional nanoparticles and molecules implementing a geochemical system into material science.

In the first part of this thesis, the detection of local pH changes during the formation of biomorphs was visually substantiated with a pH-sensitive fluorescent dye for the first time, verifying the postulated formation mechanism of the silica-biomorphs.[101] A significant pH reduction during the biomorphs' growth at their growth front was revealed. A pH oscillation was not found during these experiments. It was later proven by Montalti *et al.* by using acridine orange as a pH-sensitive dye.[113]

With the knowledge that the pH has a tremendous impact on the growth, the morphogenesis of silica-biomorphs was further investigated. As the pH also depends on the temperature as well as growth kinetics, varying the temperature must result in different biomorph architectures. During these studies, coral and trumpet structures were obtained at slightly elevated temperatures and a modified formation mechanism was established to explain these biomorph appearances.[150]

The ability to tune growth conditions, and thereby also the resulting structures, enabled the transformation of a geochemical system into a material by applying functionality onto the biomorph structures. In the first approaches, functional groups (e.g. thiols, amines, and dyes) were grafted onto biomorphs by applying silane chemistry.[119] These functional groups further acted as anchor points for secondary functionalization steps by modifying the biomorphs' surfaces with targeted molecular species, quantum dots, and nanoparticles. In a second approach, the direct functionalization during the growth of the biomorphs was accomplished, paving the way for better understanding the inner structure of the biomorphs. The direct functionalization with fluorescing silanes provided further insights into the role of silica during the formation of silica biomorphs. Attaching quantum dots or organic dyes allowed further investigations of the system with fluorescent microscopy. With gold nanoparticles, a catalytic reaction

at the silica biomorphs' surface was achieved.

The diverse functionalization concepts of biomorphs provide nearly unlimited possibilities to create functional structures for potential applications. One possible application was tackled within this thesis: biomorphs as magnetically controllable active transportation carriers. This was realized by combining silica-biomorphs with magnetite mesocrystals.[161] With the combination and the already investigated functionalization routes from ref.[119], the two self-assembled systems, mesocrystals and biomorphs, could be combined in multiple approaches. Active transportation of the structures through a solution was accomplished and was controlled and observed under a light microscope. The active dissolution of the inner core of the biomorphs with diluted acids provided a hollow interior capable to be loaded with additional substances, e.g. drugs. The combined structure of mesocrystal and biomorph shell remained intact, facilitating the magnetically-controlled and targeted transportation of the potential embedded material.

The controlled release of a substance was not possible at this stage. Therefore, the next part of the work focused on grafting switchable molecules onto the mesocrystal-biomorph superstructures with the ability to bind or release other substances triggered by an external stimulus. During the investigations, spiropyrans proved to be a highly suitable, light-switchable candidate for the controlled release of the carried substances. The switches were anchored using an as-synthesized silane-modified spiropyran binding to the silica of the mesocrystal-biomorph composite.[202] The multi-functionalized system (biomorph with magnetite mesocrystals and grafted spiropyran) enabled the guidance of the biomorphs via an external magnetic field to a precisely desired location. A subsequent light impulse switched the spiropyrans inducing controlled binding or release (depending on the states) of the carried substances.

The described biomorph-based systems exhibited a weak mechanical strength and high brittleness due to the mainly inorganic composition. To overcome these disadvantages, the first hybridization approach published in ref. [119] (by 10,12-pentacosadiynoic acid, PCDA) was developed further to yield an organic-inorganic composite material preserving the brittle structures. A full hybridization was achieved by covering the whole structure in polypyrrole (pPy).[203] Both approaches, with the previously described PCDA and the pPy, allowed passivation of the biomorph motifs within the organic polymer shell. Additionally to the passivation properties, the polymers provided further benefits through the introduction of additional functionalities. Polymer-

ized PCDA (pPCDA), for example, provides outstanding thermochromism and fluorescing properties. On the other hand, pPy as a conducting polymer could open up a completely new field of electrical applications, such as micro-structured supercapacitors.

Ultimately, to take up the introductory quotation of Gall's law, this thesis impressively demonstrates the synergistic properties by combining simple and well-controllable systems to create an innovative class of biomorph-based multifunctional materials. Thereby, the modification of silica-biomorphs with auspicious features such as catalytically active, fluorescing, moving, magnetic, conducting, switchable, and organic-inorganic hybridization functionalities were accomplished, opening novel broad applications for a geochemical system in the field of material science.

6 Zusammenfassung

Da alle Kapitel eine individuelle Zusammenfassung der entsprechenden Veröffentlichung enthalten, sollte dieses Kapitel alle Veröffentlichungen zueinander in Kontext setzen. Diese Arbeit präsentiert, wie verschieden, gut kontrollierbare Systeme zu komplexen multifunktionalen Hybridstrukturen kombiniert werden können. Der Bildungsmechanismus von Silica-Biomorphs wurde näher untersucht, um die Entstehung neuer Morphologien zu beleuchten. Die Biomorphs wurden als Grundarchitektur für die Kombination mit einer Vielzahl von funktionellen Nanopartikeln und Molekülen verwendet, um ein geochemisches System in die Materialwissenschaften zu implementieren.

Im ersten Teil dieser Arbeit wurde der Nachweis lokaler pH-Änderungen während der Bildung von Biomorphs erstmals visuell mit einem pH-sensitiven Fluoreszenzfarbstoff nachgewiesen und der postulierte Bildungsmechanismus verifiziert.[101] An der Wachstumsfront wurde eine signifikante pH-Erniedrigung beobachtet. Während dieser Experimente wurde keine pH-Oszillation beobachtet. In später veröffentlichten Experimenten von Montalti *et al.* wurde unter Verwendung von Acridinorange als pH-sensitiven Farbstoff diese Oszillation nachgewiesen.[113]

Da sich der pH-Wert, welcher auf das Biomorphwachstum einen enormen Einfluss hat, ändert, wurde die Morphogenese von Silica-Biomorphen ebenfalls näher untersucht. Die Temperaturabhängigkeit des pH-Wertes beeinflusst die Wachstumskinetik und daher muss eine Variation der Temperatur zu unterschiedlichen biomorphen Architekturen führen. Während dieser Studien wurden bei leicht erhöhten Temperaturen Korallen- und Trompetenstrukturen erhalten sowie ein modifizierter Bildungsmechanismus etabliert, um die Strukturen zu erklären. [150]

Die Möglichkeit Wachstumsbedingungen und damit die resultierenden Strukturen zu modifizieren, ermutigten dazu, ein geochemisches System in ein Material umzuwandeln. Dafür wurden funktionelle Gruppen (z. B. Thiole, Amine und Farbstoffe) durch Silanchemie auf Biomorphe aufgepfropft.[119] Diese funktionellen Gruppen fungierten als Ankerpunkte für sekundäre Funktionalisierungsschritte, indem die Oberflächen der Biomorphs mit Farbstoffmolekülen, Quantenpunkte und Nanopartikel modifiziert wurden. Eine direkte Funktionalisierung während des Biomorphwachstums war erfolgreich, womit die innere Struktur der Biomorph untersucht werden kann. Die direkte Funktionalisierung mit fluoreszierenden Silanen ermöglicht Einblicke in die

Rolle des Silica während der Bildung von Silica-Biomorphs. Durch Anbringen von Quantenpunkten oder organischen Farbstoffen konnten ebenfalls die Untersuchung des Biomorphs mit Fluoreszenzmikroskopie. Mit den eingesetzten Gold Nanopartikeln konnte eine katalytische Reaktion an der Oberfläche der Silica-Biomorphen durchgeführt werden.

Die vielfältigen Funktionalisierungskonzepte von Biomorphs bieten nahezu unbegrenzte Möglichkeiten, multifunktionale Strukturen zu designen. Eine mögliche Anwendung dieser Materialien wurde in dieser Arbeit bereits vorgestellt: Biomorphs als magnetisch steuerbare, aktive Transporter, was durch die Kombination von Silica-Biomorphen mit Magnetit Mesokristallen realisiert wurde.[161] Auf Grundlage der bereits untersuchten Funktionalisierungsmethoden aus Publikation [119], konnten die selbstorganisierten Systeme, Mesokristalle und Biomorphe, auf mehreren Wegen miteinander fusioniert werden. Der aktive Transport der Strukturen durch eine Lösung konnte realisiert und unter einem Lichtmikroskop kontrolliert und beobachtet werden. Das selektive Herauslösen des inneren Kerns durch verdünnte Säuren hinterlassen einen Hohlraum, welcher mit weiteren Substanzen, beispielsweise Arzneimitteln, beladen werden können. Die kombinierten Strukturen von Mesokristallen und Biomorphhülle blieb intakt und ermöglichte einen magnetisch gesteuerten und gezielten Transport einer eingebetteten Substanz.

Die Freisetzung einer eingebetteten Substanz konnte zu diesem Zeitpunkt noch nicht kontrolliert werden, da ein schlatbarer Ankerpunkt fehlte. Daher sollte sich der nächste Teil der Arbeit auf die Pfropfung schaltbarer Moleküle auf die mesokristall-biomorphen Superstrukturen konzentrieren, welche Substanzen mittels eines externen Impulses binden oder freisetzen können. Während der Untersuchungen wurden Spiropyrane für geeignet befunden. Die Verankerung der Schalter auf den Biomorph Oberflächen wurde durch ein synthetisiertes, silanmodifiziertes Spiropyran realisiert.[202] Das multifunktionalisierte System (Biomorphs mit Magnetit-Mesokristallen und gepfropftem Spiropyran) ermöglicht die Steuerung der Biomorphs über ein externes Magnetfeld an einen genau gewünschten Ort. Ein nachfolgender Lichtimpuls schaltete die Spiropyrane und induzierte eine kontrollierte Bindung oder Freisetzung (abhängig von dessen Zustand) der Zielspezies.

Die beschriebenen auf Biomorph basierenden Systeme zeigten eine schwache mechanische Festigkeit und eine hohe Sprödigkeit aufgrund der hauptsächlich anorganischen Komponenten. Um diese Nachteile auszuhebeln, wurde der erste Hybridisierungs-

ansatz aus der Publikation [119] (mit Hilfe von 10,12 Pentacosadiinsäure, PCDA) weiterentwickelt, um ein organisch-anorganisches Verbundmaterial zu bilden sowie die Architektur der spröden Strukturen zu passivieren. Eine vollständige Hybridisierung der gesamten Struktur wurde mit Polypyrrol (pPy) erreicht.[203] Die beiden präsentierten Ansätze ermöglichen die Passivierung der biomorphen Motive innerhalb der organischen Polymerhülle. Neben den Passivierungseigenschaften boten die Polymere aufgrund der zusätzlichen Funktionalitäten weitere Vorteile. PPCDA zeigt zum Beispiel hervorragende thermochrome und fluoreszierende Eigenschaften und pPy kann als leitendes Polymer elektrische Anwendungen ermöglichen, beispielsweise als mikrostrukturierte Superkondensatoren.

Um das einleitende Zitat des Gall'schen Gesetzes aufzugreifen, demonstriert diese Arbeit eindrucksvoll die synergistischen Eigenschaften von einfachen und gut kontrollierbaren Systemen, welche kombiniert wurden um innovative, Biomorph basierte, multifunktionale Materialien zu erhalten. Siliciumdioxid-Biomorphs konnten mit katalytischen, fluoreszierenden, magnetischen, leitenden und schaltenden Funktionalitäten ausgestattet sowie eine organisch-anorganischen Hybridisierung erreicht werden, womit sich neue Anwendungen für ein geochemisches System auf dem Gebiet der Materialwissenschaften eröffnen.

7 Concluding Remarks and Outlook

As discussed above, the formation mechanism of biomorphs is still a controversial field with the main bottleneck of in-situ investigations. First results on local pH drops in 2015, presented in chapter 4.2 [101], were refined by Montalti and Zhang with acridine orange, another pH-dependent fluorescent dye.[113] Their work revealed an oscillating pH pattern on a similar timescale as investigated here for the solidified patterns within the biomorphs. Biomorphs, especially the sheet-like structures, showed oscillating patterns manifesting the pH cycling in burst phases of carbonate precipitation. These solidified patterns, mainly in already grown biomorph sheets, were explored ex-situ by Nakouzi *et al.* without the usage of a dye.[114] Nonetheless, the favoured method to perform in-situ investigations on local pH changes during the biomorph growth includes special dyes, which might change the system and its pH response, wherefore the investigation of an additive-free formation mechanism is of particular interest for the entire understanding of biomorphs' emergence. Additive-free investigations can evade measurement artefacts like dye activation and deactivation through dynamical quenching or ion interference. Also trapping of the dye within silica outplays its pH-dependent indication ability.

To get further insights into the autocatalytic co-precipitation, in-situ methods have to be conducted. Therefore, the principle of inverted atmospheric SEM (demonstrated in ref.[204]) was utilized, visualizing the co-precipitation. In cooperation with Roland Kröger from the University of York, we were able to monitor a growing biomorph sheet in-situ (*cf.* Figure 7.1 A, results not published). Surface charges are critical for this investigation as they repel as-formed building blocks from the active region enforcing a stop of the growth. Therefore, the ideal SEM settings have to be evolved. Furthermore, the monitoring time is limited due to the restricted SiN window lifetime against solutions, beam, and the chamber vacuum, impeding the measurements. Nevertheless, this powerful technique can revolutionize the in-situ observation of crystal growth.

Further analytical techniques should also be applied to gain additional high-resolution insights of the inner core, such as energy-dispersive Laue diffraction (EDLD).[205] With this method, the individual crystals can be monitored and their orientation according to their lattice planes can be revealed by using white X-rays (synchrotron radiation) and a focused nanoscopic beam. In the first experiments on biomorph helices, the results were promising with respect to reconstructing the projected orientation of

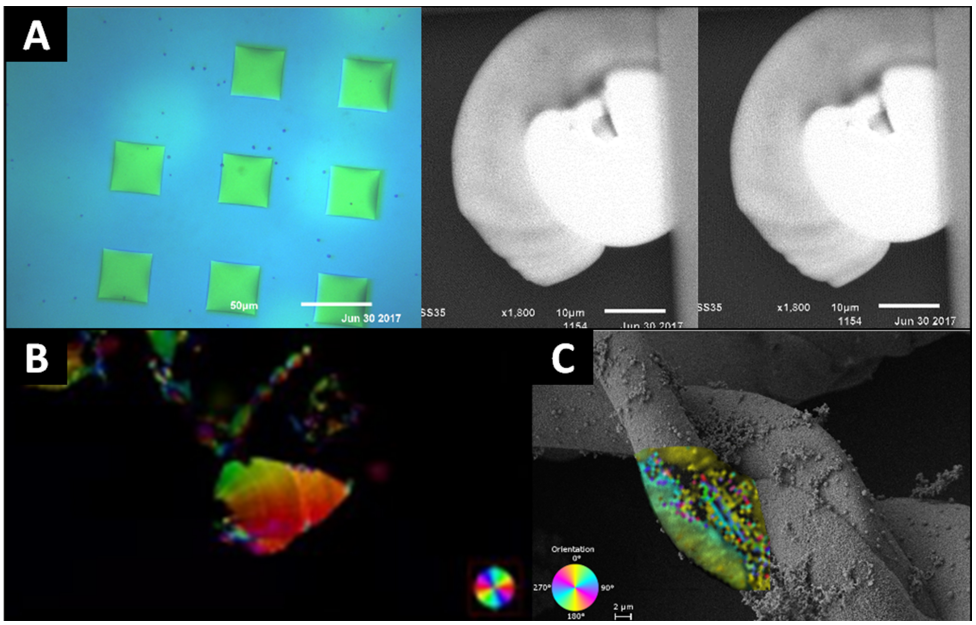

Figure 7.1: A) Inverted atmospheric scanning electron microscope (ASEM) images of a growing biomorph sheet. The first image shows a light microscopy image of the SiN windows where the structures grow on. B) Abrio microscope image of a biomorph sheet. C) Energy-dispersive Laue diffraction (EDLD) mapping fused into an SEM image of a biomorph helix.

the crystal ensemble. To achieve the total 3D reconstruction of each crystal within the structure, including its total orientation, the measurement setup must be expanded to receive confocal z-resolution what goes along with longer measuring times. So far, the quantifications of the orientation rest on the level of as utilised Abrio microscopy that is limited by Abbe's law but allows visualization of the overall orientation of the crystal ensemble (*cf.* Figure 7.1 B and C).

Analytical methods that provide a very detailed view of the silica part in the inside of the structures and can be used for in-situ investigation might need the addition of a tracer. The basis for these investigations was laid by my studies shown in chapter 4.4 by applying fluorescent silica.[119] Evading the Abbe's limitation of optical microscopy methods and take advantage of the fluorescence of silica can be realized with Photoactivated Localization (PALM) respectively Stochastic Optical Reconstruction Microscopy (STORM). These methods reveal the structure even in more detail during their formation. By applying all the mentioned, highly-specialized analytical techniques, the next level of understanding of the biomorph structure and the formation mechanism can be attained.

Additional to advanced in-situ investigations, also further parameters were tested to extend the variety of shapes. Therefore, various additives were applied, allowing the allow a precise and targeted morphology control (*cf.* Figure 7.2 A and B). As variable

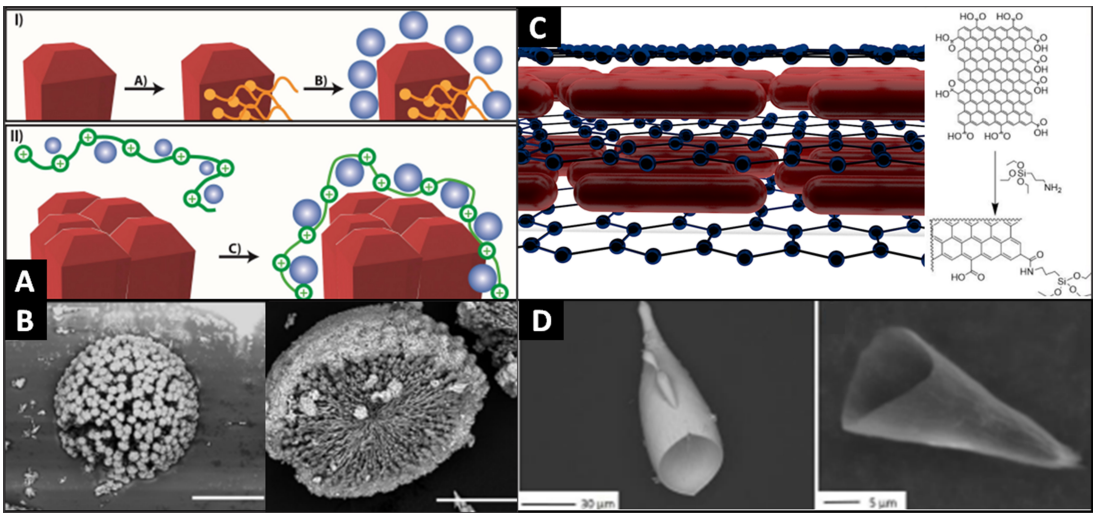

Figure 7.2: A) Schematic illustration how additives get incorporated into the biomorph structures. I) displays the attachment on the carbonate surface followed by the silica enclosing and II) the attachment of negative silica and cationic polyelectrolytes on the barium carbonate crystals. B) Biomorph blowball structures, obtained in the presence of LTAB (lauryl trimethyl ammonium bromide) as an additive. C) Animation of biomorph formation in the presence of graphene oxide to obtain structured biomorph graphene composites. D) Selective carbonate dissolution of a structure containing graphene oxide in a biomorph trumpet.

as the functionalities of the additives is (ionic, neutral, polymeric, molecular, etc.), so are the possible interactions with inorganic components. For this reason, additional detailed studies must be carried out for an entire understanding of the underlying growth processes. Nonetheless, to evaluate the effect of each additive on the crystalline component and the amorphous silica can result in special designed biomorphs. Due to the different charged surfaces, cationic, anionic and non-ionic additives were tested. Further investigations are still needed to deepen the understanding of the ongoing processes. Auxiliary surveys, characterizing the influence of polyelectrolyte films and inorganic additives, were performed by E. Nakouzi.[160, 206]

Besides modifying the structures by additives, incorporation of functional additives was examined. As a suitable candidate graphene oxide was identified providing increased stability and electric conductivity to the structures (*cf.* Figure 7.2 C and D). This method was adapted from its incorporation in biomimetic mineralization.[207] Incorporated graphene should also help to reduce the brittleness of the structures. By applying a similar approach, more flexibility of the silica was induced by substituting tetra methoxy orthosilicate (TMOS) with methylated derivates. Therefore, different amounts of methyl trimethoxy silane and dimethyl dimethoxy silane were induced. Keeping the same amount of hydrolyzed silanol groups by simultaneously lower linking degrees, more flexible silica analogues were created.[130, 208, 209] Up to now, the

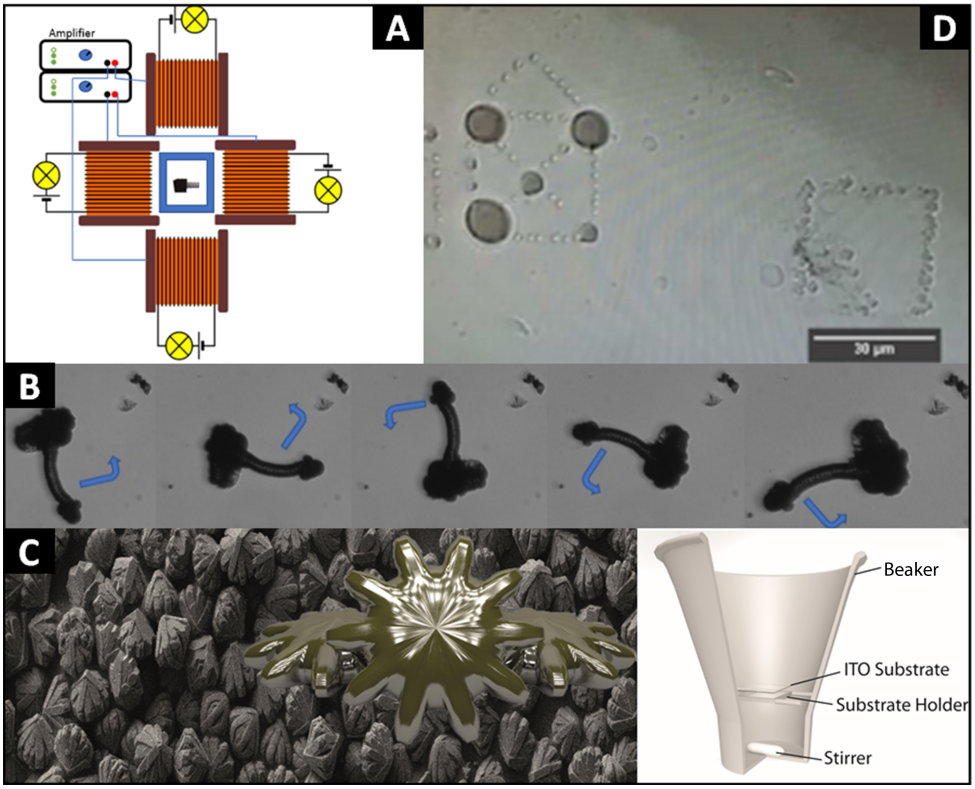

Figure 7.3: A) Copper coil setup to induce rotating magnetic fields affecting magnetized biomorphs. B) Rotating biomorph which moved through a rotating magnetic field. C) $BaCrO_4$ microwheels and a modified synthesis beaker setup D) Light-induced crystallization of $CaCO_3$ into a house pattern.

degree of substitution is limited.[58, 119] To prove the enhanced mechanical properties, nano-indentation experiments need to be conducted. The first approaches to mount biomorph structures on a holder to indent them were successful.

When it comes to functionalizations, further mesocrystal-forming nanoparticle systems should be tested creating more superstructures that benefit from the architecture of the biomorphs. First experiments to cover the structures with anisotropic (cubic) gold nanoparticles in the same process as reported for magnetite were successful. Also, the magnetite system should be further investigated. Due to the individuality of biomorphic shapes, it can be assumed that they perform different self- motions when they are propelled through rotating magnetic fields. First results indicated, that depending on the structure a rotating magnetic field induces a rotation into the magnetized biomorphs (*cf.* Figure 7.3 A and B). The structure-dependent movement in rotating magnetic fields might enable the separation of biomorph mixtures based on the migration properties.

A different functionalization approach was followed by the group of Wim Noorduin by transforming the crystalline phase from witherite to a functional semiconductor.[152,

210] They transformed the witherite to $PbCO_3$ and through the addition of methylammonium halides (CH_3NH_3X), perovskite semiconductors ($CH_3NH_3PbX_3$) in the shape of silica biomorphs were obtained. This route opens additional pathways to structured functional materials if combined with the approaches presented in this thesis. A direct formation of functional biomorphic structures was not realized yet. The formation of biomorphic structures essentially needs a co-precipitation of materials, which form in an autocatalytic process. Several candidates were already tested, e.g. $BaCrO_4$, shown in Figure 7.3 C. These first tests resulted in microscopic crystal aggregates resembling gear wheels. A modified synthesis beaker setup was applied (schematically shown in the Figure) carrying a substrate that can be used for fast analysis in an optical microscope as well as an SEM because of the conducting indium tin oxide (ITO) coating.
Additional investigations should be carried out for light-induced carrier properties of the light switchable biomorphs.[202] This system could be strongly improved towards possible applications as biomorph-based carriers by stabilizing the different states for longer time periods and preventing from external influences, e.g. surrounding media. When it comes to experiments with light, it might be possible to modify the structures by adding photoactive molecules into the growth solution providing designing on-demand of the silica-biomorph shape. Influencing a growing structure without quenching the growth itself would pave the way for controlled fabrication of designed structures. The first experiments in this field were accomplished a by proof of concept for controlled calcium carbonate formation with a photosensitive molecule (ketoprofen), which released carbonate during its decomposition (*cf.* Figure 7.3 D).[211] Designed structures like helicoidal biomorphs that are aligned in arrays can get decorated with gold nanoparticles to access chiral plasmon resonances.
As shown in this chapter, biomorphs still bear a lot of potential for future investigation. During the duration of this project, other groups adapted our published approaches to transform these fascinating structures into functional materials.

8 Experimental

This chapter presents the Materials and Methods as well as the experimental procedures for all used materials shown in this work.

8.1 Materials and Analytic Methods

Materials and Sample Preparation Barium chloride dihydrate (> 99%), sodium hydroxide (reagent grade, > 98%), lanthanum chloride heptahydrate (≥ 99.9%), and sodium silicate solution (commercial water glass, containing 10.6% Na_2O and 26.5% SiO_2 , reagent grade, density: 1.39 g/mL) were purchased from Sigma-Aldrich and used without further purification. All solutions were prepared using MilliQ water with a conductivity of 18 $\mu S/cm$. Suitable silicate sols were obtained by diluting 1.39 g of water glass in 349 mL of water. The pH of the resulting sol was adjusted to 11.3 (at 25 °C) by adding aliquots of 0.1 M NaOH solution. The used triethoxysilanes (3-MPTES: 92%; 3-APTES: 98%; DNPTES: 92%; 3-MPA: 99%) and TEOS (min. 99%) were purchased from ABCR. 10,12- Pentacosadiynoic acid (PCDA, 97%), pyrrole (reagent grade 98 %), Ellman reagent (5,5'-dithiobis(2-nitrobenzoic acid), min. 98%), 4-nitrophenol (spectrophotometric grade, min. 99.5%), resazurin sodium salt (BioReagent, dye content: 80%), fluorescein isothiocyanate (FITC, isomer I, min. 90%) and hydroxylamine solution (50% in water) were obtained from Sigma-Aldrich. Sodium borohydride (98%) was purchased from Merck. Ethyl acetate and hexane for column chromatography were purchased in technical grade and distilled before usage. All other chemicals were purchased from Sigma-Aldrich and TCI and used without further purification.

Analytic Methods The pH was measured with a Eutech pH 510 and a Metrohm pH lab 827 pH meter equipped with a glass electrode. For comparison, pH measurements were also performed with a second digital pH meter (WTW pH 537), equipped with a different glass electrode (InLab 423, Mettler-Toledo). Calibration of the instruments was performed with standard aqueous buffer solutions of pH 4.00, 7.00 and 9.00 from Metrohm. The measurement uncertainties of the pH electrodes are estimated to ≤ 0.03 pH units.

Polarised light microscopy (PLM) was performed on a Nikon AZ100 microscope (Nikon Co., Tokyo, Japan) and an Imager m2m from Zeiss EC Epiplan-Neofluar 5x/10x/20x

and LD Epiplan 50x objectives, a lambda plate, and a Zeiss AxioCam MRc 5 CCD camera for imaging.

Scanning electron microscopy (SEM) was performed on a Zeiss EVO15, Zeiss Crossbeam 1540XB, Zeiss Auriga, Zeiss Neon 40 EsB and Hitachi TM3000. To obtain suitable specimens for the SEM studies, biomorphs were grown on indium tin oxide (ITO) substrates (Osslia). Further Samples were prepared on SEM Stubs with carbon tape. The acceleration voltage was between 2 and 20 kV.

Confocal laser scanning microscopy (CLSM) was performed using a Zeiss LSM 510 Meta laser scanning microscope and a Zeiss Axiovert 200M inverted microscope, equipped with Plan-Neofluar 10x/0.3 and Plan-Neofluar 20x/0.5 objectives and PMT detectors for the transmission and fluorescence channels and a Zeiss LSM 700 with a 63x/1.40 Plan Apochromat (Oil) objective and with Laser diodes (405, 488, 555 and 637 nm). The images were recorded in fluorescence a transmission channel on two photomultipliers.

Thin-layer chromatography (TLC) was performed on Merck Silica Gel 60 F254 TLC plates with a fluorescent indicator for 254 nm excitation. Compounds were visualised under UV light at 254 nm. Column chromatography was carried out with Merck Silica Gel 60 (0.040-0.063 mm) using the specified eluents. Nuclear magnetic resonance (NMR) spectra were recorded on Bruker AV 400 and Bruker AVANCE III 500 MHz spectrometers at 27°C, using residual protonated solvent signals as internal standard (^{1}H: δ[$CDCl_3$]=7.26 ppm and ^{13}C: δ[$CDCl_3$]=77.16). Assignments are based on chemical shifts and/or DEPT spectra (where Ar is used as abbreviation to indicate aromatic moieties). High-resolution mass spectrometry (HR-MS) was performed with a Thermo Scientific Exactive Orbitrap in the positive ion mode using the Thermo Xcalibur operating and data acquisition software, or on a Waters LCT Premier XE instrument. Ultrahigh-performance liquid chromatography mass spectrometry (UPLC-MS) was performed with a Waters Acquity UPLC equipped with a Waters LCT Premier XE mass detector for high-resolution MS (ESI ionisation), and with Waters Alliance systems (consisting of a Waters Separations Module 2695, a Waters Diode Array Detector 996 and a Waters Mass Detector ZQ 2000) equipped with an Acquity BEH C18 (2.1x50 mm) column. High-resolution mass spectra (HRMS) were recorded on a Fischer Scientific Orbitrap Velos Pro.

UV/Vis absorption spectra were recorded on an Analytik Jena Specord 210 Plus spectrophotometer and a Cray 50. Steady-state fluorescence measurements were carried

out on Horiba Jobin-Yvon FluoroMax-4P and Spectronics Instrument 8100 spectrofluorometers, using standard 10 mm path length quartz cuvettes or PMMA cells. Fluorescence lifetimes were determined with a unique customised laser impulse fluorometer with picosecond time resolution, as described elsewhere.[212] The fluorescence lifetime profiles were analysed using the Horiba Scientific software package DAS 6.
Infrared spectra (IR) of thin films were measured on a Perkin Elmer Spectrum 100 spectrometer with ATR-unit.

8.2 Synthetic Procedures

Silica-Biomorph Formation Silica biomorphs were grown from aqueous solutions containing 5.0 mM $BaCl_2$, 8.4 mM SiO_2 and 8.9 mM Na^+. Optionally 2 mM $LaCl_3$ was dissolved in the $BaCl_2$ solution prior to the mixing with the silica sol. Portions of this mixture (typically 10 mL) were filled into cylindrical wells of standard polystyrene plates (VWR Nunclon 6-well plates, volume: 17 mL, area: 9.6 cm^2, depth: 1.7 cm). Subsequently, glass coverslips (15x15 mm) were placed on the bottom of the wells as substrates for growth, and the well plate was covered loosely with a lid. They were stored at room temperature (25 °C), inside a temperature-controlled oven (30-50 °C) or a cooling chamber (5 °C). The crystallisation of barium carbonate occurred upon gradual in-diffusion of CO_2 from the atmosphere into the alkaline solution (starting pH: 11.0), where it was converted to HCO_3^- and finally CO_3^{2-} ions needed for precipitation. In this way, complex structures are formed spontaneously on interfaces over periods of several hours. Their isolation is quite straightforward, as the glass substrates can simply be removed from the mother liquor with a pair of tweezers and only need to be rinsed with water and ethanol.

Synthesis of the used BODIPY Dye *8-(4-hydroxyphenyl)-1,3,5,7-tetramethyl-2,6-diethyl-4,4-bis(3,6,9,12-tetraoxaheptadec-16-ynyl)-4- bora-3a,4a-diaza-s-indacene (dye* ***2****)*: The synthesis of **2** was carried out according to a procedure adopted from ref.[213] To a solution of 2.10 g 2,5,8,11,14-pentaoxaheptadec-16-yne (8.0 mmol, 10.0 eq., synthesised as described elsewhere [214]) in 20 mL anhydrous tetrahydrofuran (THF), 9.50 mL ethylmagnesium bromide (9.5 mmol, 1.0 M solution in THF, 12.0 eq.) was added. The reaction was heated at 60°C overnight. After cooling down to room temperature, a solution of 317.0 mg **1** (0.8 mmol, 1.0 eq., synthesised as described elsewhere [109]) in

15 mL anhydrous THF was added. The resulting mixture was stirred at 60°C for additional 5 h to achieve complete consumption of the starting material. Subsequently, the solution was concentrated under reduced pressure to remove parts of the THF. Then 100 mL dichloromethane (CH_2Cl_2) was added and the organic phase was washed with 100 mL brine. After extraction of the aqueous phase for three times with CH_2Cl_2 , the combined organic solutions were dried over Na_2SO_4 and concentrated under reduced pressure. The crude product was purified by column chromatography on silica using ethyl acetate/methanol as eluent to give compound **2** as purple-brown oil (0.407 g, 60%).

Analytical data:

HR-MS (ESI+): m/z calculated for $C_{47}H_{69}BN_2O_{11}Na$ [M+Na] + : 870.4923, found: 870.4908.

^{1}H-NMR (400 MHz, $CDCl_3$) [ppm]: δ = 0.97 (t, 6H, J = 7.5 Hz, 2 × CH_2–CH_3), 1.32 (s, 6H, 2 × C–CH_3), 2.30 (q, 4H, J =7.5 Hz, 2 × CH_2–CH_3), 2.67 (s, 6H, 2 × N–C–CH_3), 3.37 (s, 6H, 2 × CH_3), 3.54 (m, 4H, 2 × CH_2), 3.64 (m, 28H, 2 × CH_2), 4.18 (d, J = 2.4 Hz, 4H, 2 ×CH_2–C), 6.92 (d, 2H, J = 8.6,2 × CH_{ar}), 7.06 (d, 2H, J = 8.6, 2 × CH_{ar}).

Absorption and emission spectra of dyes **1** and **2** in aqueous solution are shown in Fig. 9.1, while Figs. 9.2 and 9.3 summarise the pH dependence of the absorption and emission behaviour of **1** and **2**, respectively, for a change from near-neutral to alkaline conditions. Table 2 compiles the relevant spectroscopic data, including the fluorescence lifetime (τ_f).

Carboxylated Spiropyran (Compound 6) Compound **6** was synthesized in two steps from commercially available 2,3,3-trimethylindolenine by a literature-known procedure.[215] The obtained spectroscopic data are consistent with those reported previously.

^{1}H-NMR (400 MHz, DMSO) [ppm]: δ = 12.24 (bs, 1H), 8.24 (d, J = 2.8 Hz, 1H), 8.03 (dd, J = 2.8, 9.0 Hz, 1H), 7.24 (d, J = 10.3 Hz, 1H), 7.17-7.13 (m,2H), 6.88 (d, J = 9 Hz, 1H), 6.83 (t, J = 7.5 Hz, 1H), 6.69 (d, J = 7.8 Hz, 1H), 6.03 (d, J = 10.3 Hz, 1H), 3.57-3.39 (m, 2H), 2.64-2.44 (m, 2H), 1.21 (s, 3H), 1.10 (s, 3H).

Silanefunctionalized Spiropyran (Compound 7) Compound **6** (2.30 g, 6.05 mmol, 1.0 eq.), EDC·HCl (1.28 g, 6.66 mmol, 1.1 eq.) and DMAP (0.74 g, 6.05 mmol, 1.0 eq.) were dissolved in CH_2Cl_2 (20 mL) and stirred for 10 minutes. (3-Aminopropyl)

triethoxysilane (1.41 g, 6.35 mmol, 1.05 eq.) was added dropwise and the reaction was stirred for 20 hours at room temperature. The solvent was removed under reduced pressure and the crude product was purified by flash chromatography on silica gel (2:1 ethyl acetate/hexane). Compound **7** was obtained as a red solid (2.71 g, 4.64 mmol, 77% yield).

^{1}H-NMR (400 MHz, DMSO) [ppm]: δ = 8.20 (d, J = 2.8 Hz, 1H), 7.99 (dd, J = 2.8, 8.9 Hz, 1H), 7.86 (t, J =5.5 Hz, 1H), 7.18 (d, J = 10.4 Hz, 1H), 7.14-7.09 (m, 2H), 6.85 (d, J = 9.0 Hz, 1H), 6.78 (dt, J =7.4, 0.6 Hz, 1H), 6.65 (d, J = 7.7 Hz, 1H), 5.97 (d, J = 10.4 Hz, 1H), 3.70 (q, J = 7.0 Hz, 6H), 3.49-3.29 (m, 2H), 3.01-2.87 (m, 2H), 2.43-2.27 (m, 2H), 1.41-1.33 (m, 2H), 1.18 (s, 3H), 1.12 (t, J = 7.0 Hz, 9H), 1.07 (s, 3H), 0.49-0.45 (m, 2H).

^{1}3C-NMR (101 MHz, DMSO) [ppm]: 170.1, 159.2, 146.4, 140.5, 135.6, 127.9, 127.5, 125.6, 122.7, 121.9, 121.6, 119.1, 118.9, 115.4, 106.7, 106.6, 57.6, 52.4, 41.3, 39.5, 34.9, 25.5, 22.7, 19.4, 18.2, 7.4.

IR (ATR): ν(cm^{-1})= 3307, 2973, 2928, 1740, 1639, 1611, 1511, 1479, 1334, 1273, 1075, 951, 919, 808, 787, 748.

HRMS: m/z calculated for $C_{30}H_{42}N_3O_7Si^+$: 584.2787; found: 584.2785.

One-Pot Synthesis of Fluorescent Biomorphs In-situ functionalisation was achieved by replacing 5 vol% of the TEOS with 3-(2,4-dinitrophenylamino)propyltriethoxysilane (DNPTES) in the above- described procedure (i.e. 8.6 mM TEOS and 0.4 mM DNPTES). After 12-24 hours of growth, the glass substrates were removed from the mother liquor and rinsed intensively with water and ethanol.

Post-Silanisation of Biomorphs Freshly synthesised biomorphs (stuck on glass coverslips) were immersed into a 1 vol% solution of functional triethoxysilane (3-MPTES, 3-APTES or DNPTES) in a 95:5 mixture of ethanol and water. After 12 h, the substrates were removed and washed intensively with water and ethanol.

Labeling of Amine-Functionalised Biomorphs Coverslips carrying aminosilane - functionalised biomorphs were incubated in a FITC solution at pH 9 for 2 h. The FITC solution was prepared by mixing 1 mL of borax buffer with 100 μL of 1 mM FITC in ethanol. After incubation, the coverslips were washed with water and ethanol and then directly observed under the CLSM.

Labeling of Thiol-Functionalised Biomorphs with QDs Coverslips carrying thiol-modified biomorphs were immersed into 1 mL of a 20 nM solution of CdSe@ZnS quantum dots (d_{ave} = 9 nm) in toluene for 6 h. After the incubation step, the structures were removed, washed several times with water and ethanol, and then directly investigated under the CLSM.

Labeling of Thiol-Functionalised Biomorphs with AuNPs Coverslips carrying thiol-modified biomorphs were immersed into 1 mL of a 10 nM aqueous gold colloid solution (d_{ave} = 14 nm) for 24 h. During incubation, the colour of the solution changed from red to purple (cf. UV-Vis spectra in Figure 9.4b).

Formation and Post-Treatment of Silica Biomorphs Barium chloride dihydrate (99%), sodium hydroxide (98%) and sodium silicate solution (water glass with 10.6% Na_2O and 26.5% SiO_2, reagent grade) were purchased from Sigma Aldrich and used without further purification. All solutions were prepared using Milli-Q water with a conductivity of 18 $\mu S \cdot cm^{-1}$. The silicate solution for growth of biomorphs was obtained by diluting 1.39 g of sodium silicate solution in 349 ml of water. The pH was adjusted to 11.1 using 0.1 M sodium hydroxide solution. The resulting silica sol was then mixed in a 1:1 ratio with 0.01 M barium chloride solution in 6-well plates (Linbro). After 16 h exposure to the atmosphere, formed structures were recovered, washed several times with water and dried in air. Hydrophobization of the as-obtained biomorphs with silanes was performed in an Eppendorf tube by dissolving 10 μL of the silane in 1.5 mL of a 4:1 EtOH:H2O mixture. Then about 10 mg of biomorphs were added to the solution and incubated overnight. To dissolve the outer silica shell, 10 mg of biomorphs were incubated overnight in 1.5 mL of a 1 M sodium hydroxide solution. The silica-free biomorphs were then covered with a layer of oleic acid by overnight treatment with a sonicated mixture of 600 μL THF, 10 μL oleic acid, 10 μL 1 M NaOH, 2.5 mL cyclohexane and 0.5 mL EtOH. All modified structures were cleaned by repeated washing with deionized water and centrifugation, followed by drying under reduced pressure.

Formation of Mesocrystal-Biomorph Composites Iron oxide nanocrystals were prepared following a procedure described in the literature.[98, 163] Magnetite mesocrystals were obtained via destabilization of a nanocrystal dispersion in THF (5 mg/mL

magnetite nanocrystals with 3 μL/mL oleic acid) in the presence of a piece of silicon wafer or powdered biomorphs in a glass vial. The glass vial was left in an outer surrounding reservoir, which contained EtOH:THF (1:1) as a destabilizing agent that slowly diffused into the nanoparticle dispersion via the gas phase. Complete destabilization of the nanocrystal dispersion and mesocrystal formation took about one week, as observed by a color change of the dispersion from black to colorless.

Thermal Annealing of Mesocrystals In order to investigate the thermal stability mesocrystals were annealed in an oven (Uni-Temp RTP-1200) under UHV conditions using a slow ramp rate. Primarily, the oven was heated up to 90 °C to evaporate the water out of the sample to avoid damage to the crystal upon expansion at high temperatures. After, the oven was heated to the desired temperature and kept at that temperature for 7 hours before cooling down. Temperatures of 350, 380, 420 and 500°C were investigated. The obtained samples were characterized by means of SEM and XRD.

Catalytic Reduction of pNP 3.4 mL water and 4 μL of a 50 mM aqueous solution of 4-nitrophenol were given into a quartz cuvette with a stirrer. Subsequently, 1 mg of the AuNP-functionalised biomorph were dispersed in the solution. After addition of 1 mg $NaBH_4$, the reaction was monitored over time with UV/Vis spectroscopy.

Catalytic Reduction of Resazurin First, AuNP-functionalised biomorph were prepared in a μ-dish forfluorescence microscopy (ibidi GmbH, diameter: 35 mm) according to the protocol described above. After the dish had been placed on the specimen stage of the CLSM, 2 mL of a freshly prepared aqueous solution of 16 μM resazurin and 160 μM hydroxylamine were added and the progress of the conversion to resorufin was followed in the fluorescence channel of the CLSM.

pPCDA Functionalization PCDA solution was prepared by dissolving 50 mg PCDA in 10 ml tetrahydrofuran (THF). The solution was filtered through a syringe filter (pore size: 0.22 μm) and diluted with 9 ml Water and 1 ml 0.1 M NaOH solution. 10 mg of naked biomorphs were incubated for 8 h inside a PCDA solution with different concentrations and stored in the dark. After extracting and washing, the structures can be stored under UV-light for 5 minutes inducing the polymerization to pPCDA. The color of the biomorph PCDA powder changes to blue.

pPy Functionalization 10 mg naked biomorphs were added to 1 ml of a 0.01 M $CuCl_2$ solution in isopropanol (iPrOH). After 1 h, additional 750 μl were added. After 1 h the structures were centrifuged and washed twice with 200 μl iso-propanol (iPrOH). After drying the structures were stored in a desiccator containing 10 ml pyrrole. After 2 h the structures begin to darken and turned completely black after 6 h. After the polymerization the inner core of the structures was removed with 0.05 M acetic acid. The residue was washed several times with water and dried under reduced pressure.

9 Appendix

9.1 Supplementary Information

9.1.1 Tracing Local pH Variations with the LSM

In order to be able to trace local variations of pH in situ during the formation of biomorphs, growth was carried out directly underneath a confocal microscope. For this purpose, we used special microdishes that had a flat glass bottom (ibidi GmbH, μ-dish, diameter: 35 mm) and thus were ideally suited for imaging the front of sheets evolving along this interface. Initially, 4 mL of growth solution (prepared as described above) were filled into the dishes and left open to the atmosphere to absorb CO_2 over time. After 2 h (when the first structures had started to form), 0.1 mL of a 100 μM solution of **2** in water:acetone 9:1 were added (note that the small amounts of acetone introduced in this way did not affect the growth behavior of biomorphs to any noticeable extent). The final concentration of the dye in the mother liquor thus was 2.44 μM.

9.1.2 Quantification of the Degree of Functionalization with the Ellman Reagent

The amount of thiol groups anchored on the biomorphs via silanisation was determined with the help of the Ellman reagent (5,5'-dithiobis(2-nitrobenzoic acid)). In the presence of free thiol groups, this molecule splits and releases nitrothiobenzoate (NTB) in a quantitative reaction, as illustrated in Figure 9.4c for the case of a thiol-bearing biomorph. NTB exhibits significant absorption at 408 nm in alkaline solution and thus the reaction can readily be monitored by UV-Vis spectroscopy. Figure 9.4a shows a time-dependent series of corresponding spectra for a 8.8 μM solution of the Ellman reagent in borax buffer (pH 9) containing 18 mg of thiol-functionalised biomorphs, along with a plot of the area of the peak at 408 nm (red dots and line). In order to convert this data into an actual number of free thiol groups on the biomorphs, we performed reference experiments in which defined amounts of 3- mercaptopropionic acid (3-MPA) (0-7 μM) were added to 8.8 μM Ellman reagent solution buffered at pH 9. The resulting spectra after a reaction time of 15 min are shown in Figure 9.4b. Plotting the area of the peak as a function of concentration (red dots) gives a calibration curve that can be approximated by a linear fit (thick red line), which was used to calculate the actual number of thiol groups on the biomorphs after completion of the reaction shown

in Figure 9.4a. This yields an effective thiol loading of 947 ± 75 nmol per g biomorphs.

9.1.3 Estimation of the AuNP Loading on Functional Biomorphs

The amount of gold nanoparticles immobilised on the biomorphic structures was estimated in different ways. First, the catalytic activity – as derived from resazurin-to-resorufin reaction rates determined by UV/Vis spectroscopy with and without Au – was used as a measure. Here we assumed that the catalytic activity of the AuNPs bound on the surface of biomorphs is comparable to that of the same particles in a colloidal dispersion (reference experiment). Under these conditions, measured reaction rates can easily be converted to apparent AuNP loadings on biomorphs (in mol per g) if the used absolute mass of AuNP@Biomorph catalyst is known. Following this approach, it needs to be considered that the obtained value will represent a *lower limit* for the true loading, because the net catalytic activity of surface-bound particles is most likely lower than that of the same amount of dispersed particles, due to the fact that reagents need to be transported to/from the surface by diffusion and that some of surface sites may not readily be accessible. The second used method was EDX spectroscopy on intact AuNP-bearing biomorphs. Corresponding measurements gave an atomic ratio of Ba:Si:Au = 94:100:1. With the known density of solid gold (50 atoms per nm^3) and mean diameter of the used AuNPs (14 nm), the loading of AuNPs on the biomorphs can be calculated from the EDX data. The problem of this approach is that EDX is a surface-sensitive technique with a typical penetration depth of a few microns. Consequently, the contribution of elements that are enriched at the surface of the functionalised biomorph (Si and Au) will be disproportionately higher than that of the bulk material below (mainly $BaCO_3$). Therefore, the resulting value for the loading should be regarded as an *upper limit*.

The third way to calculate the loading is based on in-situ UV-Vis experiments during the functionalisation step, i.e. when thiol-modified biomorphs were incubated in a dispersion of gold colloids. In the absence of biomorphs, the dispersion showed significant absorbance at 514 nm due to surface plasmon resonance, in good agreement with the literature.[216] However, upon exposure to the thiol-bearing biomorphs, the intensity of the band at 514 nm decreased and the colour of the solution changed from red to a dark violet, accompanied by the emergence of an additional absorption peak at ca. 595 nm (Figure 9.5c). This second band indicates the formation of one-dimensional

superstructures (chains) [217] of the gold colloids in dispersion and in fact, such aggregated structures could also be observed by TEM (Figure 9.5b). Interestingly, this effect only occurred in the presence of biomorphs, while neither $BaCO_3$ nor silica particles alone did have any noticeable influence on the absorption spectra. In turn, when as-grown biomorphs were used (no thiol modification), the new band at 595 nm formed, but the peak at 514 nm did not decrease in intensity (cf. Figure 9.5d). While we cannot explain these findings in detail at the moment, a comparison of the absorbance at 514 nm (peak area) after exposure to i) unmodified biomorphs (Figure 9.5d) and ii) thiol-bearing biomorphs (blue curve in Figure 9.5c) can be taken as a measure for how many Au nanoparticles were bound on the thiol-modified biomorphs during AuNP functionalisation. Values resulting for the loading from this approach are also considered to be upper limits, because the formed aggregates of AuNPs have limited colloidal stability and hence some of them may have precipitated in the course of the experiment (thus reducing the detected absorption without actually binding to biomorphs).

Values resulting for the AuNP loading from the above-described approaches are compiled in Table 3. It is obvious that the agreement between the estimated loadings is not good, but still the data give an idea about the order of magnitude.

9.1.4 Raman and IR Analyses of Polymer-Coated Biomorphs

In addition to optical microscopy, SEM and CLSM, the composition of the biomorphs after functionalisation with PCDA was also investigated by means of Raman and IR spectroscopy. Corresponding results are summarised in Figure 9.6. Local Raman spectra (Figure 9.6a) collected from native aggregates before polymerisation show characteristic signals of $BaCO_3$ at 135, 153 and 1063 cm^{-1} , along with a strong band at 523 cm^{-1} that can be assigned to silica (blue spectrum Figure 9.6a).[218, 219] Upon treatment with 1 M NaOH, this latter signal has vanished (red spectrum in Figure 9.6a), indicating successful removal of the outer silica skin. After adsorption of PCDA and UV illumination, the obtained Raman spectrum is completely different and displays bands that can exclusively be attributed to poly(PCDA) (black spectrum in Figure 9.6a).[190] The presence of the polymer is also reflected in the curved baseline of the spectrum, which results from the fluorescence of poly(PCDA). In turn, the absence of distinct carbonate and silica modes suggests that the newly formed polymer coating is rather thick and hence the Raman signal can no longer be obtained from the inner part of the

structure.

The above findings are further confirmed by IR data (Figure 9.6b). While the spectrum measured for a biomorph after removal of the silica skin (black curve in Figure 9.6b) shows only bands typical for barium carbonate (693, 855 and 1412 cm^{-1}), new signals emerge after the polymerisation step, namely CO modes at 1511 and 1556 cm^{-1} as well as CH modes at 2748 and 2982 cm^{-1} , both being characteristic for poly(PCDA).[190]

9.2 Supplementary Figures

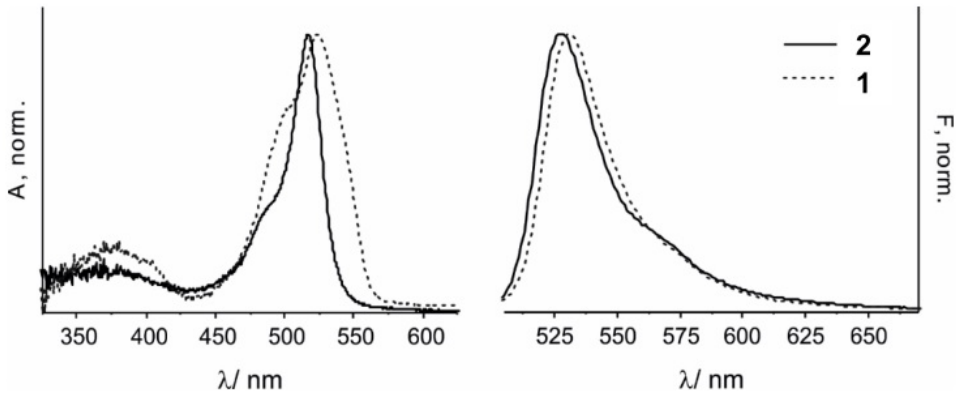

Figure 9.1: Normalized absorption (left) and emission spectra (right) of dyes **1** and **2** in water.

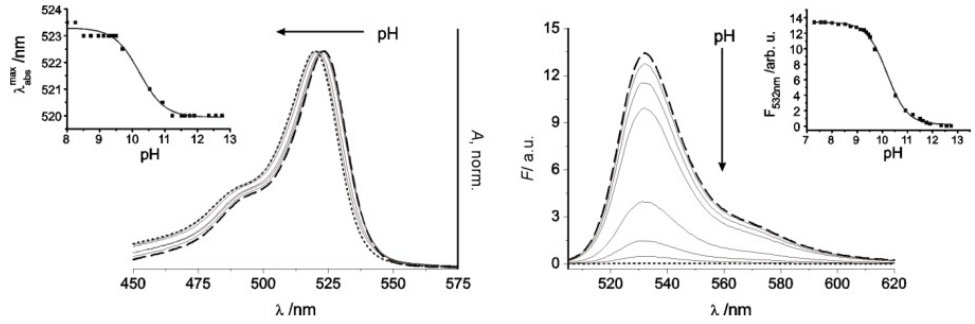

Figure 9.2: Dependence of the absorption and fluorescence of dye **1** on a change in pH from 7.3 to 12.8 upon addition of aqueous KOH solutions (λ_{ex} = 495 nm, $c_1 = 1.39 \cdot 10^{-6} M$, EtOH/$H_2O$); pH 7.3 (dashed line), pH 12.8 (dotted line); selected intermediate steps (solid lines). Insets: corresponding titration curves, given by the shift of the absorption maximum (left) and the fluorescence intensity at the emission maximum (right) as a function of pH.

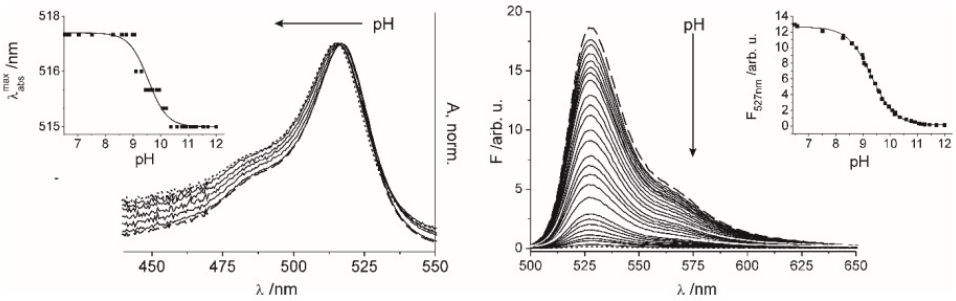

Figure 9.3: Dependence of the absorption and fluorescence of dye **2** on a change in pH from 6.5 to 12.0 in neat water (λ_{ex} = 495 nm, $c_2 = 1.39 \cdot 10^{-6} M$, H_2O); pH 6.5 (dashed line), pH 12.0 (dotted line), intermediate steps (solid lines). Insets: corresponding titration curves, given by the shift of the absorption maximum (left) and the fluorescence intensity at the emission maximum (right) as a function of pH.

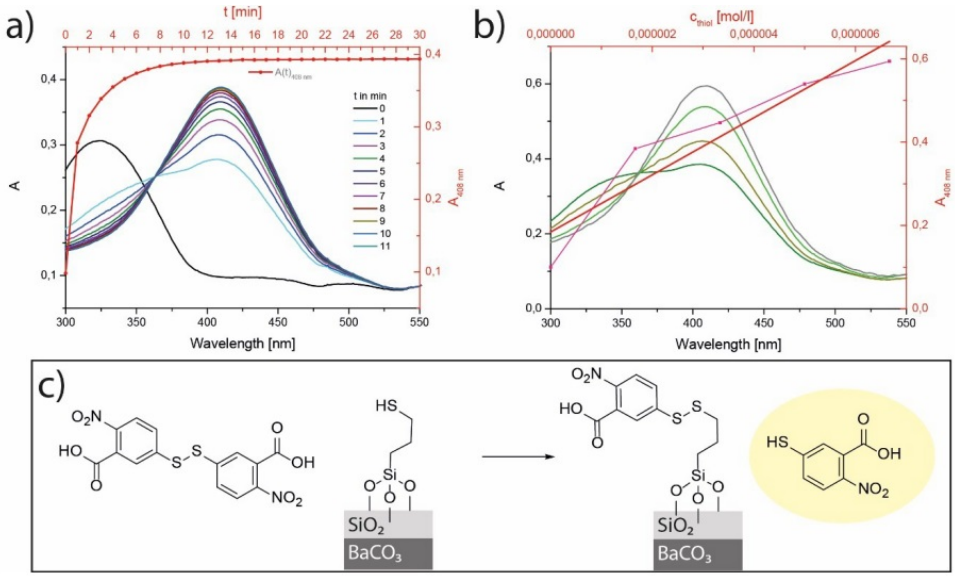

Figure 9.4: a) UV/Vis spectra showing the progress of the Ellman reaction as a function of time in the presence of 18 mg thiol-modified biomorphs at pH 9. b) UV/Vis spectra of solutions in which the Ellman reagent was converted with different amounts of 3-MPA. The thick red line is a linear fit to the experimental peak area-concentration data, which was used as a calibration curve. c) Schematic drawing of the Ellman reaction on thiol-functionalised biomorphs.

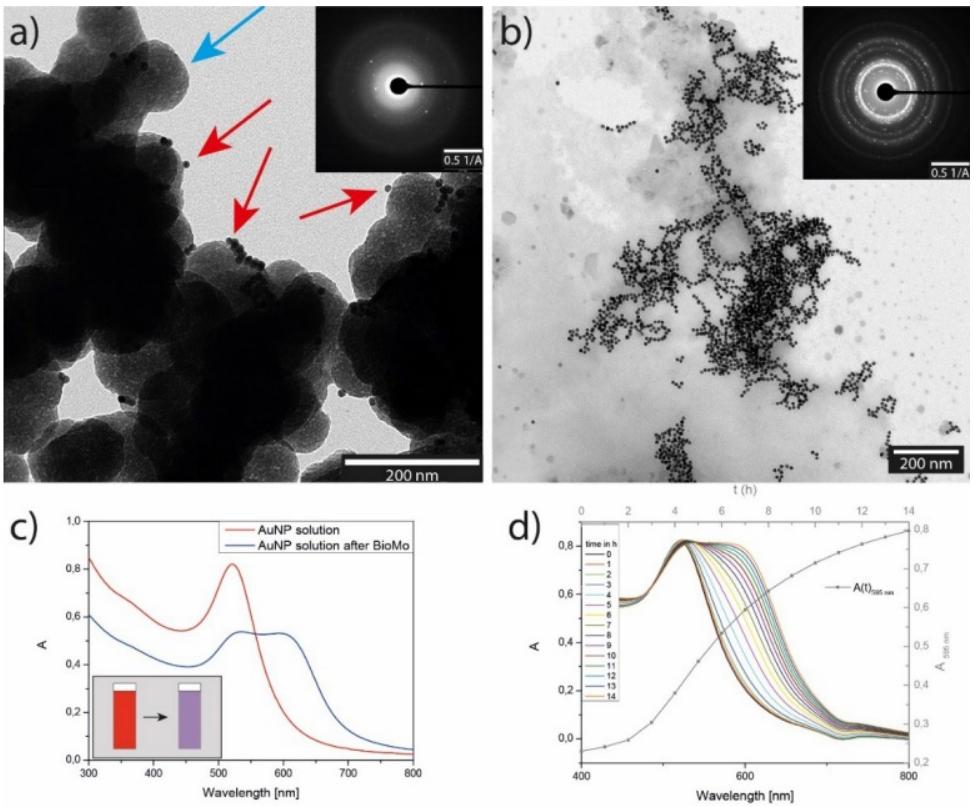

Figure 9.5: TEM image of thiol-modified biomorphs after incubation in AuNP dispersion, rinsing with water and crushing for TEM preparation. The remaining fragments consist of three components: carbonate nanocrystals (ca. 200 nm long and 50 nm wide, not shown here), silica spheres (50-200 nm in diameter, indicated by the blue arrow), and small gold colloids (14 nm) with high contrast (highlighted by red arrows) that decorate some of the silica particles. Corresponding electron diffraction (ED) patterns show strong reflections that can be assigned to crystalline gold (note that the shown area of the sample mainly contains (amorphous) silica spheres and AuNPs). b) TEM micrograph of AuNP networks that were isolated from gold dispersions after exposure to thiol-modified biomorphs. The ED pattern proves that the aggregated particles consist of Au. c) UV/Vis spectra of the colloidal AuNP dispersion before (red) and after (blue) incubation with thiol-modified biomorphs (blue). The inserted sketch illustrates how the colour of the solution changed. d) UV/Vis spectra of the AuNP dispersion at different times during incubation with unfunctionalised biomorphs (no thiol modification)

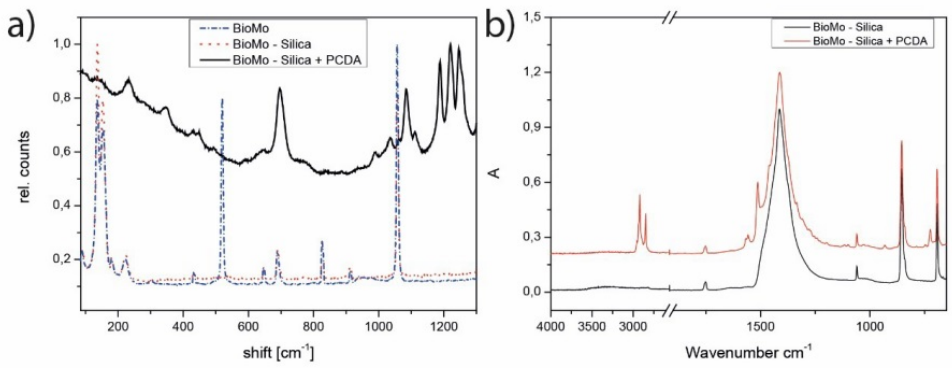

Figure 9.6: a) Local Raman spectra collected from a native biomorph (blue), a biomorph after removal of the outer silica skin (red), and a PCDA-modified biomorph (black). b) IR spectra of biomorphs after leaching in 1 M NaOH (black) and after functionalisation with PCDA (red).

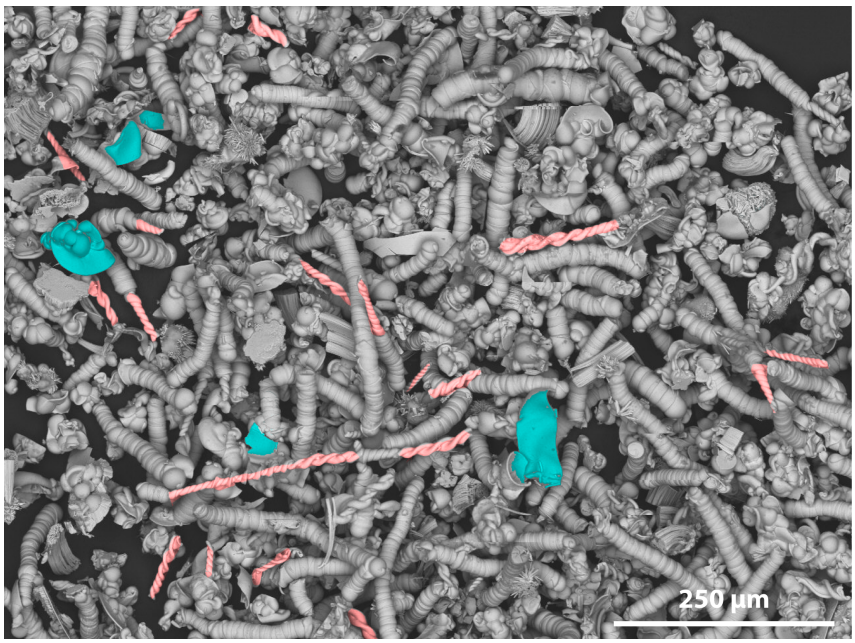

Figure 9.7: False-colored scanning electron micrograph giving an overview on typical biomorph morphologies obtained from a single synthesis batch (blue: sheets, red: helicoids, grey: worm-like braids).

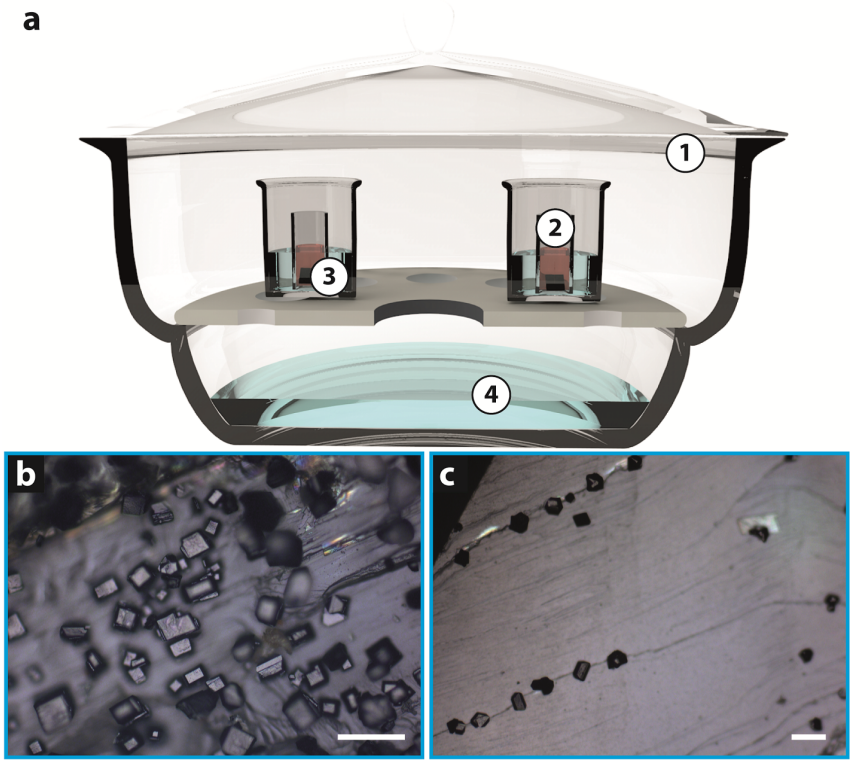

Figure 9.8: Preparation of magnetite mesocrystals. (a) Sketch of the experimental setup used for the formation of magnetite mesocrystals via diffusion of a destabilizing anti-solvent (EtOH) into a dispersion of magnetite nanocrystals (1: desiccator; 2: dispersion of magnetite nanoparticles in THF; 3: Si wafer; 4: EtOH/THF mixture). (b,c) Magnetite mesocrystals grown on single-crystalline calcium carbonate macro-substrates, namely (b) aragonite and (c) calcite (Scale bars: 100 μm).

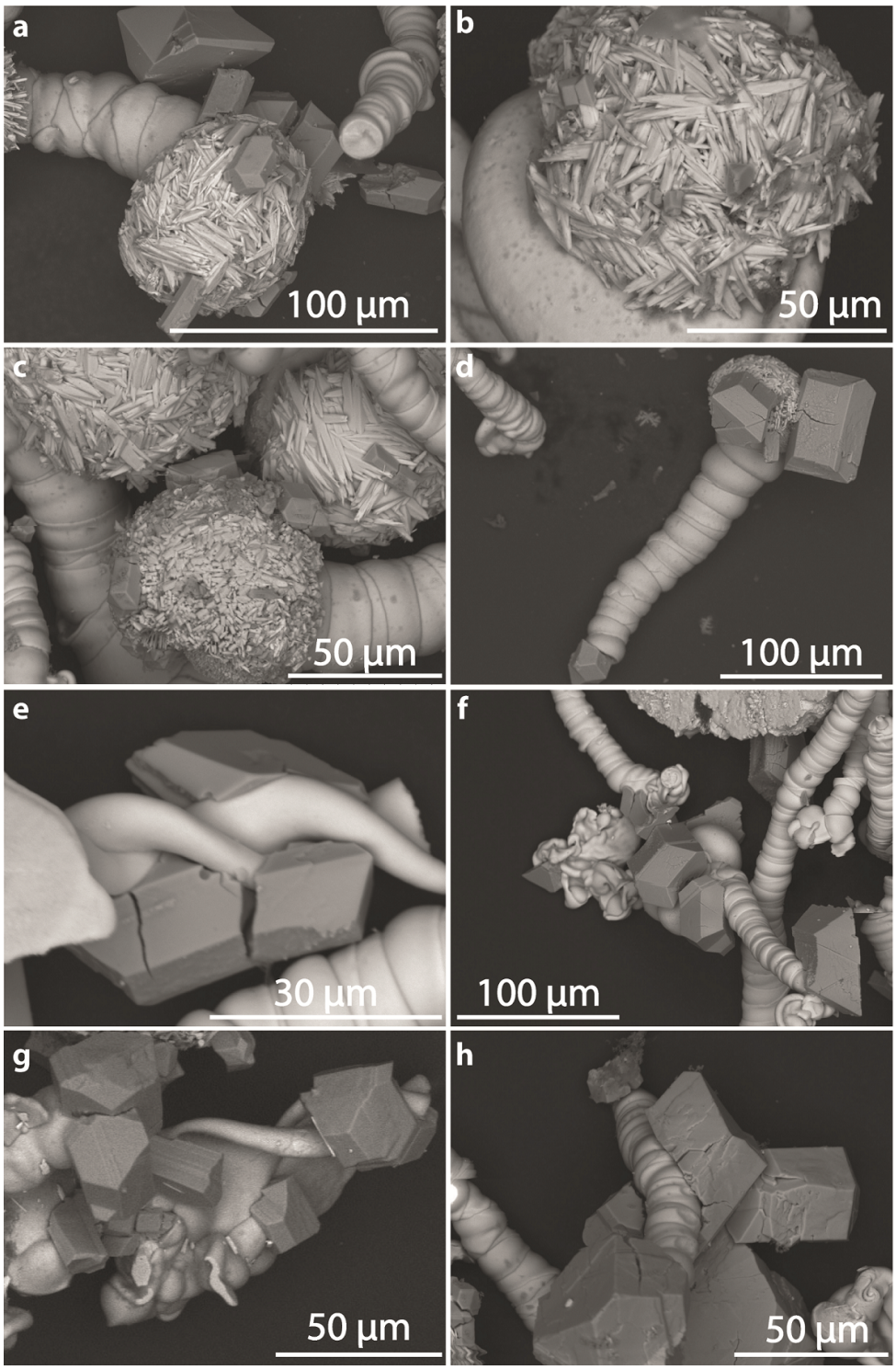

Figure 9.9: Collection of different magnetite-biomorph composite structures. Magnetite mesocrystals were grown on (a,b) native biomorphs, (c,d) biomorphs after removal of the outer silica shell, (e,f) biomorphs without silica skin after modification with oleic acid, and (g,h) biomorphs after hydrophobization of the outer silica skin with alkyl silanes.

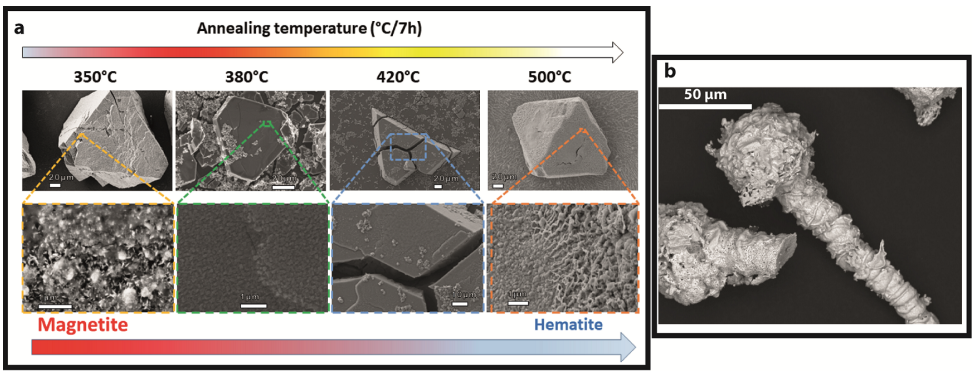

Figure 9.10: Thermal stability of mesocrystal-biomorph composites. (a) SEM images illustrating the structural features of of mesocrystals annealed at various temperatures. (b) SEM image of an annealed (1000°C) mesocrystal-biomorph composite.

9.3 Supplementary Tables

Table 2: Spectroscopic data of dyes **1** and **2** in selected solvents at 298 K.

Compound	Solvent	λ_{abs} [nm]	λ_{em} [nm]	τ_f [ns]
	MeCN	517	526	n.d.
2	H_2O/EtOH	518	527	4.72
	H_2O	517	527	3.42
	MeCN	521	531	4.72
1	H_2O/EtOH	523	532	5.57
	H_2O	523	532	2.67

Table 3: Loadings of AuNPs on biomorphs after functionalisation, as estimated by different methods.

Method	Calculated Loading [nmol/g]
Catalytic Reaction	0.03 ± 0.01
EDX	0.5 ± 0.05
UV-Vis Spectroscopy	0.74 ± 0.01

9.4 Supplementary Movie Captions

Movie S1. Schematic animation illustrating the response of a mesocrystal-biomorph composite to a moving magnet centered below the structure. The indicated delay of the response is caused by the viscosity of the surrounding (liquid) medium.

Movie S2. A magnetic worm-like aggregate follows a magnet in linear movement (according to Movie S1) through a viscous PEG-8000 solution (50 wt% in water). Movie

S3. Movement of the microarchitecture shown in Movie S2 into the opposite direction.

Movie S4. Schematic animation illustrating the response of a mesocrystal-biomorph composite to a moving magnet slightly displaced below the structure, inducing rotational movement.

Movie S5. Magnetized silica biomorphs respond to the movement of a magnet by rotation in dry state.

Movie S6. A magnetized biomorph ghost swims through less viscous 0.05 M acetic acid solution.

10 References

[1] Gall, J. General systematics: How systems work and how they fail. 1975.

[2] Garcia Ruiz, J. M.; Carnerup, A.; Christy, A. G.; Welham, N. J.; Hyde, S. T. Morphology: An ambiguous indicator of biogenicity. Astrobiology **2002**, 2, 353–369.

[3] Rickwood, P. C. The largest crystals. Am. Min. **1981**, 66, 885–907.

[4] Holl, C.; Smyth, J.; Laustsen, H.; Jacobsen, S.; Downs, R. Compression of witherite to 8 GPa and the crystal structure of BaCO3II. Phys. Chem. Miner. **2000**, 27, 467–473.

[5] Wilson, J. R. Minerals and rocks; Bookboon, 2015.

[6] Mann, S. The chemistry of form. Angew. Chem. Int. Ed. **2000**, 39, 3392–3406.

[7] Schneider, A. S.; Heiland, B.; Peter, N. J.; Guth, C.; Arzt, E.; Weiss, I. M. Hierarchical super-structure identified by polarized light microscopy, electron microscopy and nanoindentation: Implications for the limits of biological control over the growth mode of abalone sea shells. BMC Biophysics **2012**, 5, 19.

[8] Voinescu, A. E.; Kellermeier, M.; Bartel, B.; Carnerup, A. M.; Larsson, A.-K.; Touraud, D.; Kunz, W.; Kienle, L.; Pfitzner, A.; Hyde, S. T. Inorganic self-organized silica aragonite biomorphic composites. Cryst. Growth Des. **2008**, 8, 1515–1521.

[9] Politi, Y.; Arad, T.; Klein, E.; Weiner, S.; Addadi, L. Sea urchin spine calcite forms via a transient amorphous calcium carbonate phase. Science **2004**, 306, 1161–1164.

[10] Young, J. R.; Davis, S. A.; Bown, P. R.; Mann, S. Coccolith ultrastructure and biomineralisation. J. Struct. Biol. **1999**, 126, 195–215.

[11] Mann, S. Biomineralization: principles and concepts in bioinorganic materials chemistry; Oxford University Press, 2001; Vol. 5.

[12] Gower, L. B. Biomimetic model systems for investigating the amorphous precursor pathway and its role in biomineralization. Chem. Rev. **2008**, 108, 4551–4627.

[13] Sarikaya, M.; Gunnison, K.; Yasrebi, M.; Aksay, I. Mechanical property-microstructural relationships in abalone shell. MRS Online Proceedings Library Archive **1989**, 174.

[14] Currey, J.; Taylor, J. The mechanical behaviour of some molluscan hard tissues. J. Zool **1974**, 173, 395–406.

[15] Weiner, S.; Talmon, Y.; Traub, W. Electron diffraction of mollusc shell organic matrices and their relationship to the mineral phase. Int. J. Biol. Macromol. **1983**, 5, 325–328.

[16] De Yoreo, J. J.; Gilbert, P. U. P. A.; Sommerdijk, N. A. J. M.; Penn, R. L.; Whitelam, S.; Joester, D.; Zhang, H.; Rimer, J. D.; Navrotsky, A.; Banfield, J. F.; Wallace, A. F.; Michel, F. M.; Meldrum, F. C.; Cölfen, H.; Dove, P. M. Crystallization by particle attachment in synthetic, biogenic, and geologic environments. Science **2015**, 349, 6247.

[17] Nudelman, F.; Sommerdijk, N. A. J. M. Biomineralization as an Inspiration for Materials Chemistry. Angew. Chem. Int. Ed. **2012**, 51, 6582–6596.

[18] Kim, Y.-Y.; Ganesan, K.; Yang, P.; Kulak, A. N.; Borukhin, S.; Pechook, S.; Ribeiro, L.; Kröger, R.; Eichhorn, S. J.; Armes, S. P.; Pokroy, B.; Meldrum, F. C. An artificial biomineral formed by incorporation of copolymer micelles in calcite crystals. Nat. Mater. **2011**, 10, 890–896.

[19] Mirkhalaf, M.; Dastjerdi, A. K.; Barthelat, F. Overcoming the brittleness of glass through bio-inspiration and micro-architecture. Nat. Commun **2014**, 5.

[20] Oaki, Y.; Imai, H. The Hierarchical Architecture of Nacre and Its Mimetic Material. Angew. Chem. Int. Ed. **2005**, 44, 6571–6575.

[21] Rao, A.; Berg, J. K.; Kellermeier, M.; Gebauer, D. Sweet on biomineralization: effects of carbohydrates on the early stages of calcium carbonate crystallization. Eur. J. Mineral. **2014**, 26, 537–552.

[22] Perovic, I.; Chang, E. P.; Lui, M.; Rao, A.; Cölfen, H.; Evans, J. S. A nacre protein, n16. 3, self-assembles to form protein oligomers that dimensionally limit and organize mineral deposits. Biochemistry **2014**, 53, 2739–2748.

[23] Seto, J.; Ma, Y.; Davis, S. A.; Meldrum, F.; Gourrier, A.; Kim, Y.-Y.; Schilde, U.; Sztucki, M.; Burghammer, M.; Maltsev, S.; Jäger, C.; Cölfen, H. Structure-property relationships of a biological mesocrystal in the adult sea urchin spine. PNAS **2012**, 109, 3699–3704.

[24] Seto, J.; Picker, A.; Chen, Y.; Rao, A.; Evans, J. S.; Cölfen, H. Nacre protein sequence compartmentalizes mineral polymorphs in solution. Cryst. Growth Des. **2014**, 14, 1501–1505.

[25] Beniash, E.; Aizenberg, J.; Addadi, L.; Weiner, S. Amorphous calcium carbonate transforms into calcite during sea urchin larval spicule growth. PNAS **1997**, 264, 461–465.

[26] Weiner, S.; Addadi, L. Design strategies in mineralized biological materials. J. Mater. Chem **1997**, 7, 689–702.

[27] Albeck, S.; Aizenberg, J.; Addadi, L.; Weiner, S. Interactions of various skeletal intracrystalline components with calcite crystals. J. Am. Chem. Soc. **1993**, 115, 11691–11697.

[28] Aizenberg, J.; Hanson, J.; Koetzle, T.; Weiner, S.; Addadi, L. Control of macromolecule distribution within synthetic and biogenic single calcite crystals. J. Am. Chem. Soc. **1997**, 119, 881–886.

[29] Addadi, L.; Raz, S.; Weiner, S. Taking advantage of disorder: amorphous calcium carbonate and its roles in biomineralization. Adv. Mater. **2003**, 15, 959–970.

[30] Killian, C. E.; Metzler, R. A.; Gong, Y.; Olson, I. C.; Aizenberg, J.; Politi, Y.; Wilt, F. H.; Scholl, A.; Young, A.; Doran, A., et al. Mechanism of calcite co-orientation in the sea urchin tooth. J. Am. Chem. Soc. **2009**, 131, 18404–18409.

[31] Romein, A. J. T. Lineages in early Paleogene calcareous nannoplankton. Ph.D. thesis, Utrecht University, 1979.

[32] Falini, G.; Albeck, S.; Weiner, S.; Addadi, L. Control of aragonite or calcite polymorphism by mollusk shell macromolecules. Science **1996**, 271, 67–69.

[33] Addadi, L.; Weiner, S. Interactions between acidic proteins and crystals: stereochemical requirements in biomineralization. PNAS **1985**, 82, 4110–4114.

[34] Weiner, S.; Nudelman, F.; Sone, E.; Zaslansky, P.; Addadi, L. Mineralized biological materials: A perspective on interfaces and interphases designed over millions of years. Biointerphases **2006**, 1, P12–P14.

[35] Mahamid, J.; Aichmayer, B.; Shimoni, E.; Ziblat, R.; Li, C.; Siegel, S.; Paris, O.; Fratzl, P.; Weiner, S.; Addadi, L. Mapping amorphous calcium phosphate transformation into crystalline mineral from the cell to the bone in zebrafish fin rays. PNAS **2010**, 107, 6316–6321.

[36] Singh, S.; Bozhilov, K.; Mulchandani, A.; Myung, N.; Chen, W. Biologically programmed synthesis of core-shell CdSe/ZnS nanocrystals. ChemComm **2010**, 46, 1473–1475.

[37] Sone, E. D.; Zubarev, E. R.; Stupp, S. I. Semiconductor nanohelices templated by supramolecular ribbons. Angew. Chem. Int. Ed. **2002**, 41, 1705–1709.

[38] Braun, P. V.; Osenar, P.; Stupp, S. I. Semiconducting superlattices templated by molecular assemblies. Nature **1996**, 380, 325–328.

[39] Sakamoto, T.; Nishimura, Y.; Nishimura, T.; Kato, T. Photoimaging of Self-Organized CaCO3/Polymer Hybrid Films by Formation of Regular Relief and Flat Surface Morphologies. Angew. Chem. **2011**, 123, 5978–5981.

[40] Addadi, L.; Weiner, S. A pavement of pearl. Nature **1997**, 389, 912–913.

[41] Schäffer, T. E.; Ionescu-Zanetti, C.; Proksch, R.; Fritz, M.; Walters, D. A.; Almqvist, N.; Zaremba, C. M.; Belcher, A. M.; Smith, B. L.; Stucky, G. D., et al. Does abalone nacre form by heteroepitaxial nucleation or by growth through mineral bridges? Chem. Mater. **1997**, 9, 1731–1740.

[42] Donners, J. J.; Hoogenboom, R.; Schenning, A. P.; van Hal, P. A.; Nolte, R. J.; Meijer, E.; Sommerdijk, N. A. Fabrication of Organic- Inorganic Semiconductor Composites Utilizing the Different Aggregation States of a Single Amphiphilic Dendrimer. Langmuir **2002**, 18, 2571–2576.

[43] Murray, C.; Kagan, C.; Bawendi, M. Self-organization of CdSe nanocrystallites into three-dimensional quantum dot superlattices. Science **1995**, 270, 1335–1338.

[44] Peng, X.; Wilson, T. E.; Alivisatos, A. P.; Schultz, P. G. Synthesis and isolatin of a homodimer of cadmium selenide nanocrystals. Angew. Chem. Int. Ed. **1997**, 36, 145–147.

[45] Sakamoto, T.; Nishimura, Y.; Kato, T. Tuning of morphology and polymorphs of carbonate/polymer hybrids using photoreactive polymer templates. CrystEngComm **2015**, 17, 6947–6954.

[46] Meldrum, F. C.; Hyde, S. T. Morphological influence of magnesium and organic additives on the precipitation of calcite. J. Cryst. Growth **2001**, 231, 544–558.

[47] McCauley, J. W.; Roy, R. Controlled nucleation and crystal growth of various CaC03 phases by the silica gel technique. Am. Min.: Journal of Earth and Planetary Materials **1974**, 59, 947–963.

[48] Henisch, H. K. Crystals in gels and Liesegang rings; Cambridge University Press, 2005.

[49] Garciaruiz, J. M.; Amoros, J. L. MORPHOLOGICAL ASPECTS OF SOME SYMMETRICAL CRYSTAL AGGREGATES GROWN BY SILICA-GEL TECHNIQUE. J. Cryst. Growth **1981**, 55, 379–383.

[50] Garciaruiz, J. M. ON THE FORMATION OF INDUCED MORPHOLOGY CRYSTAL AGGREGATES. J. Cryst. Growth **1985**, 73, 251–262.

[51] Kellermeier, M.; Colfen, H.; Garcia-Ruiz, J. M. Silica Biomorphs: Complex Biomimetic Hybrid Materials from "Sand and Chalk". Eur. J. Inorg. Chem. **2012**, 5123–5144.

[52] Garcia-Ruiz, J. M.; Hyde, S. T.; Carnerup, A. M.; Christy, A. G.; Van Kranendonk, M. J.; Welham, N. J. Self-assembled silica-carbonate structures and detection of ancient microfossils. Science **2003**, 302, 1194–1197.

[53] Garcia-Ruiz, J. M. Carbonate precipitation into alkaline silica-rich environments. Geology **1998**, 26, 843–846.

[54] Kellermeier, M.; Melero-Garcia, E.; Glaab, F.; Eiblmeier, J.; Kienle, L.; Rachel, R.; Kunz, W.; Manuel Garcia-Ruiz, J. Growth Behavior and Kinetics of Self-Assembled Silica-Carbonate Biomorphs. Chem-Eur J **2012**, 18, 2272–2282.

[55] Zhang, G.; Delgado-Lopez, J. M.; Choquesillo-Lazarte, D.; Garcia-Ruiz, J. M. Crystallization of monohydrocalcite in a silica-rich alkaline solution. CrystEngComm **2013**, 15, 6526–6532.

[56] Hyde, S. T.; Carnerup, A. M.; Larsson, A. K.; Christy, A. G.; Garcia-Ruiz, J. M. Self-assembly of carbonate-silica colloids: between living and non-living form. Physica a-Statistical Mechanics and Its Applications **2004**, 339, 24–33.

[57] Bittarello, E.; Aquilano, D. Self-assembled nanocrystals of barium carbonate in biomineral-like structures. Eur. J. Mineral. **2007**, 19, 345–351.

[58] Voinescu, A. E.; Kellermeier, M.; Carnerup, A. M.; Larsson, A.-K.; Touraud, D.; Hyde, S. T.; Kunz, W. Co-precipitation of silica and alkaline-earth carbonates using TEOS as silica source. J. Cryst. Growth **2007**, 306, 152–158.

[59] Bittarello, E.; Massaro, F. R.; Aquilano, D. The epitaxial role of silica groups in promoting the formation of silica/carbonate biomorphs: A first hypothesis. J. Cryst. Growth **2010**, 312, 402–412.

[60] Melero-Garcia, E.; Santisteban-Bailon, R.; Garcia-Ruiz, J. M. Role of Bulk pH during Witherite Biomorph Growth in Silica Gels. Cryst. Growth Des. **2009**, 9, 4730–4734.

[61] Eiblmeier, J.; Kellermeier, M.; Rengstl, D.; Manuel Garcia-Ruiz, J.; Kunz, W. Effect of bulk pH and supersaturation on the growth behavior of silica biomorphs in alkaline solutions. CrystEngComm **2013**, 15, 43–53.

[62] Terada, T.; Yamabi, S.; Imai, H. Formation process of sheets and helical forms consisting of strontium carbonate fibrous crystals with silicate. J. Cryst. Growth **2003**, 253, 435–444.

[63] Bella, S. D.; Garcia-Ruiz, J. Textures in induced morphology crystal aggregates of CaCO3: sheaf of wheat morphologies. J. Cryst. Growth **1986**, 79, 236–240.

[64] Bella, S. D.; Garcia-Ruiz, J. Banding structures in induced morphology crystal aggregates of CaCO 3. J. Mater. Sci **1987**, 22, 3095–3102.

[65] Kellermeier, M.; Melero-Garcia, E.; Kunz, W.; Garcia-Ruiz, J. M. The ability of silica to induce biomimetic crystallization of calcium carbonate. Adv. Chem. Phys. **2012**, 151, 277.

[66] Imai, H.; Terada, T.; Yamabi, S. Self-organized formation of a hierarchical self-similar structure with calcium carbonate. ChemComm **2003**, 484–485.

[67] Imai, H.; Terada, T.; Miura, T.; Yamabi, S. Self-organized formation of porous aragonite with silicate. J. Cryst. Growth **2002**, 244, 200–205.

[68] Schopf, J. W. Microflora of the Bitter Springs formation, late Precambrian, central Australia. J. Paleontol. **1968**, 651–688.

[69] Garcia-Ruiz, J. M. INORGANIC SELF-ORGANIZATION IN PRECAMBRIAN CHARTS. Origins Life Evol. Biosphere **1994**, 24, 451–467.

[70] Garcia-Ruiz, J. M. Geochemical scenarios for the precipitation of biomimetic inorganic carbonates. **2000**,

[71] Kellermeier, M.; Glaab, F.; Carnerup, A. M.; Drechsler, M.; Gossler, B.; Hyde, S. T.; Kunz, W. Additive-induced morphological tuning of self-assembled silica-barium carbonate crystal aggregates. J. Cryst. Growth **2009**, 311, 2530–2541.

[72] Speer, J. A. Crystal chemistry and phase relations of orthorhombic carbonates. Rev. Mineral. Geochem. **1983**, 11, 145–190.

[73] Hyde, S. T.; Garcia-Ruiz, J. M. Complex materials from simple chemistry: biomorphs and biomaterials. ACTUALITE CHIMIQUE **2004**, 4–6.

[74] Garcia-Ruiz, J. M.; Melero-Garcia, E.; Hyde, S. T. Morphogenesis of Self-Assembled Nanocrystalline Materials of Barium Carbonate and Silica. Science **2009**, 323, 362–365.

[75] Busch, S.; Dolhaine, H.; DuChesne, A.; Heinz, S.; Hochrein, O.; Laeri, F.; Podebrad, O.; Vietze, U.; Weiland, T.; Kniep, R. Biomimetic Morphogenesis of Fluorapatite-Gelatin Composites: Fractal Growth, the Question of Intrinsic Electric Fields, Core/Shell Assemblies, Hollow Spheres and Reorganization of Denatured Collagen. Eur. J. Inorg. Chem. **1999**, 1999, 1643–1653.

[76] Keith, H. D.; Padden, F. J. A PHENOMENOLOGICAL THEORY OF SPHERULITIC CRYSTALLIZATION. J. Appl. Phys. **1963**, 34, 2409–&.

[77] Goldenfeld, N. Theory of spherulitic crystallization. J. Cryst. Growth **1987**, 84, 601–608.

[78] Simon, P.; Rosseeva, E.; Baburin, I. A.; Liebscher, L.; Hickey, S. G.; Cardoso Gil, R.; Eychmueller, A.; Kniep, R.; Carrillo Cabrera, W. PbS–organic mesocrystals: The relationship between nanocrystal orientation and superlattice array. Angew. Chem. **2012**, 124, 10934–10939.

[79] Kellermeier, M.; Melero-Garcia, E.; Glaab, F.; Klein, R.; Drechsler, M.; Rachel, R.; Manuel Garcia-Ruiz, J.; Kunz, W. Stabilization of Amorphous Calcium Carbonate in Inorganic Silica-Rich Environments. J. Am. Chem. Soc. **2010**, 132, 17859–17866.

[80] Kunz, W.; Kellermeier, M. MATERIALS SCIENCE Beyond Biomineralization. Science **2009**, 323, 344–345.

[81] Kellermeier, M.; Melero-Garcia, E.; Kunz, W.; Manuel Garcia-Ruiz, J. Local autocatalytic co-precipitation phenomena in self-assembled silica-carbonate materials. J. Colloid Interface Sci. **2012**, 380, 1–7.

[82] Zaikin, A.; Zhabotinsky, A. Concentration wave propagation in two-dimensional liquid-phase self-oscillating system. Nature **1970**, 225, 535–537.

[83] Nakouzi, E.; Knoll, P.; Hendrix, K. B.; Steinbock, O. Systematic characterization of polycrystalline silica-carbonate helices. Phys. Chem. Chem. Phys. **2016**, 18, 23044–23052.

[84] Sturm, E. V.; Cölfen, H. Mesocrystals: structural and morphogenetic aspects. Chem. Soc. Rev. **2016**, 45, 5821–5833.

[85] Cölfen, H.; Antonietti, M. Mesocrystals: inorganic superstructures made by highly parallel crystallization and controlled alignment. Angew. Chem. Int. Ed. **2005**, 44, 5576–5591.

[86] Song, R.-Q.; Cölfen, H. Mesocrystals—ordered nanoparticle superstructures. Adv. Mater. **2010**, 22, 1301–1330.

[87] Nagarajan, R. Nanoparticles: building blocks for nanotechnology; ACS Publications, 2008.

[88] Kelly, K. L.; Coronado, E.; Zhao, L. L.; Schatz, G. C. The optical properties of metal nanoparticles: the influence of size, shape, and dielectric environment. 2003.

[89] Haruta, M. When gold is not noble: catalysis by nanoparticles. Chem. Rec. **2003**, 3, 75–87.

[90] Zaitsev, V. S.; Filimonov, D. S.; Presnyakov, I. A.; Gambino, R. J.; Chu, B. Physical and chemical properties of magnetite and magnetite-polymer nanoparticles and their colloidal dispersions. J. Colloid Interface Sci. **1999**, 212, 49–57.

[91] Stevens, S. Y.; Sutherland, L. M.; Krajcik, J. S. The big ideas of nanoscale science and engineering; NSTA press, 2009.

[92] Li, T.; Galli, G. Electronic properties of MoS2 nanoparticles. J. Phys. Chem. C **2007**, 111, 16192–16196.

[93] Goya, G.; Berquo, T.; Fonseca, F.; Morales, M. Static and dynamic magnetic properties of spherical magnetite nanoparticles. J. Appl. Phys **2003**, 94, 3520–3528.

[94] Sepeur, S. Nanotechnology: technical basics and applications; Vincentz Network GmbH & Co KG, 2008.

[95] Baldan, A. Review progress in Ostwald ripening theories and their applications to nickel-base superalloys Part I: Ostwald ripening theories. J. Mater. Sci. **2002**, 37, 2171–2202.

[96] Zhou, L.; O'Brien, P. Mesocrystals: A New Class of Solid Materials. Small **2008**, 4, 1566–1574.

[97] Bergstroem, L.; Sturm, E. V.; Salazar-Alvarez, G.; Cölfen, H. Mesocrystals in biominerals and colloidal arrays. Acc. Chem. Res. **2015**, 48, 1391–1402.

[98] Brunner, J.; Baburin, I. A.; Sturm, S.; Kvashnina, K.; Rossberg, A.; Pietsch, T.; Andreev, S.; née Rosseeva, E. S.; Cölfen, H. Self-Assembled Magnetite Mesocrystalline Films: Toward Structural Evolution from 2D to 3D Superlattices. Adv. Mater. Interfaces **2016**, 4, 1600431.

[99] Brunner, J. J. Iron Oxide Mesocrystals. Thesis, 2019.

[100] Brunner, J.; Maier, B.; Rosenberg, R.; Sturm, S.; Cölfen, H.; Sturm, E. V. Nonclassical Recrystallization. Chem. Eur. J. **2020**, 26, 15242.

[101] Opel, J.; Hecht, M.; Rurack, K.; Eiblmeier, J.; Kunz, W.; Cölfen, H.; Kellermeier, M. Probing local pH-based precipitation processes in self-assembled silica-carbonate hybrid materials. Nanoscale **2015**, 7, 17434–17440.

[102] Noorduin, W. L.; Grinthal, A.; Mahadevan, L.; Aizenberg, J. Rationally Designed Complex, Hierarchical Microarchitectures. Science **2013**, 340, 832–837.

[103] Kellermeier, M.; Glaab, F.; Melero-Garcia, E.; Manuel Garcia-Ruiz, J. In Research Methods in Biomineralization Science; Yoreo, J. J. D., Ed.; Methods in Enzymology; 2013; Vol. 532; pp 225–256.

[104] Weiner, S.; Addadi, L. In Annual Review of Materials Research, Vol 41; Clarke, D. R., Fratzl, P., Eds.; Annual Review of Materials Research; 2011; Vol. 41; pp 21–40.

[105] Meldrum, F. C.; Coelfen, H. Controlling Mineral Morphologies and Structures in Biological and Synthetic Systems. Chem. Rev. **2008**, 108, 4332–4432.

[106] Coelfen, H.; Antonietti, M. Mesocrystals and nonclassical crystallization; John Wiley and Sons, 2008.

[107] Kellermeier, M.; Eiblmeier, J.; Melero-Garcia, E.; Pretzl, M.; Fery, A.; Kunz, W. Evolution and Control of Complex Curved Form in Simple Inorganic Precipitation Systems. Cryst. Growth Des. **2012**, 12, 3647–3655.

[108] Eiblmeier, J.; Kellermeier, M.; Deng, M.; Kienle, L.; Garcia Ruiz, J. M.; Kunz, W. Bottom-Up Self-Assembly of Amorphous Core-Shell-Shell Nanoparticles and Biomimetic Crystal Forms in Inorganic Silica-Carbonate Systems. Chem. Mater. **2013**, 25, 1842–1851.

[109] Hecht, M.; Kraus, W.; Rurack, K. A highly fluorescent pH sensing membrane for the alkaline pH range incorporating a BODIPY dye. The Analyst **2013**, 138, 325–332.

[110] Han, J.; Burgess, K. Fluorescent Indicators for Intracellular pH. Chemical Reviews **2010**, 110, 2709–2728.

[111] Eiblmeier, J.; Schuermann, U.; Kienle, L.; Gebauer, D.; Kunz, W.; Kellermeier, M. New insights into the early stages of silica-controlled barium carbonate crystallisation. Nanoscale **2014**, 6, 14939–14949.

[112] Kaplan, C. N.; Noorduin, W. L.; Li, L.; Sadza, R.; Folkertsma, L.; Aizenberg, J.; Mahadevan, L. Controlled growth and form of precipitating microsculptures. Science **2017**, 355, 1395–1399.

[113] Montalti, M.; Zhang, G.; Genovese, D.; Morales, J.; Kellermeier, M.; García-Ruiz, J. M. Local pH oscillations witness autocatalytic self-organization of biomorphic nanostructures. Nat. Commun **2017**, 8, 14427.

[114] Nakouzi, E.; Ghoussoub, Y. E.; Knoll, P.; Steinbock, O. Biomorph Oscillations Self-organize Micrometer-Scale Patterns and Nanorod Alignment Waves. J. Phys. Chem. C **2015**, 119, 15749–15754.

[115] Alexander, G. B.; Heston, W. M.; Iler, R. K. The solubility of amorphous silica in water. J. Phys. Chem. **1954**, 58, 453–455.

[116] Eiblmeier, J.; Dankesreiter, S.; Pfitzner, A.; Schmalz, G.; Kunz, W.; Kellermeier, M. Crystallization of Mixed Alkaline-Earth Carbonates in Silica Solutions at High pH. Cryst. Growth Des. **2014**, 14, 6177–6188.

[117] Nakouzi, E.; Knoll, P.; Steinbock, O. Biomorph growth in single-phase systems: expanding the structure spectrum and pH range. ChemComm **2016**, 52, 2107–10.

[118] Wang, H.; Pumera, M. Fabrication of Micro/Nanoscale Motors. Chem. Rev. **2015**, 115, 8704–8735.

[119] Opel, J.; Wimmer, F. P.; Kellermeier, M.; Cölfen, H. Functionalisation of silica–carbonate biomorphs. Nanoscale Horiz. **2016**, 1, 144–149.

[120] Busenberg, E.; Plummer, L. N. The solubility of BaCO 3 (cr)(witherite) in CO 2-H 2 O solutions between 0 and 90° C, evaluation of the association constants of BaHCO 3+(aq) and BaCO 3 0 (aq) between 5 and 80° C, and a preliminary evaluation of the thermodynamic properties of Ba 2+(aq). Geochim. Cosmochim. Acta **1986**, 50, 2225–2233.

[121] Weiss, R. F. Carbon dioxide in water and seawater: the solubility of a non-ideal gas. Mar. Chem. **1974**, 2, 203–215.

[122] Hurd, C. B.; Pomatti, R. C.; Spittle, J. H.; Alois, F. J. Studies on Silicic Acid Gels. XV. The Effect of Temperature upon the Time of Set of Alkaline Gel Mixtures. J. Am. Chem. Soc. **1944**, 66, 388–390.

[123] Krauskopf, K. B. Dissolution and precipitation of silica at low temperatures. Geochim. Cosmochim. Acta **1956**, 10, 1–26.

[124] Marshall, W. L.; Franck, E. U. Ion product of water substance, 0–1000 °C, 1–10,000 bars New International Formulation and its background. J. Phys. Chem. Ref. Data **1981**, 10, 295–304.

[125] Bittarello, E.; Massaro, F. R.; Rubbo, M.; Costa, E.; Aquilano, D. Witherite (BaCO3)/alpha-Quartz Epitaxial Nucleation and Growth: Experimental Findings and Theoretical Implications on Biomineralization. Cryst. Growth Des. **2009**, 9, 971–977.

[126] Hardy, W. B. A Preliminary Investigation of the Conditions which Determine the Stability of Irreversible Hydrosols. J. Phys. Chem. **1899**, 4, 235–253.

[127] Bergna, H. E. The Colloid Chemistry of Silica; Advances in Chemistry; American Chemical Society, 1994; Vol. 234; p 724.

[128] Zeebe, R. E.; Wolf-Gladrow, D. A. CO2 in seawater: equilibrium, kinetics, isotopes; Gulf Professional Publishing, 2001.

[129] Iler, R. K. The chemistry of silica: solubility, polimerization, colloid and surface properties, and biochemistry; Wiley Interscience, 1979.

[130] Nicole, L.; Rozes, L.; Sanchez, C. Integrative approaches to hybrid multifunctional materials: from multidisciplinary research to applied technologies. Adv. Mater. **2010**, 22, 3208–3214.

[131] Golander, C. G.; Kiss, E. QUANTITATIVE MEASUREMENTS OF AMINO SILYLATION ON PLASMA-ACTIVATED MICA SURFACE. Coll. Surf. A **1993**, 74, 217–222.

[132] Riggs, J. L.; Seiwald, R. J.; Burckhalter, J. H.; Downs, C. M.; Metcalf, T. G. ISOTHIOCYANATE COMPOUNDS AS FLUORESCENT LABELING AGENTS FOR IMMUNE SERUM. Am. J. Pathol. **1958**, 34, 1081–1097.

[133] Ellman, G. L. Tissue sulfhydryl groups. Arch. Biochem. Biophys. **1959**, 82, 70–77.

[134] Lee, J.; Park, J. C.; Song, H. A Nanoreactor Framework of a Au at SiO2 Yolk/Shell Structure for Catalytic Reduction of p Nitrophenol. Adv. Mater. **2008**, 20, 1523–1528.

[135] Xu, W.; Kong, J. S.; Yeh, Y.-T. E.; Chen, P. Single-molecule nanocatalysis reveals heterogeneous reaction pathways and catalytic dynamics. Nat. Mater. **2008**, 7, 992–996.

[136] Berman, A.; Ahn, D. J.; Lio, A.; Salmeron, M.; Reichert, A.; Charych, D. Total alignment of calcite at acidic polydiacetylene films: cooperativity at the organic-inorganic interface. Science **1995**, 269, 515–518.

[137] Dei, S.; Matsumoto, A.; Matsumoto, A. Thermochromism of polydiacetylenes in the solid state and in solution by the self-organization of polymer chains containing no polar group. Macromolecules **2008**, 41, 2467–2473.

[138] Pang, J. B.; Yang, L.; McCaughey, B. F.; Peng, H. S.; Ashbaugh, H. S.; Brinker, C. J.; Lu, Y. F. Thermochromatism and structural evolution of metastable polydiacetylenic crystals. J. Phys. Chem. B **2006**, 110, 7221–7225.

[139] Claude, C.; Garetz, B.; Okamoto, Y.; Tripathy, S. The preparation and characterization of organically modified silicates that exhibit nonlinear optical properties. Mater. Lett. **1992**, 14, 336–342.

[140] Kim, J.; Plawsky, J. L.; LaPeruta, R.; Korenowski, G. Second harmonic generation in organically modified sol-gel films. Chem. Mater. **1992**, 4, 249–252.

[141] Rabek, J. F. Photochemistry and photophysics; CRC Press, 1991; Vol. 4.

[142] George, J.; Thomas, K. G. Surface plasmon coupled circular dichroism of Au nanoparticles on peptide nanotubes. J. Am. Chem. Soc. **2010**, 132, 2502–2503.

[143] Hentschel, M.; Schaeferling, M.; Weiss, T.; Liu, N.; Giessen, H. Three-dimensional chiral plasmonic oligomers. Nano Lett. **2012**, 12, 2542–2547.

[144] Ahniyaz, A.; Sakamoto, Y.; Bergström, L. Magnetic field-induced assembly of oriented superlattices from maghemite nanocubes. PNAS **2007**, 104, 17570–17574.

[145] Giersig, M.; Hilgendorff, M. Magnetic nanoparticle superstructures. Eur. J. Inorg. Chem. **2005**, 18, 3571–3583.

[146] Gao, W.; Feng, X.; Pei, A.; Kane, C. R.; Tam, R.; Hennessy, C.; Wang, J. Bioinspired helical microswimmers based on vascular plants. Nano Lett. **2013**, 14, 305–310.

[147] Lizandara-Pueyo, C.; Dilger, S.; Wagner, M. R.; Gerigk, M.; Hoffmann, A.; Polarz, S. Li-doped ZnO nanorods with single-crystal quality–non-classical crystallization and self-assembly into mesoporous materials. CrystEngComm **2014**, 16, 1525–1531.

[148] Yin, J.; Lu, Q.; Yu, Z.; Wang, J.; Pang, H.; Gao, F. Hierarchical ZnO nanorod-assembled hollow superstructures for catalytic and photoluminescence applications. Cryst. Growth Des. **2009**, 10, 40–43.

[149] Nakouzi, E.; Steinbock, O. Self-organization in precipitation reactions far from the equilibrium. Science Adv. **2016**, 2.

[150] Opel, J.; Kellermeier, M.; Sickinger, A.; Morales, J.; Cölfen, H.; García-Ruiz, J.-M. Structural Transition of Inorganic Silica–Carbonate Composites Towards Curved Lifelike Morphologies. Minerals **2018**, 8, 75.

[151] Knoll, P.; Nakouzi, E.; Steinbock, O. Mesoscopic Reaction–Diffusion Fronts Control Biomorph Growth. J. Phys. Chem. C **2017**, 121, 26133–26138.

[152] Holtus, T.; Helmbrecht, L.; Hendrikse, H. C.; Baglai, I.; Meuret, S.; Adhyaksa, G. W. P.; Garnett, E. C.; Noorduin, W. L. Shape-preserving transformation of carbonate minerals into lead halide perovskite semiconductors based on ion exchange/insertion reactions. Nature Chem. **2018**,

[153] Palacci, J.; Sacanna, S.; Steinberg, A. P.; Pine, D. J.; Chaikin, P. M. Living Crystals of Light-Activated Colloidal Surfers. Science **2013**,

[154] Goesmann, H.; Feldmann, C. Nanoparticulate functional materials. Angew. Chem. Int. Ed. **2010**, 49, 1362–1395.

[155] Talapin, D. V.; Lee, J.-S.; Kovalenko, M. V.; Shevchenko, E. V. Prospects of colloidal nanocrystals for electronic and optoelectronic applications. Chem. Rev. **2009**, 110, 389–458.

[156] Park, J.; An, K.; Hwang, Y.; Park, J.-G.; Noh, H.-J.; Kim, J.-Y.; Park, J.-H.; Hwang, N.-M.; Hyeon, T. Ultra-large-scale syntheses of monodisperse nanocrystals. Nat. Mater. **2004**, 3, 891.

[157] Faure, B.; Wetterskog, E.; Gunnarsson, K.; Josten, E.; Hermann, R. P.; Brückel, T.; Andreasen, J. W.; Meneau, F.; Meyer, M.; Lyubartsev, A. 2D to 3D crossover of the magnetic properties in ordered arrays of iron oxide nanocrystals. Nanoscale **2013**, 5, 953–960.

[158] Brunner, J. J.; Krumova, M.; Cölfen, H.; Sturm, E. V. Magnetic field-assisted assembly of iron oxide mesocrystals: a matter of nanoparticle shape and magnetic anisotropy. Beilstein J. Nanotechnol. **2019**, 10, 894–900.

[159] Ge, J.; Hu, Y.; Biasini, M.; Beyermann, W. P.; Yin, Y. Superparamagnetic magnetite colloidal nanocrystal clusters. Angew. Chem. Int. Ed. **2007**, 46, 4342–4345.

[160] Nakouzi, E.; Rendina, R.; Palui, G.; Steinbock, O. Effect of inorganic additives on the growth of silica–carbonate biomorphs. J. Cryst. Growth **2016**, 452, 166–171.

[161] Opel, J.; Brunner, J.; Zimmermanns, R.; Steegmans, T.; Sturm, E.; Kellermeier, M.; Cölfen, H.; García-Ruiz, J.-M. Symbiosis of Silica Biomorphs and Magnetite Mesocrystals. Adv. Funct. Mater. **2019**, 29, 1902047.

[162] Kovalenko, M. V.; Bodnarchuk, M. I.; Lechner, R. T.; Hesser, G.; Schäffler, F.; Heiss, W. Fatty Acid Salts as Stabilizers in Size- and Shape-Controlled Nanocrystal Synthesis: The Case of Inverse Spinel Iron Oxide. J. Am. Chem. Soc. **2007**, 129, 6352–6353.

[163] Disch, S.; Wetterskog, E.; Hermann, R. P.; Salazar-Alvarez, G.; Busch, P.; Brückel, T.; Bergström, L.; Kamali, S. Shape Induced Symmetry in Self-

Assembled Mesocrystals of Iron Oxide Nanocubes. Nano Lett. **2011**, 11, 1651–1656.

[164] Sharifian, M. H.; Mahdavian, A. R.; Salehi-Mobarakeh, H. Effects of Chain Parameters on Kinetics of Photochromism in Acrylic–Spiropyran Copolymer Nanoparticles and Their Reversible Optical Data Storage. Langmuir **2017**, 33, 8023–8031.

[165] Kim, D.; Jeong, H.; Lee, H.; Hwang, W.-T.; Wolf, J.; Scheer, E.; Huhn, T.; Jeong, H.; Lee, T. Flexible Molecular-Scale Electronic Devices Composed of Diarylethene Photoswitching Molecules. Adv. Mater. **2014**, 26, 3968–3973.

[166] Heng, S.; Reineck, P.; Vidanapathirana, A. K.; Pullen, B. J.; Drumm, D. W.; Ritter, L. J.; Schwarz, N.; Bonder, C. S.; Psaltis, P. J.; Thompson, J. G.; Gibson, B. C.; Nicholls, S. J.; Abell, A. D. Rationally Designed Probe for Reversible Sensing of Zinc and Application in Cells. ACS Omega **2017**, 2, 6201–6210.

[167] Velema, W. A.; Szymanski, W.; Feringa, B. L. Photopharmacology: Beyond Proof of Principle. J. Am. Chem. Soc. **2014**, 136, 2178–2191.

[168] Szymanski, W.; Beierle, J. M.; Kistemaker, H. A. V.; Velema, W. A.; Feringa, B. L. Reversible Photocontrol of Biological Systems by the Incorporation of Molecular Photoswitches. Chem. Rev. **2013**, 113, 6114–6178.

[169] Borowiak, M.; Nahaboo, W.; Reynders, M.; Nekolla, K.; Jalinot, P.; Hasserodt, J.; Rehberg, M.; Delattre, M.; Zahler, S.; Vollmar, A.; Trauner, D.; Thorn-Seshold, O. Photoswitchable Inhibitors of Microtubule Dynamics Optically Control Mitosis and Cell Death. Cell **2015**, 162, 403–411.

[170] Klajn, R. Spiropyran-based dynamic materials. Chem. Soc. Rev. **2014**, 43, 148–184.

[171] Whelan, J.; Wojtyk, J. T. C.; Buncel, E. Enhanced Bistability of a Photochromic Microparticle in Condensed Medium. Chem. Mater. **2008**, 20, 3797–3799.

[172] Radu, A.; Byrne, R.; Alhashimy, N.; Fusaro, M.; Scarmagnani, S.; Diamond, D. Spiropyran-based reversible, light-modulated sensing with reduced photofatigue. J. Photochem. Photobiol. A **2009**, 206, 109–115.

[173] Zhu, M.-Q.; Zhang, G.-F.; Li, C.; Aldred, M. P.; Chang, E.; Drezek, R. A.; Li, A. D. Q. Reversible Two-Photon Photoswitching and Two-Photon Imaging of Immunofunctionalized Nanoparticles Targeted to Cancer Cells. J. Am. Chem. Soc. **2011**, 133, 365–372.

[174] Chan, Y.-H.; Gallina, M. E.; Zhang, X.; Wu, I. C.; Jin, Y.; Sun, W.; Chiu, D. T. Reversible Photoswitching of Spiropyran-Conjugated Semiconducting Polymer Dots. Anal. Chem. **2012**, 84, 9431–9438.

[175] Aznar, E.; Casasús, R.; García-Acosta, B.; Marcos, M. D.; Martínez-Máñez, R.; Sancenón, F.; Soto, J.; Amorós, P. Photochemical and Chemical Two-Channel Control of Functional Nanogated Hybrid Architectures. Adv. Mater. **2007**, 19, 2228–2231.

[176] Gorner, H. Photochromism of nitrospiropyrans: effects of structure, solvent and temperature. Phys. Chem. Chem. Phys. **2001**, 3, 416–423.

[177] Shao, N.; Jin, J. Y.; Cheung, S. M.; Yang, R. H.; Chan, W. H.; Mo, T. A Spiropyran-Based Ensemble for Visual Recognition and Quantification of Cysteine and Homocysteine at Physiological Levels. Angew. Chem. Int. Ed. **2006**, 45, 4944–4948.

[178] Fries, K. H.; Driskell, J. D.; Sheppard, G. R.; Locklin, J. Fabrication of Spiropyran-Containing Thin Film Sensors Used for the Simultaneous Identification of Multiple Metal Ions. Langmuir **2011**, 27, 12253–12260.

[179] Inouye, M.; Akamatsu, K.; Nakazumi, H. New Crown Spirobenzopyrans as Light- and Ion-Responsive Dual-Mode Signal Transducers. J. Am. Chem. Soc. **1997**, 119, 9160–9165.

[180] Suzuki, T.; Kato, T.; Shinozaki, H. Photo-reversible Pb2+-complexation of thermosensitive poly(N-isopropyl acrylamide-co-spiropyran acrylate) in water. ChemComm **2004**, 2036–2037.

[181] Wu, T.; Zou, G.; Hu, J.; Liu, S. Fabrication of Photoswitchable and Thermotunable Multicolor Fluorescent Hybrid Silica Nanoparticles Coated with Dye-Labeled Poly(N-isopropylacrylamide) Brushes. Chem. Mater. **2009**, 21, 3788–3798.

[182] Fries, K.; Samanta, S.; Orski, S.; Locklin, J. Reversible colorimetric ion sensors based on surface initiated polymerization of photochromic polymers. ChemComm **2008**, 6288–6290.

[183] Samanta, S.; Locklin, J. Formation of Photochromic Spiropyran Polymer Brushes via Surface-Initiated, Ring-Opening Metathesis Polymerization: Reversible Photocontrol of Wetting Behavior and Solvent Dependent Morphology Changes. Langmuir **2008**, 24, 9558–9565.

[184] Niazov, T.; Shlyahovsky, B.; Willner, I. Photoswitchable Electrocatalysis and Catalyzed Chemiluminescence Using Photoisomerizable Monolayer-Functionalized Surfaces and Pt Nanoparticles. J. Am. Chem. Soc. **2007**, 129, 6374–6375.

[185] Dingbin, L.; Wenwen, C.; Kang, S.; Ke, D.; Wei, Z.; Zhuo, W.; Xingyu, J. Resettable, Multi Readout Logic Gates Based on Controllably Reversible Aggregation of Gold Nanoparticles. Angew. Chem. Int. Ed. **2011**, 50, 4103–4107.

[186] Addadi, L.; Weiner, S. Kontroll und Designprinzipien bei der Biomineralisation. Angew. Chem. **1992**, 104, 159–176.

[187] Zhang, G.; Delgado-Lopez, J. M.; Choquesillo-Lazarte, D.; Garcia-Ruiz, J. M. Growth Behavior of Monohydrocalcite in Silica-Rich Alkaline Solution. Cryst. Growth Des. **2015**, 15, 564–572.

[188] Zhang, G.; Garcia-Ruiz, J. M.; Sanchez-Migallon, J. M. Growth behaviour of silica/carbonate nanocrystalline composites of calcite and aragonite. J. Mater. Chem. B **2017**,

[189] Zhang, G.; Verdugo-Escamilla, C.; Choquesillo-Lazarte, D.; Garcia-Ruiz, J. M. Thermal assisted self-organization of calcium carbonate. Nat. Commun **2018**, 9, 5221.

[190] Patlolla, A.; Zunino, J.; Frenkel, A. I.; Iqbal, Z. Thermochromism in polydiacetylene-metal oxide nanocomposites. J. Mater. Chem. **2012**, 22, 7028–7035.

[191] Göppert, A.; Cölfen, H. Infiltration of biomineral templates for nanostructured polypyrrole. Rsc. Adv. **2018**, 8, 33748–33752.

[192] Munekawa, Y.; Oaki, Y.; Imai, H. An Experimental Study on the Processes of Hierarchical Morphology Replication by Means of a Mesocrystal: A Case Study of Poly (3, 4-ethylenedioxythiophene). Langmuir **2014**, 30, 3236–3242.

[193] Oaki, Y.; Kijima, M.; Imai, H. Synthesis and morphogenesis of organic polymer materials with hierarchical structures in biominerals. J. Am. Chem. Soc. **2011**, 133, 8594–8599.

[194] Janata, J.; Josowicz, M. Conducting polymers in electronic chemical sensors. Nat. Mater. **2003**, 2, 19.

[195] Geetha, S.; Rao, C. R. K.; Vijayan, M.; Trivedi, D. C. Biosensing and drug delivery by polypyrrole. Anal. Chim. Acta **2006**, 568, 119–125.

[196] Unni, S. M.; Dhavale, V. M.; Pillai, V. K.; Kurungot, S. High Pt Utilization Electrodes for Polymer Electrolyte Membrane Fuel Cells by Dispersing Pt Particles Formed by a Preprecipitation Method on Carbon "Polished" with Polypyrrole. J. Phys. Chem. C **2010**, 114, 14654–14661.

[197] Olson, T. S.; Pylypenko, S.; Atanassov, P.; Asazawa, K.; Yamada, K.; Tanaka, H. Anion-Exchange Membrane Fuel Cells: Dual-Site Mechanism of Oxygen Reduction Reaction in Alkaline Media on Cobalt–Polypyrrole Electrocatalysts. J. Phys. Chem. C **2010**, 114, 5049–5059.

[198] Ge, H.; Wallace, G. G. High-performance liquid chromatography on polypyrrole-modified silica. J. Chromatogr. A **1991**, 588, 25–31.

[199] Choi, C.; Kim, J. H.; Sim, H. J.; Di, J.; Baughman, R. H.; Kim, S. J. Microscopically Buckled and Macroscopically Coiled Fibers for Ultra-Stretchable Supercapacitors. Adv. Energy Mater. **2017**, 7, 1602021.

[200] Siglreitmeier, M.; Wu, B.; Kollmann, T.; Neubauer, M.; Nagy, G.; Schwahn, D.; Pipich, V.; Faivre, D.; Zahn, D.; Fery, A. Multifunctional layered magnetic composites. Beilstein J. Nanotechnol. **2015**, 6, 134–148.

[201] Oaki, Y.; Imai, H. Nanoengineering in Echinoderms: The Emergence of Morphology from Nanobricks. Small **2006**, 2, 66–70.

[202] Opel, J.; Rosenbaum, L. C.; Brunner, J.; Staiger, A.; Zimmermanns, R.; Kellermeier, M.; Gaich, T.; Cölfen, H.; Garcia-Ruiz, J. M. Light-switchable anchors on magnetized biomorphic microcarriers. J. Mater. Chem. B **2020**, 8, 4831–4835.

[203] Opel, J.; Unglaube, N.; Wörner, M.; Kellermeier, M.; Cölfen, H.; García-Ruiz, J.-M. Hybrid Biomimetic Materials from Silica/Carbonate Biomorphs. Crystals **2019**, 9, 157.

[204] Verch, A.; Morrison, I. E. G.; Locht, R. v. d.; Kröger, R. In situ electron microscopy studies of calcium carbonate precipitation from aqueous solution with and without organic additives. J. Struct. Biol. **2013**, 183, 270–277.

[205] Grünewald, T. A.; Rennhofer, H.; Tack, P.; Garrevoet, J.; Wermeille, D.; Thompson, P.; Bras, W.; Vincze, L.; Lichtenegger, H. C. Photonenenergie als dritte Dimension bei der Analyse der kristallographischen Textur. Angew. Chem. **2016**, 128, 12376–12381.

[206] Nakouzi, E.; Fares, H. M.; Schlenoff, J. B.; Steinbock, O. Polyelectrolyte complex films influence the formation of polycrystalline micro-structures. Soft Matter **2018**, 14, 3164–3170.

[207] Wan, S.; Peng, J.; Jiang, L.; Cheng, Q. Bioinspired Graphene-Based Nanocomposites and Their Application in Flexible Energy Devices. Adv. Mater. **2016**, 28, 7862–7898.

[208] Hayase, G.; Kanamori, K.; Hasegawa, G.; Maeno, A.; Kaji, H.; Nakanishi, K. A Superamphiphobic Macroporous Silicone Monolith with Marshmallow-like Flexibility. Angew. Chem. Int. Ed. **2013**, 52, 10788–10791.

[209] Hayase, G.; Kanamori, K.; Fukuchi, M.; Kaji, H.; Nakanishi, K. Facile Synthesis of Marshmallow-like Macroporous Gels Usable under Harsh Conditions for the Separation of Oil and Water. Angew. Chem. Int. Ed. **2013**, 52, 1986–1989.

[210] Helmbrecht, L.; Tan, M.; Roehrich, R.; Bistervels, M. H.; Kessels, B. O.; Koenderink, A. F.; Kahr, B.; Noorduin, W. L. Directed Emission from Self Assembled Microhelices. Adv. Funct. Mater. **2019**, 30, 1908218.

[211] Nishio, T.; Naka, K. Photoinduced crystallization of calcium carbonate from

a homogeneous precursor solution in the presence of partially hydrolyzed poly(vinyl alcohol). J. Cryst. Growth **2015**, 416, 66–72.

[212] Shen, Z.; Röhr, H.; Rurack, K.; Uno, H.; Spieles, M.; Schulz, B.; Reck, G.; Ono, N. Boron–Diindomethene (BDI) dyes and their tetrahydrobicyclo precursors—en route to a new class of highly emissive fluorophores for the red spectral range. Chem. Eur. J. **2004**, 10, 4853–4871.

[213] Zhu, S.; Zhang, J.; Vegesna, G.; Luo, F.-T.; Green, S. A.; Liu, H. Highly water-soluble neutral BODIPY dyes with controllable fluorescence quantum yields. Org. Lett. **2010**, 13, 438–441.

[214] Jahnke, E.; Weiss, J.; Neuhaus, S.; Hoheisel, T. N.; Frauenrath, H. Synthesis of Diacetylene-Containing Peptide Building Blocks and Amphiphiles, Their Self-Assembly and Topochemical Polymerization in Organic Solvents. Chem. Eur. J. **2009**, 15, 388–404.

[215] Baumann, L.; Schöller, K.; de Courten, D.; Marti, D.; Frenz, M.; Wolf, M.; Rossi, R. M.; Scherer, L. J. Development of light-responsive porous polycarbonate membranes for controlled caffeine delivery. RSC Adv. **2013**, 3, 23317–23326.

[216] Liao, J.; Zhang, Y.; Yu, W.; Xu, L.; Ge, C.; Liu, J.; Gu, N. Linear aggregation of gold nanoparticles in ethanol. Colloids Surf. Physicochem. Eng. Aspects **2003**, 223, 177–183.

[217] Lin, S.; Li, M.; Dujardin, E.; Girard, C.; Mann, S. One-dimensional plasmon coupling by facile self-assembly of gold nanoparticles into branched chain networks. Adv. Mater. **2005**, 17, 2553–2559.

[218] Buzgar, N.; Apopei, A. I. The Raman study of certain carbonates. Geologie Tomul L **2009**, 2, 97–112.

[219] Cloots, R. Raman spectrum of carbonates M II CO 3. Spectrochim. Acta, Pt. A: Mol. Spectrosc. **1991**, 47, 1745–1750.

11 List of Figures

12 List of Tables

13 Publications

13.1 Records of Contribution

Publication 1:

Probing Local pH-Based Precipitation in Self-Assembled Silica-Carbonate Hybrid Materials
J. Opel, M. Hecht, K. Rurack, J. Eiblmeier, W. Kunz, H. Colfen and M. Kellermeier, *Nanoscale*, **2015**, *7*, 17434-17440.

Record of Contribution:

The study was designed by Julian Opel, Matthias Kellermeier, Josef Eiblmeier and Werner Kunz. I did all the experimental work except the synthesis and characterization of the fluorophores. The dyes were synthesized by Mandy Hecht and Knut Rurack. The manuscript was written by Matthias Kellermeier, Helmut Cölfen and me.

Acknowledgments:

The authors thank Teresa Höß (University of Regensburg) for performing parts of the experimental work, and the Bioimaging Center of the University of Konstanz for access to their instruments and advice concerning the analyses.

Publication 2:

Functionalisation of silica–carbonate biomorphs
J. Opel, F. P. Wimmer, M. Kellermeier and H. Cölfen, *Nanoscale Horiz.*, **2016**, *1*, 144-149.

Record of Contribution:

Julian Opel did all the experimental work and analytics measurements. Some spectroscopic measurements and synthesis procedures were reproduced by Florian Wimmer under the supervision of Julian Opel. The manuscript was written by Matthias Kellermeier, Helmut Cölfen and Julian Opel. JO, MK and HC designed the cover page.

Acknowledgments:

The authors thank Profs. Clément Sanchez and Werner Kunz for valuable discussions and suggestions for this work. In addition, we are grateful to Tjaard de Roo for providing the quantum dots, Tuan Anh Pham and Holger Reiner for the gold colloids, Shengtong Sun for help with the PCDA experiments, Mathias Altenburg for performing Raman microscopy, and the Bioimaging Center of the University of Konstanz for

access to their instruments.

Publication 3:

Structural Transition of Inorganic Silica–Carbonate Composites Towards Curved Lifelike Morphologies

J. Opel, M. Kellermeier, A. Sickinger, J. Morales, H. Cölfen and J.M. García-Ruiz, *Minerals*, **2018**, *8(2)*, 75.

Record of Contribution:

Julian Opel, Juan Morales and Matthias Kellermeier conceived and designed the experiments; the experiments and analytics were performed by Julian Opel, Annika Sickinger and Matthias Kellermeier; the results were discussed by Julian Opel, Juan Morales, Juan-Manuel Garcia-Ruiz, Helmut Cölfen and Matthias Kellermeier; Julian Opel wrote the paper under supervision of Juan-Manuel Garcia-Ruiz, Helmut Cölfen and Matthias Kellermeier. JO designed the cover page.

Acknowledgments:

The research leading to these results has received funding from the European Research Council under the European Union's Seventh Framework Programme (FP7/2007-2013) ERC grant agreement no. 340863.

Publication 4:

Hybrid Biomimetic Materials from Silica/Carbonate Biomorphs

J. Opel, N. Unglaube, M. Wörner, M. Kellermeier, H. Cölfen and J.M. García-Ruiz, *Crystals*, **2018**, *8(2)*, 75.

Record of Contribution:

Julian Opel, Matthias Kellermeier, Helmut Cölfen and Juanma García-Ruiz conceived and designed the experiments. The experiments where performed by Julian Opel, Niklas Unglaube (pPy part) and Melissa Wörner (pPCDA part). Analytical measurements where performed by Julian Opel, Niklas Unglaube and Melissa Wörner. Julian Opel wrote the paper under supervision of Juanma García-Ruiz , Helmut Cölfen and Matthias Kellermeier.

Acknowledgments:

The authors thank the European Research Council under the European Unions's sev-

enth Framework Program (FP7/2007-2013)/ERC grant agreement no. 340863. The authors thank the Particle Analysis Center of the University of Konstanz (SFB 1214), the Nanostructure Laboratory and the Bioimaging center of the University of Konstanz for access to their instruments and Andra-Lisa Hoyt for corrections.

Publication 5:

Symbiosis of Silica Biomorphs and Magnetite Mesocrystals

J. Opel, J. Brunner, R. Zimmermanns, T. Steegmans, E. Sturm, M. Kellermeier, H. Cölfen, and J.M. García-Ruiz *Adv. Funvt. Mater.*, **2019**, *29*, 1902047.

Record of Contribution:

Julian Opel and Julian Brunner are contributed equally to the work. Julian Opel, Julian Brunner and Ramon Zimmermanns performed the experiments. Julian Opel, Julian Brunner, Matthias Kellermeier, Helmut Cölfen and Juanma García-Ruiz conceived and designed the experiments. Analytical measurements where performed by Julian Opel, Julian Brunner, Ramon Zimmermanns and Tristan Steegmans. Elena Sturm and Tristan Steegmans supported the work with additional data for mesocrystals. Julian Opel, Julian Brunner and Matthias Kellermeier wrote the paper under supervision of Juanma García-Ruiz , Helmut Cölfen.

Acknowledgments:

The authors thank SFB 1214 (Deutsche Forschungsgemeinschaft) project B1, the Particle Analysis Center (PAC) of the University of Konstanz, the Nanostructure Laboratory of the University of Konstanz, and the European Research Council ERC (Grant Agreement No. 340863).

Publication 6:

Light-switchable anchors on magnetized biomorphic microcarriers

J. Opel, L.C. Rosenbaum, J. Brunner, A. Staiger, R. Zimmermanns, M. Kellermeier, T. Gaich, H. Cölfen, and J.M. García-Ruiz *J. Mater. Chem. B*, **2020**, *22*, 4831-4835.

Record of Contribution:

Julian Opel and Helmut Cölfen conceived the project. Lisa-Catherine Rosenbaum and Anne Staiger synthesized and analysed compound 7 under supervision of Tanja Gaich. Julian Opel, Julian Brunner and Ramon Zimmermanns designed the magne-

tized biomorphs. Julian Opel and Anne Staiger functionalized the biomorphs with compound 7. Julian Opel, Anne Staiger and Ramon Zimmermanns performed the microscope experiments. The results were discussed by all authors. The paper was writen by Julian Opel and Lisa-C. Rosenbaum. Julian Opel designed the cover page.

Acknowledgments:
The authors thank the bioimaging center Konstanz for providing the LSM700. The authors thank SFB 1214 (Deutsche Forschungsgemeinschaft) project B1, the Particle Analysis Center (PAC) of the University of Konstanz, the Nanostructure Laboratory of the University of Konstanz, and the European Research Council ERC (Grant Agreement No. 340863).

13.2 Orginal Documents

The publications in the appendix are listed chronological. Cover pages were published for publication 2, 3 and 6 are also shown in the following. The attached documents are presented in the corporate design of their individual journals.

Nanoscale

PAPER

View Article Online
View Journal | View Issue

Cite this: *Nanoscale*, 2015, **7**, 17434

Probing local pH-based precipitation processes in self-assembled silica-carbonate hybrid materials†

Julian Opel,[a] Mandy Hecht,[b] Knut Rurack,[b] Josef Eiblmeier,[c] Werner Kunz,[c] Helmut Cölfen*[a] and Matthias Kellermeier*[d]

Received 10th August 2015,
Accepted 8th September 2015

DOI: 10.1039/c5nr05399d

www.rsc.org/nanoscale

Crystallisation of barium carbonate in the presence of silica can lead to the spontaneous assembly of highly complex superstructures, consisting of uniform and largely co-oriented $BaCO_3$ nanocrystals that are interspersed by a matrix of amorphous silica. The formation of these biomimetic architectures (so-called silica biomorphs) is thought to be driven by a dynamic interplay between the components, in which subtle changes of conditions trigger ordered mineralisation at the nanoscale. In particular, it has been proposed that local pH gradients at growing fronts play a crucial role in the process of morphogenesis. In the present work, we have used a special pH-sensitive fluorescent dye to directly trace these presumed local fluctuations by means of confocal laser scanning microscopy. Our data demonstrate the existence of an active region near the growth front, where the pH is locally decreased with respect to the alkaline bulk solution on a length scale of few microns. This observation provides fundamental and, for the first time, direct experimental support for the current picture of the mechanism underlying the formation of these peculiar materials. On the other hand, the absence of any temporal oscillations in the local pH – another key feature of the envisaged mechanism – challenges the notion of autocatalytic phenomena in such systems and raises new questions about the actual role of silica as an additive in the crystallisation process.

Introduction

Silica biomorphs are a unique class of inorganic–inorganic hybrid materials, which form *via* bottom-up self-assembly of simple molecular species but nonetheless display remarkably complex shapes and structures,[1–6] comparable to solid composite frameworks generated by organisms during biomineralisation,[7] as well as artificial counterparts produced *in vitro* through state-of-the-art biomimetic crystal engineering and morphosynthesis.[8] Just by precipitating alkaline-earth carbonates in the presence of dissolved silica (usually by slow diffusion of carbon dioxide into silica-containing solutions of corresponding metal salts),[9–12] a broad variety of smoothly curved, non-crystallographic architectures can be obtained (Fig. 1). Characteristic morphologies range from flat sheets (Fig. 1a and b) over worm-like braids (Fig. 1c) to, most prominently, regular helicoids (Fig. 1d and e), but also include more elaborate 3D entities reminiscent of corals or flowers.[1,5,13–15] The formation of these unusual structures essentially occurs in a spontaneous manner as long as certain boundary conditions are met, in first place that the pH of the growth medium is sufficiently, but not too alkaline (typically between 9 and 11).[16–18] Under these circumstances, the components self-assemble into intricate superstructures that can otherwise only be achieved with the aid of relatively complex organic (macro)molecules or matrices, thus rendering silica biomorphs easy-to-handle model systems for investigating fundamental principles of self-organisation, in addition to their relevance in the context of primitive life detection.[9,19]

At the micrometre level, growth of $BaCO_3$ biomorphs was reported to proceed along a sequence of phenomenological stages.[1,3,4,12,18,20] First, an initially nucleated carbonate seed crystal experiences fractal branching[21] induced by the poisoning influence of oligomeric silicate species, and thus evolves from a pseudohexagonal rod into increasingly bifurcated forms that eventually show raspberry- or cauliflower-like morphologies (Fig. 1f). With time, these globular clusters develop laminar excrescences, which usually grow flat and in contact with the walls of the vessel or the solution–air interface

[a]*Physical Chemistry, University of Konstanz, Universitätsstrasse 10, D-78464 Konstanz, Germany. E-mail: helmut.coelfen@uni-konstanz.de; Fax: +49 7531 88 3139; Tel: +49 7531 88 4063*
[b]*Div. 1.9 Chemical and Optical Sensing, BAM Federal Institute for Materials Research and Testing, Richard-Willstätter-Strasse 11, D-12489 Berlin, Germany*
[c]*Institute of Physical and Theoretical Chemistry, University of Regensburg, Universitätsstrasse 31, D-93053 Regensburg, Germany*
[d]*Material Physics, BASF SE, GMC/O – B007, Carl-Bosch-Strasse 38, D-67056 Ludwigshafen, Germany. E-mail: matthias.kellermeier@basf.com; Fax: +49 621 66 43388; Tel: +49 621 60 43388*

†Electronic supplementary information (ESI) available: Experimental details (Section S1) and pH-dependent emission spectra of the used dyes (Fig. S1). See DOI: 10.1039/c5nr05399d

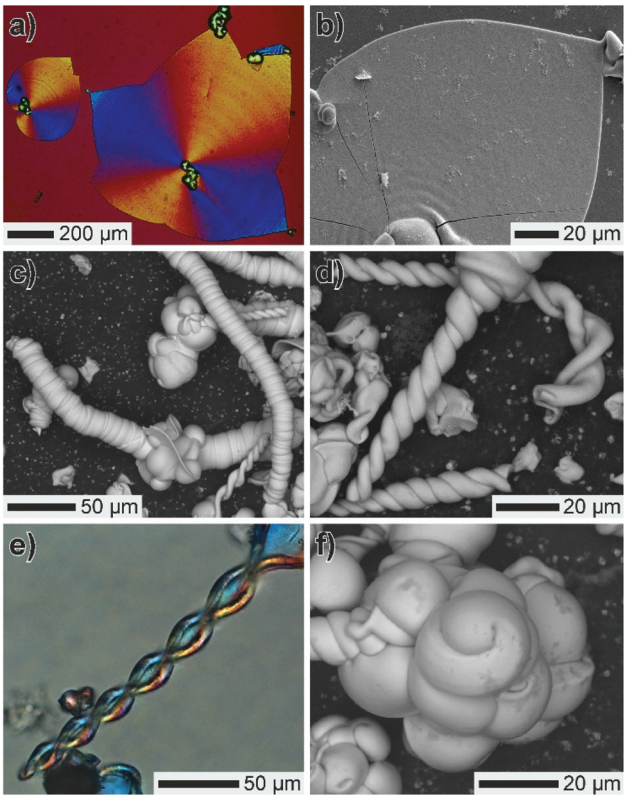

Fig. 1 Typical morphologies of silica biomorphs: (a, e) polarised optical and (b–d, f) SEM micrographs of (a, b) even sheets, (c) worm-like aggregates, (d, e) twisted filaments, and (f) globular precursor particles.

in the following. At some point, the sheets may curl and adopt scrolled margins, thus giving rise to the more complex curved ultrastructures (*i.e.* helicoids and worms),[3,4] likely governed by the role of extrinsic and intrinsic surfaces in the process of morphogenesis.[20]

At the nanoscale, silica biomorphs were found to consist of a multitude of fairly uniform rod-like carbonate crystallites, typically about 200–300 nm and ~50 nm wide,[1,9,12] each carrying a greater or lesser amount of associated silica[12,14] and being mutually arranged to establish some specific long-range orientational order.[1,13] The driving force underlying the formation and continuous supply of these nanosized building units was suggested to rely on a dynamic interplay of carbonate and silicate species at molecular scales, based on the inverse pH-dependent solubilities of the components.[1,3,4,17,18,22] The key point in the proposed model is that during crystallisation of any carbonate material in moderately alkaline solutions, the pH will be decreased at the surface of growing particles relative to the bulk due to dissociation of nearby bicarbonate ions,‡ *e.g.* according to $Ba^{2+} + HCO_3^- \rightarrow BaCO_3 + H^+$. This is thought to impact the speciation of silica by protonating charged silicate oligomers ($\equiv Si–O^- + H^+ \rightarrow \equiv Si–OH$), hence promoting condensation reactions ($\equiv Si–OH + HO–Si\equiv \rightarrow \equiv Si–O–Si\equiv + H_2O$) and ultimately leading to precipitation of silica around the carbonate particles. Continued silica polycondensation is in turn expected to re-increase the local pH (owing to the consumption of acidic Si–OH groups) and, with it, raise the supersaturation of carbonate, eventually triggering a novel event of nucleation and thus maintaining an autocatalytic cycle of alternating co-mineralisation.[23]

While the described mechanism is able to explain many experimental observations[1] and may be used to tailor or even program the morphological evolution in these systems,[5] it has remained an essentially theoretical framework to date. Indeed, the notion that growth processes occur only at local scales in the vicinity of active fronts has been confirmed indirectly by microscopy analyses of the growth behaviour in stirred solutions,[23] but still, concrete evidence supporting the proposed scenario is missing. Here we report, for the first time, experimental data that prove the envisaged local decrease in pH during the formation of silica biomorphs. For this purpose, we have used a newly developed pH-sensitive fluorescent dye with a suitable pH working range, to directly visualise subtle changes of alkaline pH in a spatially confined environment.

Analytical approach

In order to study local pH gradients during the formation of biomorphs, it is necessary to collect signals selectively from the growth front of single evolving crystal aggregates. Confocal laser scanning microscopy (CLSM) is a very promising technique in this context, due to its ability to deliver information from well-defined and highly limited depths of focus in the sample, thus avoiding superimposition of signal across the entire penetrated volume as in conventional optical microscopy. Sheets (Fig. 1a and b) are obviously the most suitable morphology for such analyses, because they grow in a quasi-two dimensional fashion along interfaces and hence, focusing on the bottom of the measurement cell should allow for facile monitoring of their development *in situ*. If, furthermore, a fluorescent dye is added to the mother liquor that responds to protons released (or consumed) during mineralisation by distinct changes in fluorescence intensity, such local variations of pH at the growth front should become directly visible. Fig. 2 illustrates the basic idea of the experiment.

The dye chosen in this work is a boron–dipyrromethene (BODIPY) derivative bearing an acidic phenol group (**1**, *cf.* inset in Fig. 3, R = F). With increasing pH, this dye shows a decrease in fluorescence intensity over a working range of *ca.* 9.0–11.5 in 1 : 1 ethanol/water mixtures, with an emission maximum at 532 nm and a pK_a of 9.98.[24] This process is reversible and was ascribed to fluorescence quenching *via* efficient electron transfer induced by the electron-rich phenolate moiety, which results in a complete switching off of the fluorescence at sufficiently high pH values. Since growth of biomorphs does hardly tolerate the presence of any organic

‡Note that the fraction of HCO_3^- ions existing in equilibrium with CO_3^{2-} is significant at conditions typical for the formation of biomorphs, ranging from *ca.* 20% at pH 11 to >90% at pH 9.[22]

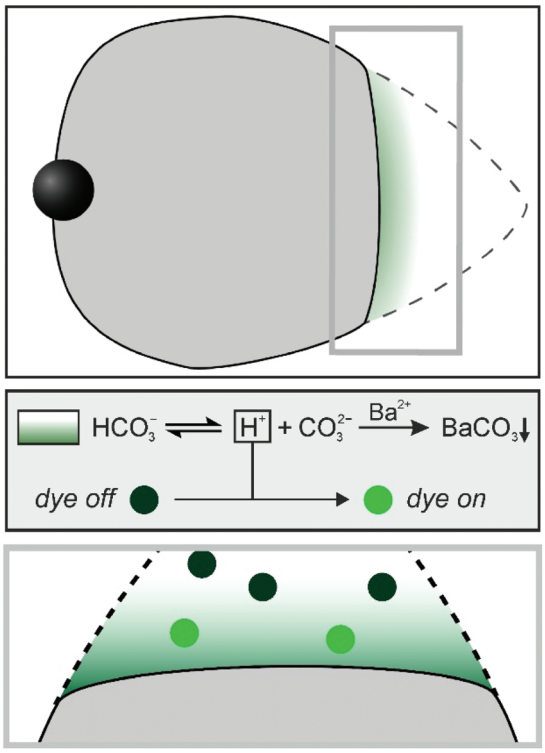

Fig. 2 Sketch of the experiment: a growing biomorph sheet (top panel) decreases the pH in the vicinity of its active front (corresponding gradient indicated in green), as bicarbonate ions will dissociate to restore the local HCO_3^-/CO_3^{2-} equilibrium during $BaCO_3$ precipitation (middle panel). A suitable pH-sensitive fluorescent dye (green circles) will respond to the locally increased proton concentrations by changing its emission behaviour, ideally switching on its fluorescence at a given excitation wavelength in regions where the pH falls below a certain threshold (bottom panel).

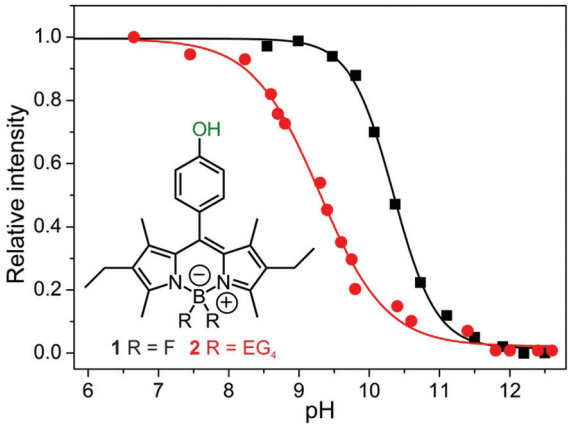

Fig. 3 Normalised intensity of fluorescence displayed by the dyes **1** (black) and **2** (red) at different pH levels. Values were derived from the maximum of the emission peak at 532 nm (see Fig. S1 in the ESI† for corresponding spectra). Data were recorded at a constant dye concentration of 1 μM. Inset: molecular structure of the BODIPY dyes, where the acidic and thus pH-sensitive phenol–OH group is highlighted in green.

(co-)solvent,[11] the first step in our study was to investigate the pH-dependence of the fluorescence of **1** in pure water, or rather in aqueous solutions containing barium ions and silicate oligomers at concentrations typical for biomorph syntheses (to check for potential interferences of these ions). A corresponding plot of the fluorescent intensity as a function of pH is given in Fig. 3 (black squares). It is evident that the dye still responds to changes in pH under these conditions, exhibiting a continuous decrease in relative intensity between pH 9.0 and 11.5. However, as can be expected for a change from H_2O/EtOH to a neat aqueous medium, a slightly higher pK_a of 10.34 is found for **1** in the biomorph growth solution. Nonetheless, the working range of the dye is in principle still suitable for probing the formation process of biomorphs, which usually occurs at bulk pH values of 10–11.[18]

Although it was possible to follow pH-dependent changes in the fluorescence of **1** in solution, we know from our earlier studies[24] that this dye is prone to aggregation in water (as is evident from the broadened absorption spectrum shown in Fig. S1 of the ESI†). Since this behaviour is not only concentration- but also environment-dependent (ionic strength, nature of electrolyte, *etc.*) and can potentially lead to adsorption/deposition of the dye on solid surfaces (like vessel walls or biomorphs), **1** is practically not suitable for performing a precise analysis of the growth process of biomorphs. Therefore, the molecular structure of the dye was modified, replacing the two fluorine substituents by tetramers of ethylene glycol (EG_4, see Section S2 in the ESI† for details on the synthesis), in order to obtain a water-soluble analogue without changing the optical properties (giving dye **2**, with a structure as shown in the inset of Fig. 3 with R = EG_4). Pegylation significantly reduced dye agglomeration (*cf.* Fig. S1†), again entailing straightforward spectroscopic BODIPY features while shifting the pK_a towards a lower value of 9.29. From the pH-dependent fluorescence intensities shown in Fig. 3 (red circles), it can be deduced that **2** will essentially be non-fluorescent in the bulk growth solution (pH > 10, deprotonation of the dye), while its fluorescence should be switched on in local regions where the pH decreases below 10 due to proton release according to the proposed mechanism.

Thus, **2** is a promising candidate that meets the dye requirements (such as high brightness and switching ratio, suitable pH working range, and good water solubility) for an experiment as depicted in Fig. 2. Therefore, it was used for all analyses described in the following.

Before turning to the results of these investigations, it is worth noting that previous efforts with conventional optical pH indicators failed, primarily because dyes covering the relevant pH regime normally contain anionic groups (like carboxylates or sulfonates)[25] that can strongly interact with Ba^{2+} ions in solution and form precipitates when added at concentrations typically required to give significant colouration and measurable effects (mM range). Here, the main advantage of **2** is its quasi-neutral character (the next-neighbour, formally zwitterionic group is not relevant in this sense) and high brightness, enabling its use at concentrations that are orders of magnitude lower (μM range).

Results and discussion

Fig. 4 shows laser scanning microscopy images representing the early stages of biomorph formation in the presence of the fluorescent dye **2**. Immediately before the appearance of a distinct structure, a faint turbidity is discernible in the transmission image (Fig. 4a), indicating the onset of mineralisation, while the fluorescence channel (Fig. 4c) does not display any noticeable features (*i.e.* **2** is in its OFF state and the pH is high). After some delay (20–30 s in this case), a raspberry-like particle is observed (Fig. 4b), which results from fractal branching of $BaCO_3$ crystals in silica-containing solutions (*cf.* Fig. 1f) and is known to be a typical precursor of the more complex biomorphic morphologies.[1,3,12,18] Interestingly, at this stage fluorescence can only be detected locally in the vicinity of the carbonate aggregate, as evidenced by Fig. 4d. These findings can be quantified by plotting the intensities of transmitted light and fluorescence as a function of time (Fig. 4e; the red squares in Fig. 4b and d mark the area from which signal was collected for the plot in Fig. 4e).

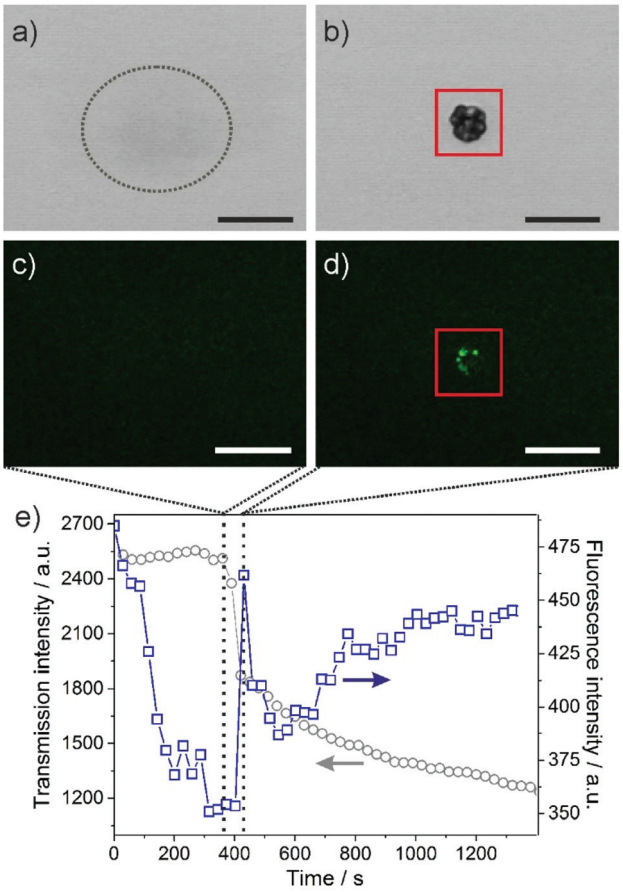

Fig. 4 Growth of a fractal barium carbonate aggregate in the presence of silica, as viewed by CLSM in (a–b) transmission and (c–d) fluorescence mode. The dashed ellipsoid in (a) highlights a slightly blurred region, in which the structure appears about 30 s later (b). (e) Plot of the transmission (grey circles) and fluorescence (blue squares) intensities measured in the area delimited by the red boxes shown in (b) and (d) over time before, during and after the formation of the carbonate structure. The vertical dashed lines mark the times corresponding to the images above. Scale bars in (a–d) are 20 μm.

As expected, the transmission signal is initially high and then decreases as the fractal structure nucleates and grows (which essentially occurs within a period of about 30 s). The fluorescence intensity, on the other hand, is generally rather low and decreases during the first 180 s prior to crystallisation. The reason for this behaviour is that the dye was added shortly after the experiment was started and deprotonation of **2** in the bulk alkaline growth medium occurs rather slowly. After this initial period of equilibration, there is a distinct peak in fluorescence that nearly coincides with the response in transmission and is well above background fluctuations (as is also clearly evident in the corresponding image, Fig. 4d). According to the pH-dependent fluorescence behaviour of **2** depicted in Fig. 3, this suggests that the pH around the globular particle is actually lower than in the surrounding bulk solution for a certain time, *i.e.* during the formation of the aggregate. These results indicate that precipitation of barium carbonate in alkaline media indeed leads to a local pH decrease at active surfaces, as envisaged in the current model for the formation mechanism of such materials.[1,3,4,17,18,22,23]

In order to confirm these observations and in particular to also show that this effect is a local phenomenon,[23] further CLSM analyses were performed at higher magnification, mainly following the growth of flat sheets (for reasons outlined above). Fig. 5 shows one such structure at two distinct stages of evolution in the presence of **2**.

The coloured vertical lines mark different positions relative to the growth front (that in this example moves from right to left), at which the fluorescence intensity was continuously monitored. Time-dependent traces resulting from these measurements (graph in Fig. 5) again display a maximum in fluorescence; however, now the signal does not come from the entire structure, but only from a confined area (here about 3 μm wide) at the respective indicated spot. With growing distance from the initial position of the sheet edge, the maximum in fluorescence intensity continuously shifts to later times. Obviously, the fluorescence starts to increase when the growth front approaches the monitored position (at around 150–200 s in Fig. 5) and reaches the highest recorded value just before the sheet edge passes. Subsequently, a relatively sharp decrease in fluorescence intensity is observed. This suggests strongly that there is a zone close to the growth front in which the pH is locally reduced and gradually increases from the rim of the evolving aggregate towards the more alkaline bulk solution – well in line with the situation drawn schematically in Fig. 2. We note that there is a continuous drift of the fluorescence towards higher values after (and partly also before) the maxima in Fig. 5 (as well as in Fig. 4e). This can most likely be ascribed to the gradual lowering of the bulk pH upon continued uptake of atmospheric CO_2 into the growth solution, as described in detail elsewhere.[12] Another factor that might play a role here is dye deposition and/or agglomeration on the forming biomorph structure, although we expect

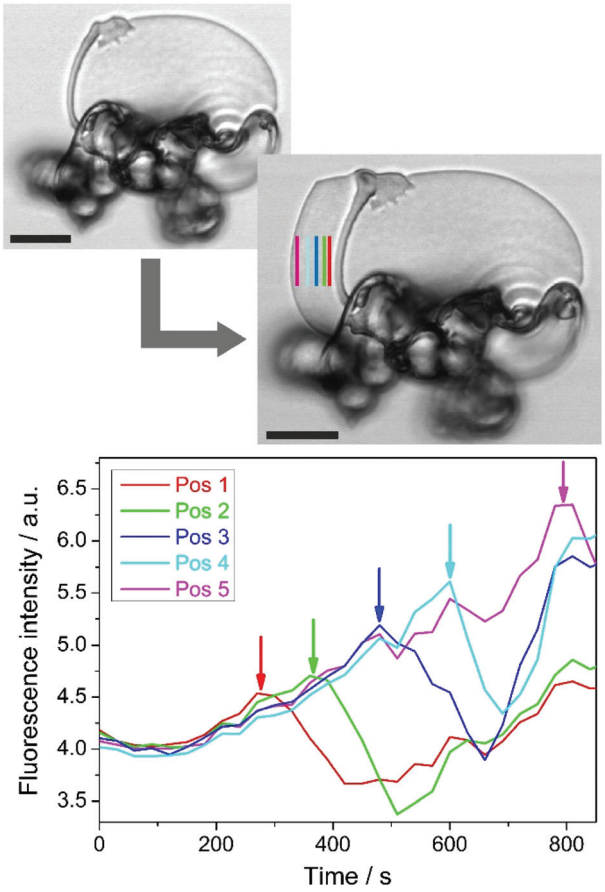

Fig. 5 *In situ* monitoring of pH changes during the formation of silica biomorphs in solution. Top: confocal micrographs of a flat sheet at the beginning and at the end of the observed period (time lapse: 15 min). Bottom: Plots of the fluorescence intensity as a function of time, measured at different positions relative to the edge of the sheet in the first image (indicated by vertical lines with the same colour code). Scale bars are 10 μm.

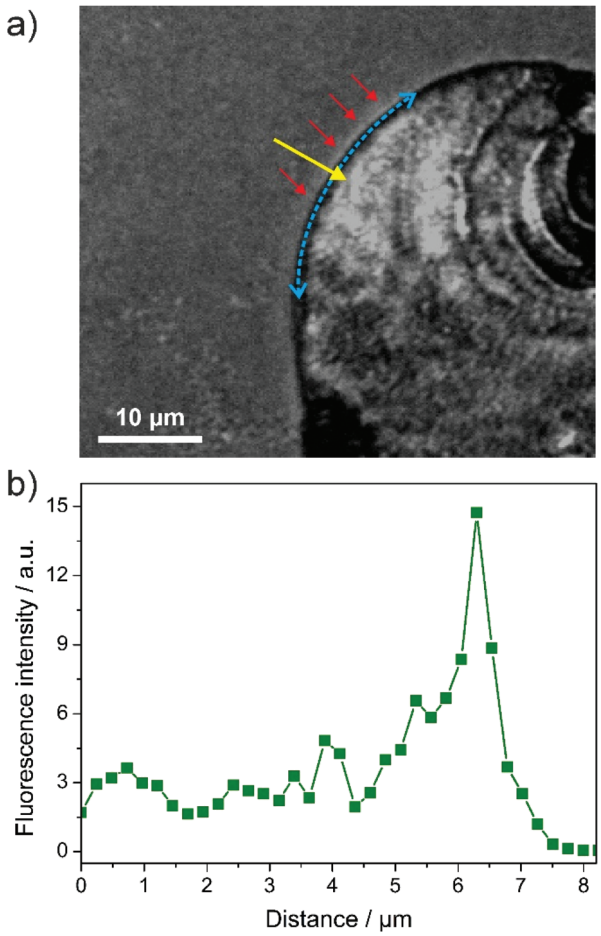

Fig. 6 Local pH gradients in silica biomorphs. (a) Fluorescence image of the edge of a sheet growing from right to left. The blue and yellow arrows visualise how line scans of fluorescence intensity were performed along the normal to the surface at different azimuthal angles, while the red arrows point to a zone of slightly higher brightness near the rim of the structure. Note that the image has been converted to greyscale in order to better illustrate the higher brightness at the rim of the structure. (b) Resulting intensity–distance profile, clearly evidencing the local decrease in pH near the growing front.

this effect to be fairly limited due to the enhanced solubility of **2** compared to **1**. In any case, the occurrence of a maximum in fluorescence intensity well above the aforementioned drift is clearly resolved by the data in Fig. 5.

Fig. 6 shows another example of a sheet growing in alkaline silica solution containing dye **2**. Here, the local pH decrease can already be discerned in the fluorescence image (Fig. 6a) as a layer of slightly higher brightness in front of the rim of the aggregate (highlighted by the red arrows). To confirm this observation, we have performed fluorescence line scans along the normal to the surface from the solution towards and over the edge of the sheet (as shown by the yellow arrow in Fig. 6a). Integration over different azimuthal angles, as illustrated by the dashed blue arrow in Fig. 6a, led to the intensity–distance profile displayed in Fig. 6b. This data unambiguously demonstrates the existence of a pH gradient at the active front of growing biomorphs, most likely originating from the dissociation of bicarbonate ions during the formation of $BaCO_3$ (as described above). From the results shown in Fig. 6, the thickness of this region can be estimated to *ca.* 2 μm (at the given level of sensitivity), which is in good agreement with indirect predictions made on the basis of simple fluid dynamics considerations in experiments at different stirring rates.[23]

It is worth noting that we could not detect any hint for a cycling of the local pH in our assays, which one would expect if carbonate and silica were mineralised in an alternating fashion according to the idea of coupled co-precipitation.[1,3,23] Although absolute pH measurements are not possible in a CLSM experiment with an ON/OFF dye such as **2**, the intensity profiles strongly suggest that the pH at the front is continually lower than in the bulk. Indeed, the lack of any oscillating behaviour may be due to limited temporal resolution in the current setup. Nevertheless, our data indicates that carbonate crystallisation dominates the local pH and that there is little

influence of silica in this context (*i.e.* co-condensation of silica does not lead to a measurable temporary increase of pH at the front) – at least under the conditions investigated in the present work. This conclusion is supported by the fact that the amount of silica co-precipitated with the carbonate phase during the growth process is relatively low, with Si/Ba atomic ratios in the core of biomorphs typically ranging from 0.05 to 0.10.[12]

Constant reduction of the pH at the growth front would imply that the supersaturation of silica is locally enhanced at all times (thus facilitating its incorporation into the forming aggregate), whereas the driving force for carbonate precipitation would in this case always be somewhat suppressed at the active surface as compared to the bulk. In our opinion, this is a plausible scenario as it was shown that the bulk mother solution of biomorphs is sufficiently supersaturated throughout the entire growth process[18] and hence $BaCO_3$ crystallisation does actually not need a local increase in supersaturation, while this is not necessarily true for silica. On the other hand, the high nucleation density observed in these materials (as manifested in the myriads of nanocrystals constituting the structures) could then no longer be explained on the basis of a locally increased driving force for precipitation.[1,23] Most probably, this behaviour is caused by the presence of silica, which may act as an efficient inhibitor for carbonate growth (thus restricting the size of the crystallites to the nanoscale)[26] and/or accelerate nucleation by lowering interfacial energies through epitaxial matching.[27]

Conclusions and outlook

In this work, we have developed a water-soluble fluorescent dye with pH sensitivity in the alkaline regime, in order to probe local changes in conditions during the formation of biomimetic silica-carbonate hybrid structures. Our results reveal the existence of a spatially confined region close to the front of growing aggregates, in which the pH is significantly reduced as compared to the bulk medium, thus lending direct experimental support to the postulated formation mechanism. This local pH gradient was found to extend over lengths of few microns into the solution and persisted over time periods of several minutes, while no oscillative behaviour could be detected. This finding challenges the notion of autocatalytic processes in these systems and stresses the role of silica as a growth-inhibiting additive. Although the present approach does not allow the quantification of local pH at every point in time, it nevertheless highlights the potential of fluorescent dyes to directly trace local precipitation phenomena in self-assembled silica-carbonate materials. Future work will be focused on the design of yet more suitable probes possessing two distinctly fluorescent species in their protonated and deprotonated form, the study of different experimental conditions in terms of pH and species concentrations, as well as on translating measured fluorescence intensities into actual local pH values.

Acknowledgements

The authors thank Teresa Höß (University of Regensburg) for performing parts of the experimental work, and the Bioimaging Center of the University of Konstanz for access to their instruments and advice concerning the analyses.

Notes and references

1 M. Kellermeier, H. Cölfen and J. M. Garcia-Ruiz, *Eur. J. Inorg. Chem.*, 2012, **32**, 5123.
2 J. M. Garcia-Ruiz and J. L. Amoros, *J. Cryst. Growth*, 1981, **55**, 379; J. M. Garcia-Ruiz, *J. Cryst. Growth*, 1985, **73**, 251.
3 J. M. Garcia-Ruiz, E. Melero-Garcia and S. T. Hyde, *Science*, 2009, **323**, 362.
4 W. Kunz and M. Kellermeier, *Science*, 2009, **323**, 344.
5 W. L. Noorduin, A. Grinthal, L. Mahadevan and J. Aizenberg, *Science*, 2013, **340**, 832.
6 M. Kellermeier, F. Glaab, E. Melero-Garcia and J. M. Garcia-Ruiz, Experimental Techniques for the Growth and Characterization of Silica Biomorphs and Silica Gardens, in *Research Methods in Biomineralization Science*, Academic Press, Burlington, 2013, vol. 532, pp. 225–256.
7 S. Mann, *Biomineralization: Principles and Concepts in Bioinorganic Materials Chemistry*, Oxford University Press, Oxford, 2001; P. Behrens and E. Bäuerlein, *Handbook of Biomineralization*, Wiley-VCH, Weinheim, 2009; S. Weiner and L. Addadi, *Annu. Rev. Mater. Res.*, 2011, **41**, 21.
8 F. C. Meldrum and H. Cölfen, *Chem. Rev.*, 2008, **108**, 4332; H. Cölfen and M. Antonietti, *Mesocrystals and Non-Classical Crystallization*, Wiley, Chichester, 2008; F. Nudelman and N. A. J. M. Sommerdijk, *Angew. Chem., Int. Ed.*, 2012, **51**, 6582.
9 J. M. Garcia-Ruiz, S. T. Hyde, A. M. Carnerup, A. G. Christy, M. J. Van Kranendonk and N. J. Welham, *Science*, 2003, **302**, 1194.
10 E. Bittarello and D. Aquilano, *Eur. J. Mineral.*, 2007, **19**, 345.
11 A. E. Voinescu, M. Kellermeier, A. M. Carnerup, A. K. Larsson, D. Touraud, S. T. Hyde and W. Kunz, *J. Cryst. Growth*, 2007, **306**, 152.
12 M. Kellermeier, E. Melero-Garcia, F. Glaab, J. Eiblmeier, L. Kienle, R. Rachel, W. Kunz and J. M. Garcia-Ruiz, *Chem. – Eur. J.*, 2012, **18**, 2272.
13 S. T. Hyde, A. M. Carnerup, A. K. Larsson, A. G. Christy and J. M. Garcia-Ruiz, *Phys. A*, 2004, **339**, 24.
14 H. Imai, T. Terada, T. Miura and S. Yamabi, *J. Cryst. Growth*, 2002, **244**, 200; A. E. Voinescu, M. Kellermeier, B. Bartel, A. M. Carnerup, A. K. Larsson, D. Touraud, W. Kunz, L. Kienle, A. Pfitzner and S. T. Hyde, *Cryst. Growth Des.*, 2008, **8**, 1515.
15 T. Terada, S. Yamabi and H. Imai, *J. Cryst. Growth*, 2003, **253**, 435; M. Kellermeier, F. Glaab, A. M. Carnerup, M. Drechsler, B. Gossler, S. T. Hyde and W. Kunz, *J. Cryst. Growth*, 2009, **311**, 2530.

16 J. M. Garcia-Ruiz, *Geology*, 1998, **26**, 843.
17 E. Melero-Garcia, R. Santisteban-Bailon and J. M. Garcia-Ruiz, *Cryst. Growth Des.*, 2009, **9**, 4730.
18 J. Eiblmeier, M. Kellermeier, D. Rengstl, J. M. Garcia-Ruiz and W. Kunz, *CrystEngComm*, 2013, **15**, 43.
19 J. M. Garcia-Ruiz, A. M. Carnerup, A. G. Christy, N. J. Welham and S. T. Hyde, *Astrobiology*, 2002, **2**, 353.
20 M. Kellermeier, J. Eiblmeier, E. Melero-Garcia, M. Pretzl, A. Fery and W. Kunz, *Cryst. Growth Des.*, 2012, **12**, 3647.
21 H. D. Keith and F. Padden, *J. Appl. Phys.*, 1963, **34**, 2409.
22 M. Kellermeier, E. Melero-Garcia, F. Glaab, R. Klein, M. Drechsler, R. Rachel, J. M. Garcia-Ruiz and W. Kunz, *J. Am. Chem. Soc.*, 2010, **132**, 17859; J. Eiblmeier, M. Kellermeier, M. Deng, L. Kienle, J. M. Garcia-Ruiz and W. Kunz, *Chem. Mater.*, 2013, **25**, 1842.
23 M. Kellermeier, E. Melero-Garcia, W. Kunz and J. M. Garcia-Ruiz, *J. Colloid Interface Sci.*, 2012, **380**, 1.
24 M. Hecht, W. Kraus and K. Rurack, *Analyst*, 2013, **138**, 325.
25 J. Han and K. Burgess, *Chem. Rev.*, 2009, **110**, 2709.
26 J. Eiblmeier, U. Schürmann, L. Kienle, D. Gebauer, W. Kunz and M. Kellermeier, *Nanoscale*, 2014, **6**, 14939.
27 E. Bittarello, F. R. Massaro and D. Aquilano, *J. Cryst. Growth*, 2010, **312**, 402; E. Bittarello, F. R. Massaro, M. Rubbo, E. Costa and D. Aquilano, *Cryst. Growth Des.*, 2009, **9**, 971.

Electronic Supplementary Material (ESI)

for

Probing local pH-based co-precipitation processes in self-assembled silica-carbonate hybrid materials

Julian Opel, Mandy Hecht, Knut Rurack, Josef Eiblmeier, Werner Kunz, Helmut Cölfen and Matthias Kellermeier

S1. Materials and Methods.

Barium chloride dihydrate (min. 99%) was purchased from Riedel-de Haën and used as received. The silica source was a commercial sodium silicate solution (so-called water glass) containing about 12.5 wt% SiO_2 and 13.8 wt% Na, as supplied by Sigma-Aldrich (reagent grade). All solvents employed for the spectroscopic measurements were of UV spectroscopic grade (Aldrich). Stock solutions (0.1 and 1 M) of hydrochloric acid, hypochlorite acid, potassium hydroxide and sodium hydroxide, required for pH adjustments, were obtained from Merck (p.a. grade). All solutions and dilutions were prepared with water of MilliQ quality, sourced from a Milli-Q Synthesis A10 system equipped with a Quantum EX Ultrapure Organex cartridge (Millipore). All air- and moisture-sensitive reactions were carried out under argon atmosphere in oven-dried glassware.

Thin layer chromatography (TLC) was performed on Merck Silica Gel 60 F254 TLC plates with a fluorescent indicator for 254 nm excitation. Compounds were visualised under UV light at 254 nm. Column chromatography was carried out with Merck Silica Gel 60 (0.040-0.063 mm) using the specified eluents. Nuclear magnetic resonance (NMR) spectra were recorded on Bruker AV 400 and Bruker AVANCE III 500 MHz spectrometers at 27°C, using residual protonated solvent signals as internal standard (^{1}H: $\delta[CDCl_3]$ = 7.26 ppm and ^{13}C: $\delta[CDCl_3]$ = 77.16 ppm). Assignments are based on chemical shifts and/or DEPT spectra (where Ar is used as abbreviation to indicate aromatic moieties). High-resolution mass spectrometry (HR-MS) was performed with a Thermo Scientific Exactive Orbitrap in the positive ion mode using the Thermo Xcalibur operating and data acquisition software, or on a Waters LCT Premier XE instrument. Ultrahigh-performance liquid chromatography mass spectrometry (UPLC-MS) was performed with a Waters Acquity UPLC equipped with a Waters LCT Premier XE mass detector for high-resolution MS (ESI ionisation), and with Waters Alliance systems (consisting of a Waters Separations Module 2695, a Waters Diode Array Detector 996 and a Waters Mass Detector ZQ 2000) equipped with an Acquity BEH C18 (2.1x50 mm) column.

UV/Vis absorption spectra were recorded on an Analytik Jena Specord 210 Plus spectrophotometer. Steady-state fluorescence measurements were carried out on Horiba Jobin-Yvon FluoroMax-4P and Spectronics Instrument 8100 spectrofluorometers, using standard 10 mm path length quartz cuvettes or PMMA cells. Fluorescence lifetimes were determined with a unique customised laser impulse fluorometer with picosecond time resolution, as described elsewhere.[S1,S2] The fluorescence lifetime profiles were analysed using the Horiba Scientific software package DAS 6.

pH values were monitored with a digital pH meter (pH lab 827, Metrohm) equipped with a glass electrode (Biotrode). For comparison, pH measurements were also performed with a second digital pH meter (WTW pH 537), equipped with a different glass electrode (InLab 423, Mettler-Toledo). Calibration of the instruments was performed with standard aqueous buffer solutions of pH 4.00, 7.00

and 9.00 from Metrohm. The measurement uncertainties of the pH electrodes are estimated to ≤ 0.03 pH units.

Polarised optical microscopy (POM) studies were carried out on a Zeiss Imager.M2m microscope equipped with EC Epiplan-Neofluar 5x/10x/20x and LD Epiplan 50x objectives, a lambda plate, and a Zeiss AxioCam MRc 5 CCD camera for imaging. For scanning electron microscopy (SEM), specimens were mounted on aluminium stubs by means of double-sided adhesive tape and subsequently investigated on a Hitachi TM3000 tabletop microscope at acceleration voltages ranging from 3 to 10 kV (without previous sputtering). Confocal laser scanning microscopy (CLSM) was performed using a Zeiss LSM 510 Meta laser scanning microscope and a Zeiss Axiovert 200M inverted microscope, equipped with Plan-Neofluar 10x/0.3 and Plan-Neofluar 20x/0.5 objectives and PMT detectors for the transmission and fluorescence channels. All studies were carried out utilising an Argon laser with a wavelength of 488 nm at a laser power of 15% to excite dye **2**. For confocal observation, the pinhole was set to 1 au (area unit).

S2. Synthesis and Characterisation of BODIPY Dyes.

8-(4-hydroxyphenyl)-1,3,5,7-tetramethyl-2,6-diethyl-4,4-bis(3,6,9,12-tetraoxaheptadec-16-ynyl)-4-bora-3a,4a-diaza-s-indacene (dye **2**): The synthesis of **2** was carried out according to a procedure adopted from ref.[S3] To a solution of 2.10 g 2,5,8,11,14-pentaoxaheptadec-16-yne (8.0 mmol, 10.0 eq., synthesised as described elsewhere[S4]) in 20 mL anhydrous tetrahydrofuran (THF), 9.50 mL ethylmagnesium bromide (9.5 mmol, 1.0 M solution in THF, 12.0 eq.) was added. The reaction was heated at 60°C overnight. After cooling down to room temperature, a solution of 317.0 mg **1** (0.8 mmol, 1.0 eq., synthesised as described elsewhere[S5]) in 15 mL anhydrous THF was added. The resulting mixture was stirred at 60°C for additional 5 h to achieve complete consumption of the starting material. Subsequently, the solution was concentrated under reduced pressure to remove parts of the THF. Then 100 mL dichloromethane (CH_2Cl_2) was added and the organic phase was washed with 100 mL brine. After extraction of the aqueous phase for three times with CH_2Cl_2, the combined organic solutions were dried over Na_2SO_4 and concentrated under reduced pressure. The crude product was purified by column chromatography on silica using ethyl acetate/methanol as eluent to give compound **2** as purple-brown oil (0.407 g, 60%).

Analytical data:

HR-MS (ESI+): m/z calculated for $C_{47}H_{69}BN_2O_{11}Na$ $[M+Na]^+$: 870.4923, found 870.4908.

^{1}H-NMR (400MHz, $CDCl_3$) [ppm]: δ = 0.97 (t, 6H, *J* = 7.5 Hz, 2 × CH_2-C$\underline{H}_3$), 1.32 (s, 6H, 2 × C-C$\underline{H}_3$), 2.30 (q, 4H, *J* =7.5 Hz, 2 × C$\underline{H}_2$-CH_3), 2.67 (s, 6H, 2 × N-C-C$\underline{H}_3$), 3.37 (s, 6H, 2 × C$\underline{H}_3$), 3.54 (m, 4H, 2 × C$\underline{H}_2$), 3.64 (m, 28H, 2 × C$\underline{H}_2$), 4.18 (d, *J* = 2.4 Hz, 4H, 2 × C$\underline{H}_2$-C), 6.92 (d, 2H, *J* = 8.6, 2 × C$\underline{H}_{ar}$), 7.06 (d, 2H, *J* = 8.6, 2 × C$\underline{H}_{ar}$).

Absorption and emission spectra of dyes **1** and **2** in aqueous solution are shown in Fig. S1, while Figs. S2 and S3 summarise the pH dependence of the absorption and emission behaviour of **1** and **2**, respectively, for a change from near-neutral to alkaline conditions. Table S1 compiles the relevant spectroscopic data, including the fluorescence lifetime (τ_f).

The protonation constant of **2** was determined to be $pK_A = 9.31 \pm 0.01$ in water by Boltzmann curve-fitting as a function of pH using the fluorescence intensity at 527 nm (cf. Fig. S3). Although the pK_A shifts by ca. 0.5 units compared to **1**, the modification with two amphiphilic PEG moieties increases the solubility in water significantly while retaining the spectroscopic properties of the parent dye **1**.

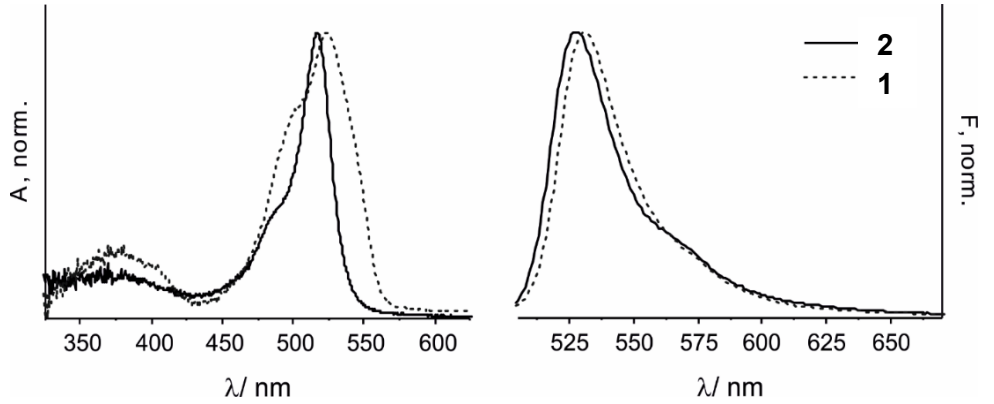

Figure S1. Normalized absorption (left) and emission spectra (right) of dyes **1** and **2** in water.

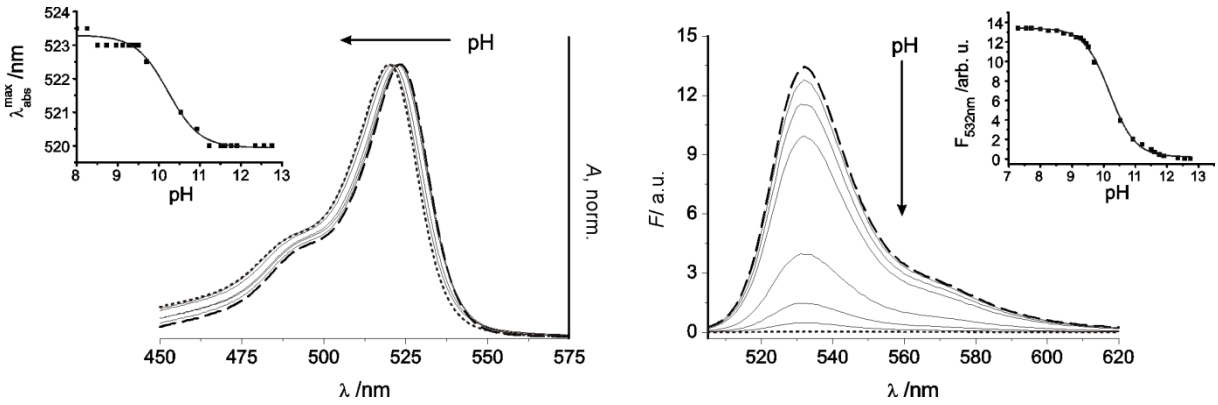

Figure S2. Dependence of the absorption and fluorescence of dye **1** on a change in pH from 7.3 to 12.8 upon addition of aqueous KOH solutions (λ_{ex} = 495 nm, $c_1 = 1.39 \cdot 10^{-6}$ M, EtOH/H_2O); pH 7.3 (dashed line), pH 12.8 (dotted line); selected intermediate steps (solid lines). Insets: corresponding titration curves, given by the shift of the absorption maximum (left) and the fluorescence intensity at the emission maximum (right) as a function of pH.

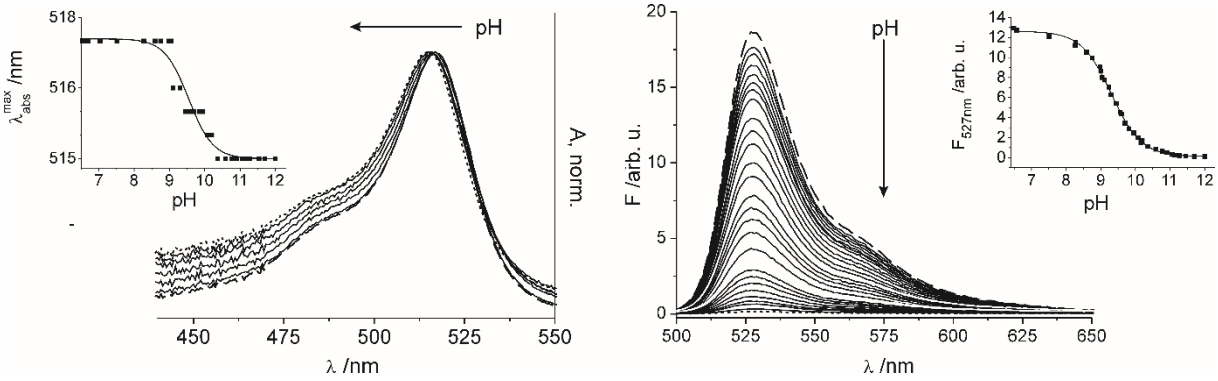

Figure S3. Dependence of the absorption and fluorescence of dye **2** on a change in pH from 6.5 to 12.0 in neat water (λ_{ex} = 495 nm, $c_2 = 1.39 \cdot 10^{-6}$ M, H_2O); pH 6.5 (dashed line), pH 12.0 (dotted line), intermediate steps (solid lines). Insets: corresponding titration curves, given by the shift of the absorption maximum (left) and the fluorescence intensity at the emission maximum (right) as a function of pH.

Table S1. Spectroscopic data of dyes **1** and **2** in selected solvents at 298 K.

Compound	Solvent	λ_{abs} / nm	λ_{em} / nm	τ_f / ns
2	MeCN	517	526	n.d.
	H_2O/EtOH	518	527	4.72
	H_2O	517	527	3.42
1	MeCN	521	531	4.72
	H_2O/EtOH	523	532	5.57
	H_2O	523	532	2.67[a]

[a] Longest lifetime component of a multiexponential fit.

S3. Growth and Characterisation of Biomorphs.

Silica biomorphs were grown from aqueous solutions containing 5.0 mM $BaCl_2$, 8.4 mM SiO_2, and 8.9 mM Na^+, prepared as described in detail elsewhere.[S6] Portions of this mixture (typically 10 mL) were filled into cylindrical wells of standard polystyrene plates (VWR Nunclon 6-well plates, volume: 17 mL, area: 9.6 cm^2, depth: 1.7 cm). Subsequently, glass coverslips (15x15 mm) were placed on the bottom of the wells as substrates for growth, and the well plate was covered loosely with a lid. Crystallisation of barium carbonate occurred upon gradual in-diffusion of CO_2 from the atmosphere into the alkaline solution (starting pH: 11.0), where it was converted to HCO_3^- and finally CO_3^{2-} ions needed for precipitation. In this way, complex structures are formed spontaneously on interfaces over periods of several hours. Their isolation is quite straightforward, as the glass substrates can simply be removed from the mother liquor with a pair of tweezers and only need to be rinsed with water and ethanol.

In order to be able to trace local variations of pH in situ during the formation of biomorphs, growth was carried out directly underneath a confocal microscope. For this purpose, we used special microdishes that had a flat glass bottom (ibidi GmbH, µ-dish, diameter: 35 mm) and thus were ideally suited for imaging the front of sheets evolving along this interface. Initially, 4 mL of growth solution (prepared as described above) were filled into the dishes and left open to the atmosphere to absorb CO_2 over time. After 2 h (when the first structures had started to form), 0.1 mL of a 100 µM solution of **2** in water:acetone 9:1 were added (note that the small amounts of acetone introduced in this way did not affect the growth behavior of biomorphs to any noticeable extent). The final concentration of the dye in the mother liquor thus was 2.44 µM.

After a promising (and still growing) aggregate had been identified in the microscope and fluorescent dye was added, the development of the structure was monitored in situ over time (as in many previous studies[S6,S7] with regular optical microscopy), while continuously collecting transmission and fluorescence data.

References.

S1. Z. Shen, H. Rohr, K. Rurack, H. Uno, M. Spieles, B. Schulz, G. Reck and N. Ono, *Chem. Eur. J.*, 2004, **10**, 4853-4871.

S2. U. Resch and K. Rurack, *Proc. SPIE-Int. Soc. Opt. Eng.* 1997, **3105**, 96-103.

S3. S. L. Zhu, J. T. Zhang, G. Vegesna, F. T. Luo, S. A. Green and H. Y. Liu, *Org. Lett.*, 2011, **13**, 438-441.

S4. E. Jahnke, J. Weiss, S. Neuhaus, T. N. Hoheisel and H. Frauenrath, *Chem. Eur. J.*, 2009, **15**, 388-404.

S5. M. Hecht, W. Kraus and K. Rurack, *Analyst*, 2013, **138**, 325-332.

S6. M. Kellermeier, F. Glaab, E. Melero-Garcia and J. M. Garcia-Ruiz, *Experimental Techniques for the Growth and Characterization of Silica Biomorphs and Silica Gardens*, in *Research Methods in Biomineralization Science*, Academic Press, Burlington, 2013, vol. 532, pp. 225-256.

S7. J. M. Garcia-Ruiz, E. Melero-Garcia and S. T. Hyde, *Science*, 2009, **323**, 362-365.

Volume 1 | Number 2 | March 2016 | Pages 83–162

Nanoscale Horizons

The home for rapid reports of exceptional significance in nanoscience and nanotechnology

rsc.li/nanoscale-horizons

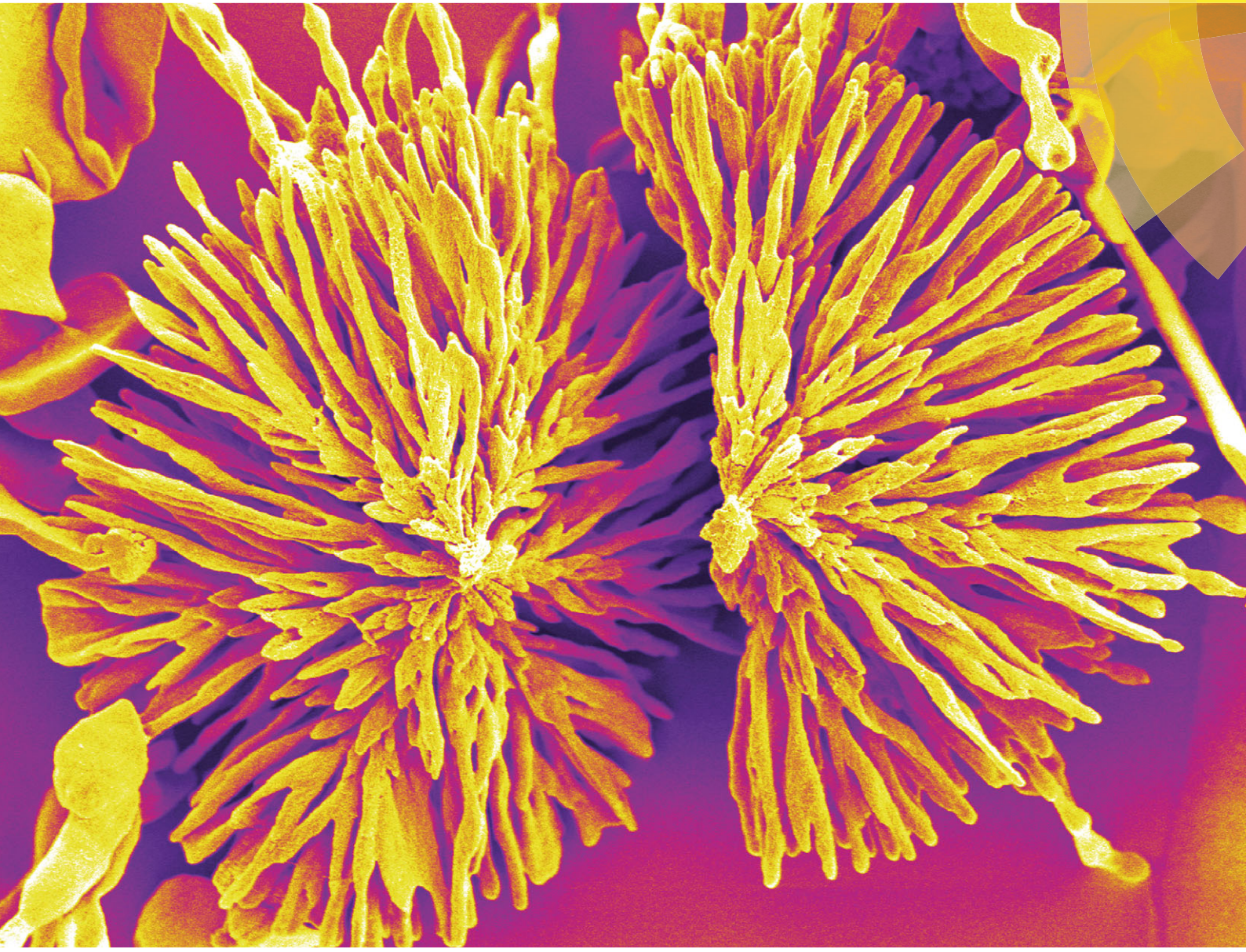

ISSN 2055-6756

ROYAL SOCIETY OF CHEMISTRY

COMMUNICATION

M. Kellermeier, H. Cölfen *et al.*

Functionalisation of silica–carbonate biomorphs

NCNST

Nanoscale Horizons

COMMUNICATION

View Article Online
View Journal | View Issue

Functionalisation of silica–carbonate biomorphs†

J. Opel,[a] F. P. Wimmer,[a] M. Kellermeier*[b] and H. Cölfen*[a]

Cite this: *Nanoscale Horiz.*, 2016, 1, 144

Received 22nd October 2015,
Accepted 11th January 2016

DOI: 10.1039/c5nh00094g

rsc.li/nanoscale-horizons

Biomorphs are a unique class of self-organised silica–carbonate mineral structures with elaborate shapes. Here we report first approaches to modify these complex inorganic architectures through silane chemistry, binding of nanoparticles, and organic polymerisation. This leads to functional nanostructures in which the complexity of the originally inorganic template is preserved, and offers new diagnostic tools to study the mechanisms underlying their formation.

Conceptual insights

Biomorphs are a unique class of self-organised nanostructured silica–carbonate mineral structures with elaborate shapes. This complexity of shapes is otherwise only formed in the living world in form of biominerals. We want to utilize the unique inorganic biomorph structures to add function to create nanostructured materials with complex shape and new and emergent properties. Here we report first approaches to modify these inorganic architectures through silane chemistry, binding of nanoparticles, and organic polymerisation. This leads to functional nanostructures in which the complexity of the originally inorganic template is preserved. The reported three examples already show the large variability of our approach and especially the post functionalization with silanes provides the possibility to attach a variety of functional nanoparticles. Therefore, our study introduces a new and variable platform towards novel functional nanostructured materials with complex shapes.

Crystallisation of alkaline-earth metal carbonates in the presence of silica at high pH can result in fascinating hybrid structures with curved morphologies and ordered textures across several length scales.[1] These so-called "biomorphs" consist of innumerous carbonate nanocrystals that are stabilised by co-precipitating silicate species and self-assemble into delicate forms like regular helicoids or sinuous sheets, which may eventually become sheathed by an outer skin of silica on the micron level.[2] Despite the absence of any organic matter, the obtained structures closely mimic biomineral frameworks produced by living organisms[3] and moreover resemble some of the oldest putative microfossils.[4] Therefore, biomorphs have been used as a model system to study biomimetic self-organisation[5] and serve as a vital proof that complex curved forms are not exclusive to the living world.[6]

Over the past ten years, the mechanism for the formation of these unusual inorganic–inorganic hybrid structures has been investigated in depth, leading to a meanwhile convergent picture of autocatalytic reaction coupling being the driving force for self-assembly at the nanoscale.[7,8] In particular, it was shown that local changes in pH at the growth front trigger the dynamic co-mineralisation of silica and carbonate due to their inverse trends of solubility with pH, as depicted schematically in Fig. 1a–c and described in more detail elsewhere.[9] The result is an array of crystalline carbonate nanoparticles (dark-grey rods in Fig. 1) embedded in a more or less continuous matrix of amorphous silica (light-grey domains in Fig. 1c), which subsequently evolves free from crystallographic constraints towards curved superstructures.[10]

Even though biomorphs exhibit many interesting features in terms of structure and morphology, they still consist of plain inorganic compounds (usually $BaCO_3$ and SiO_2) and thus bear little to no distinct functionality. To address this issue and widen the scope of biomorphs towards materials science, we have started to chemically modify the inorganic nanostructures, either *in situ* during their formation or by post-treatment. Here we present three different approaches to achieve "functional" biomorphs: (1) silane co-condensation, (2) immobilisation of metal nanoparticles and quantum dots, and (3) organic polymerisation. All three concepts yield hybrid materials with enhanced functionality and equal structural complexity as inherited from the self-assembly process of biomorphs.

[a] *Physical Chemistry, University of Konstanz, Universitätsstrasse 10, D-78464 Konstanz, Germany. E-mail: helmut.coelfen@uni-konstanz.de; Fax: +49 7531 88 3139; Tel: +49 7531 88 4063*

[b] *Material Physics, BASF SE, GMC/O – B007, Carl-Bosch-Strasse 38, D-67056 Ludwigshafen, Germany. E-mail: matthias.kellermeier@basf.com; Fax: +49 621 66 43388; Tel: +49 621 60 43388*

† Electronic supplementary information (ESI) available: Details on experimental procedures (Sections S1 and S2), quantification of the degree of thiol functionalisation (Section S3, with Fig. S1), estimation of the gold nanoparticle loading on biomorphs (Section S4, with Fig. S2), Raman and IR analyses of polymer-functionalised biomorphs (Section S5, with Fig. S3). See DOI: 10.1039/c5nh00094g

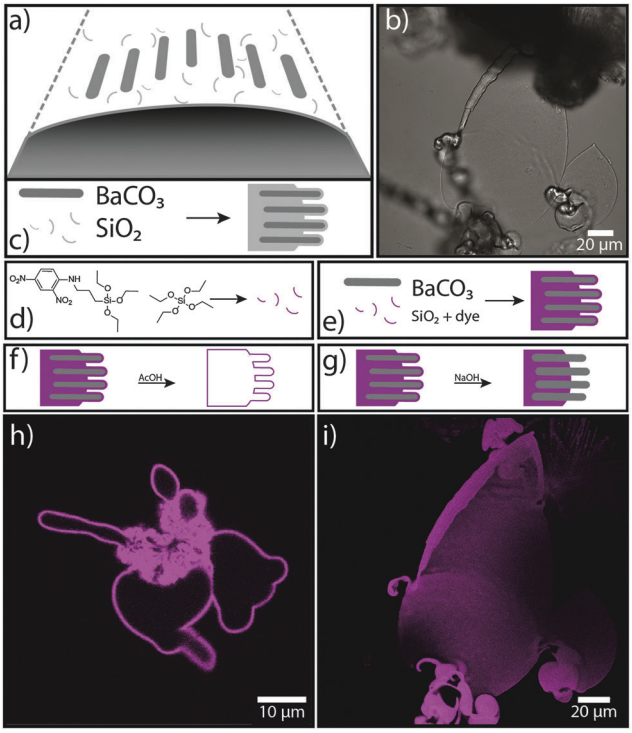

Fig. 1 *In situ* functionalisation of biomorphs by silane co-condensation. (a) Schematic drawing of the growth of a biomorph by the continuous formation of carbonate nanocrystals (dark-grey rods) in the presence of silicate species (thin light-grey threads). (b) CLSM image (transmission channel) of a biomorph sheet. (c) Co-precipitation of $BaCO_3$ nanocrystals and unfunctionalised amorphous silica. (d) Co-condensation of TEOS and DNPTES into fluorescent "functional" silica. (e) Incorporation of fluorescently labeled silanes into the siliceous component of biomorphs (magenta-coloured domains). (f) Selective dissolution of the carbonate component by acid post-treatment, leading to a hollow silica structure. (g) Partial dissolution of the (outer) silica component by NaOH post-treatment. (h and i) CLSM images (fluorescence channel) of functional biomorphs after acid and base treatment, respectively.

The idea behind approach (1) was to selectively modify the silica component in biomorphs and introduce functional groups *via* alkoxysilane chemistry.[11] In fact, Voinescu *et al.* have shown that biomorphs can be formed with tetraethoxysilane (TEOS) as an alternative organic silica source instead of commonly used inorganic water glass (sodium silicate solution).[12] To obtain typical biomorphic structures, the TEOS (*ca.* 9 mM) was pre-hydrolysed in water with sodium hydroxide before adding Ba^{2+} ions (5 mM) to the alkaline solution (pH 10–11) and inducing crystallisation by exposure to atmospheric CO_2. Based on this recipe, we grew biomorphs from mixtures of TEOS and functional triethoxysilanes like 3-mercaptopropyltriethoxysilane (3-MPTES, for introducing thiol groups), 3-aminopropyltriethoxysilane (3-APTES, for amine groups) and 3-(2,4-dinitrophenylamino)propyltriethoxysilane (DNPTES, carrying a fluorescent label) (see Sections S1 and S2 in the ESI† for experimental details). Fig. 1 summarises the results of an experiment in which 5 vol% of TEOS were replaced by DNPTES. Confocal laser scanning microscopy (CLSM) images (Fig. 1h and i) clearly evidence that the obtained biomorphs display strong fluorescence, demonstrating successful incorporation of the functional silane into the structure in a one-pot synthesis.

Bright and homogeneous fluorescence signal from all parts of the aggregates moreover suggests that co-condensation of TEOS and DNPTES leads to a statistical distribution of the fluorescent dye in the silica component of the biomorph, showing that this simple method enables a complete functionalisation of the entire structure. Apart from that, the incorporation of fluorescent groups allows the siliceous component to be easily detected and located. As already mentioned above, silica can be present both as an external skin and – to a greater or lesser extent – also in the bulk material around and in-between the carbonate nanocrystals. This can be analysed in detail by selective dissolution experiments.[6] For example, by immersing the as-grown aggregates into dilute acid (0.03 M HOAc), the carbonate component can be removed quantitatively within minutes. This leaves a hollow structure of fluorescent silica (Fig. 1f and h), corresponding to the thick outer skin covering the whole crystal assembly. On the other hand, treatment with base (1 M NaOH) dissolves this outer skin and exposes the inner carbonate-rich core (Fig. 1g and i). Owing to the fluorescent label, we are now able to confirm that silica is also an integral part of the inner structure (which is still under debate[2]), where it presumably serves as a "glue" holding the carbonate crystals together. The fact that this part of the silica was not dissolved in NaOH indicates that it is intimately associated to the carbonate phase – which is well in line with the proposed model of autocatalytic co-mineralisation of the two components at the nanoscale.[7,8] We note that pre-hydrolysis of the silanes proved to be crucial to obtain characteristic biomorphic structures directly in solution. This emphasises the key role of silica speciation in the process of morphogenesis.

Besides the above-described *in situ* functionalisation of biomorphs by co-condensation of alkoxysilanes with TEOS, we also conducted post-functionalisation experiments with already grown structures. Freshly harvested biomorphs are expected to carry free silanol groups at the surface of their outer silica skin (Fig. 2a and b), to which functional silanes can be coupled *via* well-known surface modification methods.[13] In this way, a broad range of functional groups can be imparted on the biomorphs, as illustrated by Fig. 2.

Using the fluorescent silane DNPTES (Fig. 2c), structures similar to those in Fig. 1 were obtained, but in this case, no fluorescence could be detected in the inner part (after treatment with 1 M NaOH), indicating that only the silica in the outer skin is accessible for silane coupling. Nevertheless, bright fluorescence from the outer parts confirms that surface functionalisation by post-treatment is possible. Based on these results, further functional groups were tested. For instance, amine groups were introduced by the silane 3-APTES (Fig. 2d); their presence at the surface was confirmed by direct coupling of isothiocyanate dyes like FITC (fluorescein isothiocyanate),[14] which were subsequently again detected *via* their fluorescence (*cf.* CLSM image in Fig. 2d). Other organic compounds can be coupled to the amine groups on the biomorph surface in the same way. Post-functionalisation of the structures with thiol groups was performed using the silane 3-MPTES (Fig. 2e). The presence of surface-bound thiol

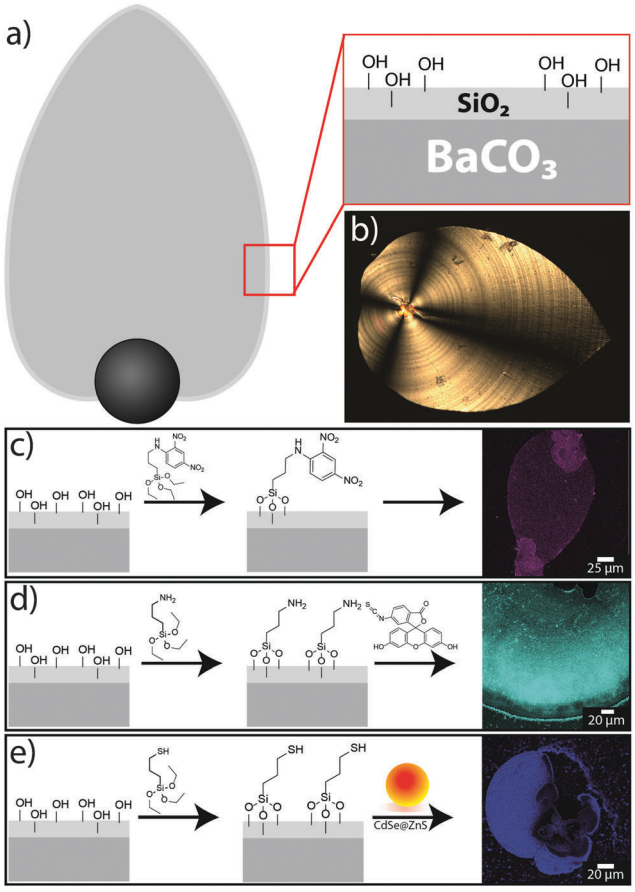

Fig. 2 Post-functionalisation of biomorphs with different trialkoxysilanes. (a) Schematic drawing of a biomorph sheet with a thick outer silica skin carrying free silanol groups accessible for coupling reactions. (b) Polarised optical micrograph of a typical biomorph sheet. (c–e) Schemes for the post-silanisation of as-grown biomorphs with (c) DNPTES, (d) 3-APTES and further functionalisation with FITC, (e) 3-MPTES and subsequent binding of CdSe@ZnS quantum dots. In all cases, successful functionalisation is proven by corresponding CLSM images (right).

groups was verified with Ellman's reagent,[15] which forms nitrothiobenzoate (NTB) adducts in slightly alkaline solutions that can be detected and quantified by their absorption at 408 nm. With the recipe used in this study, about 1 µmol g^{-1} thiol groups could be anchored on the biomorphs (see Section S3 and Fig. S1 in the ESI† for details).

Having shown that biomorphs can readily be functionalised by either *in situ* or post-silanisation, we now turn to approach (2) of our work, *i.e.* the immobilisation of functional nanoparticles on the surface of the aggregates. To achieve this, we made use of the thiol-bearing biomorphs obtained as described above (Fig. 2e), since SH groups have a strong affinity to bind to certain metals and minerals. As a proof of concept, two distinct types of nanoparticles were chosen here: CdSe@ZnS core–shell quantum dots (QDs), about 9 nm in diameter (with d_{core} = 4 nm), and spherical gold nanoparticles (AuNPs) with an average size of 14 nm. In both cases, the thiol-modified biomorphs were incubated in dispersions of the nanoparticles for several hours and rinsed afterwards to remove any loosely adhering material. Fig. 2e shows the result for a biomorph that was exposed to the quantum dots. The strong fluorescence from the flat part of the sheet-like structure demonstrates successful immobilisation of the QDs at the surface (note that the black regions within the structure in the CLSM image are not in the confocal plane and hence do not show fluorescence here). In addition, the presence of cadmium and zinc was verified by EDX measurements (atomic ratio: Ba : Si : Zn : Cd = 1 : 0.6 : 0.05 : 0.01). In the case of the AuNPs, surface modification cannot be directly confirmed by fluorescence microscopy. While EDX analyses traced certain amounts of gold at the surface (atomic ratio: Ba : Si : Au = 0.94 : 1 : 0.01), two further methods were used to study the prepared hybrid materials. First, the biomorphs were crushed after functionalisation and investigated by means of transmission electron microscopy (TEM). The resulting images show small AuNPs covering the larger silica spheres (see Fig. S2a in the ESI†), supporting the assumption that the metal nanoparticles bind to the thiol groups at the silica surface. Second, we used catalytic reactions to prove the presence of AuNPs on the structures without destroying them (Fig. 3). The chosen test reactions were the reduction of 4-nitrophenol (pNP) with sodium borohydride[16] and the reduction of resazurin with hydroxylamine (*cf.* Fig. 3c).[17,18] In the latter case, the formed resorufin could easily be observed by CLSM as a strongly fluorescent area around the biomorphic structures (Fig. 3b), suggesting that the reaction occurred directly on the surface where the AuNPs were immobilised (note that unfunctionalised structures did not show this behaviour). The resazurin-to-resorufin reaction also occurred without AuNP-

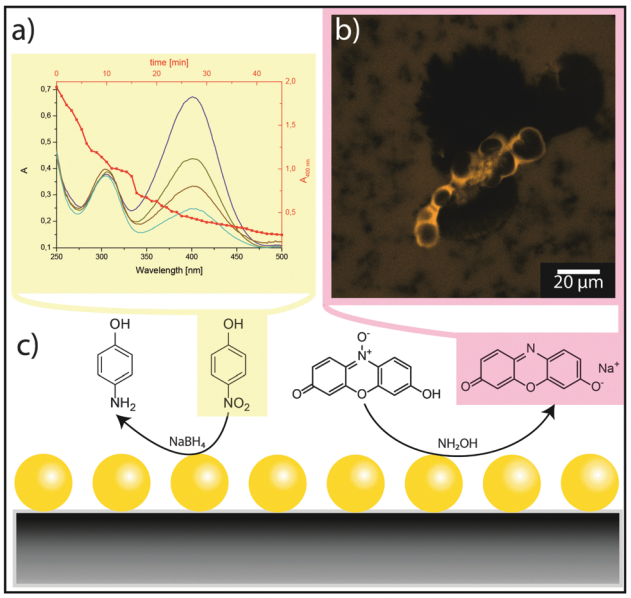

Fig. 3 Catalytic reactions with AuNPs immobilised on biomorphs. (a) UV-Vis spectra showing the reduction of *p*-nitrophenol by $NaBH_4$. (b) CLSM image of a AuNP-bearing biomorph in a solution of resazurin and hydroxylamine. The formation of the reduced state (resorufin) can be detected by enhanced fluorescence at the surface of the biomorph. (c) Schematic drawing of the two test reactions using the immobilised particles as catalyst. The coloured molecules were analytically observed.

bearing biomorphs, but at a much slower rate. This shows that the surface-bound gold particles act as a catalyst in this reaction, hence imparting distinct functionality to the biomorph structure.

The reduction of pNP by $NaBH_4$ in the presence of gold-functionalised biomorphs was traced by UV/Vis spectroscopy (Fig. 3a). In particular, the strong absorption band of pNP at 400 nm was used to monitor the progress of the reaction. The thick red line in Fig. 3a shows the change in the peak area as a function of time. It is evident that functional biomorph structures can efficiently catalyse this reaction as well (note that pNP is not reduced by $NaBH_4$ in the absence of Au). Based on reaction rates derived from similar tests under various conditions, and by using the EDX results for intact AuNP@Biomorph structures as well as UV-Vis data from gold colloid dispersions, the loading of Au nanoparticles on the inorganic template was determined to be in a range of 0.03–0.7 nmol g^{-1} (see Section S4 and Fig. S2 in ESI†). Taken together, the experiments described above clearly illustrate that functional nanoparticles can be immobilised on biomorphs, and that this yields complex ternary hybrid nanostructures with interesting catalytic properties.

Finally, in approach (3), we made attempts to coat and/or fill as-grown biomorphs by a polymer, so as to imprint the structure of the hard inorganic template into soft organic material (Fig. 4). In order to avoid uncontrolled bulk polymerisation, it is necessary to have a monomer that first binds onto the silica–carbonate aggregates and then polymerises in and/or around the inorganic architecture. A suitable candidate in this context is 10,12-pentacosadiynoic acid (PCDA), a monomer showing strong affinity to bind on carbonate surfaces *via* its carboxyl groups.[19] Moreover, PCDA polymerisation can be conveniently triggered by exposure to UV light (*cf.* Fig. 4e).

Thus, we removed the outer silica skin from native biomorphs by leaching in 1 M NaOH and subsequently incubated the exposed carbonate core in a solution of PCDA. After replacing the supernatant, the PCDA adsorbed on the biomorphs was polymerised by illumination at 365 nm. SEM images of the resulting structures (Fig. 4c) show that the treated biomorphs (a worm-like morphology in the present example) had a rougher appearance than their native analogues (Fig. 4a) and were more or less completely covered by a material with flake-like morphologies typical for poly(PCDA). This notion is corroborated by optical micrographs of the samples (Fig. 4d), in which the biomorphs display a blue-coloured rim, again characteristic of polymerised PCDA (note that poly(PCDA) can exist in two distinct forms, one blue and one red, between which the polymer can switch upon heating or cooling).[20,21]

The presence of poly(PCDA) on the crystal aggregates could furthermore be clearly demonstrated by IR and Raman analyses of biomorphs before and after functionalisation (see Section S5 and Fig. S3 in the ESI†). Another beneficial property of PCDA is that its polymerised form shows significant fluorescence. This allowed us to localise the polymer in the as-obtained hybrids by confocal microscopy. Corresponding images (Fig. 4b) reveal that the polymerisation process led to the formation of a continuous organic shell around the biomorphs (as confirmed by *Z*-stacking image series) – or in other words, that the morphology of the inorganic architecture was transferred to the emerging organic phase. Actually, this situation is inverse to common biological and biomimetic mineralisation, where usually an organic template controls the shape (and structure) of a forming inorganic phase.[22] On the other hand, our analyses suggest that polymerisation did not occur in the bulk volume of the biomorphs (*cf.* Fig. 4b), presumably due to insufficient infiltration of the PCDA monomer into the dense nanostructure. This becomes further evident when the carbonate core is dissolved in acid, leaving hollow polymer shells behind.

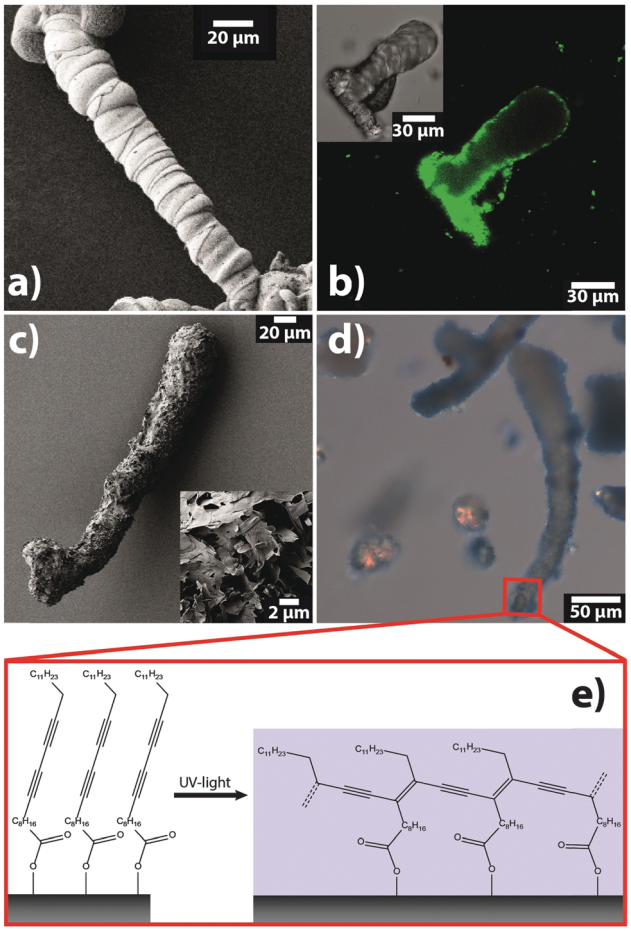

Fig. 4 Organic polymerisation on biomorphs. (a) SEM image of a structure with worm-like morphology before functionalisation. (b) CLSM images (main window: fluorescence channel ($\lambda_{exc.}$ = 561 nm), inset: transmission channel) of another worm-like structure after functionalisation. (c) SEM image of a poly(PCDA)-coated worm. The inset shows a zoom on the surface of the aggregate, revealing the flake-like character of the polymer coating. (d) Optical micrograph of biomorphs after functionalisation, showing the characteristic blue colour of poly(PCDA). (e) Schematic drawing of the polymerisation of PCDA molecules adsorbed on the biomorph surface.

Conclusion

In summary, our results highlight different approaches to add functionality to self-organised silica–carbonate structures

by rather straightforward means. We have shown that silane chemistry serves as a versatile toolbox for molecular functionalisation of the silica component in biomorphs, either by direct co-condensation during self-assembly or afterwards through surface modification, while in both cases the complex ultrastructures of the inorganic–inorganic hybrids are preserved. This represents a notable and non-trivial achievement when considering that even slightest variations in the growth conditions can change the shape and texture of biomorphs dramatically.[12] These experiments have provided new insights into the role and distribution of silica in the aggregates by direct visualisation *via* fluorescent labeling. Apart from such structural information, biomorphs carrying dinitrophenyl groups could be interesting materials for the field of non-linear optics (NLO):[23,24] DNPTES-labeled silica is known to exhibit second order non-linearity due to the non-centrosymmetric environment, and hence it should show second harmonic generation (SHG) phenomena if the dyes are aligned.[24,25] In addition to fluorescent labeling, post-silanisation of biomorphs also allows for anchoring various functional groups such as amines or thiols at the surface, which can then be used for further functionalisation. In the present work, this strategy was employed to generate biomorph-based superstructures of semiconductor and metal nanoparticles as first examples to demonstrate the variability of our approach. The resulting materials may show special optical properties, for instance through the coupling of the surface plasmons of nanoparticles immobilised on helicoidal structures,[1,2,4–10] leading to chiral plasmonics on single biomorphs.[26,27] We are furthermore confident that also other functional materials can be bound to the biomorph surfaces in a similar way. In particular, it would be desirable to orient magnetic or electric dipoles along the sinuous landscape provided by the inorganic template, as this is expected to produce complex couplings and thus give rise to new physical properties. For example, oriented attachment of suitable magnetic nanoparticles (such as iron oxides) on existing biomorph architectures could lead to long-range ordered superstructures through self-assembly,[28,29] which in the case of twisted morphologies may yield micropropellers capable of navigating in an applied external magnetic field.[30,31] In turn, electric dipole coupling could be realised by using anisotropic semiconductor nanoparticles like zinc oxide.[32] Finally, selective dissolution of the inner carbonate core gives easy access to hollow frameworks of functional materials with complex shapes and additional possible advantages in terms of properties and applications.[33]

Post-functionalisation thus appears to be a simple and universal method with great potential to benefit from the unique structures of biomorphs in the design of nanoparticle assemblies with new collective and emergent properties, which remain to be explored. Along the same lines, it is possible to shape organic matter by *in situ* polymerisation of suitable pre-adsorbed monomers on the inorganic architectures. This bears fascinating – though inverted – analogies to biomineralisation and may have profound implications for primitive life detection[4,6] as well as the early evolution of increasingly complex organic matter.

Acknowledgements

The authors thank Profs. Clément Sanchez and Werner Kunz for valuable discussions and suggestions for this work. In addition, we are grateful to Tjaard de Roo for providing the quantum dots, Tuan Anh Pham and Holger Reiner for the gold colloids, Shengtong Sun for help with the PCDA experiments, Mathias Altenburg for performing Raman microscopy, and the Bioimaging Center of the University of Konstanz for access to their instruments.

References

1 M. Kellermeier, H. Colfen and J. M. Garcia-Ruiz, *Eur. J. Inorg. Chem.*, 2012, 5123–5144.
2 M. Kellermeier, E. Melero-Garcia, F. Glaab, J. Eiblmeier, L. Kienle, R. Rachel, W. Kunz and J. M. Garcia-Ruiz, *Chem. – Eur. J.*, 2012, **18**, 2272–2282.
3 S. Weiner and L. Addadi, *Annu. Rev. Mater. Res.*, 2011, **41**, 21–40.
4 J. M. Garcia-Ruiz, S. T. Hyde, A. M. Carnerup, A. G. Christy, M. J. Van Kranendonk and N. J. Welham, *Science*, 2003, **302**, 1194–1197.
5 W. L. Noorduin, A. Grinthal, L. Mahadevan and J. Aizenberg, *Science*, 2013, **340**, 832–837.
6 J. M. Garcia Ruiz, A. Carnerup, A. G. Christy, N. J. Welham and S. T. Hyde, *Astrobiology*, 2002, **2**, 353–369.
7 J. M. García-Ruiz, E. Melero-García and S. T. Hyde, *Science*, 2009, **323**, 362–365.
8 M. Kellermeier, E. Melero-García, W. Kunz and J. M. García-Ruiz, *J. Colloid Interface Sci.*, 2012, **380**, 1–7.
9 J. Opel, M. Hecht, K. Rurack, J. Eiblmeier, W. Kunz, H. Colfen and M. Kellermeier, *Nanoscale*, 2015, **7**, 17434–17440.
10 M. Kellermeier, J. Eiblmeier, E. Melero-García, M. Pretzl, A. Fery and W. Kunz, *Cryst. Growth Des.*, 2012, **12**, 3647–3655.
11 L. Nicole, L. Rozes and C. Sanchez, *Adv. Mater.*, 2010, **22**, 3208–3214.
12 A. E. Voinescu, M. Kellermeier, A. M. Carnerup, A.-K. Larsson, D. Touraud, S. T. Hyde and W. Kunz, *J. Cryst. Growth*, 2007, **306**, 152–158.
13 C. G. Golander and E. Kiss, *Colloids Surf., A*, 1993, **74**, 217–222.
14 J. L. Riggs, R. J. Seiwald, J. H. Burckhalter, C. M. Downs and T. G. Metcalf, *Am. J. Pathol.*, 1958, **34**, 1081–1097.
15 G. L. Ellman, *Arch. Biochem. Biophys.*, 1959, **82**, 70–77.
16 J. Lee, J. C. Park and H. Song, *Adv. Mater.*, 2008, **20**, 1523–1528.
17 W. Xu, J. S. Kong, Y.-T. E. Yeh and P. Chen, *Nat. Mater.*, 2008, **7**, 992–996.
18 G. De Cremer, B. F. Sels, D. E. De Vos, J. Hofkens and M. B. Roeffaers, *Chem. Soc. Rev.*, 2010, **39**, 4703–4717.
19 A. Berman, D. J. Ahn, A. Lio, M. Salmeron, A. Reichert and D. Charych, *Science*, 1995, **269**, 515–518.
20 S. Dei, A. Matsumoto and A. Matsumoto, *Macromolecules*, 2008, **41**, 2467–2473.
21 J. B. Pang, L. Yang, B. F. McCaughey, H. S. Peng, H. S. Ashbaugh, C. J. Brinker and Y. F. Lu, *J. Phys. Chem. B*, 2006, **110**, 7221–7225.

22 F. C. Meldrum and H. Cölfen, *Chem. Rev.*, 2008, **108**, 4332–4432.
23 C. Claude, B. Garetz, Y. Okamoto and S. Tripathy, *Mater. Lett.*, 1992, **14**, 336–342.
24 J. Kim, J. L. Plawsky, R. LaPeruta and G. Korenowski, *Chem. Mater.*, 1992, **4**, 249–252.
25 J. F. Rabek, *Photochemistry and photophysics*, CRC Press, 1991.
26 J. George and K. G. Thomas, *J. Am. Chem. Soc.*, 2010, **132**, 2502–2503.
27 M. Hentschel, M. Schäferling, T. Weiss, N. Liu and H. Giessen, *Nano Lett.*, 2012, **12**, 2542–2547.
28 A. Ahniyaz, Y. Sakamoto and L. Bergström, *Proc. Natl. Acad. Sci. U. S. A.*, 2007, **104**, 17570–17574.
29 M. Giersig and M. Hilgendorff, *Eur. J. Inorg. Chem.*, 2005, 3571–3583.
30 W. Gao, X. Feng, A. Pei, C. R. Kane, R. Tam, C. Hennessy and J. Wang, *Nano Lett.*, 2013, **14**, 305–310.
31 H. Wang and M. Pumera, *Chem. Rev.*, 2015, **115**, 8704–8735.
32 C. Lizandara-Pueyo, S. Dilger, M. R. Wagner, M. Gerigk, A. Hoffmann and S. Polarz, *CrystEngComm*, 2014, **16**, 1525–1531.
33 J. Yin, Q. Lu, Z. Yu, J. Wang, H. Pang and F. Gao, *Cryst. Growth Des.*, 2009, **10**, 40–43.

Electronic Supplementary Material (ESI)

for

Functionalisation of Silica-Carbonate Biomorphs

Julian Opel, Florian Wimmer, Matthias Kellermeier and Helmut Cölfen**

S1. Materials and Methods.

Barium chloride dihydrate (min. 99%) was purchased from Riedel-de Haën and used as received. The silica source was a commercial sodium silicate solution (so-called water glass) containing about 12.5 wt% SiO_2 and 13.8 wt% Na, as supplied by Sigma-Aldrich (reagent grade). All used solvents were of UV spectroscopic grade (Aldrich). Stock solutions (0.1 and 1 M) of hydrochloric acid and sodium hydroxide, required for pH adjustments, were obtained from Merck (p.a. grade), while borax/HCl buffer solution (pH 9) was received from Fluka. All solutions and dilutions were prepared with water of MilliQ quality, sourced from a Milli-Q Synthesis A10 system equipped with a Quantum EX Ultrapure Organex cartridge (Millipore). The used triethoxysilanes (3-MPTES: 92%; 3-APTES: 98%; DNPTES: 92%; 3-MPA: 99%) and TEOS (min. 99%) were purchased from ABCR. 10,12-Pentacosadiynoic acid (PCDA, 97%), Ellman reagent (5,5'-dithiobis(2-nitrobenzoic acid), min. 98%), 4-nitrophenol (spectrophotometric grade, min. 99.5%), resazurin sodium salt (BioReagent, dye content: 80%), fluorescein isothiocyanate (FITC, isomer I, min. 90%) and hydroxylamine solution (50% in water) were obtained from Sigma-Aldrich. Sodium borohydride (98%) was purchased from Merck.

Polarised optical microscopy studies were carried out on a Zeiss Imager.M2m microscope equipped with EC Epiplan-Neofluar 5x/10x/20x and LD Epiplan 50x objectives, a lambda plate, and a Zeiss AxioCam MRc 5 CCD camera for imaging. The used confocal laser scanning microscope was a Zeiss LSM780. All CLSM measurements were done with the PlanApo 63x / 1.40_{Oil} objective, using an Ar^+ laser diode (458, 488, 514 nm), a DPSS laser (561 nm) or a HeNe laser (633 nm) as light source. The microscope was equipped with three fluorescence detectors (one GaAsP array and two PMTs) and another PMT for transmission images. For scanning electron microscopy and EDX analysis, specimens were mounted on aluminium stubs by means of double-sided adhesive tape and were subsequently investigated on a Hitachi TM3000 tabletop microscope at acceleration voltages ranging from 3 to 10 kV (without previous sputtering). High-resolution SEM images were acquired with a Zeiss Crossbeam 1540XB microscope with the SE2 detector at 5-15 kV. TEM studies were carried out on a Zeiss Libra 120 microscope at 120 kV. UV-Vis and fluorescence spectra were recorded using an Agilent Cary 50 spectrophotometer and a Perkin Elmer LS 50B fluorescence spectrometer, respectively. Measurements were performed in quartz cuvettes with a path length of 10 mm from Hellma Analytics. A Perkin Elmer Spektrum 100 ATR-FTIR instrument was used for IR spectroscopy, while Raman microspectroscopy was performed by a custom-built setup installed with a confocal Leica microscope with two lasers (488 and 633 nm).

S2. Growth and Characterisation of Native and Functionalised Biomorphs.

Synthesis of native biomorphs: Silica biomorphs were grown from aqueous solutions containing 5.0 mM $BaCl_2$ and 9 mM SiO_2, the latter being introduced either directly as sodium silicate (water glass) or through hydrolysis of TEOS at pH 11.3 (adjusted by NaOH) prior to mixing with the barium

solution. 10 mL of the reaction mixture were filled into cylindrical wells of standard polystyrene plates (VWR Nunclon 6-well plates, volume: 17 mL, area: 9.6 cm^2, depth: 1.7 cm). Subsequently, glass coverslips (15x15 mm) were placed on the bottom of the wells as substrates for growth, and the well plate was covered loosely with a lid. Crystallisation of barium carbonate occurred upon gradual in-diffusion of CO_2 from the atmosphere into the alkaline solution (starting pH: 11.0), where it was converted to HCO_3^- and finally CO_3^{2-} ions needed for precipitation. In this way, complex structures are formed spontaneously on interfaces over periods of several hours. Their isolation is quite straightforward, as the glass substrates can simply be removed from the mother liquor with a pair of tweezers and only need to be rinsed with water and ethanol.

One-pot synthesis of fluorescent biomorphs: In-situ functionalisation was achieved by replacing 5 vol% of the TEOS with 3-(2,4-dinitrophenylamino)propyltriethoxysilane (DNPTES) in the above-described procedure (i.e. 8.6 mM TEOS and 0.4 mM DNPTES). After 12-24 hours of growth, the glass substrates were removed from the mother liquor and rinsed intensively with water and ethanol.

Post-silanisation of biomorphs: Freshly synthesised biomorphs (stuck on glass coverslips) were immersed into a 1 vol% solution of functional triethoxysilane (3-MPTES, 3-APTES or DNPTES) in a 95:5 mixture of ethanol and water. After 12 h, the substrates were removed and washed intensively with water and ethanol.

Labeling of amine-functionalised biomorphs: Coverslips carrying aminosilane-functionalised biomorphs were incubated in a FITC solution at pH 9 for 2 h. The FITC solution was prepared by mixing 1 mL of borax buffer with 100 µL of 1 mM FITC in ethanol. After incubation, the coverslips were washed with water and ethanol and then directly observed under the CLSM.

Labeling of thiol-functionalised biomorphs with QDs: Coverslips carrying thiol-modified biomorphs were immersed into 1 mL of a 20 nM solution of CdSe@ZnS quantum dots (d_{ave} = 9 nm) in toluene for 6 h. After the incubation step, the structures were removed, washed several times with water and ethanol, and then directly investigated under the CLSM.

Labeling of thiol-functionalised biomorphs with AuNPs: Coverslips carrying thiol-modified biomorphs were immersed into 1 mL of a 10 nM aqueous gold colloid solution (d_{av} = 14 nm) for 24 h. During incubation, the colour of the solution changed from red to purple (cf. UV-Vis spectra in Figure S1b). Afterwards, the coverslips were removed and washed several times with water and ethanol before inspection under the CLSM.

Catalytic reduction of pNP: 3.4 mL water and 4 µL of a 50 mM aqueous solution of 4-nitrophenol were given into a quartz cuvette with a stirrer. Subsequently, 1 mg of the AuNP-functionalised biomorph were dispersed in the solution. After addition of 1 mg $NaBH_4$, the reaction was monitored over time with UV/Vis spectroscopy.

Catalytic reduction of resazurin: First, AuNP-functionalised biomorph were prepared in a µ-dish for fluorescence microscopy (ibidi GmbH, diameter: 35 mm) according to the protocol described above. After the dish had been placed on the specimen stage of the CLSM, 2 mL of a freshly prepared aqueous solution of 16 µM resazurin and 160 µM hydroxylamine were added and the progress of the conversion to resorufin was followed in the fluorescence channel of the CLSM.

Synthesis of PCDA-functionalised biomorphs: First, 20 mg of native biomorphs were treated with 1 M sodium hydroxide solution for 12 h to remove the outer silica skin. After repeated washing with water, the biomorphs were re-dispersed in 4 mL 1 M NaOH and 100 mg PCDA in 1 mL THF were added through a syringe filter. After 12 h incubation (adsorption of PCDA), the structures were washed

several times with water to remove non-adsorbed monomers, followed by exposure to UV light (λ = 365 nm) for 5 min to trigger polymerisation.

S3. Quantification of the Degree of Thiol Functionalisation with the Ellman Reaction

The amount of thiol groups anchored on the biomorphs via silanisation was determined with the help of the Ellman reagent (5,5'-dithiobis(2-nitrobenzoic acid)). In the presence of free thiol groups, this molecule splits and releases nitrothiobenzoate (NTB) in a quantitative reaction, as illustrated in Figure S1c for the case of a thiol-bearing biomorph. NTB exhibits significant absorption at 408 nm in alkaline solution and thus the reaction can readily be monitored by UV-Vis spectroscopy. Figure S1a shows a time-dependent series of corresponding spectra for a 8.8 µM solution of the Ellman reagent in borax buffer (pH 9) containing 18 mg of thiol-functionalised biomorphs, along with a plot of the area of the peak at 408 nm (red dots and line). In order to convert this data into an actual number of free thiol groups on the biomorphs, we performed reference experiments in which defined amounts of 3-mercaptopropionic acid (3-MPA) (0-7 µM) were added to 8.8 µM Ellman reagent solution buffered at pH 9. The resulting spectra after a reaction time of 15 min are shown in Figure S1b. Plotting the area of the peak as a function of concentration (red dots) gives a calibration curve that can be approximated by a linear fit (thick red line), which was used to calculate the actual number of thiol groups on the biomorphs after completion of the reaction shown in Figure S1a. This yields an effective thiol loading of 947 ± 75 nmol per g biomorphs.

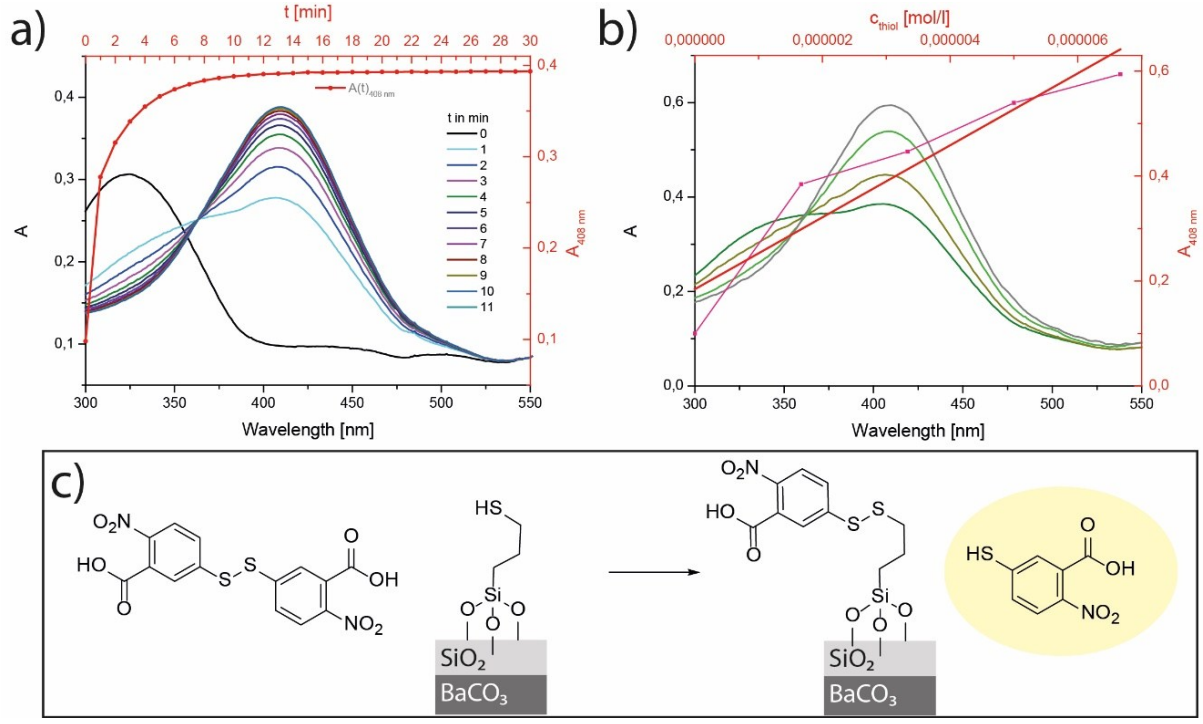

Figure S1. a) UV/Vis spectra showing the progress of the Ellman reaction as a function of time in the presence of 18 mg thiol-modified biomorphs at pH 9. b) UV/Vis spectra of solutions in which the Ellman reagent was converted with different amounts of 3-MPA. The thick red line is a linear fit to the experimental peak area-concentration data, which was used as a calibration curve. c) Schematic drawing of the Ellman reaction on thiol-functionalised biomorphs.

S4. Estimation of the AuNP Loading on Functionalised Biomorphs.

The amount of gold nanoparticles immobilised on the biomorphic structures was estimated in different ways. First, the catalytic activity – as derived from resazurin-to-resorufin reaction rates determined by UV/Vis spectroscopy with and without Au – was used as a measure. Here we assumed that the catalytic activity of the AuNPs bound on the surface of biomorphs is comparable to that of the same particles in a colloidal dispersion (reference experiment). Under these conditions, measured reaction rates can easily be converted to apparent AuNP loadings on biomorphs (in mol per g) if the used absolute mass of AuNP@Biomorph catalyst is known. Following this approach, it needs to be considered that the obtained value will represent a *lower limit* for the true loading, because the net catalytic activity of surface-bound particles is most likely lower than that of the same amount of dispersed particles, due to the fact that reagents need to be transported to/from the surface by diffusion and that some of surface sites may not readily be accessible.

The second used method was EDX spectroscopy on intact AuNP-bearing biomorphs. Corresponding measurements gave an atomic ratio of Ba:Si:Au = 94:100:1. With the known density of solid gold (50 atoms per nm^3) and mean diameter of the used AuNPs (14 nm), the loading of AuNPs on the biomorphs can be calculated from the EDX data. The problem of this approach is that EDX is a surface-sensitive technique with a typical penetration depth of a few microns. Consequently, the contribution of elements that are enriched at the surface of the functionalised biomorph (Si and Au) will be disproportionately higher than that of the bulk material below (mainly $BaCO_3$). Therefore, the resulting value for the loading should be regarded as an *upper limit*.

The third way to calculate the loading is based on in-situ UV-Vis experiments during the functionalisation step, i.e. when thiol-modified biomorphs were incubated in a dispersion of gold colloids. In the absence of biomorphs, the dispersion showed significant absorbance at 514 nm due to surface plasmon resonance, in good agreement with the literature.[S1] However, upon exposure to the thiol-bearing biomorphs, the intensity of the band at 514 nm decreased and the colour of the solution changed from red to a dark violet, accompanied by the emergence of an additional absorption peak at ca. 595 nm (Figure S2c). This second band indicates the formation of one-dimensional superstructures (chains)[S2] of the gold colloids in dispersion and in fact, such aggregated structures could also be observed by TEM (Figure S2b). Interestingly, this effect only occurred in the presence of biomorphs, while neither $BaCO_3$ nor silica particles alone did have any noticeable influence on the absorption spectra. In turn, when as-grown biomorphs were used (no thiol modification), the new band at 595 nm formed, but the peak at 514 nm did not decrease in intensity (cf. Figure S2d). While we cannot explain these findings in detail at the moment, a comparison of the absorbance at 514 nm (peak area) after exposure to i) unmodified biomorphs (Figure S2d) and ii) thiol-bearing biomorphs (blue curve in Figure S2c) can be taken as a measure for how many Au nanoparticles were bound on the thiol-modified biomorphs during AuNP functionalisation. Values resulting for the loading from this approach are also considered to be *upper limits*, because the formed aggregates of AuNPs have limited colloidal stability and hence some of them may have precipitated in the course of the experiment (thus reducing the detected absorption without actually binding to biomorphs).

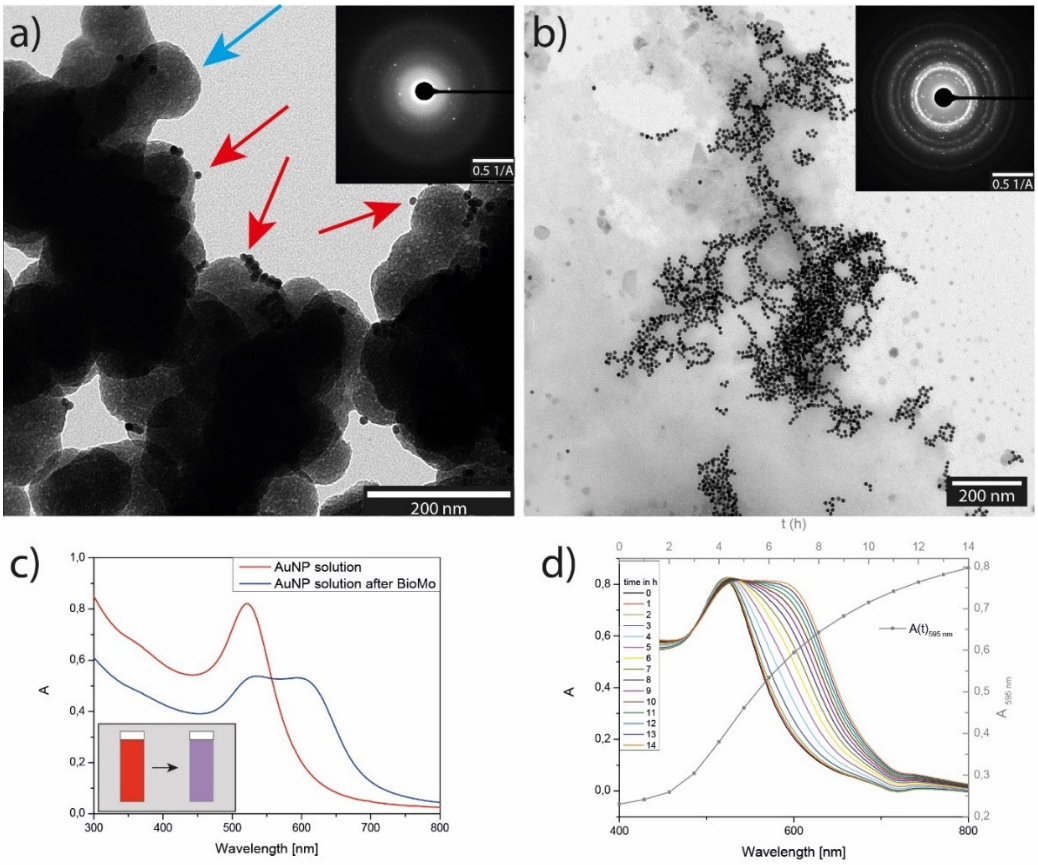

Figure S2. a) TEM image of thiol-modified biomorphs after incubation in AuNP dispersion, rinsing with water and crushing for TEM preparation. The remaining fragments consist of three components: carbonate nanocrystals (ca. 200 nm long and 50 nm wide, not shown here), silica spheres (50-200 nm in diameter, indicated by the blue arrow), and small gold colloids (14 nm) with high contrast (highlighted by red arrows) that decorate some of the silica particles. Corresponding electron diffraction (ED) patterns show strong reflections that can be assigned to crystalline gold (note that the shown area of the sample mainly contains (amorphous) silica spheres and AuNPs). b) TEM micrograph of AuNP networks that were isolated from gold dispersions after exposure to thiol-modified biomorphs. The ED pattern proves that the aggregated particles consist of Au. c) UV/Vis spectra of the colloidal AuNP dispersion before (red) and after (blue) incubation with thiol-modified biomorphs (blue). The inserted sketch illustrates how the colour of the solution changed. d) UV/Vis spectra of the AuNP dispersion at different times during incubation with unfunctionalised biomorphs (no thiol modification).

Values resulting for the AuNP loading from the above-described approaches are compiled in Table S1. It is obvious that the agreement between the estimated loadings is not good, but still the data give an idea about the order of magnitude.

Method	Calculated Loading [nmol/g]
Catalytic Reaction	0.03 ± 0.01
EDX	0.50 ± 0.05
UV-Vis Spectroscopy	0.74 ± 0.01

Table S1. Loadings of AuNPs on biomorphs after functionalisation, as estimated by different methods.

S5. Raman and IR Analyses of Polymer-Coated Biomorphs.

In addition to optical microscopy, SEM and CLSM, the composition of the biomorphs after functionalisation with PCDA was also investigated by means of Raman and IR spectroscopy. Corresponding results are summarised in Figure S3. Local Raman spectra (Figure S3a) collected from native aggregates before polymerisation show characteristic signals of $BaCO_3$ at 135, 153 and 1063 cm^{-1}, along with a strong band at 523 cm^{-1} that can be assigned to silica (blue spectrum Figure S3a).[S3,S4] Upon treatment with 1 M NaOH, this latter signal has vanished (red spectrum in Figure S3a), indicating successful removal of the outer silica skin. After adsorption of PCDA and UV illumination, the obtained Raman spectrum is completely different and displays bands that can exclusively be attributed to poly(PCDA) (black spectrum in Figure S3a).[S5] The presence of the polymer is also reflected in the curved baseline of the spectrum, which results from the fluorescence of poly(PCDA). In turn, the absence of distinct carbonate and silica modes suggests that the newly formed polymer coating is rather thick and hence the Raman signal can no longer be obtained from the inner part of the structure.

The above findings are further confirmed by IR data (Figure S3b). While the spectrum measured for a biomorph after removal of the silica skin (black curve in Figure S3b) shows only bands typical for barium carbonate (693, 855 and 1412 cm^{-1}), new signals emerge after the polymerisation step, namely CO modes at 1511 and 1556 cm^{-1} as well as CH modes at 2748 and 2982 cm^{-1}, both being characteristic for poly(PCDA).[S5]

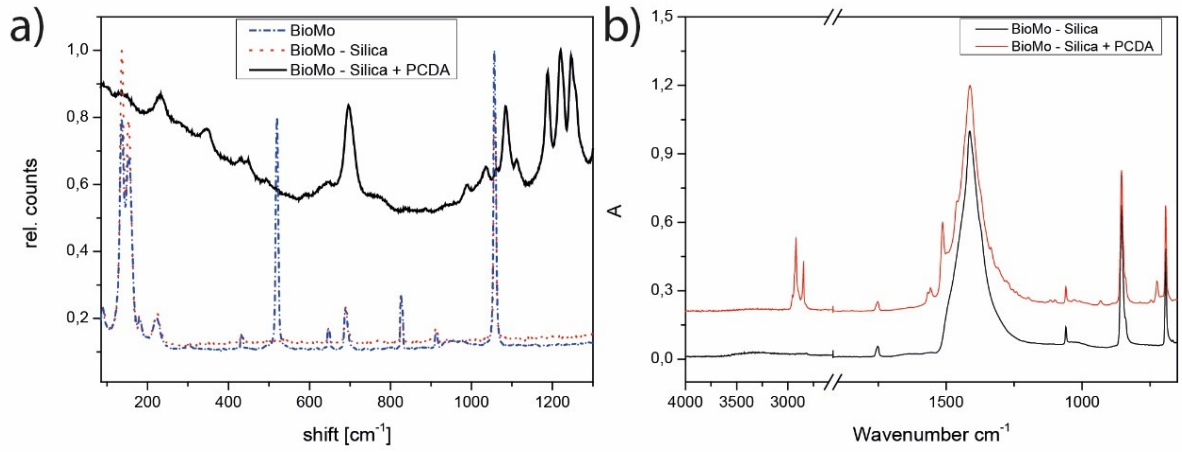

Figure S3. a) Local Raman spectra collected from a native biomorph (blue), a biomorph after removal of the outer silica skin (red), and a PCDA-modified biomorph (black). b) IR spectra of biomorphs after leaching in 1 M NaOH (black) and after functionalisation with PCDA (red).

References.

S1. J. Liao, Y. Zhang, W. Yu, L. Xu, C. Ge, J. Liu and N. Gu, *Colloids Surf. Physicochem. Eng. Aspects*, 2003, **223**, 177-183.
S2. S. Lin, M. Li, E. Dujardin, C. Girard and S. Mann, *Adv. Mater.*, 2005, **17**, 2553-2559.
S3. R. Cloots, *Spectrochim. Acta, Pt. A: Mol. Spectrosc.*, 1991, **47**, 1745-1750.
S4. N. Buzgar and A. I. Apopei, *Geologie Tomul L.*, 2009, **2**, 97-112.
S5. A. Patlolla, J. Zunino, A. I. Frenkel and Z. Iqbal, *J. Mater. Chem.*, 2012, **22**, 7028-7035.

minerals

Nucleation of Minerals: Precursors, Intermediates and Their Use in Materials Chemistry

Edited by
Denis Gebauer

Printed Edition of the Special Issue Published in *Minerals*

www.mdpi.com/journal/minerals

MDPI

minerals

MDPI

Article

Structural Transition of Inorganic Silica–Carbonate Composites Towards Curved Lifelike Morphologies

Julian Opel [1,2], Matthias Kellermeier [3], Annika Sickinger [1], Juan Morales [2,4], Helmut Cölfen [1,*] and Juan-Manuel García-Ruiz [2,*]

[1] Physical Chemistry, University of Konstanz, Universitätsstrasse 10, D-78457 Konstanz, Germany; julian.opel@uni-konstanz.de (J.O.); annika.sickinger@uni.kn (A.S.)
[2] Laboratorio de Estudios Cristalográficos, Instituto Andaluz de Ciencias de la Tierra (CSIC-UGR), Avenida de las Palmeras N° 4, E-18100 Armilla, Granada, Spain; jmgruiz@ugr.es
[3] Material Physics, BASF SE, RAA/OS–B007, Carl-Bosch-Strasse 38, D-67056 Ludwigshafen, Germany; matthias.kellermeier@basf.com
[4] Instituto de Geología Económica Aplicada (GEA), Universidad de Concepción, 4030000 Concepción, Chile
* Correspondence: helmut.coelfen@uni-konstanz.de (H.C.); jmgruiz@ugr.es (J.-M.G.-R.); Tel.: +49-7531-884063 (H.C.); +34-958-230000 (J.-M.G.-R.)

Received: 2 February 2018; Accepted: 14 February 2018; Published: 18 February 2018

Abstract: The self-assembly of alkaline earth carbonates in the presence of silica at high pH leads to a unique class of composite materials displaying a broad variety of self-assembled superstructures with complex morphologies. A detailed understanding of the formation process of these purely inorganic architectures is crucial for their implications in the context of primitive life detection as well as for their use in the synthesis of advanced biomimetic materials. Recently, great efforts have been made to gain insight into the molecular mechanisms driving self-assembly in these systems, resulting in a consistent model for morphogenesis at ambient conditions. In the present work, we build on this knowledge and investigate the influence of temperature, supersaturation, and an added multivalent cation as parameters by which the shape of the forming superstructures can be controlled. In particular, we focus on trumpet- and coral-like structures which quantitatively replace the well-characterised sheets and worm-like braids at elevated temperature and in the presence of additional ions, respectively. The observed morphological changes are discussed in light of the recently proposed formation mechanism with the aim to ultimately understand and control the major physicochemical factors governing the self-assembly process.

Keywords: biomorphs; barium carbonate; silica; self-assembly; temperature; precipitation kinetics

1. Introduction

Silica biomorphs are an interesting type of self-assembling inorganic–inorganic composite material with remarkably complex architectures. They form in silica-rich solutions at high pH in the presence of alkaline earth metal cations like barium, strontium, and calcium under ambient conditions [1–6]. Upon diffusion of atmospheric carbon dioxide into the system, slow crystallisation of carbonate under the influence of dissolved silicate species results in the spontaneous formation of unusual ultrastructures that consist of uniform elongated carbonate nanocrystals (approximately 200–300 nm long), which maintain long-range co-orientation and are interspersed by certain amounts of amorphous silica; the whole structure is surrounded by a silica skin (typical Si/Ba ratios are 0.1–0.3) [4,7]. On the multimicron scale, these assemblies display intricate morphologies such as flat sheets, helicoids, or tightly wound worms, as shown in Figure 1. While most of the work on silica biomorphs has been carried out with witherite ($BaCO_3$) as the carbonate phase [4], there is increasing

evidence that similar structures can also be obtained with other carbonates, including orthorhombic analogues like strontianite ($SrCO_3$) [8,9] or aragonite ($CaCO_3$) [10–12].

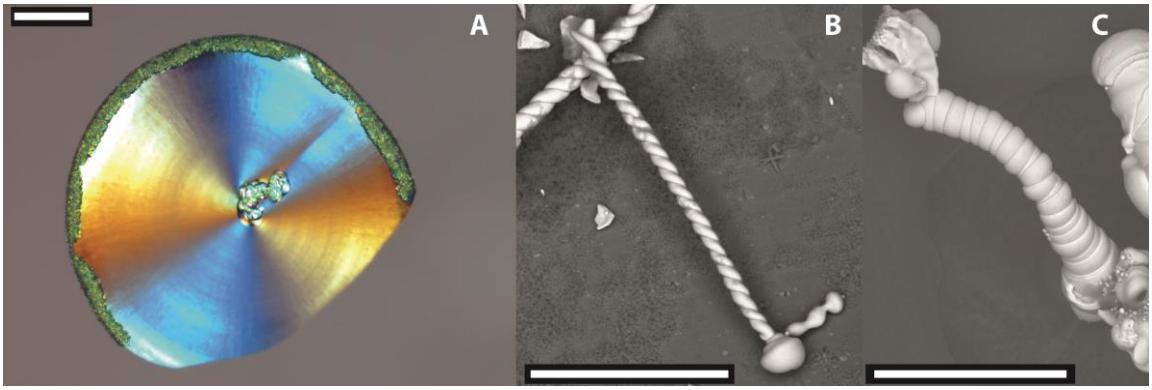

Figure 1. Polarised light microscopy (PLM) and SEM images of the most common architectures displayed by silica biomorph structures grown at room temperature from solutions containing 8.9 mM silica and 5 mM barium chloride: (**A**) flat sheet, (**B**) regular helicoid, (**C**) tightly wound worm. Scale bars are 100 μm.

The mechanisms enabling the structural and morphological complexity observed in this simple inorganic system have been investigated in detail over the past decade, focusing on both the molecular interactions driving self-assembly at the nanoscale and phenomenological aspects determining the final appearance at the micro- and nanoscales [6,13–16]. With respect to the latter, it was found that growth of biomorphs occurs in two general stages. At the beginning of the crystallisation process, small witherite crystals nucleate and grow in a more or less classical way. With time, oligomeric silica species induce fractal branching at the tips of the carbonate crystal, causing progressive bifurcation and ultimately resulting in closed cauliflowerlike spherulites [2,17–19]. At this point, the system passes into the second stage, which is characterised by polycrystalline growth, i.e. numerous nanocrystals are nucleated continuously and/or episodically and co-assemble into aggregates with shapes beyond any constraints of crystallographic symmetry. Typically, the first type of morphologies observed in this stage are flat sheets (Figure 1A), which grow along vessel walls or the solution–air interface. Randomly, these laminar structures start to curl at their rim and assume a new (orthogonal) growth direction along the perimeter of the sheet, which arrests radial advancement and gives birth to more complex three-dimensional shapes. The final morphology is then determined by the interplay of various local parameters, including the relative velocities of growth for different segments as well as their heights. The most common twisted forms obtained at ambient conditions are double helices (Figure 1B) and more tightly scrolled so-called worms (Figure 1C) [2]. In many cases, the carbonate-rich core of the aggregates becomes covered by a layer of amorphous silica, as a result of secondary silica precipitation in the later stages of growth when the bulk pH has been lowered (due to CO_2 uptake) to values where the solubility of silica is noticeably decreased [20].

At the molecular level, the unique behaviour of these inorganic precipitation systems has been ascribed to the pH-mediated coupling of the speciations of carbonate and silicate in solution [2]. As the two components have opposite trends in terms of solubility as a function of pH, it was proposed that they continuously stimulate each other's mineralisation by periodic changes in the local conditions at actively growing fronts: carbonate crystallisation reduces the pH in the microenvironment and thus increases the local supersaturation of silica, which in turn will precipitate and thereby re-increase the pH-shifting the local carbonate speciation to the side of CO_3^{2-} and hence triggering a new event of carbonate nucleation. This coupled chemistry allows numerous silica-coated carbonate nanocrystals to be produced and integrated into the forming superstructures as building units. Indeed, the postulated local pH-cycling at the growing front could be verified experimentally in recent studies by using pH-sensitive fluorescent dyes [14,16].

Interestingly, most of the observations supporting the mechanisms described above were made for the formation of biomorphs in solution or gels under ambient conditions and within a narrow range of concentrations suitable for the growth of the most striking morphologies. However, it is well known already from early works [21] that the structural variety of silica biomorphs is not at all limited to the forms displayed in Figure 1, but can be significantly expanded by adjusting conditions such as pH, salinity and temperature, or by introducing certain additives that are able to interfere with the growth process [3,6,7,22–25]. In the present work, we have re-evaluated the role of temperature in biomorph formation, in order to discuss corresponding changes of structure and morphology in light of the current model of morphogenesis. We show that temperature variation is a straightforward means to obtain further interesting ultrastructures, if the conditions are carefully chosen. The resulting narrow distribution of morphologies highlights the possibility of shape control in these systems, which seems crucial for the targeted design of related materials with potential for actual applications [26,27]. Further experiments performed in the presence of added multivalent ions at room temperature expand the range of accessible morphologies and provide support for a morphogenetic scenario in which the relative rates of silica and carbonate mineralisation determine the evolution of the system on the micron scale.

2. Materials and Methods

2.1. Materials and Sample Preparation

Barium chloride dihydrate (>99%), sodium hydroxide (reagent grade, >98%), lanthanum chloride heptahydrate (≥99.9%), and sodium silicate solution (commercial water glass, containing ~10.6% Na_2O and ~26.5% SiO_2, reagent grade, density: 1.39 g/mL) were purchased from Sigma-Aldrich and used without further purification. All solutions were prepared using MilliQ water with a conductivity of 18 μS/cm. Suitable silicate sols were obtained by diluting 1.39 g of water glass in 349 mL of water. The pH of the resulting sol was adjusted to 11.3 (at 25 °C) by adding aliquots of 0.1 M NaOH solution. Crystallisation experiments were carried out in 24-well plates (Linbro) by mixing 1 mL of the dilute silicate solution with 1 mL of $BaCl_2$ solution at different concentrations (5–500 mM). Optionally, 2 mM $LaCl_3$ was dissolved in the $BaCl_2$ solution prior to mixing with the silica sol. Subsequently, the well plates were covered loosely with a lid and stored, respectively, at room temperature (25 °C) or inside a temperature-controlled oven (30–50 °C) or a cooling chamber (5–20 °C) for 12 h in contact with air, to enable diffusion of CO_2 into the systems and slow crystallisation of $BaCO_3$ under the influence of silica species.

2.2. Analytical Methods

The pH of the mother solutions was measured by a pH meter (Eutech pH 510) before growth. The formed mineral structures were characterised routinely by means of polarised light microscopy (PLM), using a Nikon AZ100 microscope (Nikon Co., Tokyo, Japan) and an Imager m2m from Zeiss (Jena, Germany). In selected cases, scanning electron microscopy (SEM) was performed on a Zeiss EVO15 microscope (Carl Zeiss SMY Ltd., Cambridge, UK). To obtain suitable specimens for the SEM studies, biomorphs were grown on indium tin oxide (ITO) substrates (Osslia), which were placed in Petri dishes with either 35 or 60 mm diameter and covered with 4–8 mL of growth solution.

3. Results and Discussion

In order to investigate the effect of temperature on the formation of silica biomorphs, barium carbonate was crystallised using silica-containing solutions at a fixed composition ([SiO_2] = 17.8 mM and pH = 11.3 (at 25 °C) before mixing with $BaCl_2$ solution) and varying the temperature between 5 and 50 °C. Figure 2 provides an overview on characteristic structures formed at different temperatures and barium concentrations (i.e., a so-called morphodrome).

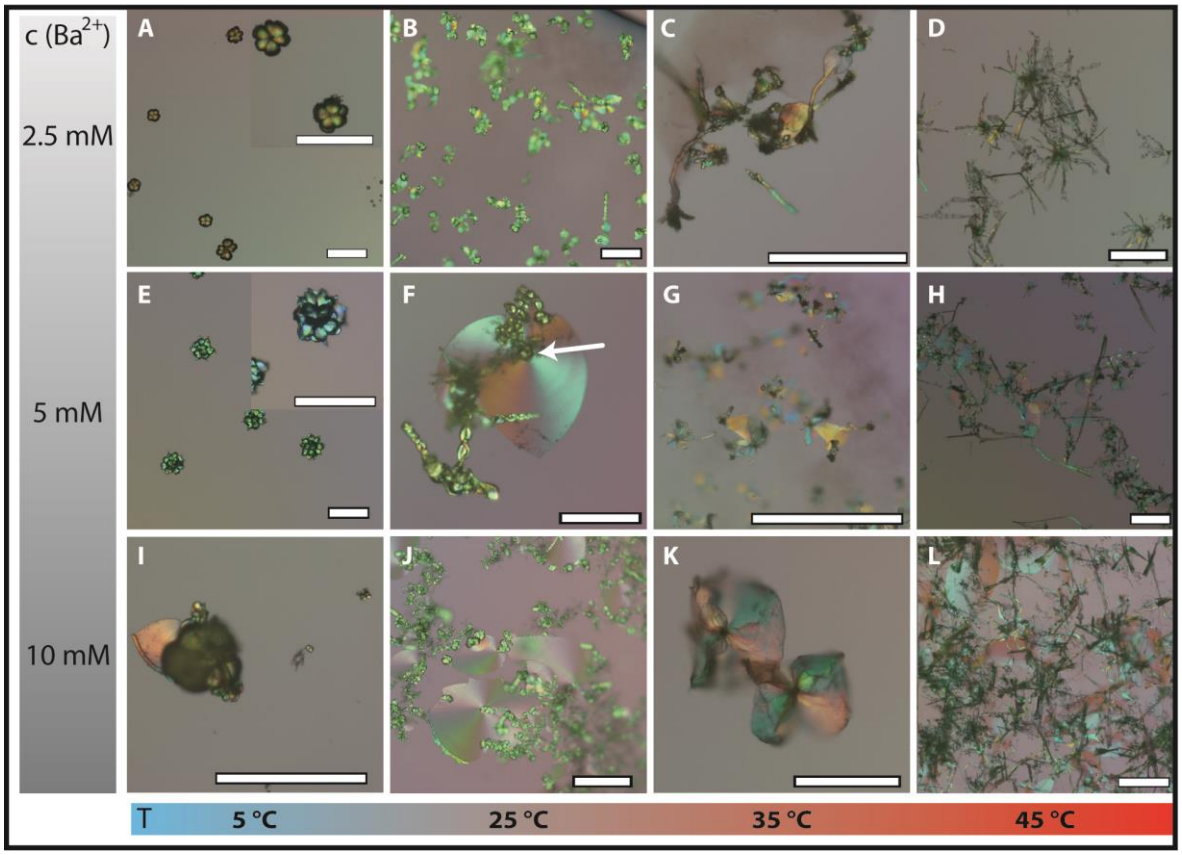

Figure 2. (**A–L**) PLM images of typical biomorphic morphologies obtained at varying barium concentrations and temperatures (as indicated) after a growth period of 12 h using a silica solution with [SiO_2] = 8.9 mM and an initial pH of 11.3 (determined at 25 °C before mixing with barium chloride solution). Note the presence of peculiar 3D trumpetlike shapes in (**G**), as visualised by the optical depth of field. The arrow in (**F**) indicates a closed globular particle, from which a polycrystalline sheet-like aggregate has emerged. Scale bars are 200 μm.

Under "standard" conditions (25 °C and 5 mM $BaCl_2$, Figure 2F), extended flat sheets and helicoids (often intergrown) are observed, as expected and similar to the structures shown in Figure 1. These morphologies can thus be considered as a reference. We note that most of these complex structures emerge from small closed globular particles (or aggregates thereof, as indicated by the arrow in Figure 2F). They form in the fractal regime which has to be very short/fast for such small and discrete morphologies to be observed at the end of the chosen period of growth (12 h).

When the barium concentration is increased to 10 mM (Figure 2J), the total number of aggregates is higher and in particular the sheets grew slightly larger on average. In turn, a Ba^{2+} concentration of 2.5 mM results in fewer, smaller, and less defined structures (Figure 2B), but generally the morphologies are not strongly altered at both higher and lower amounts of cations in the given concentration range. By contrast, lowering the temperature to 5 °C changes the picture fundamentally, as most of the morphologies observed at 2.5 and 5 mM $BaCl_2$ were isolated globular or cauliflowerlike structures (Figures 2A and 2E), and only few poorly developed polycrystalline aggregates were formed at 10 mM even after 24 h (such as the small sheet in Figure 2I). This indicates that growth is terminated at the end of the fractal stage in most cases, i.e., the system fails to enter the second stage of dynamic nanocrystal formation and aggregation. In other words, the conditions prevailing in these experiments do not allow for chemically coupled co-precipitation to be initiated and/or maintained. Probably, this behaviour is related to temperature-dependent changes in the kinetics of carbonate and/or silica mineralisation, caused by differences in either diffusive transport of reactants or the relative rates of precipitation. Generally, the following trends and related consequences are expected with increasing temperature:

- Decrease in the solubility of $BaCO_3$ [28]: higher carbonate supersaturation, higher driving force for carbonate precipitation (thermodynamic factor);
- Decrease in the solubility of CO_2 in water [29]: reduced rate of CO_2 uptake from the atmosphere, slower carbonate precipitation due to diffusion limitation (kinetic factor);
- Acceleration of silica condensation kinetics [30]: reduced rate of silica polymerisation, faster SiO_2 precipitation (kinetic factor);
- Increased solubility of silica [31]: decrease in silica supersaturation, lower driving force for precipitation (thermodynamic factor);
- Increase in the ionic product of water [32]: higher effective pH at the same composition, leading to lower carbonate solubility and higher silica solubility (thermodynamic factor).

Based on these qualitative considerations, it seems reasonable to assume that the growth rates of both silica and carbonate are not sufficiently high to allow for complex ultrastructures to form at lower temperatures. This can be resolved to some extent by increasing the barium concentration (Figure 2I), but the influence of temperature appears to be dominant.

At higher temperatures (35 and 45 °C), there are also regions in the morphodrome where well-developed biomorphs are barely observed. This is particularly true for lower and higher barium concentration (Figures 2C, D, K and L). In the former case (2.5 mM $BaCl_2$), the slower rate of carbonate formation (lower supersaturation and reduced CO_2 uptake) can probably not supply enough building units to keep the pace of the accelerated silica condensation processes. In turn, at 10 mM $BaCl_2$ another effect comes into play, namely the electrostatic screening of negative charges on silicate species by dissolved divalent cations like Ba^{2+} [22]. This bridging interaction catalyses silica condensation and—along with the higher temperature—is expected to accelerate silica precipitation kinetics in a way that is less or not suitable for coupling with carbonate formation. As opposed to that, proper conditions for 3D self-assembly are still maintained at the "standard" barium concentration of 5 mM and temperatures up to 45 °C. Here, however, the resulting biomorphs show substantially different morphologies than at room temperature and 5 mM Ba^{2+} ion concentration, with large (>100 μm) trumpetlike forms representing the major population of ultrastructures. When the temperature is increased to 45 °C the biomorphic landscape changes again and highly branched crystal networks are observed, as shown in Figures 2D,H,L. These structures likely derive from a fractal route that shows substantially different branching behaviour than at room temperature. Here, the initial pseudo-hexagonal twinned crystal core transforms into an open star-like architecture that is poorly filled with silica–carbonate composite matter. In some cases, sheet-like domains are formed in between branches, but these structures are often heavily bended and limited in their growth by the mother crystal branches (*cf*. Figure 2H). This suggests that an increase in temperature changes the branching kinetics, presumably via modulated interactions between growing carbonate surfaces and dissolved silicate species that adsorb specifically on certain witherite faces. One potential scenario is that the accelerated carbonate precipitation gives the silica less time to interfere. Alternatively, the speciation of silica in solution may shift to larger oligomers that show different affinities to interact with specific carbonate faces, thus resulting in a different branching behaviour. In any case, high temperature in combination with high barium concentrations leads to a significant increase in the amount of precipitated matter (probably due to faster carbonate and silica formation). This is shown in Figure 2L, where large networks of tubular filaments and/or twisted ribbons are seen along with various other types of biomorphic morphologies. Interestingly, these forms are much thinner than biomorphs grown at ambient temperature, again indicating important changes in relative growth rates of the components. In summary, the most outstanding feature of the morphodrome established in our study was the formation of biomorphic ultrastructures with trumpetlike appearance. They can sporadically be obtained at temperatures above 30 °C and replace all sheet-like and most twisted morphologies at temperatures above 40 °C.

The formation process of the trumpetlike structures was analysed in more detail, in particular with respect to both differences and similarities compared to biomorph growth at room temperature, which leads to twisted (worms and helicoids) and flat sheet-like (as described in previous works [2–

4] and shown in Figure 1). Figure 3 provides schematic representations of the occurring processes (panels A and B–E) along with selected SEM images showing the relevant stages of growth (panels F–H).

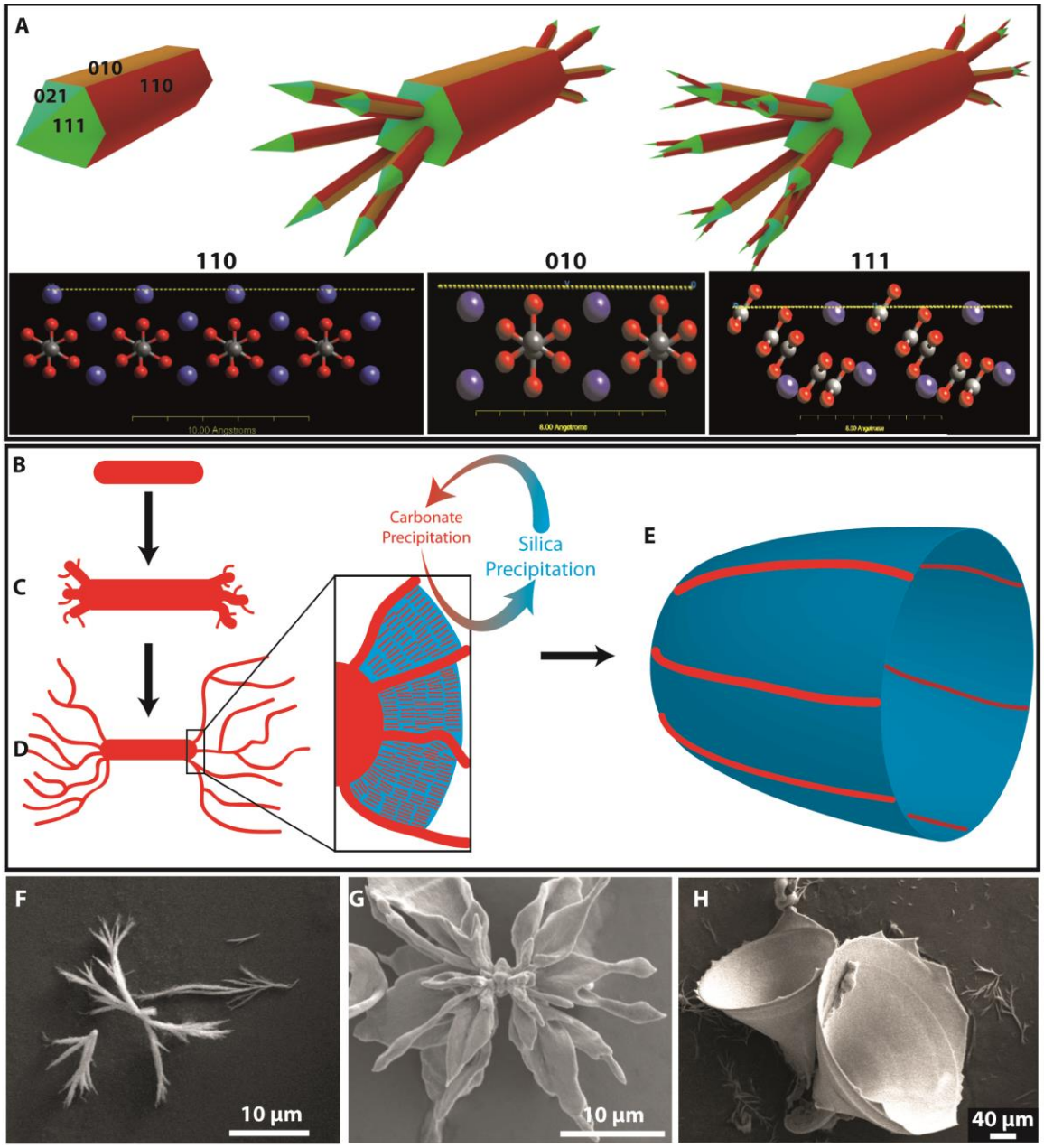

Figure 3. Formation of trumpet-like morphologies at 45 °C and 5 mM $BaCl_2$. (**A**) Scheme of a primary witherite crystal (top), which successively becomes branched due to specific interactions of silica with different faces of the carbonate crystal. Vacuum surface cuts of these faces (bottom) indicate that the (110) faces are positively charged and thus prone to be blocked by negatively charged silicate species. Also, (010) is polar and therefore also likely to interact with negative silica species. Further growth thus occurs through the neutral (021) and (111) faces, so that up to six branches can emerge from the pseudo-hexagonal base. Repetition of this process leads to multiple branching generations. (**B**–**E**) Schematic overview of the growth process of a trumpet-like structure: an initial elongated $BaCO_3$ twin crystal seed grows and undergoes fractal branching as described in (A). At high temperature, this leads to open architectures with large branches, between which polycrystalline growth (i.e., autocatalytic co-precipitation of silica/witherite nanoparticles) occurs and slowly fills up the empty space (inset). Depending on the orientation of the branching, trumpet-like aggregates are formed. (**F**–**H**) SEM micrographs of the initial stage of open fractal branching (**F**), followed by filling of the branches with biomorphic composite material (**G**), ultimately leading to trumpet-like forms (**H**).

Despite the absence of any of the three "standard" morphologies, the nature of the polycrystalline growth mechanism in the second stage of morphogenesis seems comparable to the corresponding processes at room temperature, based on the characteristic thickness oscillations observed for example in Figure 3H and detailed analysis of the texture of the aggregates at the nanoscale [3,15,16]. Consequently, the main difference leading to distinct final shapes must occur at the beginning of the structure formation. As at ambient conditions, morphogenesis starts with fractal branching of a twinned pseudo-hexagonal witherite crystal due to the poisoning influence of oligomeric silica species (Figure 3A). Closer analysis of the carbonate surfaces suggests that adsorption of silicate species (Bittarello et al. [33]) will mainly occur on the positively charged (110) faces but also on the polar (010) faces (cf. Figure 3A). At higher temperatures, the branching behaviour is different, though, and the first step is a splitting into up to six crystal arms, as silicate-covered (110) and (010) faces are blocked while the remaining (021) and (111) faces can serve for heterogeneous nucleation of the up to six crystal arms in a more or less unhindered fashion, as indicated in Figure 3A. This process repeats itself and produces second-generation branches. Increasing the temperature leads to more ordered and larger branched entities as drawn in Figures 3B-D, compared to the much smaller and heavily bifurcated dumbbell-shaped, spherical or raspberry-like forms observed at room temperature (cf. Figure 1). This suggests that branching at high temperature is more symmetric and of lower dimensionality than at ambient conditions, where a much higher branching density and thus much less symmetric architectures are observed. In other words, branching is more chaotic at low temperature and becomes well-defined at high temperature. This could be related to changes in silica condensation kinetics at higher temperatures, leading to different silica speciation and thus to different affinities of silicate species to adsorb on the different relevant carbonate faces, as already proposed above. That, together with changes in the growth rates of carbonate faces, could explain the different branching behaviour at elevated temperatures [28,30]. Once these open branched structures are formed (Figure 3F), the system enters into the second stage of morphogenesis, where the accelerated kinetics of the precipitation of both components leads to a fortification of the autocatalytic mechanism, which then seems to stay in the tolerant zone for coupled co-precipitation to work. However, the resulting nanocrystals do not assemble into the well-known shapes observed at room temperature, but seem to fill the space in between the large branches formed in the first stage of fractal branching (Figure 3G), leading to selective biomorphic growth from open branched fractals into trumpet-like structures (Figure 3H) according to a mechanism as indicated schematically in Figures 3D–E. Thereby, each structure is unique and shows its own interesting shape, which seems to depend on the orientation of the branches. The pathway to the trumpet structure skips the formation of globular particles and leads directly to 3D architectures of silica–barium carbonate composites with curved surfaces. The dominant effect causing this behaviour could be the increased silica solubility, which allows the system more time to develop in a defined manner throughout the fractal stage. Then, the second stage of morphogenesis is entered before a high degree of branching would lead to closed globular structures. Interestingly, the multiple limbs lead to only one final trumpet structure in most cases, suggesting that the different smaller leaf-like domains fuse to one surface or only the most pronounced leaf develops to the final shape.

During the secondary growth process, the orientation of the growing crystals is crucial. When the experiments are conducted under the same conditions but in petri dishes, where the surface/volume ratio is much higher than in the linbro plates, the reaction leads to trumpet-like structures with wider spreading exhausts. Some examples of these forms are shown in Figures 4A and C.

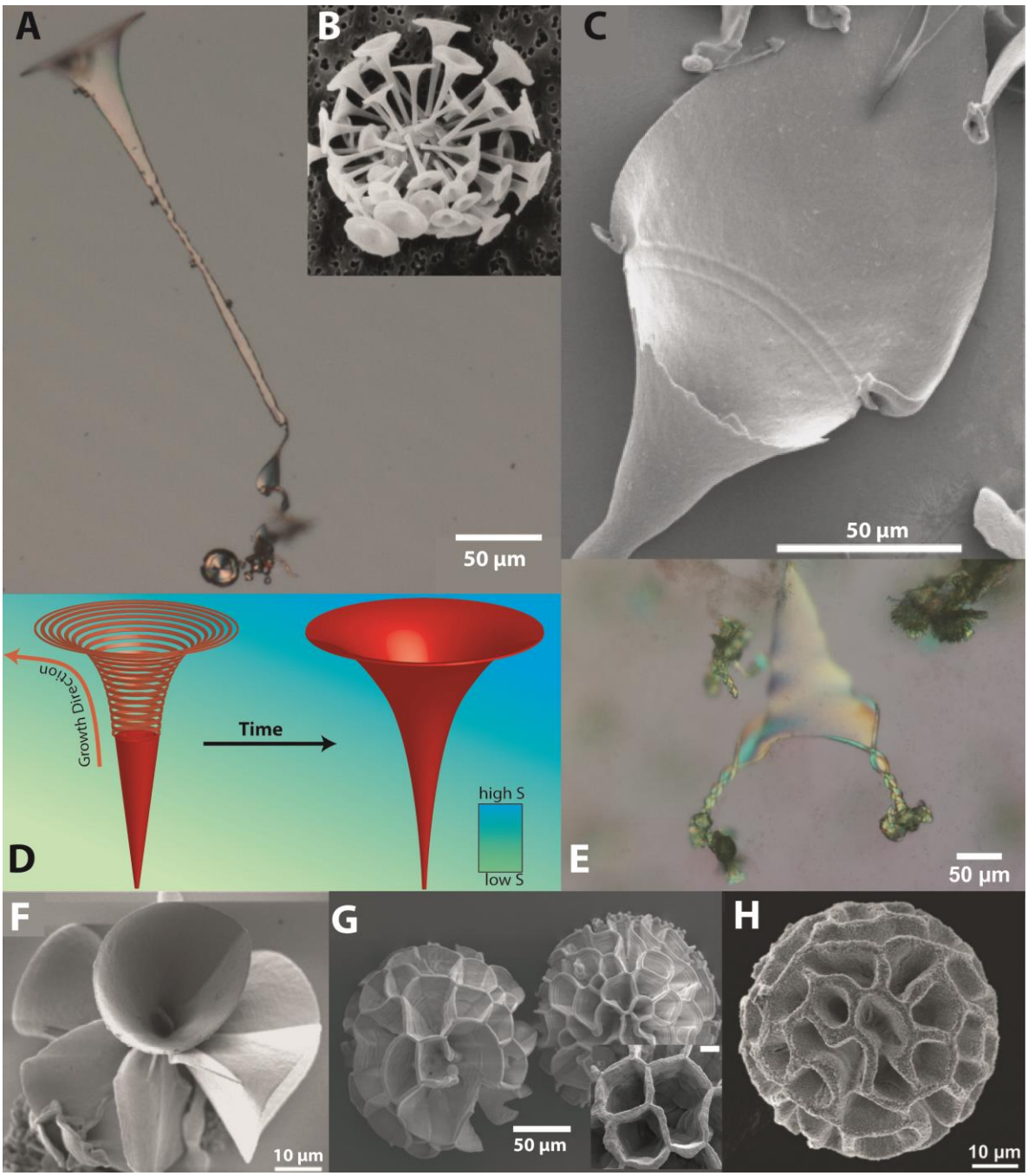

Figure 4. Biomorphs with lifelike morphologies. (**A**,**C**) PLM and SEM images of biomorphs in the shape of a marine coccolith. Formed from solution, containing 5 mM Ba^{2+} and 9 mM silica at 40 °C. (**B**) SEM image of a natural marine coccolith (Reproduced with permission from ref. [24], Copyright 2012 Wiley-VCH Verlag GmbH & Co KGaA). (**D**) Schematic illustration of the formation process of coccolith morphologies illustrating the supersaturation gradient into the solution. (**E**) PLM micrograph of a biomorph structure grown at higher temperature (40 °C) showing a trumpet structure exfolding into two helicoidal structures. (**F**) SEM micrograph of a flower-like biomorph grown from a 5 mM Ba^{2+} solution containing alkaline silica sol at 50 °C. (**G**) SEM micrograph of a coral-like biomorph structure grown at higher Ba^{2+} concentration (250 mM; scale bar of the inlet: 10 µm) (**H**) SEM micrograph grown from a 5 mM Ba^{2+} solution containing alkaline silica sol with 1 mM La^{3+} ions.

As it can be noticed, these structures look similar to a marine coccolith element (*cf.* Figure 4B) [34]. A model of the possible mechanism is presented in Figure 4D. When linbro plates are used, supersaturation is lower and biomorphic aggregates have a narrower shape. Since the petri dish setup favours the availability of CO_2 and therefore the carbonate in the growing front, a higher

supersaturation with respect to barium carbonate and a consequently sharper drop of pH (and higher supersaturation with respect to silica) would be explained. This phenomenon is even more evident once the precipitation occurs nearer to the solution/atmosphere interface. It would also explain the spreading of the branches due to a faster (secondary) growth stage. A similar behaviour was already observed in higher concentrated solution and the spreading could be triggered with a CO_2 burst [35]. Therefore, it can be assumed that this sharp saturation gradient explains this behaviour when completely upright structures are forming. When tilted structures form under the influence of the CO_2, biomorphic aggregates develop irregular exhaust orientation as the one shown in Figure 4C. Additionally, a continuum of different morphologies can be detected in Figures 4A, C, and F. In Figure 4A a transformation from a sheet over a small ribbon to the final trumpet can be found while C shows a reverse exfoliation from a rolled-up trumpet to a 2D sheet-like structure while Figure 4E demonstrates a continuum of shapes and a transition of a trumpet at elevated temperatures into two helicoidal structures.

Further lifelike morphologies can be produced by increasing the barium concentration (Figure 4G; $[Ba^{2+}]$ = 250–500 mM), which shift the formation mechanism as well. [36]. The obtained brain coral-like structures skip the formation of a globular centre, have a nearly perfect spherical shape, and consist of a network of interpenetrating sheet-like units which merge out of the leaf-like parts liked at the seed crystal (similar pathway presented in Figure 3). Their formation is already described by Hyde et al. [36] and reviewed here with consideration of newly obtained knowledge. The formation of these structures follows a similar pathway compared to the trumpets because their formation skips the production of a globular centre. Coral-like architectures can be obtained in a modified way with 5 mM Ba^{2+} ions in solution by using modifiers such as cationic surfactants like CTAB [7] or multivalent ions like La^{3+}. Using such modifiers, similar but more homogenous morphologies were obtained and are shown in the SEM micrograph in Figure 4H. The formation is again influenced in the first stage of the formation which is in good accordance with time-resolved experiments with CTAB additions. An addition of CTAB after a few minutes does not lead to coral structures and "standard" biomorphs will be obtained. At first sight, it is comprehensible that an increase of the pure number of multivalent ions like Ba^{2+} (tested before) or La^{3+} has a similar effect on the system despite the effect on silica precipitation, which is in good accordance with the Schulze–Hardy law [37]. A faster silica formation and a reduced colloidal stability by multivalent cations show similarity to the ultrastructures obtained at elevated temperature. Multivalent ions are known as efficient agents to bridge charged colloids or oligomers like silica [38]. Furthermore, these ions will not be free charged ions within this system due to their tendencies to form complexes with hydroxide, carbonate, and silicate ions to reduce their effective charge. In the end it should be noted that La^{3+} as an additive has less effect on the carbonate precipitation rate and that no significant lanthanum adsorption within the $BaCO_3$ lattice was detected. Additionally, a higher ionic strength depresses the CO_2 uptake rate and its solubility in water, which again leads to a deterioration of the carbonate formation [39]. Therefore, we can assume an extreme of a reduced fractal regime time in the case of coral-like structures. As shown in literature, upon the addition of sodium chloride (note the single charge of Na^+) to the standard procedure, the process will not enter the second stage at all and the crystal formation stops after the formation of the globular particles formed in the first stage (described by Eiblmeier et al. [22]). A reason for this might be the shifting of the equilibrium of free and sodium-coordinated silicate species to the sodium terminated side [40]. Therefore, less silica is available for the autocatalytic process, which is in line with observations made with decreased silica concentrations, and the resident time in the fractal regime is much longer and globules are formed.

4. Conclusions

The presented work describes the influence of several parameters on biomorph growth and highlights the formation process of reported and unreported lifelike morphologies. The individual impact of the temperature, supersaturation, and ions as additives on carbonate and silica formation is discussed in detail and meaningful, plausible explanations were given for the formation mechanism of the strongly bended morphologies. We showed a linkage between coral- and trumpet-

like structures and that a continuum of shapes is possible. Influences of the various and further tuning parameters like the effects of the growth direction and surface/volume ratio were tested. The most exciting growth conditions to lifelike morphologies were highlighted and allow a superior reproducibility.

Acknowledgments: The research leading to these results has received funding from the European Research Council under the European Union's Seventh Framework Programme (FP7/2007-2013)/ERC grant agreement no. 340863

Author Contributions: Julian Opel, Juan Morales and Matthias Kellermeier conceived and designed the experiments; the experiments and analytics were performed by Julian Opel, Annika Sickinger and Matthias Kellermeier; the results were discussed by Julian Opel, Juan Morales, Juan-Manuel Garcia-Ruiz, Helmut Cölfen and Matthias Kellermeier; Julian Opel wrote the paper under supervision of Juan-Manuel Garcia-Ruiz, Helmut Cölfen and Matthias Kellermeier.

Conflicts of Interest: The authors declare no conflict of interest.

References

1. García-Ruiz, J.M.; Hyde, S.T.; Carnerup, A.M.; Christy, A.G.; Van Kranendonk, M.J.; Welham, N.J. Self-assembled silica-carbonate structures and detection of ancient microfossils. *Science* **2003**, *302*, 1194–1197.
2. García-Ruiz, J.M.; Melero-García, E.; Hyde, S.T. Morphogenesis of self-assembled nanocrystalline materials of barium carbonate and silica. *Science* **2009**, *323*, 362–365.
3. Kellermeier, M.; Colfen, H.; Garcia-Ruiz, J.M. Silica biomorphs: Complex biomimetic hybrid materials from "sand and chalk". *Eur. J. Inorg. Chem.* **2012**, *32*, 5123–5144.
4. Kellermeier, M.; Melero-Garcia, E.; Glaab, F.; Eiblmeier, J.; Kienle, L.; Rachel, R.; Kunz, W.; Garcia-Ruiz, J.M. Growth behavior and kinetics of self-assembled silica-carbonate biomorphs. *Chem. - A Eur. J.* **2012**, *18*, 2272–2282.
5. García-Ruiz, J.M. On the formation of induced morphology crystal aggregates. *J. Cryst. Growth* **1985**, *73*, 251–262.
6. Bittarello, E.; Aquilano, D. Self-assembled nanocrystals of barium carbonate in biomineral-like structures. *Eur. J. Mineral.* **2007**, *19*, 345–351.
7. Kellermeier, M.; Glaab, F.; Carnerup, A.M.; Drechsler, M.; Gossler, B.; Hyde, S.T.; Kunz, W. Additive-induced morphological tuning of self-assembled silica-barium carbonate crystal aggregates. *J. Cryst. Growth* **2009**, *311*, 2530–2541.
8. Voinescu, A.E.; Kellermeier, M.; Carnerup, A.M.; Larsson, A.-K.; Touraud, D.; Hyde, S.T.; Kunz, W. Co-precipitation of silica and alkaline-earth carbonates using teos as silica source. *J. Cryst. Growth* **2007**, *306*, 152–158.
9. Terada, T.; Yamabi, S.; Imai, H. Formation process of sheets and helical forms consisting of strontium carbonate fibrous crystals with silicate. *J. Cryst. Growth* **2003**, *253*, 435–444.
10. Imai, H.; Terada, T.; Miura, T.; Yamabi, S. Self-organized formation of porous aragonite with silicate. *J. Cryst. Growth* **2002**, *244*, 200–205.
11. Bittarello, E.; Roberto Massaro, F.; Aquilano, D. The epitaxial role of silica groups in promoting the formation of silica/carbonate biomorphs: A first hypothesis. *J. Cryst. Growth* **2010**, *312*, 402–412.
12. Voinescu, A.E.; Kellermeier, M.; Bartel, B.; Carnerup, A.M.; Larsson, A.-K.; Touraud, D.; Kunz, W.; Kienle, L.; Pfitzner, A.; Hyde, S.T. Inorganic self-organized silica aragonite biomorphic composites. *Cryst. Growth Des.* **2008**, *8*, 1515–1521.
13. Kaplan, C.N.; Noorduin, W.L.; Li, L.; Sadza, R.; Folkertsma, L.; Aizenberg, J.; Mahadevan, L. Controlled growth and form of precipitating microsculptures. *Science* **2017**, *355*, 1395–1399.
14. Montalti, M.; Zhang, G.; Genovese, D.; Morales, J.; Kellermeier, M.; García-Ruiz, J.M. Local ph oscillations witness autocatalytic self-organization of biomorphic nanostructures. *Nat. Commun.* **2017**, *8*, 14427.
15. Nakouzi, E.; Ghoussoub, Y.E.; Knoll, P.; Steinbock, O. Biomorph oscillations self-organize micrometer-scale patterns and nanorod alignment waves. *J. Phys. Chem. C* **2015**, *119*, 15749–15754.
16. Opel, J.; Hecht, M.; Rurack, K.; Eiblmeier, J.; Kunz, W.; Colfen, H.; Kellermeier, M. Probing local pH-based precipitation processes in self-assembled silica-carbonate hybrid materials. *Nanoscale* **2015**, *7*, 17434–17440.
17. García-Ruiz, J.M.; Carnerup, A.; Christy, A.G.; Welham, N.J.; Hyde, S.T. Morphology: An ambiguous indicator of biogenicity. *Astrobiology* **2002**, *2*, 353–369.

18. Kellermeier, M.; Eiblmeier, J.; Melero-García, E.; Pretzl, M.; Fery, A.; Kunz, W. Evolution and control of complex curved form in simple inorganic precipitation systems. *Cryst. Growth Des.* **2012**, *12*, 3647–3655.
19. Kunz, W.; Kellermeier, M. Beyond biomineralization. *Science* **2009**, *323*, 344–345.
20. Alexander, G.B.; Heston, W.; Iler, R.K. The solubility of amorphous silica in water. *J. Phys. Chem.* **1954**, *58*, 453–455.
21. García-Ruiz, J.M. Inorganic self-organization in precambrian charts. *Origins Life Evol. Biosphere* **1994**, *24*, 451–467.
22. Eiblmeier, J.; Dankesreiter, S.; Pfitzner, A.; Schmalz, G.; Kunz, W.; Kellermeier, M. Crystallization of mixed alkaline-earth carbonates in silica solutions at high ph. *Cryst. Growth Des.* **2014**, *14*, 6177–6188.
23. Nakouzi, E.; Knoll, P.; Steinbock, O. Biomorph growth in single-phase systems: Expanding the structure spectrum and ph range. *Chem. Commun. (Camb)* **2016**, *52*, 2107–2110.
24. Melero-Garcí'a, E.; Santisteban-Bailón, R.; Garcí'a-Ruiz, J.M. Role of bulk ph during witherite biomorph growth in silica gels. *Cryst. Growth Des.* **2009**, *9*, 4730–4734.
25. Eiblmeier, J.; Kellermeier, M.; Rengstl, D.; García-Ruiz, J.M.; Kunz, W. Effect of bulk ph and supersaturation on the growth behavior of silica biomorphs in alkaline solutions. *CrystEngComm* **2013**, *15*, 43–53.
26. Opel, J.; Wimmer, F.P.; Kellermeier, M.; Cölfen, H. Functionalisation of silica–carbonate biomorphs. *Nanoscale Horiz.* **2016**, *1*, 144–149.
27. Wang, G.; Zhao, X.; Möller, M.; Moya, S.E. Interfacial reaction-driven formation of silica-carbonate biomorphs with subcellular topographic features and their biological activity. *ACS Appl. Mater. Interfaces* **2015,** *7(42)*, 23412-23417.
28. Busenberg, E.; Plummer, L.N. The solubility of $BaCO_3$ (cr)(witherite) in CO_2-H_2O solutions between 0 and 90 °C, evaluation of the association constants of $BaHCO_3^+$ (aq) and $BaCO_3$ (aq) between 5 and 80 °C, and a preliminary evaluation of the thermodynamic properties of Ba^{2+}(aq). *Geochim. Cosmochim. Acta* **1986**, *50*, 2225–2233.
29. Weiss, R.F. Carbon dioxide in water and seawater: The solubility of a non-ideal gas. *Mar. Chem.* **1974**, *2*, 203–215.
30. Hurd, C.B.; Pomatti, R.C.; Spittle, J.H.; Alois, F.J. Studies on silicic acid gels. XV. The effect of temperature upon the time of set of alkaline gel mixtures. *J. Am. Chem. Soc.* **1944**, *66*, 388–390.
31. Krauskopf, K.B. Dissolution and precipitation of silica at low temperatures. *Geochim. Cosmochim. Acta* **1956**, *10*, 1–26.
32. Marshall, W.L.; Franck, E.U. Ion product of water substance, 0–1000 °C, 1–10,000 bars new international formulation and its background. *J. Phys. Chem. Ref. Data* **1981**, *10*, 295–304.
33. Bittarello, E.; Massaro, F.R.; Rubbo, M.; Costa, E.; Aquilano, D. Witherite ($BaCO_3$)/α-quartz epitaxial nucleation and growth: Experimental findings and theoretical implications on biomineralization. *Cryst. Growth Des.* **2009**, *9*, 971–977.
34. Mann, S. The chemistry of form. *Angew. Chem. Int. Ed.* **2000**, *39*, 3392–3406.
35. Noorduin, W.L.; Grinthal, A.; Mahadevan, L.; Aizenberg, J. Rationally designed complex, hierarchical microarchitectures. *Science* **2013**, *340*, 832–837.
36. Hyde, S.T.; Carnerup, A.M.; Larsson, A.K.; Christy, A.G.; García-Ruiz, J.M. Self-assembly of carbonate-silica colloids: Between living and non-living form. *Physica A* **2004**, *339*, 24–33.
37. Hardy, W.B. A preliminary investigation of the conditions which determine the stability of irreversible hydrosols. *J. Phys. Chem.* **1899**, *4*, 235–253.
38. Bergna, H.E. *The Colloid Chemistry of Silica*. American Chemical Society: Washington DC, US, 1994; Vol. 234, p 724.
39. Zeebe, R.E.; Wolf-Gladrow, D.A. *CO_2 in Seawater: Equilibrium, Kinetics, Isotopes*. Elsevier Sience, Amsterdam, Netherlands, 2001.
40. Iler, K.R. *The chemistry of silica. Solubility, Polymerization, Colloid and Surface Properties and Biochemistry of Silica.* John Wiley & Sons, Inc.: New York, NY, USA, **1979**.

crystals

MDPI

Communication

Hybrid Biomimetic Materials from Silica/Carbonate Biomorphs

Julian Opel [1,2], Niklas Unglaube [1], Melissa Wörner [1], Matthias Kellermeier [3], Helmut Cölfen [1,*] and Juan-Manuel García-Ruiz [2,*]

[1] Physical Chemistry, University of Konstanz, Universitätsstrasse 10, D-78457 Konstanz, Germany; julian.opel@uni-konstanz.de (J.O.); niklas.unglaube@uni.kn (N.U.), melissa.woerner@uni.kn (M.W.)

[2] Laboratorio de Estudios Cristalográficos, Instituto Andaluz de Ciencias de la Tierra (CSIC-UGR), Avenida de las Palmeras 4, E-18100 Armilla, Granada, Spain

[3] Material Physics, BASF SE, RAA/OS–B007, Carl-Bosch-Strasse 38, D-67056 Ludwigshafen, Germany; matthias.kellermeier@basf.com

* Correspondence: helmut.coelfen@uni-konstanz.de (H.C.); jmgruiz@ugr.es (J.-M.G.-R.); Tel.: +49-7531-884063 (H.C.); +34-669434700 (J.-M.G.-R.)

Received: 28 February 2019; Accepted: 14 March 2019; Published: 18 March 2019

Abstract: The formation of a polymer protection layer around fragile mineral architectures ensures that structures stay intact even after treatments that would normally destroy them going along with a total loss of textural information. Here we present a strategy to preserve the shape of silica-carbonate biomorphs with polymers. This method converts non-hybrid inorganic-inorganic composite materials such a silica/carbonate biomorphs into hybrid organic/carbonate composite materials similar to biominerals.

Keywords: biomorphs; barium carbonate; silica; PCDA; pyrrole

1. Introduction

Silica-earth-alkaline carbonate composites show exceptional shapes which is so far a one-of-a-kind appearance within the field of pure inorganic composites [1,2]. They were named silica-biomorphs due to their morphology, which resembles primitive living organisms and their inner textures mimic biominerals [3]. Compared to biominerals, which are normally hierarchically ordered hybrid composites consisting of inorganic minerals and structure conducting organic matter [4–6], biomorphs are purely inorganic composite materials, the structuring role of organic compounds being taken over by amorphous silica. They are self-organized structures that forms upon the coupled co-precipitation of silica (SiO_2) and alkaline -earth metal carbonates, namely witherite ($BaCO_3$), strontianite ($SrCO_3$) or either aragonite or monohydrocalcite ($CaCO_3$) [7–10]. The formation of biomorphs can be described in three stages which are related to pH [11]. In the first stage, the initial single crystal of alkaline -earth metal carbonate experiences splitting provoked by selective adsorption of silica. Iterative splitting triggers fractal growth and eventually leads to primary globular particles [12–14]. The precipitation of the carbonate induces a local and bulk decrease of the pH that can be monitored even at this very early stage [11,15,16]. At this stage nearly no silica is adsorbed within the structure [11]. The second stage starts after some time (depending on the initial pH) and more complex structures form by determining the final shape of the biomorph. During this stage a polycrystalline growth of a myriad of elongated witherite nanorods with a typical size of 200–400 nm in length and 30–50 nm in thickness can be observed [11]. Once the pH drops far enough, the biomorph formation enters the last stage where only secondary precipitation processes occur. Due to

the inverse solubility of silica with respect to pH [17,18], the structures become embedded in a thick silica shell, which grows bigger if the structures mature in the mother solution.

Once extracted from the mother solution, the biomorphs can be further treated as shown in Figure 1. The composite is hollowed by acidic treatment. A diluted hydrochloric or acetic acid can be used to dissolve the inner part within minutes [19]. The result is a hollow structure, which is called a biomorph "ghost." Alternatively, an alkaline treatment with sodium hydroxide solution allows the removal of the silica shell and excavates the so-called "naked" biomorph (*cf*. Figure 1) [20]. A naked biomorph is useful for attachment of molecules or particles with carboxylate groups. One example for an attachment of a monomeric carboxylate species is 10,12-pentacosadiynoic acid (PCDA), a light-polymerizable diacetylen [20]. Poly-PCDA (pPCDA), as a member of the polydiacetylene family, comes with thermochromic properties and can be reversibly or irreversibly switched from a blue into a red state [21,22]. Besides PCDA, conductive polymers like polypyrrole (pPy) or poly thiophenes generated a growing interest in the field of biomineral preservation and replication [23–25]. Furthermore they provide some additional functionality and are used as chemical sensors [26,27], in drug delivery [27], as electronic devices like fuel cells [28] or electro-catalysts [29] and in combination with silica for chromatographic applications [30]. Choi *et al.* presented hierarchically structured pPy in helicoidal shapes and consequently, a pPy replica of a biomorph helix should also be usable as stretchable supercapacitors [31].

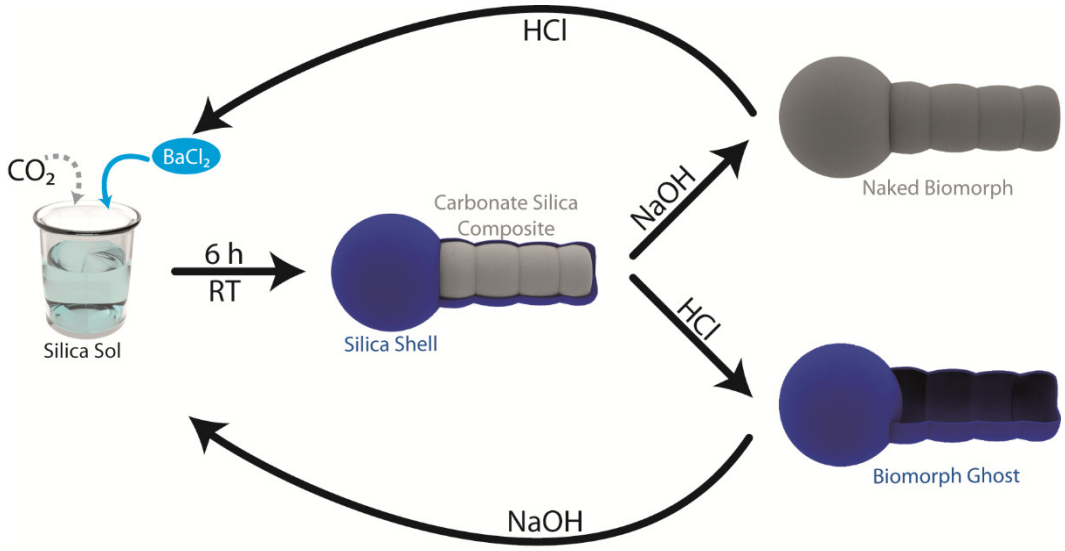

Figure 1. Schematic illustration of biomorph formation at room temperature (RT) and pathways to dissolve each part of composite selectively and return to its precursor state. As intermediate a naked biomorph with an excavated carbonate surface or a hollow biomorph ghost can be obtained.

So far, two known strategies exist to transfer hierarchical structures of a given material into a new one of different composition. The first method is to demineralize a biomineral to obtain an organic template and re-infiltrate the matrix with the new compound [32]. The second strategy consists of replacing the organic matrix with a new material, as shown by Imai and co-workers with dyes or polymers between nanocrystals [33,34]. We show here that a polymer layer around a biomorphic structure sustains the morphology after additional treatment with alkaline and/or acidic solutions while an unpreserved structure vanishes into its precursor state. In total, the following work demonstrates a successful preservation of micro-sculptures with two chosen straightforward pathways and elaborate a third strategy to transfer hierarchical structures into functional organic materials.

2. Materials and Methods

Barium chloride dihydrate (>99%), sodium hydroxide (reagent grade, >98%), sodium silicate solution (commercial water glass, containing 10.6% Na_2O and 26.5% SiO_2, reagent grade, density 1.39

g/ml), copper chloride (97%), 10,12-pentacosadiynoic acid (>97%) and pyrrole (reagent grade, 98%) were purchased from Sigma-Aldrich and used without further purification. Aqueous solutions were prepared using MilliQ water with a conductivity of 18 μS/cm.

2.1. Biomorph Formation

Silica-biomorphs were grown from alkaline silica sol which was prepared by 1.39 g of silica solution diluted with 349 ml of water. The pH of the solution was adjusted to 11.3 with aliquots of 0.1 M NaOH solution. The crystallization occurs in a 6-wells linbro plate by mixing 4 ml of the silica solution with 4 ml of a 10 mM $BaCl_2$ solution. After 8-16 h the structures were extracted from the wells and washed several times with water and ethanol (EtOH). The outer silica layer was removed by incubating 20 mg biomorph powder in 1 ml of a 1 M NaOH solution for 6 h.

2.2. pPCDA Functionalization

PCDA solution was prepared by dissolving 50 mg PCDA in 10 ml tetrahydrofuran (THF). The solution was filtered through a syringe filter (pore size: 0.22 μm) and diluted with 9 ml water and 1 ml 0.1 M NaOH solution. 10 mg of naked biomorphs were incubated for 8 h inside a PCDA solution with different concentrations and stored in the dark. After extracting and washing, the structures can be stored under UV-light for 5 minutes inducing the polymerization to pPCDA. The colour of the biomorph PCDA powder changes to blue.

2.3. pPy Functionalization

10 mg naked biomorphs were added to 1 ml of a 0.01 M $CuCl_2$ solution in isopropanol (iPrOH). After 1 h, additional 750 μl were added. After 1 h the structures were centrifuged and washed twice with 200 μl iso-propanol (iPrOH). After drying the structures were stored in a desiccator containing 10 ml pyrrole. After 2 h the structures begin to darken and turned completely black after 6 h. After the polymerization the inner core of the structures was removed with 0.05 M acetic acid. The residue was washed several times with water and dried under reduced pressure.

2.4. Analytical Methods

The pH of the solutions was measured with a pH meter (Eutech pH 510, Eutech Instruments, Singapore). Scanning electron microscopy (SEM) images were recorded on a Hitachi Tabletop SEM TM3000 (Hitachi-Hightech, Krefeld, Germany) with a backscatter detector and a Zeiss Crossbeam 1540XB (Zeiss, Oberkochen, Germany) with a secondary electron (SE2) and an inlens detector. Energy dispersive X-ray spectroscopy (EDX) was also performed on the Hitachi TM3000. Light microscopy was performed on a Zeiss Imager m2m (Zeiss, Jena, Germany) and Axio Zoom (Zeiss, Jena, Germany). Confocal laser scanning microscopy (cLSM) was performed on a Zeiss LSM700 (Zeiss, Jena, Germany). Attenuated total reflection Fourier transformed infrared (ATR-FTIR) spectroscopy was performed on a Perkin Elmer Spectrum 100 (PerkinElmer, Waltham, MA, USA).

3. Results and Discussion

3.1. Preservation with pPCDA

The first preservation route focuses on a light-polymerizable surfactant named PCDA. This molecule is immobilized on the witherite surface by incubating naked biomorphs (without an outer silica shell) in a mixture of sodium hydroxide, THF and water with different PCDA concentrations (120–12000 ppm). The attachment process is schematically shown in Figure 2 A. To make sure that

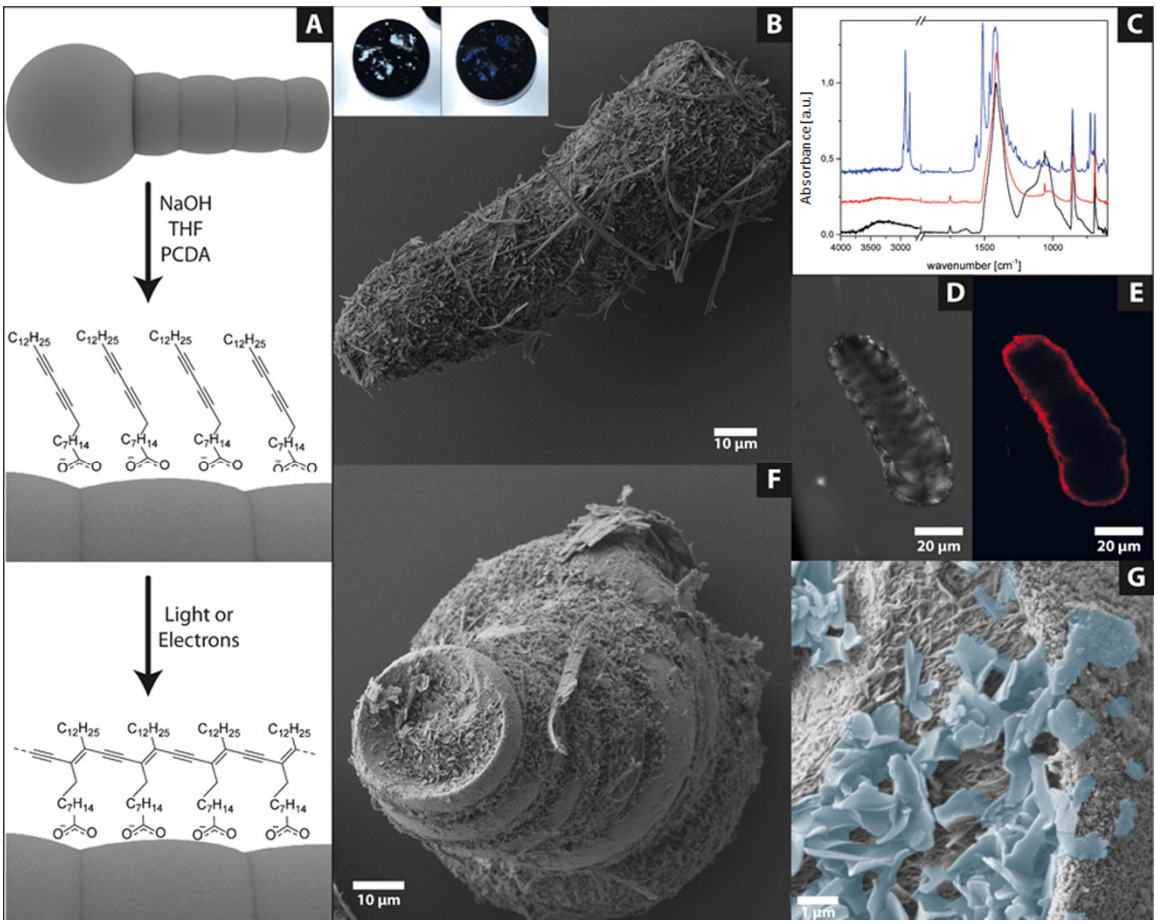

Figure 2. (**A**) Scheme of biomorph coverage with 10,12-pentacosadiynoic acid (PCDA) and the polymerization to pPCDA. (**B**) Scanning electron microscope (SEM) image of a fully covered biomorph worm (inlet: colour transformation of the powder after SEM investigation; c(PCDA) = 12000 ppm). (**C**) Attenuated total reflection Fourier transformed infrared (ATR-FTIR) spectra of an untreated biomorph (black) a naked biomorph (red) and a pPCDA covered biomorph (blue). (D/E) Confocal Laser scanning microscopy (cLSM) images of a fully covered biomorph worm in the transmission (**D**) and fluorescence (**E**) channel. (**F**) SEM image of a partially covered biomorph worm (c(PCDA) = 2000 ppm) with the corresponding image at higher magnification (**G**), the blue coloured flakes indicate the pPCDA).

only the monomer is attached on the surface the solution was pushed through a syringe filter to remove polymer particles from the solution. The naked biomorphs were immersed in the colourless solution for several hours. To ensure that the PCDA does not polymerize during the attachment process, the samples were stored in darkness. After the chosen incubation time (4–16 h) the solution was removed and the modified biomorphs were dried under reduced pressure. The obtained modified structures were investigated with scanning electron microscopy (SEM). Observation of the structures with the electron beam induces polymerization of the attached monomers to the bluish pPCDA (*cf*. inlet photos of the SEM stub before and after the SEM investigation in Figure 2 B). To demonstrate the attachment of the PCDA on the structure, the process was observed by FTIR-spectroscopy. The transformation of the silica-biomorphs to the pPCDA-biomorphs is shown in Figure 2 C. The black spectrum shows the characteristic carbonate (witherite) vibrations as well as the most abundant signal for amorphous silica (peak at 1000 cm^{-1}). After treatment with NaOH and the transformation to the naked biomorphs, the broad peak vanishes and only the witherite signals remain (red spectrum). The modification with PCDA is observable as lines at 2870 and 2965 cm^{-1}, which are the symmetric and asymmetric C-H vibrations. The carboxyl signal of the PCDA appears at 1540 cm^{-1} which is in good accordance to the literature [22]. Choosing a higher concentration of PCDA in the functionalization solution leads to the full coverage of the biomorph worm with pPCDA

flakes, which preserve and display the outline of the structure beneath quite well. A detailed replica of the topography is not achievable with these high monomer concentrations. In previous work, we have demonstrated that the shape of the biomorph structure was preserved in acidic solutions even after removing the outer silica layer [20]. To ensure that a full coverage was achieved confocal laser scanning microscopy (cLSM) was used due to the strong fluorescence of pPCDA [20,35] (*cf*. Figure 2 D/E). Smoothening the reprint might be possible by reducing the amount of monomer but a full coverage is not sustainable because an enrichment of PCDA was found inside of the notches of the biomorph worm (*cf*. Figure 2 F/G). In Figure 2 G at higher magnification the witherite nanorods and pPCDA flakes (false coloured in blue) can be visualized alongside each other. Excavated carbonate rods are not able to resist acidic solutions and therefore, the structures vanish completely after acid treatment. Also, the pPCDA flakes do not stick together and a polymer replica of the structures does not remain. The pPCDA coverage is useful to passivate bigger carbonate structures but a smooth and detailed replica cannot be obtained. Nevertheless, it still remains a readily applicable strategy to produce inverse biominerals.

3.2. Preservation with pPy

Polypyrrole has gained attention due to its ability to produce polymer replicas of biominerals like sea urchin spines [25]. Recent breakthroughs in the preparation of polymer replicas on the micro scale are a huge improvement to preserve fragile structures and it now seems transferable to silica-biomorphs [23]. To obtain a full pPy coating around a biomorph we followed the route presented in Figure 3 A. At first $CuCl_2$ is brought onto the structure as a catalyst. Due to the rough surface of the naked biomorph, many small crystals of $CuCl_2$ attach on the surface. These small crystals do not affect the shape as can be seen in Figure 3 B. After drying, the structures were transferred into a desiccator. On the bottom of the desiccator, pyrrole was deposited creating a pyrrole saturated atmosphere. The pyrrole molecules diffuse to the catalyst and begin to polymerize. During this process, a colour change of the biomorphs can be observed by the naked eye. After 3 h the white powder turns grey and after 6 h a black powder was obtained. To ensure that the polymer layer is neither growing too big nor crosslinks the structures, the incubation time was kept at 6 h. After extracting the structures from the desiccator, the shapes of the naked biomorphs used as starting material remained nearly unchanged. Elemental analysis via energy dispersive X-ray spectroscopy (EDX) showed Ba, Cu, Cl, C, O, N and traces of Si. Except the higher amount of N and the signals from the catalyst, the spectrum looks identical to an EDX of the naked biomorphs. The most meaningful proof of the full coverage and subsequent preservation of the biomorph form is the dissolution of the inner core which was achieved with 0.05 M acetic acid. The core dissolves much slower compared to normal silica-biomorphs and as a result hollow structures were obtained and shown in the SEM image in Figure 3 C. Note that the SEM images were recorded with a backscatter detector, which gives a good material contrast. The structures in Figure 3 B show a higher contrast compared to the hollow structures without $BaCO_3$ in C. The EDX spectrum of these polymer replicas as well as their preliminary stages are shown in Figure 3 D. The black spectrum shows the silica-biomorphs, the red spectrum the naked biomorphs with $CuCl_2$, which can be found at 8.02 eV. Here we can see that the outer silica layer has vanished and no Si signal was measured at 1.75 eV. In the upper blue spectrum, the Ba signals (green rectangular outline) have vanished and only traces of the raw material (Ba: 0.24; Si: 0.25 at.%) and the catalyst (0.4 at.%) are detected. The main component consists of carbon and nitrogen. Therefore, the pPy route is most suitable to preserve micro-sculptures on the microscale and to obtain conductive inverse biominerals.

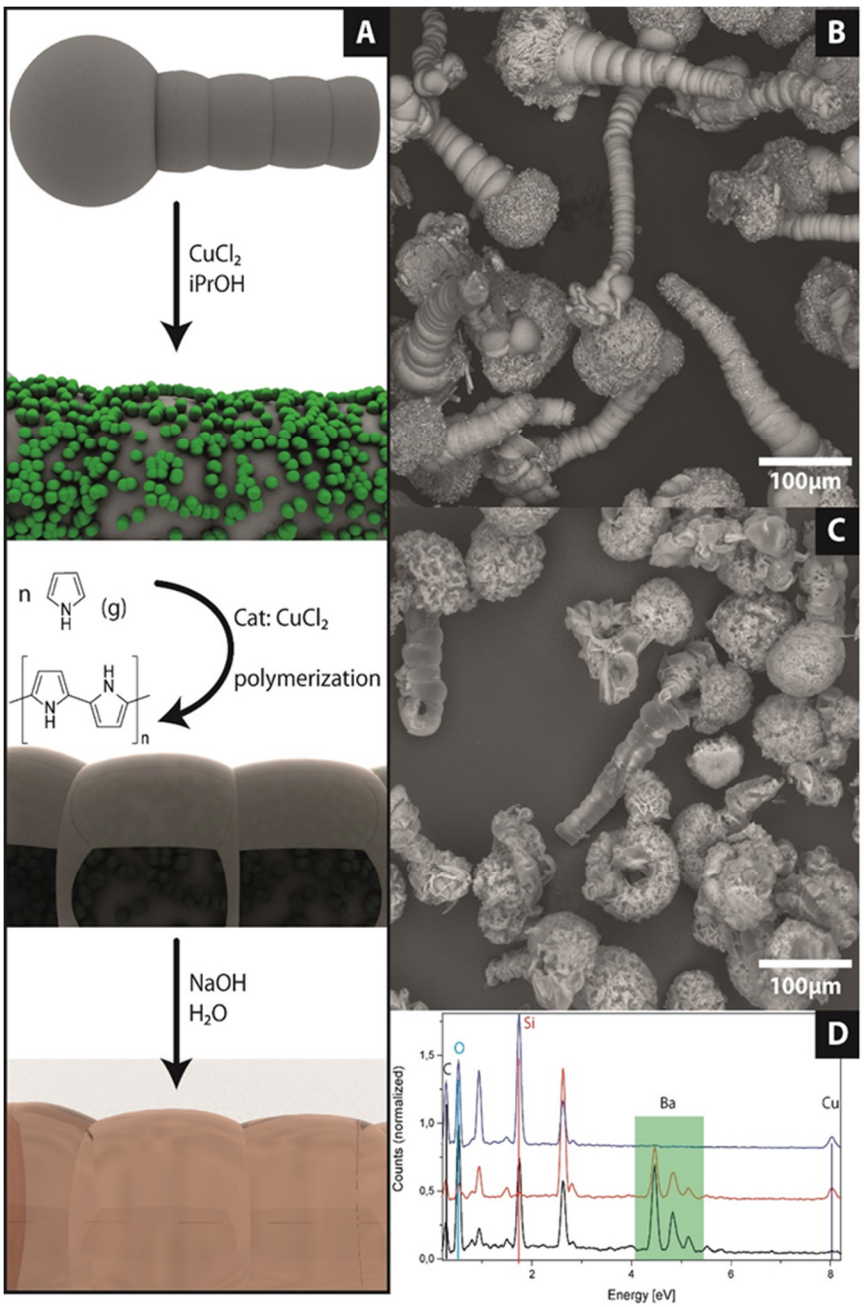

Figure 3. (**A**) Schematic illustration of the pPy route to preserve biomorphic structures. $CuCl_2$ crystals are attached from iPrOH solution on the surface of a naked biomorph. In the next step pyrrole diffuses via the gas phase onto the surface and is polymerized by $CuCl_2$. After the polymerization the inner parts can be removed by sodium hydroxide solution. (**B**) SEM image of catalyst crystals attached on biomorph worms. (**C**) Inverse biomorphs after Polymerization of pyrrole (Py) and removal of the inner part. (**D**) Energy dispersive X-ray (EDX) spectra of the different steps to plastic biomorphs. The untreated biomorphs are shown in black. Naked biomorphs with $CuCl_2$ in red and the final inverse biomorphs without inorganics are shown in blue.

4. Conclusions

We have achieved a full coverage of silica-carbonate composites by using PCDA and pyrrole to form an organic layer around the inorganic motifs. Thus, we have converted purely inorganic-inorganic composites into hybrids than can be named inverse biomorphs. The pathways to obtain these organic or hybrid structural motifs are described in detail and the methodology can be adapted to other microscopic biominerals or synthetic biomimetic architectures. Furthermore, the inorganic and structuring part of the biomorphs can be removed at ambient conditions resulting in a structured

organic replica of the biomorph. With this straight-forward method, micro-structured functional materials can be formed and used as stretchable supercapacitors.

Author Contributions: J.O., M.K., H.C. and J.-M.G.-R. conceived and designed the experiments. The experiments where performed by J.O., N.U. (pPy part) and M.W. (pPCDA part). Analytical measurements where performed by J.O., N.U. and M.W. J.O. wrote the paper under supervision of J.-M.G.-R., H.C. and M.K.

Funding: The authors thank the European Research Council under the European Union's seventh Framework Program (FP7/2007-2013)/ERC grant agreement no. 340863.

Acknowledgments: The authors thank the Particle Analysis Center of the University of Konstanz (SFB 1214), the Nanostructure Laboratory and the Bioimaging center of the University of Konstanz for access to their instruments and Andra-Lisa Hoyt for corrections.

Conflicts of Interest: The authors declare no conflict of interest.

References

1. Kellermeier, M.; Colfen, H.; Garcia-Ruiz, J.M. Silica biomorphs: Complex biomimetic hybrid materials from "sand and chalk". *Eur. J. Inorg. Chem.* **2012**, *2012*, 5123–5144.
2. Nakouzi, E.; Steinbock, O. Self-organization in precipitation reactions far from the equilibrium. *Sci. Adv.* **2016**, *2*, e1601144.
3. Garcia-Ruiz, J.M.; Hyde, S.T.; Carnerup, A.M.; Christy, A.G.; Van Kranendonk, M.J.; Welham, N.J. Self-assembled silica-carbonate structures and detection of ancient microfossils. *Science* **2003**, *302*, 1194–1197.
4. Mann, S. The chemistry of form. *Angew. Chem. Int. Ed.* **2000**, *39*, 3392–3406.
5. Addadi, L.; Weiner, S. Control and design principles in biological mineralization. *Angew. Chem. Int. Ed.* **1992**, *31*, 153–169.
6. Lowenstam, H.A.; Weiner, S.; Weiner, S. *On Biomineralization*; Oxford University Press: New York, NY, USA, 1989; Volume 324.
7. Kellermeier, M.; Melero-García, E.; Kunz, W.; García-Ruiz, J.M. Local autocatalytic co-precipitation phenomena in self-assembled silica-carbonate materials. *J. Colloid Interface Sci.* **2012**, *380*, 1–7.
8. Zhang, G.; Delgado-Lopez, J.M.; Choquesillo-Lazarte, D.; Garcia-Ruiz, J.M. Growth behavior of monohydrocalcite (caco3 center dot h2o) in silica-rich alkaline solution. *Cryst. Growth Des.* **2015**, *15*, 564–572.
9. Zhang, G.; Garcia-Ruiz, J.M.; Sanchez-Migallon, J.M. Growth behaviour of silica/carbonate nanocrystalline composites of calcite and aragonite. *J. Mater. Chem. B* **2017**, *5*, 1658–1663.
10. Zhang, G.; Verdugo-Escamilla, C.; Choquesillo-Lazarte, D.; Garcia-Ruiz, J.M. Thermal assisted self-organization of calcium carbonate. *Nat. Commun.* **2018**, *9*, 5221.
11. Kellermeier, M.; Melero-Garcia, E.; Glaab, F.; Eiblmeier, J.; Kienle, L.; Rachel, R.; Kunz, W.; Garcia-Ruiz, J.M. Growth behavior and kinetics of self-assembled silica-carbonate biomorphs. *Chem. Eur. J.* **2012**, *18*, 2272–2282.
12. García-Ruiz, J.M.; Melero-García, E.; Hyde, S.T. Morphogenesis of self-assembled nanocrystalline materials of barium carbonate and silica. *Science* **2009**, *323*, 362–365.
13. Opel, J.; Kellermeier, M.; Sickinger, A.; Morales, J.; Cölfen, H.; García-Ruiz, J.-M. Structural transition of inorganic silica–carbonate composites towards curved lifelike morphologies. *Minerals* **2018**, *8*, 75.
14. Bittarello, E.; Roberto Massaro, F.; Aquilano, D. The epitaxial role of silica groups in promoting the formation of silica/carbonate biomorphs: A first hypothesis. *J. Cryst. Growth* **2010**, *312*, 402–412.
15. Opel, J.; Hecht, M.; Rurack, K.; Eiblmeier, J.; Kunz, W.; Colfen, H.; Kellermeier, M. Probing local ph-based precipitation processes in self-assembled silica-carbonate hybrid materials. *Nanoscale* **2015**, *7*, 17434–17440.
16. Montalti, M.; Zhang, G.; Genovese, D.; Morales, J.; Kellermeier, M.; García-Ruiz, J.M. Local ph oscillations witness autocatalytic self-organization of biomorphic nanostructures. *Nat. Commun.* **2017**, *8*, 14427.
17. Alexander, G.B.; Heston, W.; Iler, R.K. The solubility of amorphous silica in water. *J. Phys. Chem.* **1954**, *58*, 453–455.
18. Iler, K.R. *The Chemistry of Silica. Solubility, Polymerization, Colloid and Surface Properties and Biochemistry of Silica*; John Wiley & Sons: Hoboken, NJ, USA, 1979.
19. Garcia Ruiz, J.M.; Carnerup, A.; Christy, A.G.; Welham, N.J.; Hyde, S.T. Morphology: An ambiguous indicator of biogenicity. *Astrobiology* **2002**, *2*, 353–369.

20. Opel, J.; Wimmer, F.P.; Kellermeier, M.; Cölfen, H. Functionalisation of silica–carbonate biomorphs. *Nanoscale Horiz.* **2016**, *1*, 144–149.
21. Pang, J.B.; Yang, L.; McCaughey, B.F.; Peng, H.S.; Ashbaugh, H.S.; Brinker, C.J.; Lu, Y.F. Thermochromatism and structural evolution of metastable polydiacetylenic crystals. *J. Phys. Chem. B* **2006**, *110*, 7221–7225.
22. Patlolla, A.; Zunino, J.; Frenkel, A.I.; Iqbal, Z. Thermochromism in polydiacetylene-metal oxide nanocomposites. *J. Mater. Chem.* **2012**, *22*, 7028–7035.
23. Göppert, A.; Cölfen, H. Infiltration of biomineral templates for nanostructured polypyrrole. *Rsc. Adv.* **2018**, *8*, 33748–33752.
24. Munekawa, Y.; Oaki, Y.; Imai, H. An experimental study on the processes of hierarchical morphology replication by means of a mesocrystal: A case study of poly (3, 4-ethylenedioxythiophene). *Langmuir* **2014**, *30*, 3236–3242.
25. Oaki, Y.; Kijima, M.; Imai, H. Synthesis and morphogenesis of organic polymer materials with hierarchical structures in biominerals. *J. Am. Chem. Soc.* **2011**, *133*, 8594–8599.
26. Janata, J.; Josowicz, M. Conducting polymers in electronic chemical sensors. *Nat. Mater.* **2003**, *2*, 19–24.
27. Geetha, S.; Rao, C.R.K.; Vijayan, M.; Trivedi, D.C. Biosensing and drug delivery by polypyrrole. *Anal. Chim. Acta* **2006**, *568*, 119–125.
28. Unni, S.M.; Dhavale, V.M.; Pillai, V.K.; Kurungot, S. High pt utilization electrodes for polymer electrolyte membrane fuel cells by dispersing pt particles formed by a preprecipitation method on carbon "polished" with polypyrrole. *J. Phys. Chem. C* **2010**, *114*, 14654–14661.
29. Olson, T.S.; Pylypenko, S.; Atanassov, P.; Asazawa, K.; Yamada, K.; Tanaka, H. Anion-exchange membrane fuel cells: Dual-site mechanism of oxygen reduction reaction in alkaline media on cobalt-polypyrrole electrocatalysts. *J. Phys. Chem. C* **2010**, *114*, 5049–5059.
30. Ge, H.; Wallace, G.G. High-performance liquid chromatography on polypyrrole-modified silica. *J. Chromatogr. A* **1991**, *588*, 25–31.
31. Choi, C.; Kim, J.H.; Sim, H.J.; Di, J.; Baughman, R.H.; Kim, S.J. Microscopically buckled and macroscopically coiled fibers for ultra-stretchable supercapacitors. *Adv. Energy Mater.* **2017**, *7*, 1602021.
32. Siglreitmeier, M.; Wu, B.; Kollmann, T.; Neubauer, M.; Nagy, G.; Schwahn, D.; Pipich, V.; Faivre, D.; Zahn, D.; Fery, A.; et al. Multifunctional layered magnetic composites. *Beilstein J. Nanotechnol.* **2015**, *6*, 134–148.
33. Oaki, Y.; Imai, H. The hierarchical architecture of nacre and its mimetic material. *Angew. Chem. Int. Ed.* **2005**, *44*, 6571–6575.
34. Oaki, Y.; Imai, H. Nanoengineering in echinoderms: The emergence of morphology from nanobricks. *Small* **2006**, *2*, 66–70.
35. Dei, S.; Matsumoto, A.; Matsumoto, A. Thermochromism of polydiacetylenes in the solid state and in solution by the self-organization of polymer chains containing no polar group. *Macromolecules* **2008**, *41*, 2467–2473.

Symbiosis of Silica Biomorphs and Magnetite Mesocrystals

Julian Opel, Julian Brunner, Ramon Zimmermanns, Tristan Steegmans, Elena Sturm, Matthias Kellermeier, Helmut Cölfen,* and Juan-Manuel García-Ruiz**

Silica biomorphs are extraordinary inorganic superstructures formed via autocatalytic co-precipitation and bottom-up self-assembly of alkaline-earth carbonates and silica. However, they show no inherent functionality except for their striking textural motifs and curved morphologies. This work presents strategies to magnetize silica biomorphs, thus creating thermally stable ceramic microswimmers with unique elaborate shapes. This is achieved by growing super paramagnetic magnetite mesocrystals on and around the complex curved surfaces of biomorphs, while keeping their morphology and maintaining mesocrystal integrity. Selective mesocrystal formation on certain parts of the substrates is induced by chemical modification of the biomorph surface, increasing the loading of magnetite on the silica–carbonate structures and, in suitable cases, rendering them able to respond to external magnetic fields and move as microswimmer entities. In this way, the complex ultrastructure of silica biomorphs is successfully used as a template for functional ceramics. Furthermore, selective dissolution of the carbonate core from the biomorphs leads to hollow magnetic structures that could be filled with actives, thus serving as microcarriers with considerable loading capacity.

1. Introduction

Controlled movement on the microscale is a worthwhile goal in materials science. In principle, it necessitates a swimming unit and a responding unit or engine, which interacts with outer fields or converts fuel.[1] However, so far, it has been challenging to fabricate microswimmers with varying complex shapes within a single batch, which may enable interesting features such as self-propelling. Silica–carbonate "biomorphs" could be promising archetypes for the design of such swimming units, since they form spontaneously by self-assembly and grow into elaborate curved architectures on the multi-micrometer to millimeter scale.[2] Among the morphologies commonly displayed by these inorganic–inorganic hybrids, the most interesting shapes for swimming or carrying applications are the chiral filamentous forms, i.e., worm-like braids, helicoids, and twisted ribbons. All these peculiar structures can be obtained in a simple one-pot synthesis from aqueous media at ambient conditions. Indeed, biomorphs form on addition of alkaline-earth metal cations like barium, strontium, or calcium to alkaline, silica-rich solutions-, or gels, with subsequent diffusion of atmospheric CO_2 triggering the slow crystallization of carbonates under the influence of silicate species.[2a,3]

The formation of complex ultrastructures relies on an autocatalytic co-precipitation mechanism that produces uniform carbonate nanocrystals, which self-assemble on the mesoscale and become embedded in a matrix of amorphous silica.[2a] The rich structural variety of biomorphs is shown in **Figure 1**a–e (also compare with Figure S1a in the Supporting Information for an overview on typical structures obtained from a single batch) and can be explained based on differences in local growth velocities during the formation process, which can induce local curling and thus give rise to curved and twisted architectures.[3a,4] Once these structures are formed and self-assembly has ceased, secondary precipitation of silica (due to the lowered bulk pH) often leads to the deposition of a continuous skin of amorphous silica all over the structures.[5] Moreover, long reaction times can also cause secondary precipitation of (regular) carbonate crystals, which typically grow more or less selectively at the apex of the structures and their outer edges. In this stage, no coupled precipitation occurs and carbonate formation is preferred (note that both of these secondary processes will be used for functionalization below).

While many previous studies on silica biomorphs were focused on their morphogenesis and structural control[2b,3c,6] as well as relevance for primitive life detection,[3d] possible functional properties of biomorphs have hardly been explored until recently. The first successful surface functionalization of the as-obtained silica–carbonate hybrids was achieved using silane chemistry

J. Opel, J. Brunner, R. Zimmermanns, T. Steegmans, Dr. E. Sturm, Prof. H. Cölfen
Physical Chemistry
University of Konstanz
Universitätsstraße 10, D-78457 Konstanz, Germany
E-mail: helmut.coelfen@uni-konstanz.de

J. Opel, Prof. J.-M. García-Ruiz
Laboratorio de Estudios Cristalográficos
Instituto Andaluz de Ciencias de la Tierra (CSIC-UGR)
Avenida de las Palmeras N° 4, ES-18100 Armilla, Granada, Spain
E-mail: jmgruiz@ugr.es

Dr. M. Kellermeier
Material Physics
BASF SE
RAA/OS–B007, Carl-Bosch-Strasse 38, D-67056 Ludwigshafen, Germany
E-mail: matthias.kellermeier@basf.com

The ORCID identification number(s) for the author(s) of this article can be found under https://doi.org/10.1002/adfm.201902047.

DOI: 10.1002/adfm.201902047

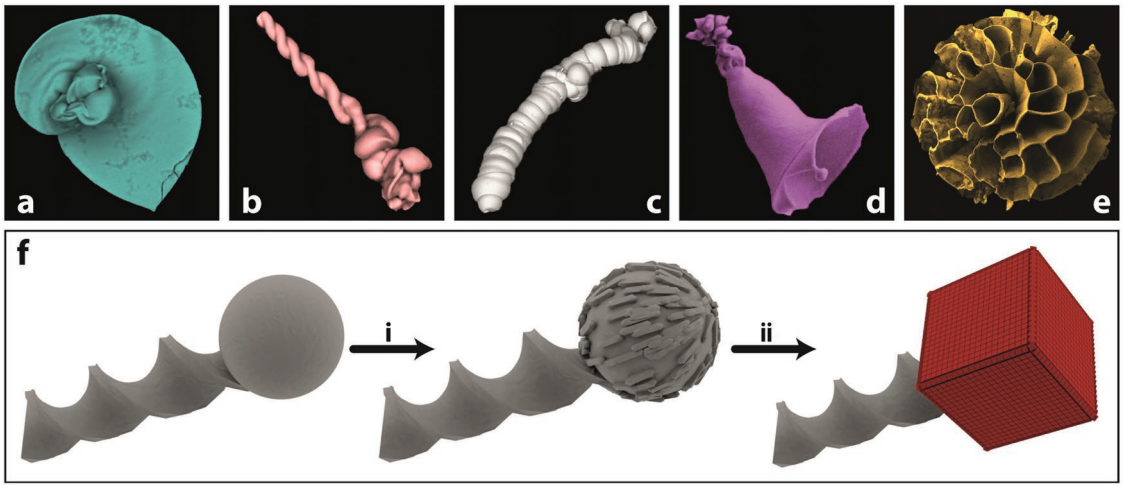

Figure 1. Morphological variety of silica biomorphs and the approach to magnetize them. a–e) Scanning electron microscopy images in false colors of a) a biomorphs' sheet, b) helix, c) worm-like braid, d) trumpet, and e) coral. f) Magnetization approach with magnetite mesocrystals. Methodological approach of the magnetization of silica biomorphs by heterogeneous nucleation of magnetite mesocrystals. In the first step, i) decoration of the globular end with witherite crystals is followed by ii) the selective mesocrystal formation.

in combination with nanoparticles or by controlled polymerization of organic matter around the inorganic template.[7] Later, the entire bulk composition of biomorphs was changed after growth by ion exchange and subsequent conversion to semiconducting perovskites.[8] In the present work, we have investigated the potential of biomorphs to serve as swimming units in microscale motors able to operate even at high temperature. Biomorph shapes which have a potential as a swimming unit are the helicoidally and the wormlike braids (cf. Figure 1b,c) and therefore this work focuses on this two types of morphologies.

To control the movement of silica biomorphs on the micrometer scale, they need to be equipped with a suitable engine or responding unit. One such engine could, in principle, be iron oxide catalysts, which would have to be immobilized on the biomorph surface, where they could then decompose hydrogen peroxide and generate gas bubbles that drive the motion of the microswimmers, as reported previously for other systems.[1a,9] However, since the size of biomorphs is typically in the range of at least tens of micrometers, they are likely too heavy to be propelled by this type of motor pretested. Instead, they require a stronger driving force—such as that provided by an external physical field. Here we have chosen to equip silica biomorphs with a magnetic responding unit that should allow them to navigate in an applied magnetic field. A suitable responding unit for magnetic biomorph microswimmers was obtained by particle-based crystallization, namely the assembly of super paramagnetic magnetite nanoparticles into "mesocrystals."[10] Mesocrystals are superstructures consisting of nanocrystals that share the preferred crystallographic orientation over long-range distances. Compared to bulk materials, nanocrystals often show outstanding size-dependent properties, but, in turn, they are difficult to handle as a material.[11] The assembly of nanocrystals into mesocrystals provides an important route to processability while maintaining the unique properties of nanocrystals during "scale-up" to micrometer-sized or even macroscopic structures. In the case of magnetite (Fe_3O_4), nanocrystals with sizes less than 30 nm show super paramagnetic behavior at room temperature.[12] This behavior allows them to affect mesocrystal formation using a magnetic field to create rather uncommon mesocrystals (in terms of morphology and structure) as compared to those formed without the influence of a magnetic field.[13] However, the super paramagnetic properties of the nanocrystals are preserved as reported for millimeter-sized mesocrystals, e.g., by Yin and co-workers and a further advantage is that the magnetic moments of the individual nanocrystals in the mesocrystal add up leading to excellent collective magnetization.[14] An advantage of super paramagnetic functionalized biomorphs is their preparation for further experiments compared to ferrimagnetic materials. Ferrimagnetic materials would permanently attract each other and simply agglomerate. A preparation of a single specimen would be rather difficult. For these reasons, magnetic mesocrystals seem to be a perfectly suited responding unit for microswimmers upon interaction with external magnetic fields. Uniting the concepts of silica biomorphs and magnetite mesocrystals, a variety of new self-assembled ultrastructures with interesting functional properties can be prepared via explicitly simple approaches, as summarized in Figure 1f. In this approach, a selective anchor point should be generated at its end with witherite crystals followed by the mesocrystal formation. The most promising symbiosis between barium carbonate (witherite) biomorphs and super paramagnetic mesocrystals—leading to high temperature stable (up to 420 °C), ceramic, responsive microarchitectures—is highlighted in this work.

2. Results and Discussion

Magnetite mesocrystals as responding unit for microswimmers were formed via gas diffusion of an antisolvent into an organic solvent–based dispersion of magnetite nanoparticles stabilized by oleic acid (see Figures S1b–d and S2a in the Supporting

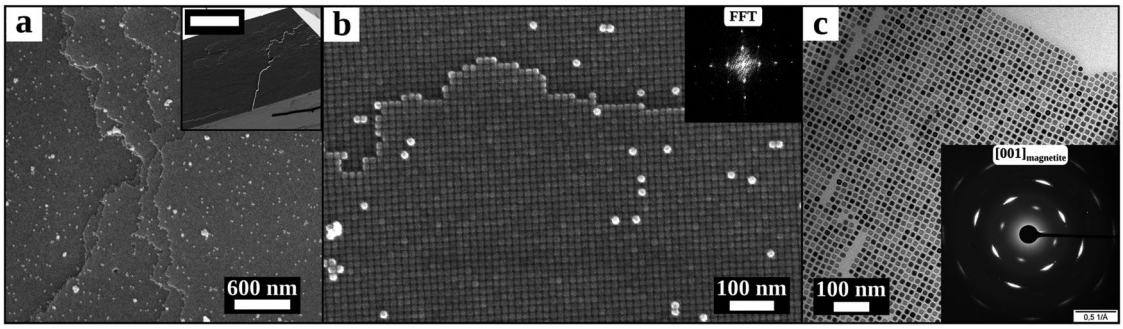

Figure 2. a,b) SEM images of mesocrystals at different magnifications to visualize the nanocrystal packing. Inset in panel (b): scale bars are 20 µm. The fast Fourier transformed (FFT) pattern shows the *p4mm* packing symmetry of the mesocrystal surface. c) Transmission electron microscopy (TEM) image of a mesocrystalline monolayer with its corresponding electron diffraction pattern. The indexed pattern is shown in Figure S2b (Supporting Information).

Information for details on the synthesis, a sketch of the setup used for the formation of mesocrystals and their imaging). The mesocrystals form on silicon wafers by a continuous and slow decrease of the colloidal stability of the nanoparticle dispersion, leading to well-defined superstructures as shown in **Figures 2** and **3**b,c, respectively.

Their morphology can be described as a tetragonal truncated pyramid exposing a *p4mm* projected symmetry on the basal (001) face, which shows *p4mm* plane group symmetry of nanoparticles packing (Figures 2a,b and 3b,c; Figure S1b–d, Supporting Information).[15] To act as a responding unit, these mesocrystals must crystallize on carbonate-rich surfaces as commonly displayed by biomorphs. This precondition was tested by replacing the usual silicon wafer as growth substrate with single crystals of aragonite (see Figure S2b in the Supporting Information) and calcite (see Figure S2c in the Supporting Information). Indeed, magnetite mesocrystals were found to grow on carbonate surfaces, with preferred occurrence on notches and roughness, indicating heterogeneous nucleation. Based on these observations, as-grown biomorphs were used directly and without any further chemical modification as microscopic substrates to create magnetic microswimmers in a straightforward procedure (Route III in Figure 3a). The result is shown in Figure 3g, demonstrating a successful combination of a biomorph worm and quite large magnetite mesocrystals, which have grown around the globular apex from which the worm has emerged. Here, selective attachment of the mesocrystals to the apex is ascribed to the presence of regular witherite crystals (i.e., bare carbonate surfaces without significant amounts of silica) on this part of the biomorph (as shown in Figure 3I and in Figure S3 in the Supporting Information), which have been generated by increasing the growth time from 8–10 h (bulk pH: 10.5) to 16–48 h (bulk pH: 8.5). At the lower bulk pH, the chemical coupling between carbonate and silicate speciation is no longer active; hence, the two components mineralize independently of one another (yielding regular carbonate crystals at the apex and a continuous silica skin over the rest of the aggregate). When the size of the magnetite mesocrystals is decreased (by adding less oleic acid stabilizer in the nanoparticle dispersion), the regular carbonate crystals covering the apex become visible and the selective growth of many small mesocrystals on these surfaces is clearly observed (see Figure 3e,i).

To further increase the mesocrystal loading, the surface of the biomorphs was modified in different ways, as summarized by the scheme in Figure 3a. This provides a toolbox allowing for the controlled deposition of mesocrystals at various positions of the biomorph, which would be impossible for nanocrystals only. For instance, treating the as-grown biomorphs with NaOH solution removes the outer silica layer (as proven by attenuated total reflection Fourier transformed infrared (ATR-FTIR) spectroscopy; cf. Figure 3d) and exposes their bare core, which consists mainly of co-aligned barium carbonate nanorods (Route I in Figure 3a). Such rough carbonate-rich surfaces should be an excellent substrate for the immobilization of magnetite nanocrystals enabling magnetite mesocrystal formation. Moreover, the obtained biomorphs without silica shell can be used to hydrophobize the surface via adsorption of a layer of oleic acid (Route II in Figure 3a; binding of oleic acid to the bare biomorph surface is confirmed by the two IR bands at 2852 and 2922 cm^{-1} in the black spectrum in Figure 3d). A hydrophobic surface should lead to enhanced interaction with the oleic acid stabilizer shell around the magnetite nanoparticles and thus to a denser coverage of the entire structure with the nanoparticles. Alternatively, biomorphs that still carry an outer silica skin can be hydrophobized by using alkyl triethoxysilanes (e.g., octadecyltriethoxysilane) (Route IV in Figure 3a).[7] Again, successful functionalization is shown by IR spectroscopy (Figure 3d).

Having obtained a collection of biomorphs exposing different surface chemistries (neat silica (hydrophilic), silane-modified silica (hydrophobic), neat carbonate (hydrophilic), and oleic acid–modified carbonate (hydrophobic)), we tested their ability to act as substrates for enhanced magnetite mesocrystal formation. Bare carbonate as well as hydrophobized surfaces (regardless of whether silanes or oleic acid is used) showed an increased, though less site-specific, adsorption of magnetite nanoparticles at various positions all over the biomorph architecture. The strong affinity of magnetite nanoparticles toward bare or hydrophobized surfaces is also supported by transmission electron microscopy (TEM) studies on crushed specimens. Figure 3f shows a single carbonate nanorod, which is decorated by numerous smaller magnetite particles. Analysis of several such carbonate rods suggests that they are covered with mono- or multilayers of magnetite nanocubes on most faces. Due to the strong affinity for magnetite to bind, bare carbonate and hydrophobic surfaces thus favor mesocrystal

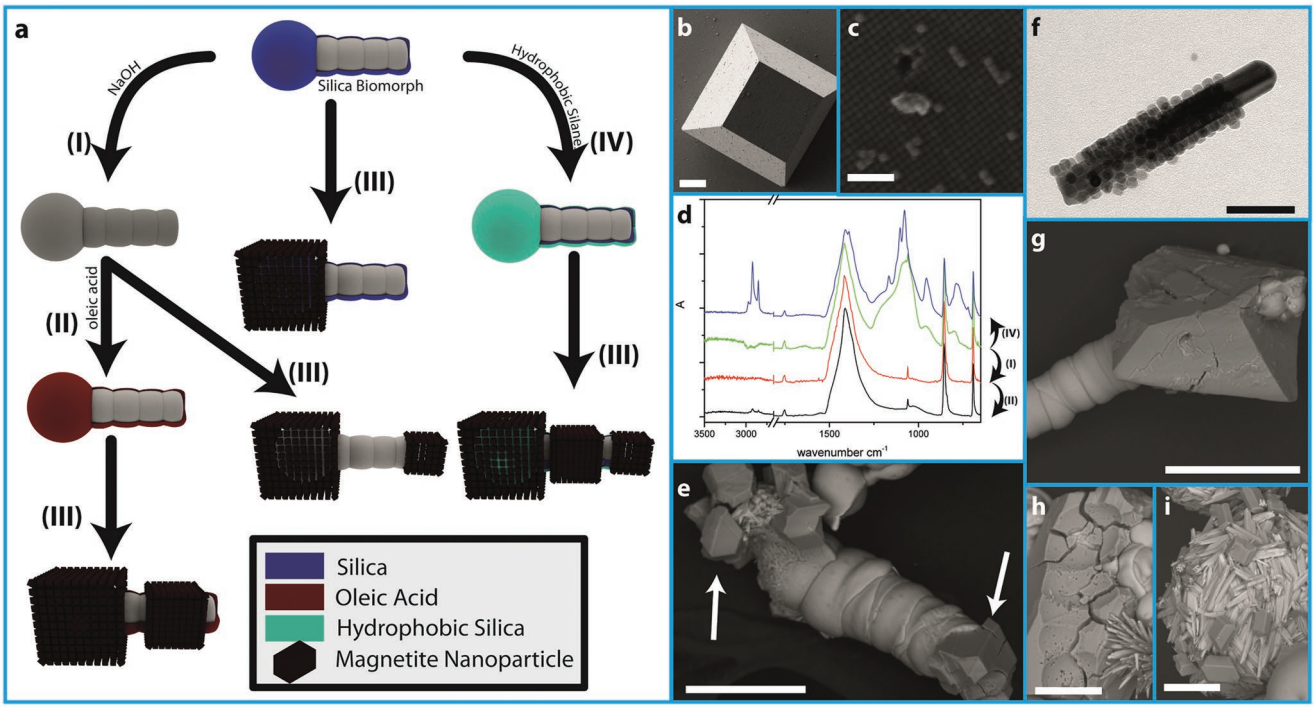

Figure 3. Functionalization of silica biomorphs with magnetite mesocrystals. a) Scheme illustrating the various pathways leading to different composites of magnetite mesocrystals and worm-like silica biomorphs. I) Dissolution of the outer silica shell of biomorphs with NaOH solution to obtain "naked" carbonate surfaces. II) Subsequent hydrophobization of the naked biomorph with oleic acid. III) Magnetite mesocrystal formation via "gas diffusion method" on top of the biomorph structure at different, potentially multiple positions. IV) Hydrophobization of the outer silica shell via post-treatment with alkyl triethoxysilanes. The indicated positions and amounts of the mesocrystals covering the biomorph worm are meant to illustrate the quality and selectivity of the functionalization. b,c) Scanning electron microscopy (SEM) images of magnetite mesocrystals grown from tetrahydrofuran (THF) solution upon destabilization via gas diffusion. d) ATR-FTIR spectra of biomorphs after modification according to pathways I, II, and IV in panel (a). e) SEM image showing the successful formation of magnetite mesocrystals (white arrows) around the apex and the tip of a worm-like biomorph that has been postfunctionalized with dodecyl triethoxysilane. f) TEM image of a carbonate nanocrystal obtained from the core of a biomorph, which was functionalized with oleic acid and subsequently became covered with magnetite nanocubes. g) SEM image of an unfunctionalized silica biomorph after mesocrystal formation. h) SEM image of a magnetite mesocrystal showing a negative imprint of a biomorph worm around which it originally grew. i) SEM image of the apex of a biomorph worm, which shows pronounced overgrowth with regular barium carbonate crystals (long rods), which themselves have been decorated by small magnetite mesocrystals (grown at reduced oleic acid concentration). Scale bars are b) 10 µm, c,f) 100 nm, e,g) 50 µm, and h,i) 25 µm, respectively.

formation on several different positions on one given biomorph architecture (cf. white arrows in Figure 3e), while on untreated biomorphs, rough areas like those carrying secondary witherite crystals (usually the globular apex, cf. Figure 3i) become preferentially overgrown by magnetite mesocrystals. The formation and growth of mesocrystals can also occur in between two or several neighboring biomorph structures, where the available (reduced) space is filled by the mesocrystals with no noticeable interference due to the confinement. One such example can be seen in Figure 3h, where a negative imprint of a biomorph worm is present on the mesocrystal (presumably the two domains were torn apart during isolation). This underlines the adaptability of the mesocrystals to existing template structures without abandoning the co-orientation of their nanoparticulate building units. In the light of the different presented functionalization methods as well as the broad intrinsic structural variability of silica biomorphs (including numerous other interesting morphologies beyond those addressed here, such as coral- or flower-like forms), it seems obvious that a large spectrum of magnetic microarchitectures can be designed using the concept introduced above. With respect to microswimmer applications, each of these forms may show different hydrodynamic behavior and thus can be selected from the morphological pool for a given purpose.

To test the response of the mesocrystal–biomorph composites to an external magnetic field, they were placed in a Petri dish that was mounted on a fixed platform under a light microscope (cf. **Figure 4**a–c). A permanent magnet (≈100 mT at the sample/290 mT at the magnet surface) was then fixed to the stage of the microscope underneath the sample, enabling an exact tracking of the position of the magnet. First, the swimming behavior in liquid media was studied by placing a magnetic microstructure (biomorph worm carrying two magnetite mesocrystals) on the surface of a highly viscous aqueous solution of (PEG, $M_W = 8000$ g mol^{-1}; 50 wt%; $\eta = 325.5$ mPa s), on which it floated randomly when no external field was applied. In the presence of the magnet, the superstructure can travel along predefined pathways through the solution (cf. Figure 4b; Movie S1 in the Supporting Information). Figure 4b′ shows a time-lapse sequence of images illustrating the linear movement of the responsive microarchitecture (see Movie S2 in the Supporting Information for the corresponding video)

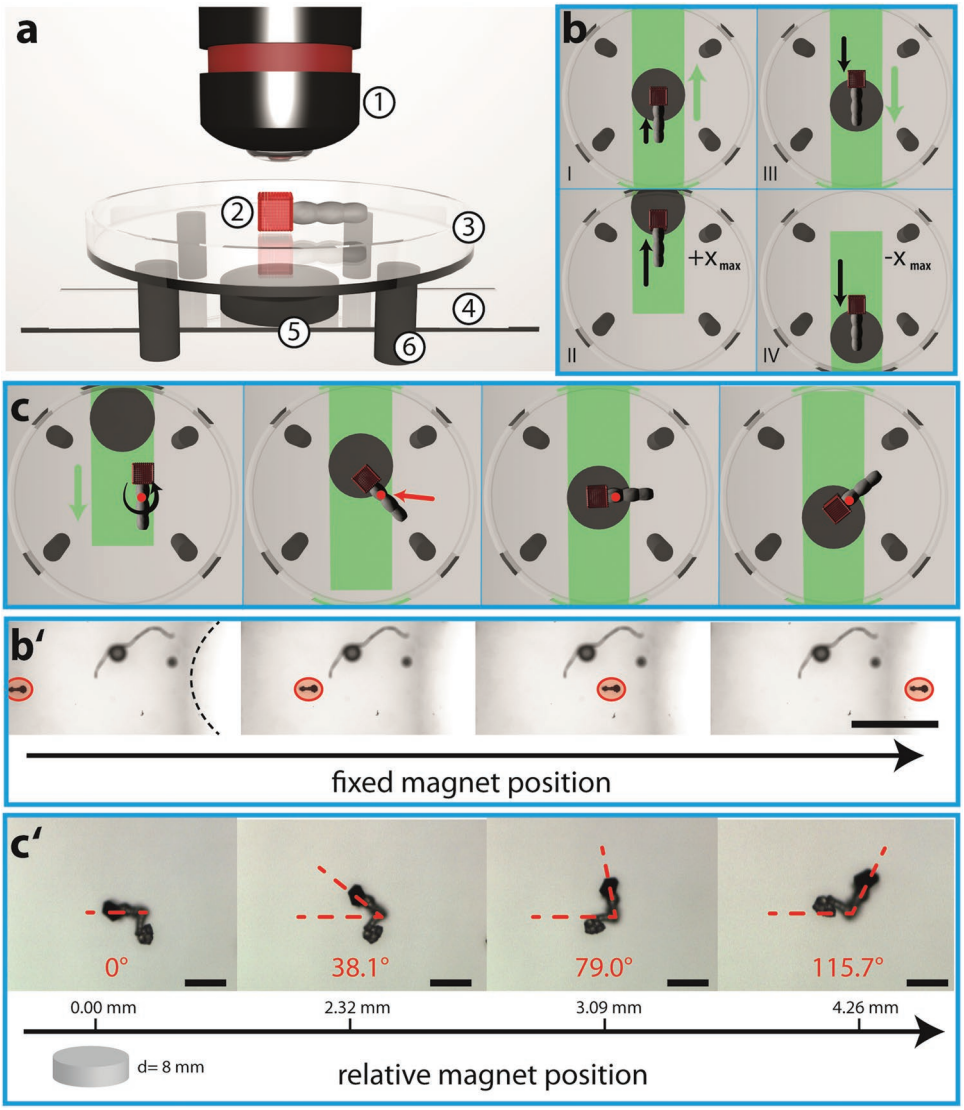

Figure 4. Biomorphs as responsive microarchitectures. a) Schematic illustration of the experimental setup used to move magnetized biomorphs in an external magnetic field—1: objective, 2: sample, 3: fixed Petri dish, 4: moving glass slide, 5: permanent magnet, and 6: holders for Petri dish. Moving the object holder will only displace the magnet (and not the sample), whose relative position is tracked at all times. b) Sketch of a linear displacement of a magnetized biomorph across a highly viscous aqueous polyethylene glycol (PEG) solution guided by a permanent magnet. Green and black arrows indicate the movement of the glass slide carrying the magnet below the Petri dish and the delayed response of the biomorph above, respectively. b′) Snapshots of an experiment according to the setup in panel (b), where the magnet is located at the right end of the field of view as indicated by the dashed black line, while the magnetized microstructure (highlighted in red) is moving toward it. Scale bars are 1 mm. c) Sketch of a rotating movement (indicated by the black arrow) of a dry magnetized biomorph in response to a linear displacement of the permanent magnet (green arrow). The red dot marks the position where the biomorph is fixed to the substrate (rotation axis), which in this case is not centered on the path travelled by the magnet. c′) Snapshots of an experiment according to the setup in panel (c). The biomorph–mesocrystal composite responds to the movement of the magnet (relative positions are given below the microscopic images) by rotation as indicated by the drawn angles. Scale bars are 100 µm.

induced by locating the magnet at a fixed position on the right side of the field of view (indicated by the black dashed line). The biomorph microswimmer moves directly toward the magnet through the viscous medium and can also be forced to travel forth and back following a continuous displacement of the magnet (as shown in Figure 4b and in Movie S3 in the Supporting Information). It is furthermore evident that response of the structure is somewhat delayed with respect to the displacement of the magnet, likely due to inertial effects caused by the high viscosity of the medium. In a second experiment, a biomorph worm carrying one magnetite mesocrystal at its apex (cf. Figure 3g) was put on a dry Petri dish, with its contact point (red dot in Figure 4c) slightly displaced relative to the center of the path travelled by the moving magnet. This induces a rotating movement when the magnet passes the structure, as illustrated schematically in Figure 4c and in Movie S4 (Supporting Information), and observed experimentally in Figure 4c′ and in Movie S5 (Supporting Information). Here, the self-assembled composite responds directly (due to the lower viscosity) to the displacement of the magnet

(relative magnet positions are indicated as pointing angles by the red lines in Figure 4c′, with 0° corresponding to the starting position). It should be noted that the biomorph–mesocrystal aggregate was not immobilized on the surface of the Petri dish, but nevertheless remained at a fixed position and only rotated. Furthermore, as can be seen in Movie S5 (Supporting Information), also single mesocrystals follow the movement of the magnet. They are a byproduct from the preparation procedure. This shows that the motion of the microarchitecture can be precisely controlled in the dry state if the applied forces are not too pronounced. All these observations clearly demonstrate that magnetite mesocrystals attached to silica biomorphs indeed work as responding units in an external magnetic field, enabling controlled movement on the micrometer scale.

Another very promising aspect about these materials is the possibility of transforming the magnetized architectures into hollow microcarriers, which can easily be achieved by removing the carbonate core with diluted acid, leaving behind a hollow silica "ghost" that still carries the mesocrystal responding unit. Such structures could serve as carriers for molecular cargo, which after filling with actives travel to predefined locations and release their cargo there (targeted microrelease and/or spatial reaction control in microenvironments). Movie S6 in the Supporting Information shows such a hollow ghost and its ability for controlled movement in an external magnetic field (note that this structure moves through a less viscous acetic acid solution and therefore the response to the moving magnet has no visible delay compared to the experiments in PEG solution). It could further be envisaged that the hollow silica framework is functionalized by silane chemistry to enable selective uptake and release.

At least, one should keep in mind that for a pure inorganic system with these responsive architectures, a high thermal stability is expected. To further investigate the thermal stability of mesocrystal–biomorph composites, the magnetite mesocrystals were annealed at different temperatures in the range between 350 and 500 °C, which is below the decomposition temperature of barium carbonate (Materials and Methods section in the Supporting Information). Within the tested temperature range, the specimens preserve the initial shape of the mesocrystals; however, at 350–420 °C the magnetite nanoparticles partially fuse together forming "mosaic" structures on the aggregate surfaces. At 500 °C, the phase transformation of magnetite to hematite is observed, and the faces of the specimens are overgrown by plate-like nanocrystals (Figure S4a, Supporting Information). Morphologically and compositionally the mesocrystal–biomorph composites should therefore be stable at least up to 420 °C. At even higher temperatures (1000 °C) the outer shape of the composite is still preserved (Figure S4b, Supporting Information), but new phases (including barium silicate, barium oxide, crystalline SiO_2 (tridymite), and hematite) have replaced the original materials which also goes along with a change of the magnetic responsivity.

3. Conclusion

In summary, our work highlights the successful symbiosis of two prominent examples for complex self-assembly in the field of crystallization: silica biomorphs and mesocrystals. Their combination leads to functional microscopic ultrastructures in straightforward processes at ambient conditions. Given the large variety of morphologies and structures accessible within one batch of biomorph synthesis (going far beyond the proof of concept established in this work), numerous types of responsive microtools can be generated in just a few processing steps. By targeted modification of the surfaces of silica biomorphs, the adsorption of super paramagnetite nanoparticles and their assembly into mesocrystals on the biomorph substrate can be controlled. This approach gives access to magnetic microarchitectures that can be applied as responsive tools ranging from microswimmers over microcarriers to micromanipulators. In the present work, it was demonstrated that external magnetic fields can be used to precisely control the movements of the architectures in a simplified setup. Since these structures are composed of purely inorganic material, they show high-temperature stability. Finally, the possibility of removing certain components selectively—e.g., carbonate by acid or silica by alkaline post-treatment, leaving a hollow silica ghost or an open porous carbonate network, respectively—offers further handles for enhanced functionality, such as the incorporation and/or transport of active compounds, which could eventually enable targeted release from the moving structure.

4. Experimental Section

Formation and Post-Treatment of Silica Biomorphs: Barium chloride dihydrate (>99%), sodium hydroxide (>98%), and sodium silicate solution (water glass with ≈10.6% Na_2O and ≈26.5% SiO_2, reagent grade) were purchased from Sigma Aldrich and used without further purification. All solutions were prepared using Milli-Q water with a conductivity of 18 µS cm^{-1}. The silicate solution for growth of biomorphs was obtained by diluting 1.39 g of sodium silicate solution in 349 mL of water. The pH was adjusted to 11.1 using 0.1 M sodium hydroxide solution. The resulting silica sol was then mixed in a 1:1 ratio with 0.01 M barium chloride solution in 6-well plates (Linbro). After 16 h exposure to the atmosphere, formed structures were recovered, washed several times with water and dried in air.

Hydrophobization of the as-obtained biomorphs with silanes was performed in an Eppendorf tube by dissolving 10 µL of the silane in 1.5 mL of a 4:1 EtOH:H_2O mixture. Then about 10 mg of biomorphs was added to the solution and incubated overnight. To dissolve the outer silica shell, 10 mg of biomorphs was incubated overnight in 1.5 mL of a 1 M sodium hydroxide solution. The silica-free biomorphs were then covered with a layer of oleic acid by overnight treatment with a sonicated mixture of 600 µL THF, 10 µL oleic acid, 10 µL 1 M NaOH, 2.5 mL cyclohexane, and 0.5 mL EtOH. All modified structures were cleaned by repeated washing with deionized water and centrifugation, followed by drying under reduced pressure.

Formation of Mesocrystal–Biomorph Composites: Iron oxide nanocrystals were prepared following a procedure described in the literature.[15a,16] Magnetite mesocrystals were obtained via destabilization of a nanocrystal dispersion in THF (5 mg mL^{-1} magnetite nanocrystals with 3 µL mL^{-1} oleic acid) in the presence of a piece of silicon wafer or powdered biomorphs in a glass vial. The glass vial was left in an outer surrounding reservoir, which contained EtOH:THF (1:1) as a destabilizing agent that slowly diffused into the nanoparticle dispersion via the gas phase. Complete destabilization of the nanocrystal dispersion and mesocrystal formation took about 1 week, as observed by a color change of the dispersion from black to colorless.

Thermal Annealing of Mesocrystals: In order to investigate the thermal stability, mesocrystals were annealed in an oven (Uni-Temp RTP-1200) under ultra high vacuum (UHV) conditions using a slow ramp rate. Primarily, the oven was heated up to 90 °C to evaporate the water out of the sample to avoid damage to the crystal upon expansion at high temperatures. After, the oven was heated to the desired temperature and kept at that temperature for 7 h before cooling down. Temperatures of 350, 380, 420, and 500 °C were investigated. The obtained samples were characterized by means of scanning electron microscopy (SEM) and X-ray diffraction (XRD).

Analytical Methods: The pH was controlled by a pH meter (Eutech pH 510). For polarized light microscopy (PLM), a Zeiss Imager M2m equipped with a $\lambda/4$ plate, EC Epiplan Neofluar objectives (5×, 10×, and 20×), a LD Epiplan 50× objective, and an Axiocam MRc 5 was used. SEM was performed with a Hitachi table-top SEM TM3000 at an acceleration voltage of 15 kV and a Zeiss Crossbeam at 5 kV. TEM studies were carried out on a Zeiss Libra 120 operated at an acceleration voltage of 120 kV. For measurement, the samples were mounted on carbon-coated 200 mesh Cu grids. ATR-FTIR measurements were performed on a Perkin-Elmer Spectrometer 100.

Supporting Information

Supporting Information is available from the Wiley Online Library or from the author.

Acknowledgements

J.O. and J.B. contributed equally to this work. The authors thank SFB 1214 (Deutsche Forschungsgemeinschaft) project B1, the Particle Analysis Center (PAC) of the University of Konstanz, the Nanostructure Laboratory of the University of Konstanz, and the European Research Council ERC (Grant Agreement No. 340863).

Conflict of Interest

The authors declare no conflict of interest.

Keywords

barium carbonate, biomorph, magnetite, mesocrystal, microswimmer

Received: March 9, 2019
Revised: June 17, 2019
Published online:

[1] a) H. Wang, M. Pumera, *Chem. Rev.* **2015**, *115*, 8704; b) T. Li, J. Li, H. Zhang, X. Chang, W. Song, Y. Hu, G. Shao, E. Sandraz, G. Zhang, L. Li, J. Wang, *Small* **2016**, *12*, 6098; c) B. A. Grzybowski, H. A. Stone, G. M. Whitesides, *Nature* **2000**, *405*, 1033; d) J. Burdick, R. Laocharoensuk, P. M. Wheat, J. D. Posner, J. Wang, *J. Am. Chem. Soc.* **2008**, *130*, 8164.

[2] a) M. Kellermeier, H. Colfen, J. M. Garcia-Ruiz, *Eur. J. Inorg. Chem.* **2012**, *2012*, 5123; b) W. L. Noorduin, A. Grinthal, L. Mahadevan, J. Aizenberg, *Science* **2013**, *340*, 832; c) E. Nakouzi, O. Steinbock, *Sci. Adv.* **2016**, *2*, e1601144.

[3] a) J. M. García-Ruiz, E. Melero-García, S. T. Hyde, *Science* **2009**, *323*, 362; b) M. Kellermeier, E. Melero-Garcia, F. Glaab, J. Eiblmeier, L. Kienle, R. Rachel, W. Kunz, J. M. Garcia-Ruiz, *Chem. - Eur. J.* **2012**, *18*, 2272; c) J. Opel, M. Kellermeier, A. Sickinger, J. Morales, H. Cölfen, J.-M. García-Ruiz, *Minerals* **2018**, *8*, 75; d) J. M. Garcia-Ruiz, S. T. Hyde, A. M. Carnerup, A. G. Christy, M. J. Van Kranendonk, N. J. Welham, *Science* **2003**, *302*, 1194.

[4] M. Kellermeier, E. Melero-García, W. Kunz, J. M. García-Ruiz, *J. Colloid Interface Sci.* **2012**, *380*, 1.

[5] G. B. Alexander, W. Heston, R. K. Iler, *J. Phys. Chem.* **1954**, *58*, 453.

[6] a) E. Bittarello, F. Roberto Massaro, D. Aquilano, *J. Cryst. Growth* **2010**, *312*, 402; b) M. Kellermeier, F. Glaab, A. M. Carnerup, M. Drechsler, B. Gossler, S. T. Hyde, W. Kunz, *J. Cryst. Growth* **2009**, *311*, 2530; c) P. Knoll, E. Nakouzi, O. Steinbock, *J. Phys. Chem. C* **2017**, *121*, 26133.

[7] J. Opel, F. P. Wimmer, M. Kellermeier, H. Cölfen, *Nanoscale Horiz.* **2016**, *1*, 144.

[8] T. Holtus, L. Helmbrecht, H. C. Hendrikse, I. Baglai, S. Meuret, G. W. P. Adhyaksa, E. C. Garnett, W. L. Noorduin, *Nat. Chem.* **2018**, *10*, 740.

[9] J. Palacci, S. Sacanna, A. P. Steinberg, D. J. Pine, P. M. Chaikin, *Science* **2013**, *339*, 936.

[10] a) E. V. Sturm, H. Colfen, *Chem. Soc. Rev.* **2016**, *45*, 5821; b) H. Cölfen, M. Antonietti, *Angew. Chem., Int. Ed.* **2005**, *44*, 5576.

[11] a) H. Goesmann, C. Feldmann, *Angew. Chem., Int. Ed.* **2010**, *49*, 1362; b) D. V. Talapin, J.-S. Lee, M. V. Kovalenko, E. V. Shevchenko, *Chem. Rev.* **2010**, *110*, 389.

[12] a) J. Park, K. An, Y. Hwang, J. G. Park, H. J. Noh, J. Y. Kim, J. H. Park, N. M. Hwang, T. Hyeon, *Nat. Mater.* **2004**, *3*, 891; b) B. Faure, E. Wetterskog, K. Gunnarsson, E. Josten, R. P. Hermann, T. Bruckel, J. W. Andreasen, F. Meneau, M. Meyer, A. Lyubartsev, L. Bergstrom, G. Salazar-Alvarez, P. Svedlindh, *Nanoscale* **2013**, *5*, 953.

[13] J. J. Brunner, M. Krumova, H. Cölfen, E. V. Sturm, *Beilstein J. Nanotechnol.* **2019**, *10*, 894.

[14] J. Ge, Y. Hu, M. Biasini, W. P. Beyermann, Y. Yin, *Angew. Chem., Int. Ed.* **2007**, *46*, 4342.

[15] a) J. Brunner, I. A. Baburin, S. Sturm, K. Kvashnina, A. Rossberg, T. Pietsch, S. Andreev, E. Sturm, H. Cölfen, *Adv. Mater. Interfaces* **2017**, *4*, 1600431; b) L. Bergström, E. V. Sturm, G. Salazar-Alvarez, H. Cölfen, *Acc. Chem. Res.* **2015**, *48*, 1391; c) A. Ahniyaz, Y. Sakamoto, L. Bergström, *Proc. Natl. Acad. Sci. USA* **2007**, *104*, 17570.

[16] S. Disch, E. Wetterskog, R. P. Hermann, G. Salazar-Alvarez, P. Busch, T. Brückel, L. Bergström, S. Kamali, *Nano Lett.* **2011**, *11*, 1651.

ADVANCED FUNCTIONAL MATERIALS

Supporting Information

for *Adv. Funct. Mater.*, DOI: 10.1002/adfm.201902047

Symbiosis of Silica Biomorphs and Magnetite Mesocrystals

Julian Opel, Julian Brunner, Ramon Zimmermanns, Tristan Steegmans, Elena Sturm, Matthias Kellermeier, Helmut Cölfen,* and Juan-Manuel García-Ruiz**

Supporting Information

Symbiosis of Silica-Biomorphs and Magnetite Mesocrystals

Julian Opel, Julian Brunner, Ramon Zimmermanns, Tristan Steegmans, Elena Sturm, Matthias Kellermeier, Helmut Cölfen* and Juan-Manuel García-Ruiz**

This PDF file includes:

Supplementary Figures:

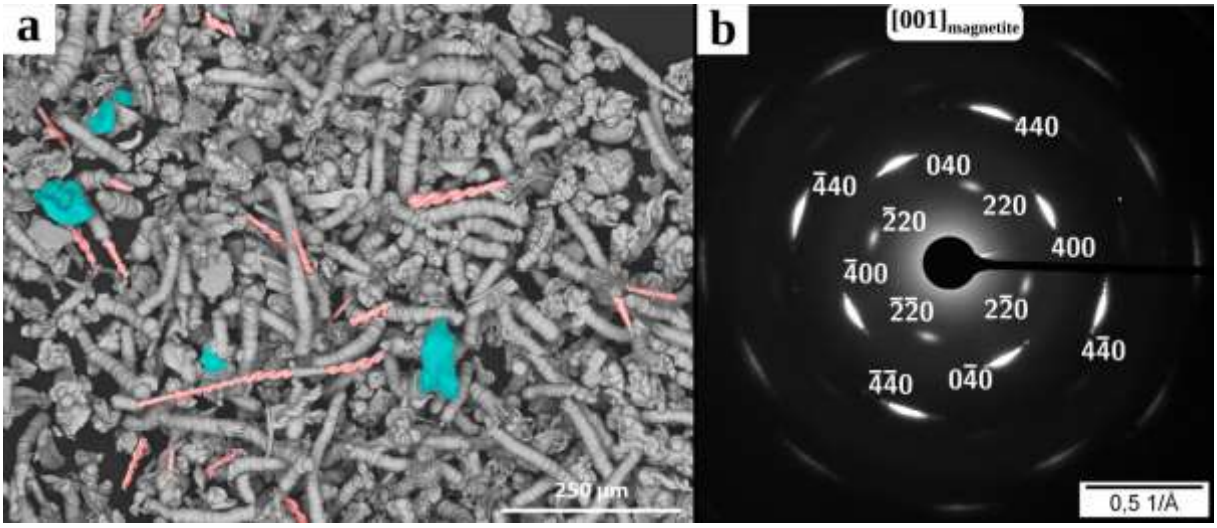

Figure S1. a) False-colored scanning electron micrograph giving an overview on typical biomorph morphologies obtained from a single synthesis batch (blue: sheets, red: helicoids, grey: worm-like braids). b) Indexed pattern of the mesocrystalline iron oxide film depicted in Figure 2.

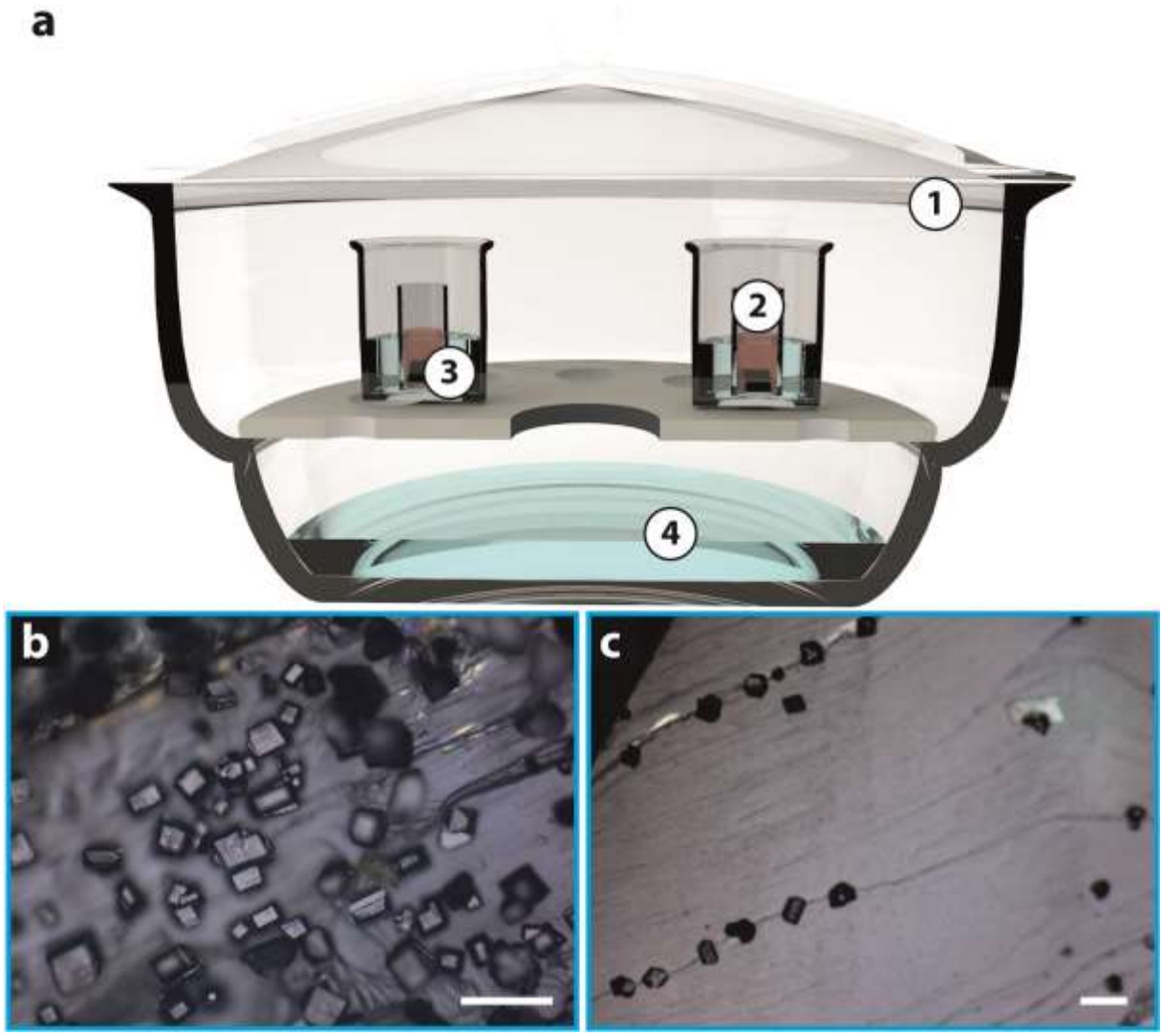

Figure S2. Preparation of magnetite mesocrystals. (a) Sketch of the experimental setup used for the formation of magnetite mesocrystals via diffusion of a destabilizing anti-solvent (EtOH) into a dispersion of magnetite nanocrystals (1: desiccator; 2: dispersion of magnetite nanoparticles in THF; 3: Si wafer; 4: EtOH/THF mixture). (b,c) Magnetite mesocrystals grown on single-crystalline calcium carbonate macro-substrates, namely (b) aragonite and (c) calcite (Scale bars: 100 µm).

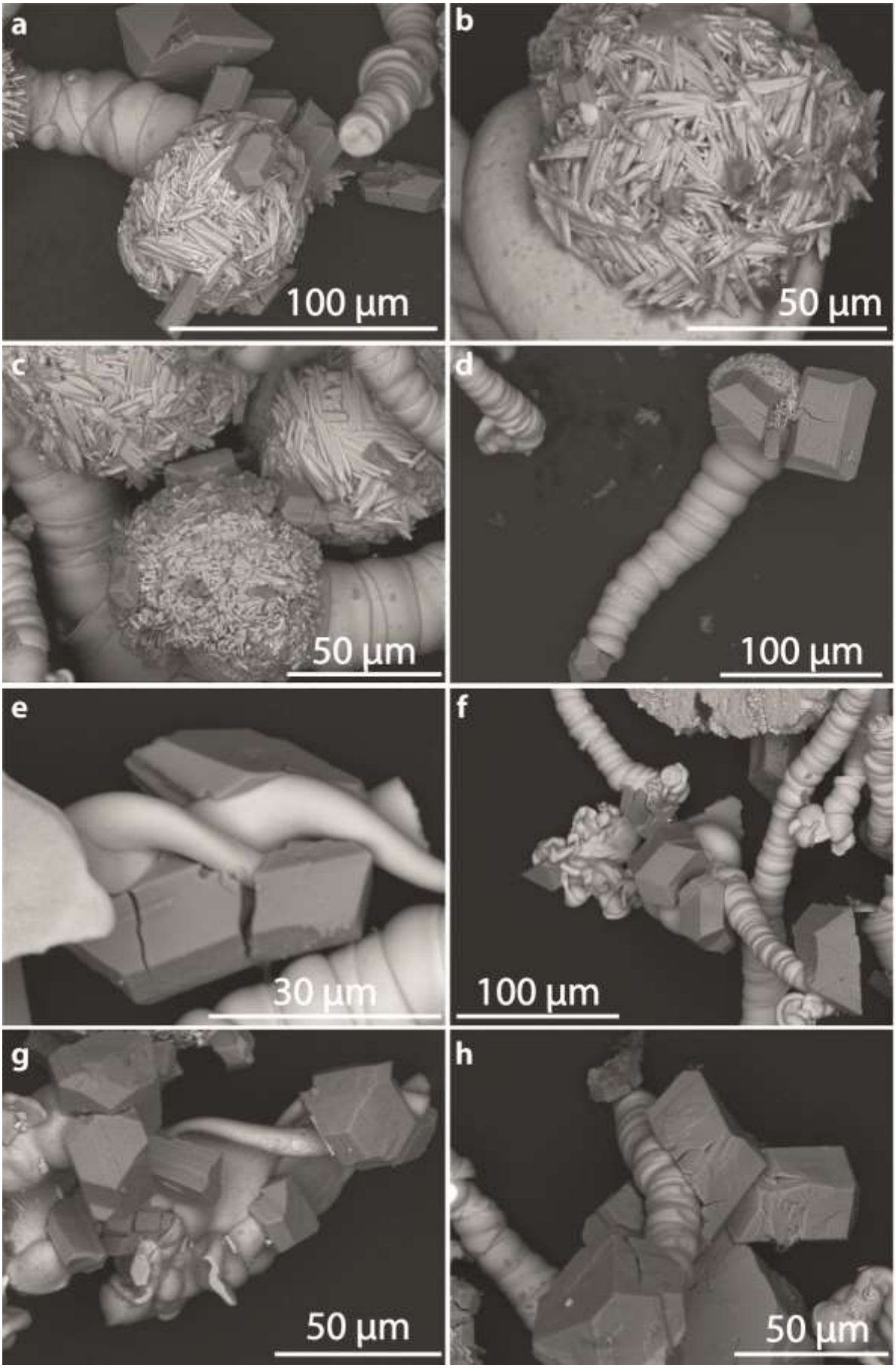
a
100 µm
b
50 µm
c
50 µm
d
100 µm
e
30 µm
f
100 µm
g
50 µm
h
50 µm

Figure S3. Collection of different magnetite-biomorph composite structures. Magnetite mesocrystals were grown on (a,b) native biomorphs, (c,d) biomorphs after removal of the outer silica shell, (e,f) biomorphs without silica skin after modification with oleic acid, and (g,h) biomorphs after hydrophobization of the outer silica skin with alkyl silanes.

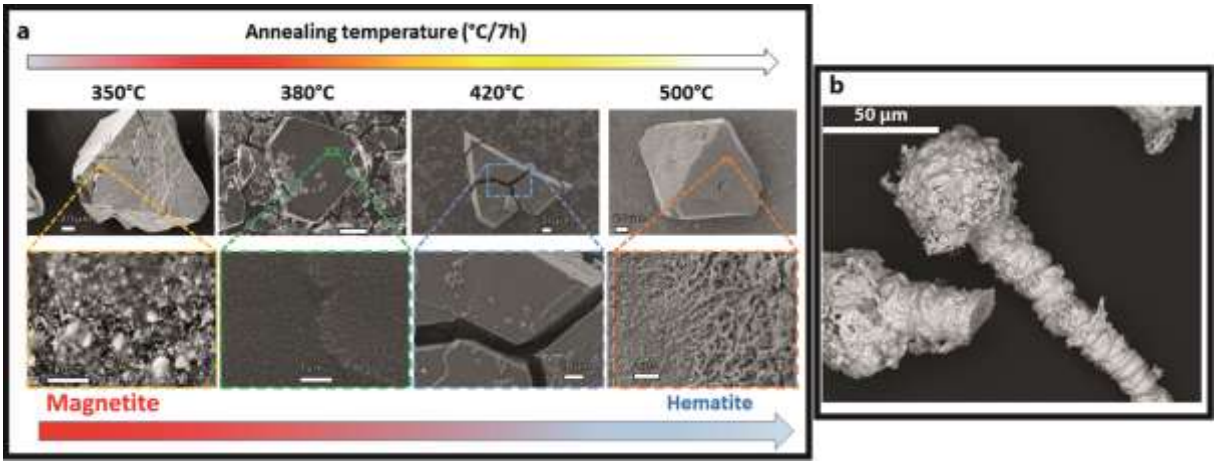

Figure S4. Thermal stability of mesocrystal-biomorph composites. (a) SEM images illustrating the structural features of of mesocrystals annealed at various temperatures. (b) SEM image of an annealed (1000°C) mesocrystal-biomorph composite.

Movie Captions:

Movie S1. Schematic animation illustrating the response of a mesocrystal-biomorph composite to a moving magnet centered below the structure. The indicated delay of the response is caused by the viscosity of the surrounding (liquid) medium.

Movie S2. A magnetic worm-like aggregate follows a magnet in linear movement (according to Movie S1) through a viscous PEG-8000 solution (50 wt% in water).

Movie S3. Movement of the microarchitecture shown in Movie S2 into the opposite direction.

Movie S4. Schematic animation illustrating the response of a mesocrystal-biomorph composite to a moving magnet slightly displaced below the structure, inducing rotational movement.

Movie S5. Magnetized silica biomorphs respond to the movement of a magnet by rotation in dry state.

Movie S6. A magnetized biomorph ghost swims through less viscous 0.05 M acetic acid solution.

Volume 8
Number 22
14 June 2020
Pages 4703–4964

Journal of Materials Chemistry B

Materials for biology and medicine

rsc.li/materials-b

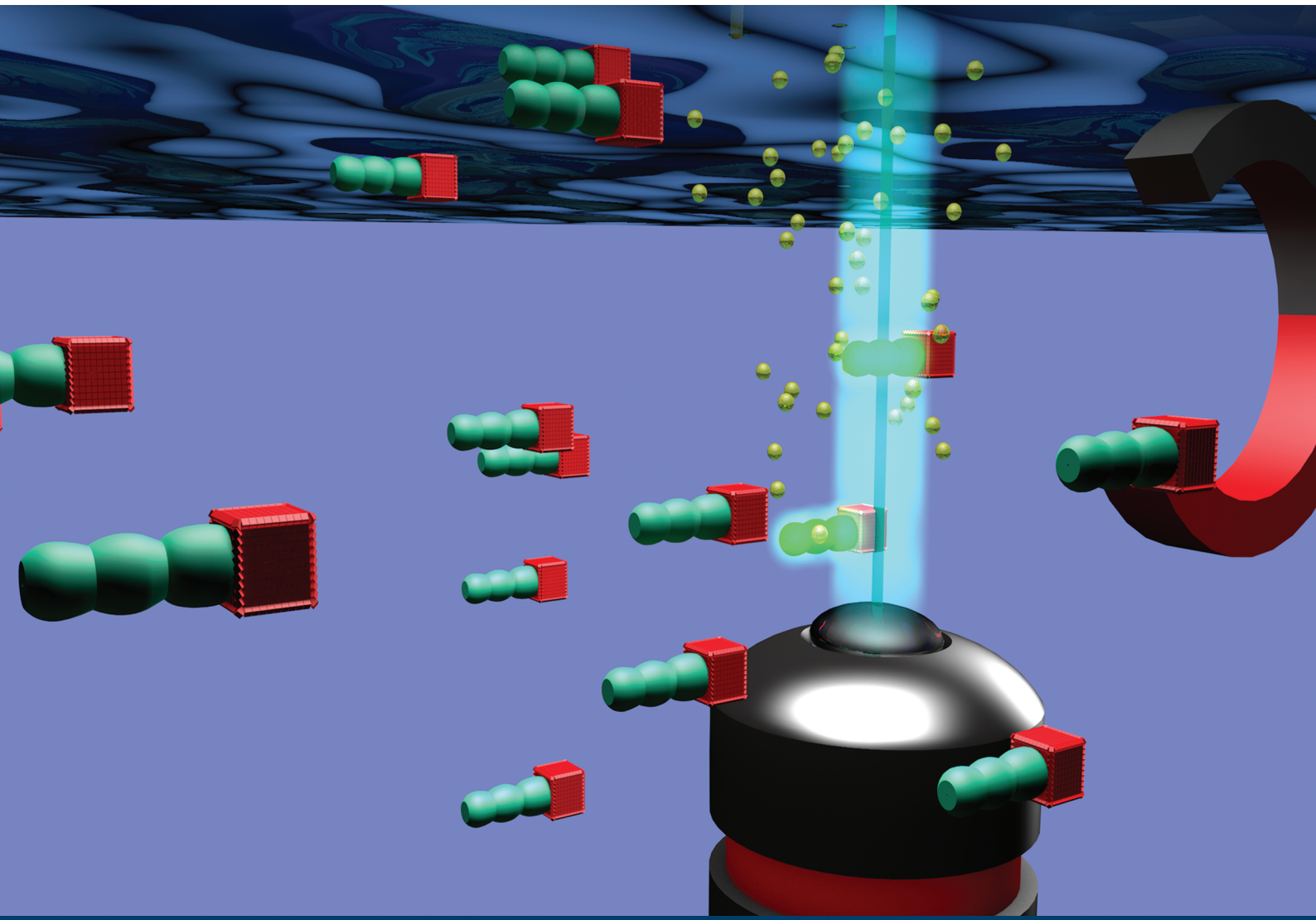

Themed issue: Hybrid Nanoparticle Composites

ISSN 2050-750X

ROYAL SOCIETY OF CHEMISTRY

COMMUNICATION

Helmut Cölfen, Juan-Manuel García-Ruiz *et al.*
Light-switchable anchors on magnetized biomorphic microcarriers

Journal of Materials Chemistry B

ROYAL SOCIETY OF CHEMISTRY

COMMUNICATION

View Article Online
View Journal

Cite this: DOI: 10.1039/c9tb02955a

Received 29th December 2019,
Accepted 24th April 2020

DOI: 10.1039/c9tb02955a

rsc.li/materials-b

Light-switchable anchors on magnetized biomorphic microcarriers

Julian Opel,†[ab] Lisa-Catherine Rosenbaum, †[c] Julian Brunner,[a] Anne Staiger, [ac] Ramon Zimmermanns,[a] Matthias Kellermeier,[d] Tanja Gaich,[c] Helmut Cölfen *[a] and Juan-Manuel García-Ruiz*[b]

Microcarriers with the ability to release and catch substances are highly desired metamaterials and difficult to obtain. Herein, we report a straightforward strategy to synthesize these materials by combining silica-biomorphs with mesocrystals. An easy access to microcarrier hulls with covalently bound spiropyrans as light-switchable anchor points is presented.

Introduction

The so-called silica-biomorphs are purely inorganic composite materials that exhibit outstanding shapes.[1–3] They are prepared in alkaline, silica-rich solutions containing earth-alkaline metal ions, such as Ba^{2+}, Sr^{2+} and Ca^{2+}.[4,5] Their formation mechanism is assumed to be based on autocatalytic co-precipitation of earth-alkaline carbonates and silica linked to a local pH cycling induced by alternating silica and carbonate precipitation.[6–8] A huge variety of self-assembled carbonate nanorods are attractive for several applications. The elongated architecture of worm-like and helicoidal shaped biomorphs renders them with the potential to be used as microcarrier hulls.[9] Magnetic nanoparticles like magnetite nanocubes are used as responding units, which are needed for controlled movement through various media.[10,11] The benefit of this system is the ability to attach mesocrystals at specific sides of the biomorph (*cf.* Fig. 1).[9,12] Mesocrystals form in a non-classical pathway *via* the oriented assembly of non-spherical nanocrystals into superlattices.[13,14]

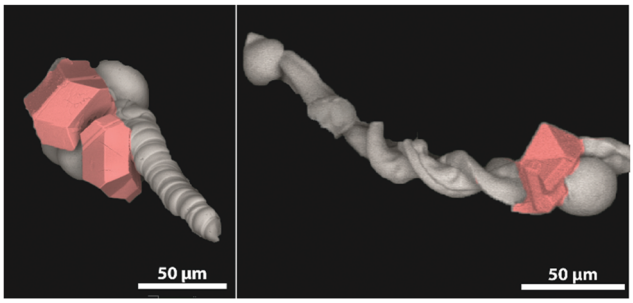

Fig. 1 Scanning electron micrographs of a biomorph worm (left) and a biomorph helix (right) decorated with magnetite mesocrystals (highlighted in red) at the globular apex of the structures.

In order to create further functionality, the structures must be equipped with an additional responding unit that allows addressing of a switchable anchor point for controlled compound load/release. Previous studies employed post-functionalization by the use of silane coupling chemistry.[9,15]

The incorporation of light-switchable molecules into various systems and the development of so-called dynamic materials came into the focus of attention during the last decades. Not only the synthesis of materials for data storage,[16] electronic devices[17] or sensors[18] but also the biological applications of photo-responsive compounds, *e.g.* in photopharmacology,[19–21] have been investigated. Photo-switchable molecules show reversible transformation between at least two different thermodynamically stable isomers induced by irradiation with light of a particular wavelength. Among the wide range of photo-switches, spiropyrans achieved a privileged status since they enable the production of materials that are responsive to multiple external stimuli in an orthogonal fashion. The two isomeric structures of a spiropyran show vastly different properties, which results in an isomerization process that is not only induced by irradiation with light but also by several other external stimuli including temperature, solvent and pH-value.[22] In addition, the covalent

[a] Physical Chemistry, University of Konstanz, Universitätsstrasse 10, D-78457 Konstanz, Germany. E-mail: helmut.coelfen@uni-konstanz.de; Fax: +49 7531 88 3139; Tel: +49 7531 88 4063
[b] Laboratorio de Estudios Cristalográficos, Instituto Andaluz de Ciencias de la Tierra (CSIC-UGR), Avenida de las Palmeras No. 4, E-18100 Armilla, Granada, Spain. E-mail: juanmanuel.garcia@csic.es; Fax: +34 958 552620; Tel: +34 958 230000
[c] Organic Chemistry, University of Konstanz, Universitätsstrasse 10, D-78457 Konstanz, Germany. E-mail: Tanja.Gaich@uni-konstanz.de
[d] Material Physics, BASF SE, GMC/O – G201, Carl-Bosch-Strasse 38, D-67056 Ludwigshafen, Germany. E-mail: matthias.kellermeier@basf.com; Fax: +49 621 66 43388; Tel: +49 621 60 43388
† JO and LCR wrote the paper and have contributed equally to the work.

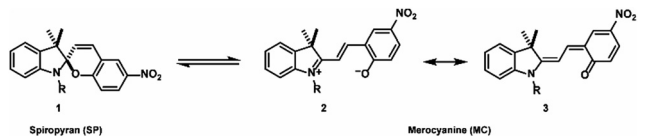

Fig. 2 Typical structural formula of a spiroindolinopyran.

attachment of spiropyran units to a solid support results in numerous advantages compared to the non-immobilized counterparts, including an improved fatigue resistance,[23,24] and the possibility to obtain biocompatible photoresponsive materials.[25,26]

The incorporation of silane-containing switchable molecules like spiropyrans is a desired method to obtain new metamaterials.[22,27]

The typical structural formula of a spiroindolinopyran (SP) is shown in Fig. 2, consisting of an indoline and a chromene moiety, which are connected *via* a spiro-center. The isomeric merocyanine (MC) is accessible by heterolytic cleavage of the C_{spiro}–O bond induced by irradiation with UV-light. The population of the excited state is followed by an intersystem crossing process to the corresponding triplet state in which the ring opening takes place.[28] Internal rotation in the ground state to the *cis*- and *trans*-isomers is in most cases followed by a thermal isomerization to the *trans*-isomer. The open-ring isomer exists as either zwitterionic (**2**) or quinoidal species (**3**).

Merocyanine often shows strong fluorescence and exhibits a remarkably higher affinity to different chemical structures,[29] a property that is caused by the additional free oxygen acting as a donor function. The zwitterionic merocyanine has already been described as a ligand for (divalent) metal ions[30–32] whereas the neutral spiropyran is a rather unfavorable donor. Utilizing the huge differences in the properties of the isomers, multi-fluorescent hybrid particles,[33] traps for ions[34] and small molecules[35] are prepared, the hydrophobicity of solid surfaces[36] can be tuned reversibly, and the electrochemical properties of a surface[37] are controlled. Reverse isomerization to the initial spiro-compound is possible by either thermal relaxation or irradiation with visible light. These properties made the spiropyran–merocyanine system to be the focus of our interest with regard to the design of a magnetized biomorphic microcarrier system.

Experimental

Materials and methods

The purchased ethyl acetate and hexane for column chromatography were of technical grade and distilled before usage. All other chemicals were purchased from Sigma-Aldrich and TCI and used without further purification. NMR spectra were recorded on a Bruker Avance III 400. Chemical shifts are referred relative to the solvent residual peaks. Data are reported as: chemical shift, multiplicity, coupling constant *J*, and integration. Infrared spectra (IR) of thin films were recorded on a PerkinElmer Spectrum 100 spectrometer with an ATR-unit. UV/Vis spectra were recorded on a Cary 50 spectrometer. High-resolution mass spectra (HRMS) were recorded on a Fischer Scientific Orbitrap Velos Pro. Scanning electron micrographs (SEM) were recorded on a Hitachi table-top SEM TM3000 with an acceleration voltage of 15 kV. Laser scanning micrographs (LSM) were recorded on a Zeiss LSM 700 with a 63×/1.40 Plan Apochromat (Oil) objective and with laser diodes (405, 488, 555 and 637 nm). The images were recorded in fluorescence and transmission channel on two photomultipliers.

Synthesis of magnetite mesocrystal silica-biomorph composites

The formation of silica biomorphs and the needed functionalization for mesocrystal attachment is described elsewhere.[9] The analysis of the structures was performed by IR-spectroscopy, light- and scanning electron microscopy.

Synthesis of compound 6

Compound **6** was synthesized in two steps from commercially available 2,3,3-trimethylindolenine by a literature-known procedure.[38] The obtained spectroscopic data are consistent with those reported previously.

^{1}H-NMR (400 MHz, DMSO): δ [ppm] = 12.24 (bs, 1H), 8.24 (d, $^3J_{HH}$ = 2.8 Hz, 1H), 8.03 (dd, $^3J_{HH}$ = 2.8′, 9.0 Hz, 1H), 7.24 (d, $^3J_{HH}$ = 10.3 Hz, 1H), 7.17–7.13 (m, 2H), 6.88 (d, $^3J_{HH}$ = 9.0 Hz, 1H), 6.83 (t, $^3J_{HH}$ = 7.5 Hz, 1H), 6.69 (d, $^3J_{HH}$ = 7.8 Hz, 1H), 6.03 (d, $^3J_{HH}$ = 10.3 Hz, 1H), 3.57–3.39 (m, 2H), 2.64–2.44 (m, 2H), 1.21 (s, 3H), 1.10 (s, 3H).

Synthesis of compound 7

Compound **6** (2.30 g, 6.05 mmol, 1.0 eq.), EDC·HCl (1.28 g, 6.66 mmol, 1.1 eq.) and DMAP (0.74 g, 6.05 mmol, 1.0 eq.) were dissolved in CH_2Cl_2 (20 mL) and stirred for 10 minutes. (3-Aminopropyl)triethoxysilane (1.41 g, 6.35 mmol, 1.05 eq.) was added dropwise and the reaction was stirred for 20 hours at room temperature. The solvent was removed under reduced pressure and the crude product was purified by flash chromatography on silica gel (2 : 1 ethyl acetate/hexane). Compound **7** was obtained as a red solid (2.71 g, 4.64 mmol, 77% yield).

^{1}H-NMR (400 MHz, DMSO): δ [ppm] = 8.20 (d, $^3J_{HH}$ = 2.8 Hz, 1H), 7.99 (dd, $^3J_{HH}$ = 2.8, 8.9 Hz, 1H), 7.86 (t, $^3J_{HH}$ = 5.5 Hz, 1H), 7.18 (d, $^3J_{HH}$ = 10.4 Hz, 1H), 7.14–7.09 (m, 2H), 6.85 (d, $^3J_{HH}$ = 9.0 Hz, 1H), 6.78 (dt, $^3J_{HH}$ = 7.4, 0.6 Hz, 1H), 6.65 (d, $^3J_{HH}$ = 7.7 Hz, 1H), 5.97 (d, $^3J_{HH}$ = 10.4 Hz, 1H), 3.70 (q, $^3J_{HH}$ = 7.0Hz, 6H), 3.49–3.29 (m, 2H), 3.01–2.87 (m, 2H), 2.43–2.27 (m, 2H), 1.41–1.33 (m, 2H), 1.18 (s, 3H), 1.12 (t, $^3J_{HH}$ = 7.0 Hz, 9H), 1.07 (s, 3H), 0.49–0.45 (m, 2H).

^{13}C-NMR (101 MHz, DMSO): δ [ppm] = 170.1, 159.2, 146.4, 140.5, 135.6, 127.9, 127.5, 125.6, 122.7, 121.9, 121.6, 119.1, 118.9, 115.4, 106.7, 106.6, 57.6, 52.4, 41.3, 39.5, 34.9, 25.5, 22.7, 19.4, 18.2, 7.4.

IR (ATR): $\tilde{\nu}$ [cm^{-1}] = 3307, 2973, 2928, 1740, 1639, 1611, 1511, 1479, 1334, 1273, 1075, 951, 919, 808, 787, 748.

HRMS: *m*/*z* calculated for $C_{30}H_{42}N_3O_7Si^+$: 584.2787; found: 584.2785.

Functionalization of mesocrystal-biomorph composites with compound 7

A 1% solution of compound **7** in a mixture of EtOH:water (95 : 5) was prepared. 10 mg of mesocrystal biomorph composites were

incubated in 2 mL of the solution overnight. After reaction, the material was centrifuged and washed several times with milliQ water. The structures were dried in a vacuum oven at 40 °C and reduced pressure.

Results and discussion

The synthesis of a silane-functionalized spiropyran is desired for a carrier system based on mesocrystal-biomorph composites (MCBCs). Spiropyrans for the desired silica-modification were already published in the literature,[27] but their accessibility and feasibility were improved in this approach. Based on a literature-known synthesis of a spiropyran bearing a carboxylic acid group,[39] the desired compound was accessible by peptide coupling with 3-aminopropyl triethoxysilane. The reaction scheme is shown in Fig. 3A. Compound 7 was subsequently immobilized on silica-biomorphs. The attachment of functional silanes to various biomorphs was already proven and allowed the desired functionalization of the particle surface with spiropyrans.[15] The scheme of this procedure is shown in Fig. 3B.

Silica-biomorphs were precipitated from barium-containing alkaline silica sol through continued CO_2 diffusion into the sol. The structures remained in the mother sol for 16 h to reach the secondary precipitation stage, where an outer silica shell and additional witherite attach to the structures.[9] A thicker silica layer around the structures is desirable to improve the stability once the inner core dissolves for an improved carrier capacity of the MCBCs. Selective secondary precipitation of witherite crystals around the tips of the structures is desired to induce the heterogeneous magnetite mesocrystal formation. The obtained solid from the biomorph synthesis was rinsed several times with deionized water and dried. The biomorph powder mainly consisted of worm-like braids and helicoidal structures, decorated with witherite crystals on the former globular tips of the biomorphs. The structures were transferred into a magnetite nanocube solution in THF containing a certain amount of oleic acid. The biomorphs act as substrates for the mesocrystal formation. Mesocrystals were formed through gas phase diffusion of the anti-solvent (ethanol) into the magnetite nanocube solution. The particle and the oleic acid concentrations were accurately chosen in order to generate mesocrystals in the range of the tip size (*cf.* Fig. 1). The decreased nanocube concentration leads to smaller mesocrystals and a lower total magnetite loading of the structures. The result is a different responding behaviour in the magnetic field. The decreased oleic acid concentration results in an increased number of smaller mesocrystals. The total magnetite loading remained constant.[9] The obtained MCBCs allow a further post-functionalization treatment with synthesized compound 7 by incubation of the structures in a 1 wt% solution in ethanol/water (95 : 5) for several hours. The generated

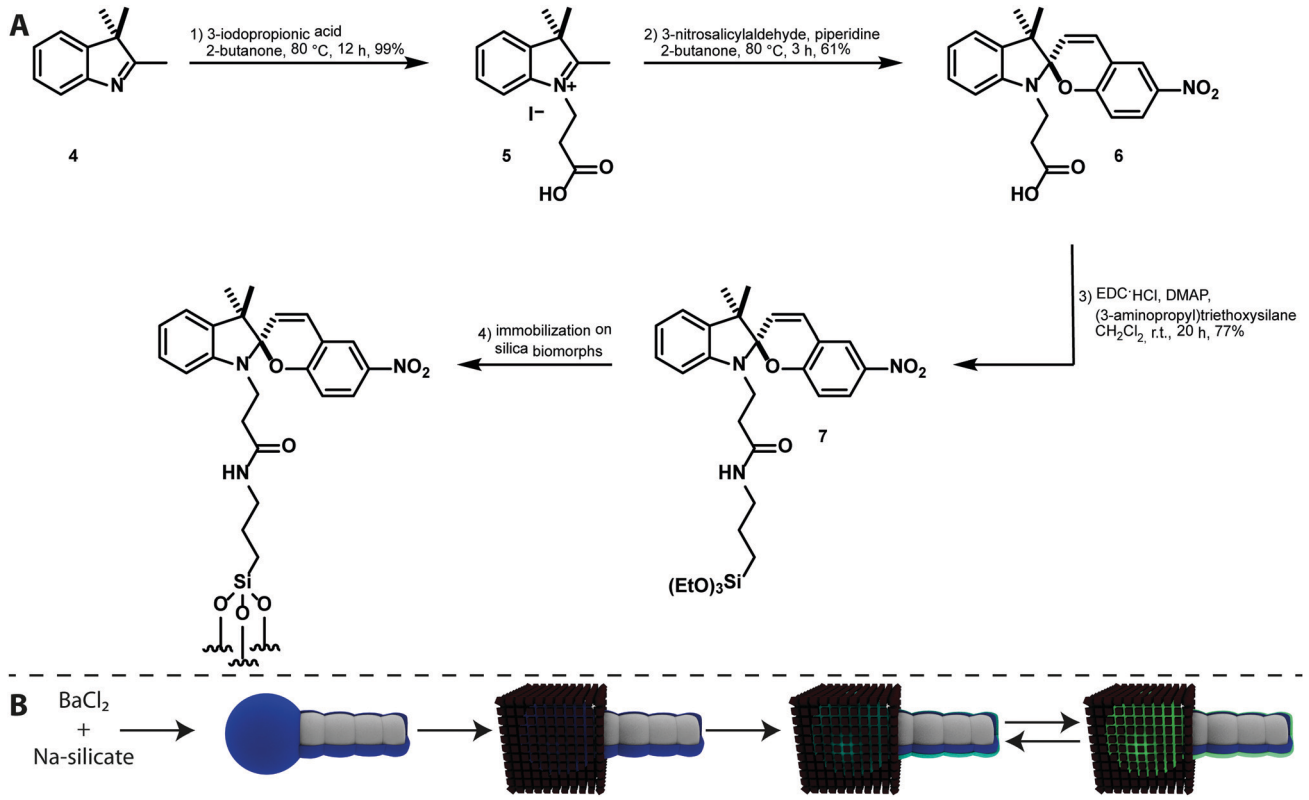

Fig. 3 (A) Synthesis route of the silane functionalized spiropyran (target compound **7**). (B) Formation scheme of the light switchable MCBCs *via* the selective formation of magnetite mesocrystals around silica-biomorphs tips and the post functionalization of their silica shell with compound **7** and its ability of light induced switching on the MCBC surface which induces the glowing (bright green).

functionalized silica layer can be seen in Fig. 3B as a blue layer in the SP form. The UV-irradiation of the material induces the spiro-compound to switch to the MC form, which is indicated by the glowing green colored layer (Fig. 3B). As previously mentioned in the literature, the vastly different properties of the two isomers can be further used for selective catch and release of compounds.[27]

To prove the postulated scheme of the formation of light switchable MCBCs, laser scanning microscopy (LSM) was used. A selective switching of the SP by using the bleach mode was induced with a different wavelength. Therefore, the excitation and emission spectra of compound **7** were recorded and are shown in Fig. 4A. The black spectrum shows the excitation spectrum of the SP-form detecting the intensity of fluorescence at 625 nm while the excitation wavelength changes. The spectrum has a maximum at 555 nm and a shoulder at 520 nm. In addition, several emission spectra were recorded to elaborate the obtained fluorescence as the subject of the excitation wavelength. Using an excitation wavelength of 555 nm, the highest fluorescence intensity was obtained (green spectrum), while an excitation wavelength of 490 nm exhibited lower fluorescence yields (blue spectrum). Nevertheless, the excitation wavelength of 490 nm is the most important result due to the equipped analysing lasers on the LSM. For the fluorescence experiments on the LSM, the imaging was performed with a 488 nm laser (1% laser power, pin hole: 1 a.u.). Imaging the structures with visible light continuously decreased the obtained fluorescence. The degradation of fluorescence is worse with the 555 nm laser, which was additionally chosen in other experiments to turn off the fluorescence while switching the MC back to the SP form. To generate a high amount of fluorescent MCs on the surface, the structures were "bleached" in a region of interest (ROI) with a 405 nm laser (20% laser power, 4 scans). The result is shown in Fig. 4B. The bleaching of the ROI occurred after the first and every third following cycle, indicated by the bluish bars. The measured data originated from a programmed times series. A continuous decrease of the fluorescence intensity in the 3 steps after excitation to a level lower than before the bleaching explains the ongoing decrease of the overall fluorescence intensity. The effect becomes even clearer by considering several cycles. An example is shown in Fig. 4C, where 72 cycles are recorded in the same area. To visualize this effect, Fig. 4D shows a functionalized MCBC in its OFF state, before the frame was illuminated with 405 nm light. Fig. 4E shows the activated structure after excitation. It has to be mentioned that the pictures show a lower end of a functionalized biomorph worm, and the lowest part is in focus. The pin hole cuts off the fluorescent light emitted from the upper part, allowing for an improved image quality and spatial resolution. Therefore, LSM seems to be an appropriate method to prove the incorporation of the functional silane on the structures. This has also been shown in previous studies[15] and demonstrates the suitability of spiropyrans as switchable anchor points on biomorph-based microcarriers.

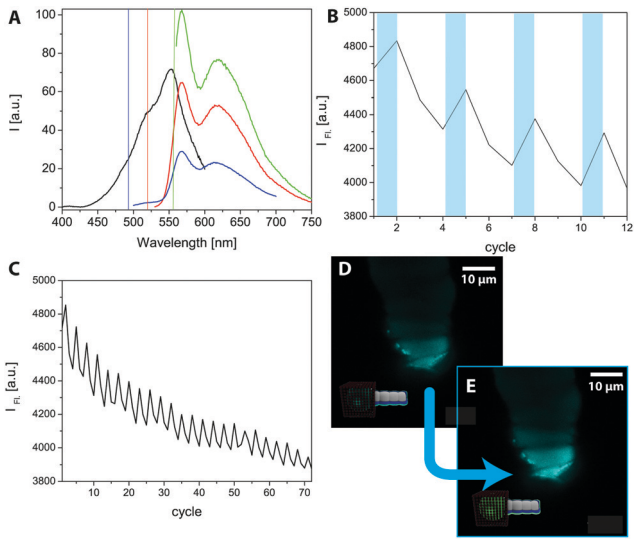

Fig. 4 (A) Excitation (black) and emission spectra of the synthesized compound **7** in ethanol. The vertical coloured lines correspond to the excitation wavelength (blue: 490 nm; red: 520 nm; green: 555 nm). (B) ROI (region of interest) intensity measurement over twelve scanning cycles on the LSM. Bleaching of the region (405 nm; 20% laser power; 4 scans; after the 1st and every following 3rd image) is indicated as bluish areas. (C) Long-term cycling at the ROI over 72 cycles with the same settings chosen for B. (D) LSM image (excitation wavelength: 488 nm, 1% laser power) in false colours of a SP functionalized structure in the OFF (SP) state. (E) LSM image of a SP functionalized structure in the ON (MC) state.

Conclusions

This work highlights a rationally designed pathway to generate easily accessible microcarriers by utilising the silane chemistry toolbox linked to light switchable spiropyrans and the exceptionally shaped ultrastructures called silica-biomorphs. On top a magnetite mesocrystal is used as a responding unit, which results in a full functional metamaterial extending the frontiers in all three used fields (biomorphs, mesocrystals and spiropyrans). The materials described here have potential in a number of applications. Since it is already known from the literature that the merocyanine form can bind metal cations,[30–32] the microcarriers could be used for the transport of metal ions by a magnetic field. Ion release by switching to the spiropyran form would allow reactions of the released cations like catalysis, mineralization, complexation, *etc.* One could also think of binding polar nanoparticles to the merocyanine form, which can be released by light at the location of interest. Also, polar drugs could be bound, transported and released. If the spiropyran form could be used for binding of unipolar species (drugs, molecules, *etc.*), release by light switching to the merocyanine form would enhance the application spectrum of the microcarriers a lot. Future studies will show exciting applications, which will become possible with the mesocrystal functionalized biomorph microcarriers.

Authors contributions

JO and HC conceived the project. LCR and AS synthesized and analysed compound **7** under supervision of TG. JO, JB and RZ

designed the magnetized biomorphs. JO and AS functionalized the biomorphs with compound 7. JO, AS and RZ performed the microscope experiments. The results were discussed by all authors.

Conflicts of interest

The authors declare that there is no conflict of interests regarding the publication of this communication.

Acknowledgements

The authors thank the bioimaging center Konstanz for providing the LSM700 and the European Research Council under the European Unions's Seventh Framework Programme (FP7/2007–2013)/ERC grant agreement no. 340863. The Deutsche Forschungsgemeinschaft (DFG) is acknowledged for funding of the work on mesocrystals within SFB 1214 (project B1).

Notes and references

1 J. M. Garcia-Ruiz, S. T. Hyde, A. M. Carnerup, A. G. Christy, M. J. Van Kranendonk and N. J. Welham, *Science*, 2003, **302**, 1194–1197.
2 J. M. García-Ruiz, E. Melero-García and S. T. Hyde, *Science*, 2009, **323**, 362–365.
3 M. Kellermeier, H. Colfen and J. M. Garcia-Ruiz, *Eur. J. Inorg. Chem.*, 2012, 5123–5144.
4 E. Nakouzi and O. Steinbock, *Sci. Adv.*, 2016, **2**, e1601144.
5 E. Nakouzi, R. Rendina, G. Palui and O. Steinbock, *J. Cryst. Growth*, 2016, **452**, 166–171.
6 M. Montalti, G. Zhang, D. Genovese, J. Morales, M. Kellermeier and J. M. García-Ruiz, *Nat. Commun.*, 2017, **8**, 14427.
7 J. Opel, M. Hecht, K. Rurack, J. Eiblmeier, W. Kunz, H. Colfen and M. Kellermeier, *Nanoscale*, 2015, **7**, 17434–17440.
8 M. Kellermeier, E. Melero-García, W. Kunz and J. M. García-Ruiz, *J. Colloid Interface Sci.*, 2012, **380**, 1–7.
9 J. Opel, J. Brunner, R. Zimmermanns, T. Steegmans, E. Sturm, M. Kellermeier, H. Cölfen and J. M. García-Ruiz, *Adv. Funct. Mater.*, 2019, **0**, 1902047.
10 M. V. Kovalenko, M. I. Bodnarchuk, R. T. Lechner, G. Hesser, F. Schäffler and W. Heiss, *J. Am. Chem. Soc.*, 2007, **129**, 6352–6353.
11 S. Disch, E. Wetterskog, R. P. Hermann, G. Salazar-Alvarez, P. Busch, T. Brückel, L. Bergström and S. Kamali, *Nano Lett.*, 2011, **11**, 1651–1656.
12 J. Brunner, I. A. Baburin, S. Sturm, K. Kvashnina, A. Rossberg, T. Pietsch, S. Andreev, E. Sturm and H. Cölfen, *Adv. Mater. Interfaces*, 2017, **4**, 1600431.
13 H. Cöelfen and M. Antonietti, *Mesocrystals and nonclassical crystallization*, John Wiley & Sons, 2008.
14 H. Cölfen and M. Antonietti, *Angew. Chem., Int. Ed.*, 2005, **44**, 5576–5591.
15 J. Opel, F. P. Wimmer, M. Kellermeier and H. Cölfen, *Nanoscale Horiz.*, 2016, **1**, 144–149.
16 M. H. Sharifian, A. R. Mahdavian and H. Salehi-Mobarakeh, *Langmuir*, 2017, **33**, 8023–8031.
17 D. Kim, H. Jeong, H. Lee, W.-T. Hwang, J. Wolf, E. Scheer, T. Huhn, H. Jeong and T. Lee, *Adv. Mater*, 2014, **26**, 3968–3973.
18 S. Heng, P. Reineck, A. K. Vidanapathirana, B. J. Pullen, D. W. Drumm, L. J. Ritter, N. Schwarz, C. S. Bonder, P. J. Psaltis, J. G. Thompson, B. C. Gibson, S. J. Nicholls and A. D. Abell, *ACS Omega*, 2017, **2**, 6201–6210.
19 W. A. Velema, W. Szymanski and B. L. Feringa, *J. Am. Chem. Soc.*, 2014, **136**, 2178–2191.
20 W. Szymański, J. M. Beierle, H. A. V. Kistemaker, W. A. Velema and B. L. Feringa, *Chem. Rev.*, 2013, **113**, 6114–6178.
21 M. Borowiak, W. Nahaboo, M. Reynders, K. Nekolla, P. Jalinot, J. Hasserodt, M. Rehberg, M. Delattre, S. Zahler, A. Vollmar, D. Trauner and O. Thorn-Seshold, *Cell*, 2015, **162**, 403–411.
22 R. Klajn, *Chem. Soc. Rev.*, 2014, **43**, 148–184.
23 J. Whelan, J. T. C. Wojtyk and E. Buncel, *Chem. Mater.*, 2008, **20**, 3797–3799.
24 A. Radu, R. Byrne, N. Alhashimy, M. Fusaro, S. Scarmagnani and D. Diamond, *J. Photochem. Photobiol., A*, 2009, **206**, 109–115.
25 M.-Q. Zhu, G.-F. Zhang, C. Li, M. P. Aldred, E. Chang, R. A. Drezek and A. D. Q. Li, *J. Am. Chem. Soc.*, 2011, **133**, 365–372.
26 Y.-H. Chan, M. E. Gallina, X. Zhang, I. C. Wu, Y. Jin, W. Sun and D. T. Chiu, *Anal. Chem.*, 2012, **84**, 9431–9438.
27 E. Aznar, R. Casasús, B. García-Acosta, M. D. Marcos, R. Martínez-Máñez, F. Sancenón, J. Soto and P. Amorós, *Adv. Mater.*, 2007, **19**, 2228–2231.
28 H. Gorner, *Phys. Chem. Chem. Phys.*, 2001, **3**, 416–423.
29 N. Shao, J. Y. Jin, S. M. Cheung, R. H. Yang, W. H. Chan and T. Mo, *Angew. Chem., Int. Ed.*, 2006, **45**, 4944–4948.
30 K. H. Fries, J. D. Driskell, G. R. Sheppard and J. Locklin, *Langmuir*, 2011, **27**, 12253–12260.
31 M. Inouye, K. Akamatsu and H. Nakazumi, *J. Am. Chem. Soc.*, 1997, **119**, 9160–9165.
32 T. Suzuki, T. Kato and H. Shinozaki, *Chem. Commun.*, 2004, 2036–2037, DOI: 10.1039/B407342H.
33 T. Wu, G. Zou, J. Hu and S. Liu, *Chem. Mater.*, 2009, **21**, 3788–3798.
34 K. Fries, S. Samanta, S. Orski and J. Locklin, *Chem. Commun.*, 2008, 6288–6290, DOI: 10.1039/B818042C.
35 E. Aznar, R. Casasús, B. García-Acosta, M. D. Marcos, R. Martínez-Máñez, F. Sancenón, J. Soto and P. Amorós, *Adv. Mater.*, 2007, **19**, 2228–2231.
36 S. Samanta and J. Locklin, *Langmuir*, 2008, **24**, 9558–9565.
37 T. Niazov, B. Shlyahovsky and I. Willner, *J. Am. Chem. Soc.*, 2007, **129**, 6374–6375.
38 L. Baumann, K. Schöller, D. de Courten, D. Marti, M. Frenz, M. Wolf, R. M. Rossi and L. J. Scherer, *RSC Adv.*, 2013, **3**, 23317–23326.
39 L. Dingbin, C. Wenwen, S. Kang, D. Ke, Z. Wei, W. Zhuo and J. Xingyu, *Angew. Chem., Int. Ed.*, 2011, **50**, 4103–4107.